DISSERTATION

submitted to the
Combined Faculties of the Natural Sciences and Mathematics
of the Ruperto-Carola-University of Heidelberg, Germany
for the degree of
Doctor of Natural Sciences

Put forward by
M. Sc. Stephan Andreas Häfner
born in: Essen, Germany

Oral examination: December 18th, 2017

From two-body to many-body physics in an ultracold Bose-Fermi mixture of Li and Cs atoms

Referees: Prof. Dr. Matthias Weidemüller
Prof. Dr. Selim Jochim

Zusammenfassung Diese Arbeit beschreibt Streuexperimente an einem ultrakalten Gemisch aus leichten fermionischen ^{6}Li und schweren bosonischen ^{133}Cs Atomen mittels derer Effekte der Zwei-, Wenig- und Vielteilchenphysik untersucht werden. Zu diesem Zweck wird die bestehende Apparatur zur Erzeugung von ultrakalten Gasen erweitert und durch Kühlung der ^{6}Li Atome mittels grauer Melasse sowie einen neuen Aufbau zur hochauflösenden Absorptionsabbildung verbessert. Mittels Atomverlust- und Bindungsenergiespektroskopie werden *s*-, *p*- und *d*-Wellen Feshbachresonanzen in den beiden energetisch niedrigsten Hyperfeinkanälen nachgewiesen. Diese Messungen in Kombination mit einer *Coupled-Channels*-Modellierung ermöglichen eine zehnfach verbesserte Parametrisierung der *s*-Wellen Streulänge sowie eine präzise Bestimmung der LiCs Molekülpotentialkurven. Zum ersten Mal werden Effekte der Spin-Rotations-Kopplung an Feshbachresonanzen beobachtet. Diese spiegeln sich in einer Triplettaufspaltung der *p*-Wellen Komponenten wider. Der Einfluss der Intraspeziesstreulänge auf den heteronuklearen Efimoveffekt wird mittels Messungen der Dreikörperverlustraten in der Nähe zweier Feshbachresonanzen untersucht, welche entweder eine positive oder negative Intraspeziesstreulänge aufweisen. Die Experimente werden quantitativ mit dem hypersphärischen adiabatischen Formalismus verglichen. Die positive Intraspeziesstreulänge kann dabei als Dreikörperparameter interpretiert werden. Die Auswirkungen der Wenigkörperphysik auf das Polaronproblem der Vielteilchenphysik werden diskutiert und Perspektiven für die Realisierung von quantenentarteten Bose-Fermi-Mischungen mit großem Massenungleichgewicht werden vorgestellt.

Abstract This thesis reports on scattering experiments performed with an ultracold mixture of fermionic ^{6}Li and bosonic ^{133}Cs atoms, studying two-, few-, and many-body effects in a highly mass-imbalanced system. To this end, the existing apparatus for the creation of ultracold gases is extended and improved by gray molasses cooling of ^{6}Li and high-resolution absorption imaging. *s*-, *p*-, and *d*-wave Feshbach resonances in the two energetically lowest hyperfine channels are detected via atom-loss and binding energy spectroscopy. These measurements in combination with the coupled channels modeling provide a ten-fold improved parametrization of the interspecies *s*-wave scattering length and precise determination of the LiCs molecular potential curves. For the first time effects of spin-rotation coupling in Feshbach resonances are observed, reflected in a triplet splitting of the *p*-wave components. The influence of the intraspecies scattering length on the heteronuclear Efimov scenario is studied by means of three-body loss rate measurements in the vicinity of two Feshbach resonances, characterized either by a positive or negative intraspecies scattering length. The measurements are quantitatively compared to the hyperspherical adiabatic formalism. The positive intraspecies scattering length can be interpreted as three-body parameter. The impact of few-body physics in the many-body impurity problem is discussed and prospects for realization of quantum degenerate Bose-Fermi mixtures with large mass imbalance are provided.

Parts of this thesis are based on the following manuscript and publications:

Spin-rotation coupling in higher partial wave Feshbach resonances
S. Häfner, B. Zhu, B. Tran, M. Gerken, J. Ulmanis, E. Tiemann, and M. Weidemüller
Manuscript in preparation

Role of the intraspecies scattering length in the Efimov scenario with large mass difference
S. Häfner, J. Ulmanis, E.D. Kuhnle, Y. Wang, C.H. Greene, and M. Weidemüller
Physical Review A **95**, 062708 (2017)

Heteronuclear Efimov scenario with positive intraspecies scattering length
J. Ulmanis, S. Häfner, R. Pires, E.D. Kuhnle, Y. Wang, C.H. Greene, and M. Weidemüller
Physical Review Letters **117**, 153201 (2016)

Universal three-body recombination in an ultracold Li-Cs mixture
J. Ulmanis, S. Häfner, R. Pires, F. Werner, D. Petrov, E.D. Kuhnle, and M. Weidemüller
Physical Review A **93**, 022707 (2016)

Universality of weakly bound dimers and Efimov trimers close to Li-Cs Feshbach resonances
J. Ulmanis, S. Häfner, R. Pires, E.D. Kuhnle, M. Weidemüller, and E. Tiemann
New Journal of Physics **17**, 055009 (2015)

Observation of Efimov Resonances in a Mixture with Extreme Mass Imbalance
R. Pires, J. Ulmanis, S. Häfner, M. Repp, A. Arias, E.D. Kuhnle, and M. Weidemüller
Physical Review Letters **112**, 250404 (2014)

The author furthermore contributed to the following review article:

Heteronuclear Efimov resonances in ultracold quantum gases
J. Ulmanis, S. Häfner, E.D. Kuhnle, and M. Weidemüller
Natlional Science Review **3**, 174 (2016)

Contents

Introduction

Scattering of radiation and particles is ubiquitous in nature. It is responsible for everyday life phenomena like the blue color of the sky and the appearance of rainbows [Nussenzveig, 1977]. It is also the central approach in the study of nuclear, high energy, condensed matter, molecular, and atomic physics. Indeed, most of our current knowledge about the structure of matter has been obtained by either performing scattering experiments, meaning the study of the systems in the continuum, or spectroscopy, the analysis of bound states. Scattering experiments at increasing collision energies allowed to resolve smaller and smaller structures of matter, starting with the discovery of atomic structure by scattering of α particles from gold atoms [Rutherford, 1911], the composition of nucleons evident from electron-proton scattering [Hofstadter, 1961], and eventually investigations of deep inelastic scattering of electrons which eventually led to the verification of quarks. In the study of elementary particles collisions do not only disclose the structure of matter, but also serve as main production mechanism for new particles such as pion production or the creation of the Higgs boson [ATLAS Collaboration, 2012; CMS Collaboration, 2012]. In low energy physics neutron-, electron- or x-ray scattering is used for the study of solid state systems, e.g. for the investigation of crystallographic and magnetic structure [Price, 2015]. Considering this history, it is impossible to overemphasize the importance of collision experiments for the understanding of composite systems in nature.

In the realm of atomic and molecular physics scattering experiments are a major method to investigate the interaction potentials between the scatterers and gain information about their structure. Since these systems are typically probed at low kinetic energy, the wave-nature of the colliding atoms has to be taken into account, thus requiring a quantum mechanical treatment of the scattering process as soon as the de Broglie wavelength of the scatterers is comparable to the characteristic length scale of the interactions. In contrast to classical particle scattering, the wave-like behavior of the scattering particles leads to interference effects, such as apparent in the impressive example of atomic and nuclear “rainbow scattering” [Hundhausen and Pauly, 1964; Goldberg and Smith, 1972; Khoa et al., 2007], where the constructive interference of different possible scattering pathways leads to a strong enhancement of the scattering amplitude at the rainbow angle. Another phenomenon, known as Ramsauer-Townsend effect [Ramsauer, 1921; Bailey and Townsend, 1921], results in a minimum of the scattering cross-section of low-energy electrons by noble gas atoms due to destructive interference. Besides the wave-nature of the colliding particles, the quantum statistics of the scatterers plays an important role. While particles with integer spin obey the Bose-Einstein statistics, half-integer spin particles behave according to the Fermi-Dirac statistics, implying either symmetrization or antisymmetrization of the wavefunction. In the scattering of indistinguishable particles this causes the appearance of symmetry oscillations [Feltgen et al., 1982] in the elastic scattering cross-section.

In the limit of low relative collision energies, the elastic and inelastic scattering cross-sections exhibit threshold behavior and scale with the de Broglie wavelength of the colliding particles [Bethe, 1935; Wigner, 1948; Julienne and Mies, 1989]. As the relative kinetic energy approaches zero, the scattering process only occurs in the zero angular momentum partial wave ($l = 0$) leading to isotropic scattering. Hence, the entire scattering process can be described by a single quantity, the s-wave scattering length a. Thus, in this regime, the particles exhibit universal low-energy scattering behavior which is insensitive to the short-range details of the *two*-body interaction potential. Scattering experiments can not distinguish between two different potentials yielding the same scattering length, since the outcome of the scattering event at low energies will be exactly the same. In the field of ultracold atomic gases, where the de Broglie wavelength is typically much larger than the extent of the interaction potential, the scattering event can be described in this simplified way. Furthermore, the quantum statistics of the scatterers has far reaching consequences at ultracold temperatures. Since identical fermions can only collide in odd partial waves, they will eventually not scatter from each other [DeMarco et al., 1999].

Why is it interesting to study collisions in the ultracold regime, if the scattering event is fully determined by a single parameter? The answer lies in the existence of *resonance* phenomena. Scattering resonances occur if the energy of a quasi-bound state of the two scatterers is equal to the relative kinetic energy of the colliding pair of particles. One particularly interesting type are so-called Fano-Feshbach resonances[1] [Feshbach, 1958, 1962; Fano, 1961], in which a bound state of an excited molecular state is present in the scattering continuum of the colliding pair. Coupling of the scattering atoms to this molecular state will lead to interference structures and resonant behavior, meaning the scattering length a diverges, if the two states are degenerate. The energy of the colliding atoms and the bound-state are controlled via external magnetic fields which enables the relative tuning of their energies and allows to bring both states into degeneracy. Feshbach resonances provide precise control and manipulation of the scattering properties by means of exposing the atoms to an external magnetic field [Chin et al., 2010]. Today, they have become a widely applied technique to effectively control interparticle interactions in the field of ultracold atomic gases, which enabled remarkable achievements such as the investigation of the Bose-Einstein condensate

---

[1] In accord with common nomenclature we refer to them as Feshbach resonances throughout this thesis.

(BEC) to Bardeen-Cooper-Schrieffer (BCS) superfluid crossover [Bartenstein et al., 2004; Regal et al., 2004; Bourdel et al., 2004].

Besides offering control over the scattering length a, the precise characterization of Feshbach resonances provides valuable information about the interatomic interaction potentials by relating the observed resonance positions to energies of molecular bound states. For example the investigation of a series of Feshbach resonances, occurring through coupling to different vibrational and rotational states, gives access to the vibrational and rotational energy levels near the atomic asymptote. Furthermore, weak molecular interactions such as magnetic spin-spin interaction [Stoof et al., 1988; Moerdijk et al., 1995; Ticknor et al., 2004], second-order spin-orbit coupling [Mies et al., 1996; Kotochigova et al., 2000], or even spin-rotation coupling [Hund, 1926; Van Vleck, 1929; Kramers, 1929] become apparent in the multiplet splitting of Feshbach resonances, which allows to precisely determine their coupling strength. Thus, the two fields of molecular spectroscopy and scattering physics mutually profit from each other: Feshbach resonances provide valuable information about bound state energies in regions where conventional spectroscopy is not applicable and thus can be viewed as a high-precision tool of molecular spectroscopy. Molecular physics in turn sheds light on the Feshbach resonance properties and the magnetic field dependent scattering length.

A different resonance phenomenon is the so-called *shape* resonance, which occurs when quasi-bound states that have an energy above the asymptotic energy are present. Such states exist in cases where a potential barrier forms in the effective potential. In case of degeneracy with the relative collision energy of the particles this leads to a resonance phenomenon. Such resonances have been observed for example in the collision of ^{87}Rb atoms [Boesten et al., 1997], where the scattering state is trapped in a long-living compound behind a centrifugal barrier, yielding enhanced photoassociation rates. In ultracold atomic systems, shape resonances are for example used to investigate universal *three*-body bound states, the Efimov states. In the collision of three atoms a three-body recombination resonance, the Efimov resonance, occurs if the energy of an Efimov state, situated behind an effective potential barrier, coincides with the collision energy. These resonances appear as enhancements of the three-body recombination rate [Esry et al., 1999; Nielsen and Macek, 1999; Bedaque et al., 2000]. They have become a standard tool in the exploration of the Efimov scenario, predicting an infinite series of three-body bound states in the limit of resonant two-body interactions. The universality of the Efimov effect, i.e. its existence in different physical systems, may be tested by performing three-body scattering experiments. Measurements of resonance positions for various homonuclear atomic systems revealed unexpected universal behavior, such as the connection between absolute resonance position and the van der Waals interaction of the atomic pair [Berninger et al., 2011]. A series of consecutive Efimov resonances, as observed in this thesis for a heteronuclear system, allows to study the discrete scale invariance of the Efimov scenario and deviations from it.

Scattering is the unifying topic throughout this thesis for the exploration of the quantum mechanical *one-, two-, three-,* and *many*-body systems in an ultracold mixture of fermionic ^{6}Li and bosonic ^{133}Cs atoms. In Ch. 1, the scattering of photons by atoms is used for slowing, cooling and trapping of the two atomic species. The apparatus used in the experiments, including cooling techniques, an approach to simultaneous trapping of this highly mass-imbalanced combination of atomic species in a bichromiatic optical dipole trap, as well as the preparation and detection scheme are introduced. The scattering properties of *two*-bodies, i.e. one Li and one Cs atom, are studied in detail in Ch. 2 by detection and analysis of s-, p-, and d-wave Feshbach resonances. The high-precision measurements provide a precise characterization of the Li-Cs Feshbach resonance properties, i.e. resonance positions and widths. By modeling with a full coupled channels calculation the knowledge of the magnetic field dependence of the two-body interaction strength, the s-wave scattering length a, is improved by almost one order of magnitude in comparison to previous studies [Repp et al., 2013; Tung et al., 2013; Pires et al., 2014a]. Structure analysis of the observed Feshbach resonances provides information not only about the molecular interaction potential, but also high-precision spectroscopy of weak molecular interaction effects such as direct spin-spin interaction or even weaker effects of spin-rotation coupling, as observed for the first time within this thesis. Collisions of *three* particles are extensively investigated in Ch. 3. The existence of shape resonances, the Efimov resonances, allow for the exploration of the heteronuclear Efimov effect by means of three-body loss spectroscopy. In total five Efimov resonances in the vicinity of two Li-Cs Feshbach resonances, that allow to study the universal and non-universal behavior in the Efimov scenario, as well as the role of the intraspecies scattering length are observed. Under certain conditions, we find a new interpretation of the three-body parameter, namely the intraspecies scattering length. In Ch. 4 the complementary approach of spectroscopy is employed to infer the properties of impurities immersed into a *many*-body environment. The Bose polaron in the Li-Cs system and its close connection to few-body physics are introduced. First experimental studies of the polaron by means of rf-spectroscopy are presented. Prospects for the observation of polaronic effects by means of Bragg scattering are given and changes in the experimental apparatus are proposed in order to explore many-body phenomena in the Li-Cs system.

One

1

The invention of laser-cooling and trapping of neutral atoms, for which the Nobel prize was awarded in 1997 [Phillips, 1998; Chu, 1998; Cohen-Tannoudji, 1998], marked the foundation of a new field in physics: the field of ultracold quantum gases. The ability to cool, trap and manipulate neutral atoms enables one to experimentally access the regime of quantum degenerate gases at ultralow temperatures. These tremendous achievements finally led to the first observation of Bose-Einstein condensation [Davis et al., 1995; Anderson et al., 1995] and quantum degenerate Fermi gases [DeMarco and Jin, 1999], triggering the detailed study of their properties via observation of their phase coherence [Andrews et al., 1997; Hall et al., 1998] or quantized vortices of a rotating superfluid [Matthews et al., 1999; Madison et al., 2000; Abo-Shaeer et al., 2001]. Ultracold atom experiments are nowadays realized in many laboratories, providing access to the investigation of quantum physics in a well-controlled and flexible way. In these experiments one (or multiple) atomic species are selectively cooled and trapping under ultra-high vacuum conditions, which isolates these systems extremely well from the environment. By cooling the atoms close to absolute zero one can separate the atomic level spacings from thermal excitations and thus prepare the atoms in well-defined internal states. Furthermore, their two-body interactions are simple to describe and even tunable via magnetic Feshbach resonances (see Ch. 2). These favorable properties enabled tremendous progress in the investigation of few- [Blume, 2012; Wang et al., 2015] and many-body [Bloch et al., 2008, 2012] quantum physics.

In our experiments we study scattering phenomena in ultracold mixtures of fermionic ^{6}Li and bosonic ^{133}Cs atoms. In order to address the universal regimes of two-, few-, and many-body physics we need to cool the two species to temperatures on the order of 100 nK or even below. In this chapter we describe the preparation of ultracold atomic gases from a *one*-body perspective. We start our discussion by studying the behavior of *one* atom in the presence of magnetic and light fields and introduce our experimental approach for the cooling, trapping, and imaging of ultracold Li and Cs samples. The experimental apparatus is introduced in Sec. 1.1.1, followed by a discussion and characterization of the magnetic field coils in Sec. 1.1.2. Our approach to laser cooling of Li and Cs atoms is presented in Sec. 1.2. We introduce the newly implemented gray molasses cooling of Li, which will be beneficial for the future generation of quantum degenerate Li-Cs mixtures (cf. Sec. 1.2.2). The preparation procedure of the highly mass-imbalanced Li-Cs mixture based on our approach of gravitational sag compensation by usage of a bichromatic optical dipole trap is discussed in Sec. 1.3. The newly implemented high-resolution absorption imaging system for the detection of the sample properties is introduced in Sec. 1.4.

1.1. Setup

The experimental apparatus consists of an ultra-high vacuum (UHV) apparatus in which we perform experiments with ultracold ^{6}Li and ^{133}Cs atoms. External magnetic fields, necessary for cooling and manipulation of the atoms are provided by a set of magnetic field coils installed around the main experimental chamber. The light for laser cooling of the two species is generated by frequency stabilized external cavity diode lasers placed on a separate optical table and their light is transmitted through optical fibers to the experiment (see Sec. 1.2). Three lasers provide the light fields for simultaneous optical dipole trapping of Li and Cs, which is described in Sec. 1.3.1. The apparatus has been described in detail in earlier work [Repp, 2013; Repp et al., 2013, 2014; Pires, 2014]. Thus only a brief description with focus on changes in the experimental apparatus and preparation scheme is given. We start with an overview of the ultra-high vacuum apparatus in Sec. 1.1.1, followed by a description and detailed characterization of the various magnetic field coils installed in our setup Sec. 1.1.2.

1.1.1. Vacuum apparatus

Experiments involving ultacold atoms require ultra-high vacuum conditions in order to isolate them from the room temperature environment. Otherwise, collisions with hot background gas lead to fast loss of atoms from the trap and severely limit the lifetime of the sample. However, in the first step of our experiments we need to evaporate the ^{6}Li and ^{133}Cs samples in order to load the atoms in the magneto-optical traps and subsequently perform experiments with them. This generates relatively high pressures and thus we divide our experimental apparatus, shown in Fig. 1.1, into three parts with vastly different pressures: the atomic beam source, the Zeeman slowing region, and the experimental chamber.

The atoms effuse from a double species oven, which is a modified version of the design by Stan and Ketterle [2005]. It was adapted to produce intensive atomic beams of ^{6}Li and ^{133}Cs with independent control over their atomic fluxes by regulating the temperatures of the separated ^{6}Li and ^{133}Cs reservoirs [Repp, 2013]. Typical pressures at the operational temperatures of $T_{\mathrm{Li}} = 625$ K and $T_{\mathrm{Cs}} = 375$ K are on the order of 10^{-3} mbar. The oven section is pumped by a turbomolecular pump with a pumping speed of 80 l/s. The atomic source is connected to the Zeeman slowing region via a differential pumping stage, realized by a 103 mm long tube with a diameter of 7 mm,

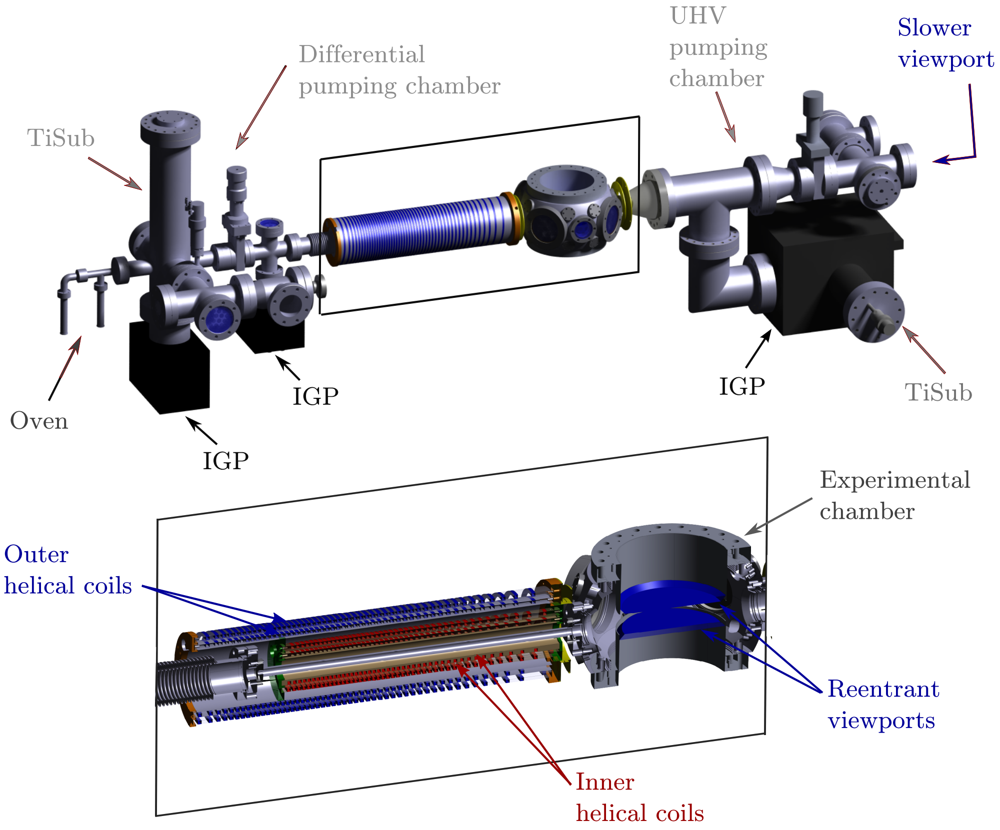

Figure 1.1.: Overview of the vacuum apparatus for cooling and trapping of ^{6}Li and ^{133}Cs. The upper panel shows the complete setup, including the atomic beam source, differential pumping stages, the Zeeman slower, and the main experimental chamber. The ultra-high vacuum conditions are maintained by ion getter pumps (IGP), titanium sublimation (TiSub) pumps, and a non-evaporable getter material. The lower panel displays a cut of the Zeeman slower and the experimental chamber. Reprinted from Repp [2013].

followed by an ion getter pump which further reduces the pressure. The Zeeman slower tube, connecting to the main experimental vacuum chamber, effectively acts as a second differential pumping stage [Repp, 2013]. The magnetic field coils required for sequential Zeeman slowing of ^{6}Li and ^{133}Cs (see Sec 1.1.2) are wound around this tube (see lower panel of Fig. 1.1). The two subsequent differential pumping sections between the atomic source and the main chamber allow to maintain pressure differences of several orders of magnitude. In the main experimental chamber, which is pumped by a combined ion getter/titanium sublimation pump and a non-evaporable getter coating [Benvenuti et al., 1999], we achieve pressures on the order of 10^{-11} mbar, yielding measured $1/e$ lifetimes of the optically trapped atomic samples on the order of one minute.

The main experimental chamber provides optical access for cooling, trapping and manipulation of the atomic samples through four CF63 and two CF40 viewports in horizontal direction. Custom made CF150 reentrant viewports on the top and bottom of the chamber allow the magnetic field coils, described in Sec. 1.1.2, to be placed at a distance of only 19.5 mm from the center of the vacuum chamber, where the atoms are trapped. This reduces the required currents in order to achieve magnetic fields of up to 1350 G. All viewports are anti-reflection coated for the appropriate wavelengths (670 nm, 852 nm, 1064 nm) and are made of Suprasil 3001 in order to minimize absorption of near infrared light and thus reducing thermal lensing effects. The optical access for Zeeman slowing of the atoms emitted from the atomic oven is provided by a viewport mounted opposite to the oven (“Slower viewport” in Fig. 1.1).

1.1.2. Magnetic fields

Magnetic fields, in addition to light fields, are an established tool for the creation and manipulation of neutral atoms at ultracold temperatures. Due to the Zeeman effect, the energies of the atomic hyperfine states with total angular momentum f split according to their projection m_f onto the quantization axis. The Breit-Rabi diagram for ^{6}Li and ^{133}Cs atoms in their electronic ground state are shown in Fig. 1.2. Throughout this thesis, we label the atomic states by their total angular momentum f at zero magnetic field and its projection m_f, combined to $|f, m_f\rangle$. The Zeeman effect allows to tune the energy difference between different hyperfine, as well as electronic energy levels.

Here, we give an overview of the magnetic fields coils employed in our experiments for Zeeman deceleration, magneto-optical trapping and further cooling steps such as degenerate Raman sideband cooling of ^{133}Cs. Furthermore, magnetic fields offer the possibility of spin-selective detection, magnetic levitation, and control over the inter- and intraspecies scattering length via magnetic Feshbach resonances (see Ch. 2). In the last part we present the calibration procedure and characterization of the homogeneous magnetic fields.

Zeeman slower coils

A crucial requirement for the loading of a magneto-optical trap (MOT) is the generation of an atomic beam with high flux and low velocities. The velocity distribution of ^{133}Cs and ^{6}Li atoms emitted from the mixing chamber at a typical temperature of 625 K peaks at approx. 400 m/s and 1700 m/s, respectively [Repp, 2013]. This is orders of magnitude higher than typical capture velocities of the MOT. Two approaches have turned out to be well suited to achieve low-velocity atomic beams: either the use of a two-dimensional MOT [Lu et al., 1996] loaded from a vapor gas, or, as employed in our experiment, the deceleration of atoms emitted from an effusive source by the

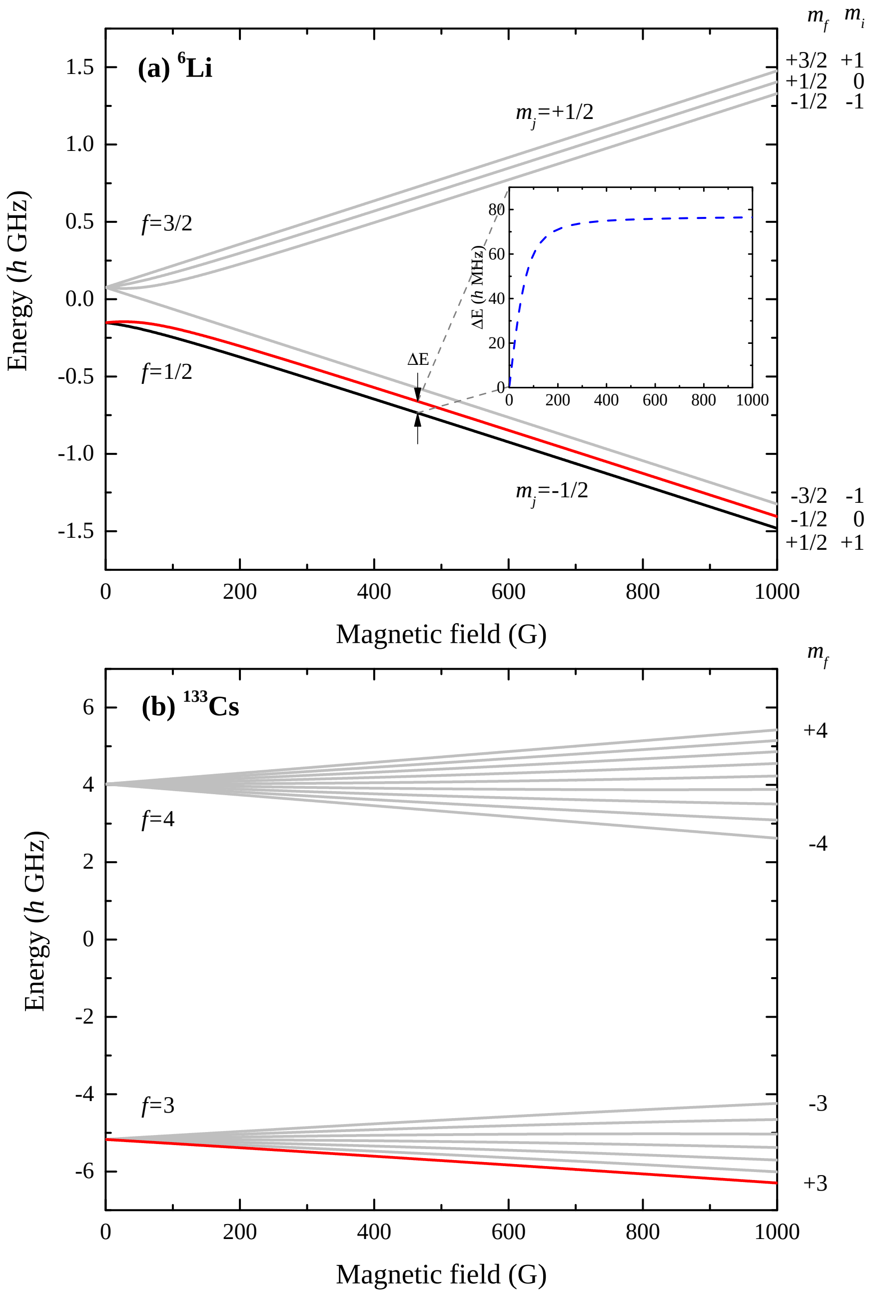

Figure 1.2.: Energy of hyperfine states of (a) ^{6}Li and (b) ^{133}Cs in their electronic ground state in dependence of the magnetic field. f represents the total angular momentum of the atom and m_f, m_j, and m_i are the magnetic quantum numbers of the total angular momentum, electronic angular momentum, and nuclear spin, respectively. In case of ^{6}Li the states are grouped by their total spin $f = 1/2, 3/2$ at low magnetic fields, while at high magnetic fields the two groups are characterized by $m_j = -1/2$ (lower three states) and $m_j = +1/2$ (upper three states). The inset in (a) shows the energy difference between the two energetically lowest hyperfine states, which is between $h \times 74$ MHz and $h \times 77$ MHz for the magnetic field range from 300 G to 1000 G as studied in our experiments. Due to the large hyperfine interaction of Cs, the total angular momentum f and its projection m_f are good quantum numbers in the shown magnetic field range. The states typically used in our experiments are marked in black and red. The magnetic field is conveniently given in units of Gauss, where 1 G $= 10^{-4}$ T.

use of a Zeeman slower [Phillips and Metcalf, 1982], where the atoms are decelerated by the net light force induced by absorption of photons from a laser beam counter propagating to their direction of movement. However, the moving atoms experience a Doppler shift which changes as the atoms are slowed down. We keep the atoms on resonance with the laser light by compensating the Doppler shift with the Zeeman effect in the presence of appropriately shaped magnetic fields. The ideal magnetic field profile scales as $B \propto 1/\Delta\mu\sqrt{1/m}$ [Repp et al., 2014], where $\Delta\mu$ is the difference in magnetic moments of ground and excited states and m is the atomic mass. Thus, the necessary field strengths for Zeeman deceleration of ^{6}Li and ^{133}Cs atoms differ by about a factor of five, which makes slowing with a common magnetic field profile inefficient. However, in order to maintain good optical access to the experimental chamber, we generate the magnetic fields with a single, double-species Zeeman slower, which can be switched between optimized configurations for slowing of ^{6}Li and ^{133}Cs atoms. The coils are implemented as four interleaved helical coils with a variable pitch (see lower panel of Fig. 1.1), following a design by Bell et al. [2010]. The outer pair of coils generate the optimized fields for slowing of ^{133}Cs atoms, while for ^{6}Li all four coils are used. The advantage of this design lies in the lower currents necessary for creation of the Zeeman slowing fields compared to a single coil design. This in turn will lead to lower heating of the coils, while assuring fast switching times between the two different configurations. The last phase of Zeeman slowing is performed in the magnetic quadrupole field of the MOT coils. This procedure minimizes the transversal expansion of the atomic beam [Schünemann et al., 1998] and increases the achievable MOT loading rates. However, in this scheme a smooth transition between Zeeman slower and MOT fields is required, which is assured by two additional adaption coils. The heat generated by the high currents is dissipated by water cooling through the hollow core wires. More details of the design and construction of this double Zeeman slower concept can be found in Repp [2013] and Repp et al. [2014].

Magnetic quadrupole fields

In the following we present technical details of the generation of magnetic gradient fields in our experiment by two pairs of coils: the MOT coils and the Curvature coils that are used for magneto-optical trapping and magnetic levitation of the atomic species.

MOT coils The required quadrupole fields for the MOT are generated by two coils connected in anti-Helmholtz configuration. Each coil is realized by 6 layers of 12 windings with a minimal radius of 100 mm and a minimal distance to the center of the chamber of 102 mm. At the design currents of $\mathrm{I_{Cs}}$=30 A and $\mathrm{I_{Li}}$=97.7 A the coils generate magnetic field gradients of $\partial \mathrm{B_{Cs}}/\partial z$=9.5 G/cm and $\partial B_{\mathrm{Li}}/\partial z$=31 G/cm for the loading of ^{133}Cs and ^{6}Li MOT, respectively. At the same time, the radial fields of

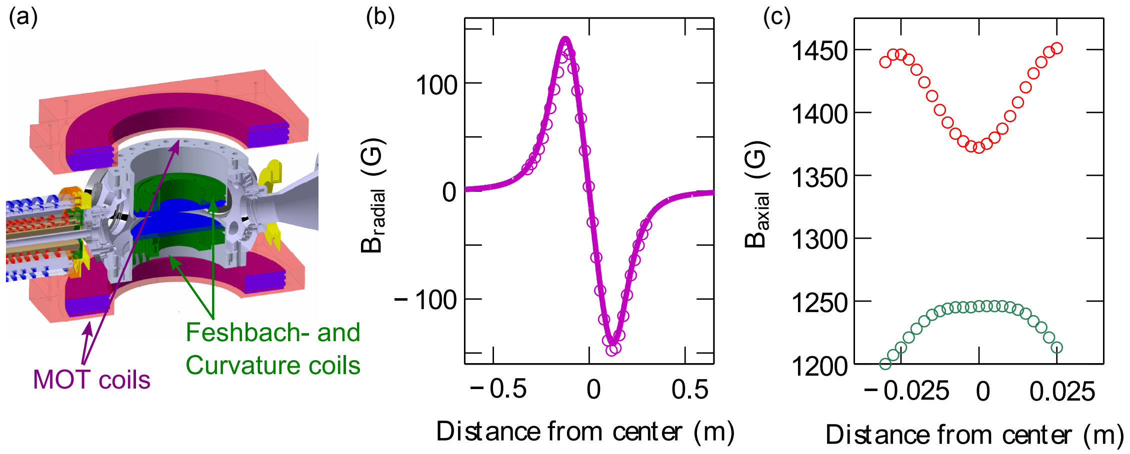

Figure 1.3.: Magnetic field coils around the experimental chamber. (a) Arrangement of the MOT coils (violet), Feshbach and curvature coils (green) at the chamber. (b) Calculated and measured radial magnetic field of the MOT coils. (c) Measured field generated by the Feshbach coils at a current of 400 A (red points). For the green points the inhomogeneity was compensated by the curvature coils. Figure adapted from Repp [2013].

the MOT coils provide the magnetic fields for the last part of Zeeman deceleration, as described previously. In order to dissipate the heat generated by the large currents, the coils are cooled by water flowing through the hollow core wire. The large inductance and eddy currents in our setup limit the switch-off times of the MOT-coils to $\gtrsim$10 ms. Details of their implementation can be found in Repp [2013]

Curvature coils The curvature coils were initially designed to compensate the residual curvature of the magnetic field generated by the Feshbach coils [see Fig. 1.3(c)]. They are implemented as a pair of coils consisting of two layers with two windings each and are placed inside the Feshbach coils. Their construction, production and cooling procedure is similar to the Feshbach coils and can be found in Pires [2014]. In the current setup the curvature coils are connected in anti-Helmholtz configuration in order to generate quadrupole magnetic fields. In contrast to the MOT coils, they offer faster switching times on the order of 1-2 ms, which proved to be crucial for efficient degenerate Raman sideband cooling of ^{133}Cs atoms and gray molasses cooling of ^{6}Li, presented in Sec. 1.2.2.

Homogeneous magnetic fields

Homogeneous magnetic fields are employed for the Feshbach tuning of the inter- and intraspecies scattering lengths, degenerate Raman sideband cooling of ^{133}Cs atoms and controlling the center position of the MOTs. In the following we give details on the

Feshbach coils, Raman coils, offset coils, and compensation coils implemented in our apparatus.

Feshbach coils In order to tune the intra- and interspecies scattering lengths in the Li-Cs mixture we need to generate homogeneous magnetic fields of up to 1000 G (see Ch. 2). This is achieved by placing a pair of Helmholtz coils with a total of 24 windings inside the recess of the reentrant viewports [see Fig. 1.3(a)]. The exact dimensions and production procedure are listed in Pires [2014]. The temperature of the coils is stabilized by cooling water supplied from a custom made industrial cooling unit. At the maximum current of 400 A of our power supplies we achieve magnetic fields of 1350 G. Since the coils are not mounted in perfect Helmholtz configuration, the field in the center of the chamber is inhomogeneous, as can be seen in Fig. 1.3(c). We extract the magnetic field dependence along the axial direction $\mathrm{B}_z = \mathrm{B} + \alpha \mathrm{B} z^2$ with a residual field curvature of $\alpha = 0.0145\ \mathrm{cm}^{-2}$. The current through the coils is measured by a current transducer and actively stabilized with a PID controller. The resolution is limited to ≈ 20 mG by our experimental control system.

Raman coils and offset coils Three additional pairs of coils are installed in order to generate small homogeneous magnetic fields used either for fast displacement of the MOT position or Raman sideband cooling. The coils have a low winding number and are wound directly around the CF63 and CF150 viewports of the main chamber. They offer fast switching times of only 1-2 ms and create fields on the order of $150 - 300$ mG/A. The Raman coils, mounted on the top and bottom reentrant viewports, are additionally used for fine tuning of the external magnetic field in order to precisely control the scattering length in the measurements presented in Ch. 2 and 3. They offer a maximum tuning range of ± 2 G with a theoretical resolution of 0.2 mG, given by the minimal step size of the digital-to-analog converters of our control system.

Compensation coils Many laser cooling techniques, e.g., sub-Doppler and gray molasses cooling, are susceptible to magnetic stray fields. Therefore, we compensate the earth's magnetic field and other stray fields by three pairs of coils. Their dimensions are 800 mm $\times 1380$ mm $\times$ 660 mm with 100 windings in the vertical and one horizontal direction and 150 windings in the other horizontal direction. The compensation cage can create homogeneous magnetic fields of up to 2 G.

Magnetic field calibration

Homogeneous magnetic fields are the key method to control and tune the intra- and interspecies scattering lengths in ultracold atomic samples via magnetic Feshbach resonances (see Ch. 2). Thus, a precise knowledge of the magnetic field strength and

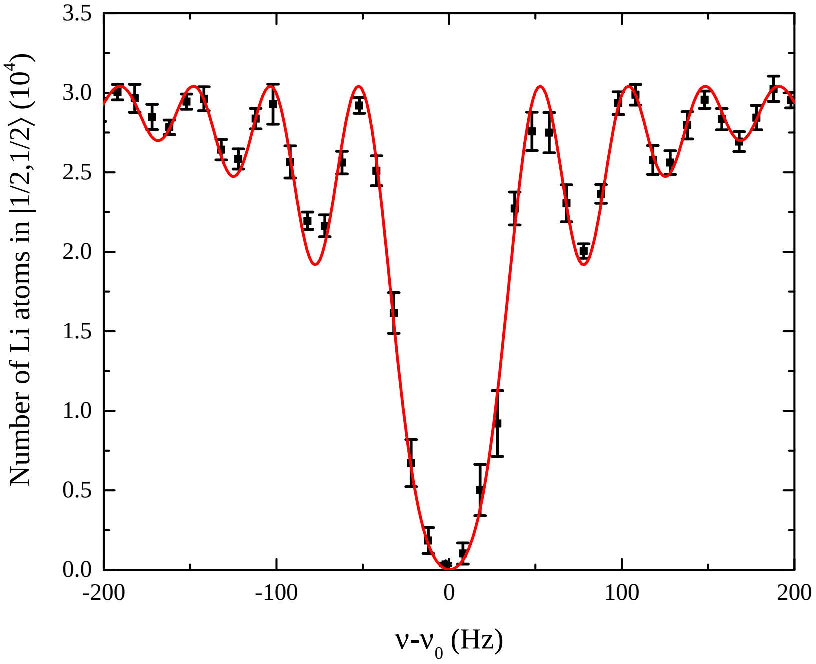

Figure 1.4.: Radio-frequency spectroscopy of the $|1/2, 1/2\rangle$ to $|1/2, -1/2\rangle$ transition. The plot shows the remaining number of Li atoms in state $|1/2, 1/2\rangle$ versus the frequency detuning $\delta = \nu - \nu_0$ from atomic resonance ν_0. The red line is a fit of Eq. (1.1) to the measurements performed with an rf-pulse length of $\tau = 25$ ms. We extract a resonance frequency of $\nu_0 = 76.165892(1)$ MHz, corresponding to a magnetic field of 764.169(1) G, and an on-resonance Rabi frequency of $\Omega_0 = 2\pi \times 60.3(2)$ Hz. The data are averaged over at least 8 measurements and the error bars represent the standard error of the mean.

profile is of major importance for the measurements performed within the course of this thesis. We perform radio-frequency (rf) and microwave (mw) spectroscopy in order to measure the energy difference between two Zeeman states of ^{6}Li in presence of an external magnetic field.

The Breit-Rabi energy diagram of ^{6}Li in its electronic ground state $2^2\mathrm{S}_{1/2}$ is shown in Fig. 1.2(a). Magnetic field calibration is performed by driving transitions between the two energetically lowest states Li$|1/2, 1/2\rangle$ and Li$|1/2, -1/2\rangle$, corresponding to a nuclear spin flip with $\Delta m_i = \pm 1$. The energy difference ΔE between the two lowest states is plotted in the inset of Fig. 1.2(a). In the interesting magnetic field range between 300 G and 1000 G, where the Li-Cs Feshbach resonances occur, this energy difference varies from $h \times 74$ MHz to $h \times 77$ MHz.

A typical rf-spectrum at a magnetic field of 764.191(1) G is illustrated in Fig. 1.4. For these measurements, we prepare a spin-polarized Li sample in spin state $|1/2, 1/2\rangle$ and perform spectroscopy on the transition to state $|1/2, -1/2\rangle$ by applying a rectangular rf-pulse with length τ. The remaining number of Li atoms in state $|1/2, 1/2\rangle$ is recorded and fitted with the lineshape function

$$N(\nu) = N_0 \left[1 - \Omega_0^2 \left(\frac{\sin\left(\Omega_{\text{eff}}(\nu)/2 \times \tau\right)}{\Omega_{\text{eff}}(\nu)} \right)^2 \right], \tag{1.1}$$

where N_0 is the total number of Li atoms, Ω_0 the on-resonance Rabi frequency, τ the rf-pulse length, and $\Omega_{\text{eff}}(\nu) = \sqrt{\Omega_0^2 - (2\pi\delta)^2}$ the effective Rabi frequency, where $\delta = \nu - \nu_0$ is the detuning from the atomic resonance frequency ν_0 and ν is the frequency of the driving field.

We obtain the magnetic field strength by comparison to the Breit-Rabi energy difference. The typical statistical error in the determination of the resonance frequency is on the 1 Hz level corresponding to magnetic field uncertainties of <1 mG.

Magnetic field calibration is typically performed by recording rf-spectra for 4 to 6 uniformly distributed magnetic field control parameters within the range where the experiments are performed. From the resonance frequencies we determine the magnetic field dependence on the control parameter and fit it with a linear function. The magnetic field strength for each control parameter is inferred from this fit and exhibits a typical uncertainty of 9 mG.

The total magnetic field uncertainty is furthermore influenced by the following effects:

- **Field inhomogeneity.** As outlined above, the setup of the Feshbach coils does not correspond to an exact Helmholtz configuration and therefore its magnetic field exhibits a finite curvature even on the symmetry axis of the coils. The magnetic field profile is recorded by performing rf-spectroscopy for different positions of the Li atoms confined in the dimple trap. The obtained profile in the horizontal plane is shown in Fig. 1.5. For the later performed experiments the position of the atoms has been adjusted to the maximum of the measured field, where the inhomogeneity is minimal.

  In addition, we perform mw-spectroscopy on the ^{6}Li electron spin flip transition $|1/2, 1/2\rangle \rightarrow |3/2, +3/2\rangle$. From the measured linewidth we estimate an upper limit of the residual field curvature over the extension of the atomic sample of 8 mG [Ulmanis, 2015]. Part of the linewidth may be a result of other broadening effects, such as short-term fluctuations of the magnetic field.

- **Long-term stability.** Since measurements and magnetic field calibration are not performed simultaneously, we have to consider the absolute stability of the field. Some of the experiments, especially the loss rate measurements presented in Ch. 3, require continuous operation for several days. During this time the temperature of the magnetic field coils or position of the optically trapped atoms might slightly change. This in turn will lead to a slowly varying magnetic field

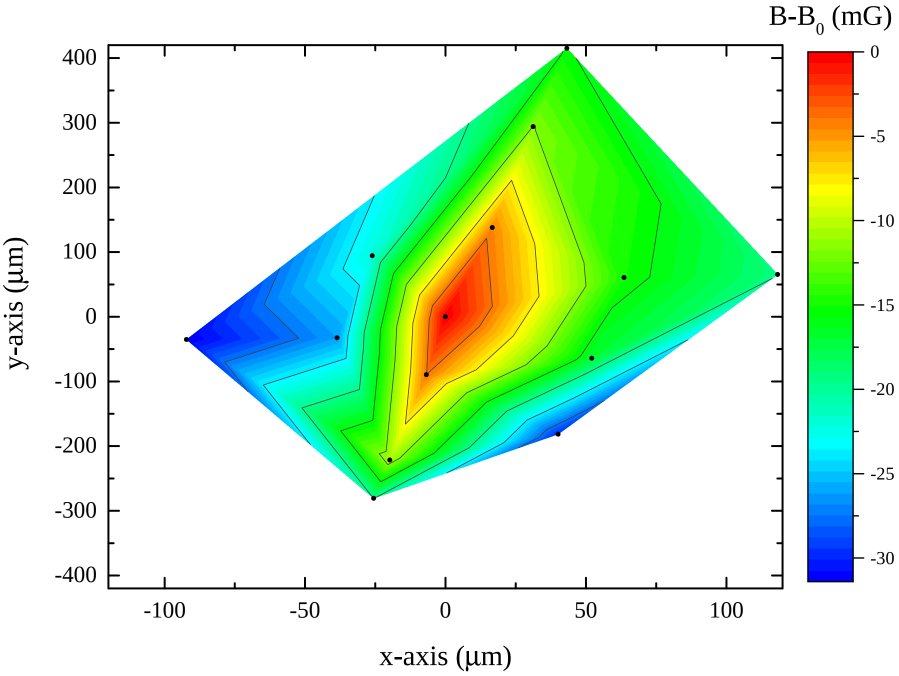

Figure 1.5.: Magnetic field profile in the horizontal plane. The magnetic field is measured by rf-spectroscopy at the position of the black points and is given as deviation from its maximum value $B_0 = 898.327$ G.

strength. We extensively characterized the stability of the magnetic field and obtained a maximum deviation from the mean of 8 mG [Ulmanis, 2015].

- **Length of experimental sequence and pausing of experiments.** As outlined above, high stability of the magnetic field is essential. Highest stability is reached once the whole experimental apparatus has reached a thermal steady state. As soon as the experiments are paused or the length of the experimental sequence is changed, the resistive heat deposited in the magnetic field coils is altered and may lead to deformation and changes in alignment of the pair of coils. The effect on the field value is estimated to be 8 mG [Ulmanis, 2015].

- **Switching time.** Typical times, necessary for the field to stabilize to the new set value, are on the order of 20 ms for a step size of 50 G. We circumvent this limitation in the measurements by a first magnetic field jump to a couple of G away from the measurement interval, where we wait for the field to stabilize. The final field value is then set within <1 ms, which is much shorter than the timescale of the experimentally studied loss processes.

We assume the uncertainties to be uncorrelated and thus add them up quadratically. The total systematic uncertainty of the magnetic field amounts to 16 mG.

1.2. Cooling

In this section we give a short overview of the deceleration and cooling techniques employed in the experiments. We introduce the basic setup for standard laser cooling on the D_2-lines of Li and Cs, focusing on changes with respect to the experimental apparatus extensively described in Repp [2013] and Pires [2014]. In Sec. 1.2.2 we present a newly implemented cooling technique for sub-Doppler cooling of ^{6}Li atoms, namely gray molasses cooling.

1.2.1. Laser cooling on the D_2-lines of Li and Cs

As a first step in the production of ultracold atomic gases the atoms are commonly collected and trapped in magneto-optical traps (MOT), where they are cooled to temperatures in the μK regime. The arrangement of the individual cooling and trapping beams with respect to the main experimental chamber is depicted in Fig. 1.6. The atoms are trapped in a MOT formed by the quadrupole field of the MOT coils (Sec. 1.1.2) and three pairs of counter-propagating laser beams ("Cs MOT" and "Li MOT" in Fig. 1.6) with σ^+-σ^- polarization along all three directions. For Li we use three retro-reflected beams, while for Cs we use six independent beams. However, the fast atoms emitted from the effusive oven (see Sec. 1.1) need to be decelerated in order be trappable by the MOT. In our design, this is achieved by a double-species Zeeman slower (Sec. 1.1.2), where the atoms are slowed by a combination of light fields and magnetic fields. For this, we shine in red detuned laser light from the opposite side of the oven ("Li+Cs Slower beams" in Fig. 1.6).

The necessary light for laser cooling, trapping, and detection (see Sec. 1.4) of Li and Cs is generated by external cavity diode lasers (ECDL) and subsequent amplification by tapered amplifier (TA) systems. The Li laser system consists of one commercially available TA laser with a wavelength of 671 nm (Toptica TA pro 670) and an additional amplification by a homebuilt TA system, designed in the group of S. Whitlock [Faraoni, 2014]. Its frequency is stabilized by modulation transfer spectroscopy on the ^{6}Li D_2-line [Häfner, 2013]. The laser system for manipulation of ^{133}Cs atoms includes two commercial laser sources (Toptica TA pro 850 and Toptica DL pro 850). Their frequency is stabilized to the ^{133}Cs D_2 transition from either of the two hyperfine ground states [Schmidt, 2011; SchÃ¶nhals, 2013]. They provide the cooling and repumping light for Zeeman slowing, magneto-optical trapping, and degenerate Raman sideband cooling of ^{133}Cs atoms.

The required laser frequencies for the different cooling and detection techniques are generated from the laser sources by frequency shifting with acousto-optical modulators (AOMs). The individual light beams are coupled into optical fibers and distributed by fiber port clusters (Schäfter und Kirchhoff) to the experiment. The MOT light for

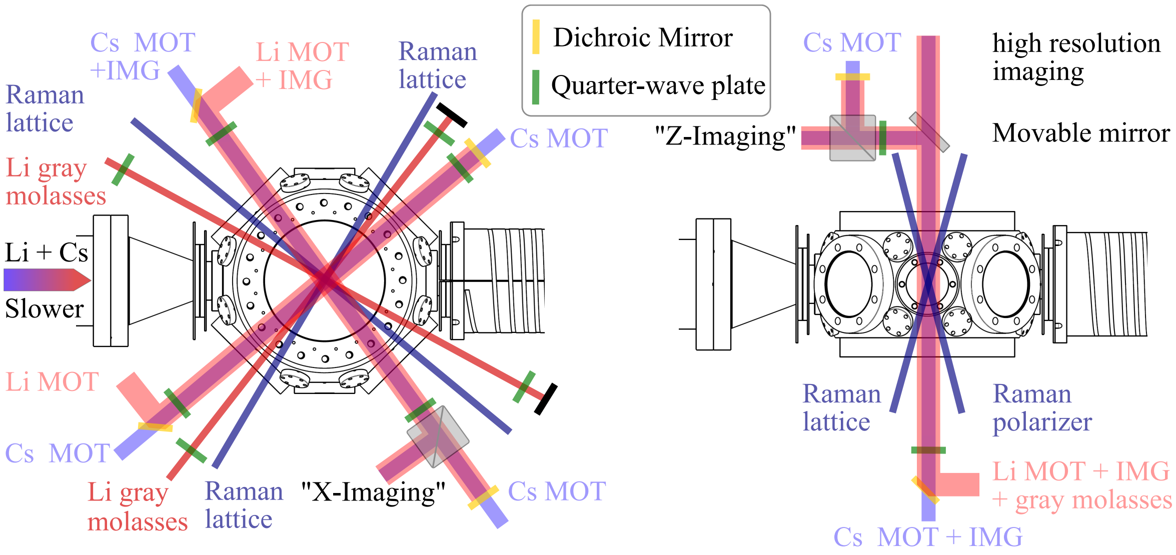

Figure 1.6.: Laser beams for trapping, cooling, and detection of ^{6}Li and ^{133}Cs atoms from a top view (left) and side view (right). Several beams are overlapped with dichroic optics. Figure adapted from Repp [2013].

Li and Cs is overlapped on dichroic mirrors and circular polarized by dual-wavelength quarter-wave plates. Additional beams are used for Zeeman slowing, degenerate Raman sideband cooling of ^{133}Cs, and gray molasses cooling of ^{6}Li. The imaging light is separated from the MOT light by polarizing beam splitters and detected by two cameras. In vertical direction, the imaging light can be directed to a high resolution imaging system, that has recently been implemented (see Sec. 1.4), by moving out a mirror mounted on a translation stage.

We achieve typical MOT loading rates on the order of 5×10^{7} atoms/s for Li and Cs. After the magneto-optical trapping the Li cloud has a typical temperature of 300 μK, while the Cs cloud is cooled further by sub-Doppler cooling and degenerate Raman sideband cooling to temperatures of roughly 1 μK.

1.2.2. Gray molasses cooling of Li

After the standard laser cooling techniques described previously, the temperatures of Li and Cs differ by more than two orders of magnitude. Thus, both species request a vastly different depth of the optical dipole trapping potential (see Sec. 1.3). Due to the relatively high temperature of the magneto-optically trapped Li atoms, the Li sample needs to be cooled evaporatively before the two species are mixed and interact with each other. One possible advancement in our experiments is to lower the temperature of the Li cloud before transferring it into the optical dipole trap, thus providing improved starting conditions for forced evaporative cooling [Ketterle and van Druten, 1996]. However, due to the unresolved hyperfine splitting of the excited

$2^2P_{3/2}$ of ^{6}Li, standard sub-Doppler cooling techniques [Lett et al., 1988] do not work and thus the Doppler temperature of 140 μK is the limit.

In the past few years, two approaches have been introduced: Narrow-line cooling [Duarte et al., 2011; McKay et al., 2011] performed on the $2^2S_{1/2} \rightarrow 3^2P_{3/2}$ transition of ^{6}Li at 323 nm, where the Doppler temperature is reduced to 18 μK, was employed to cool to temperatures of 60 μK. The other method, which has been implemented in our experiment, is so-called gray molasses cooling on the D_1-line. This process is reminiscent to Sisyphus cooling [Castin et al., 1991] and based on the concept of velocity selective coherent population trapping (VSCPT) [Grynberg and Courtois, 1994; Weidemüller et al., 1994]. With this technique sub-Doppler cooling to temperatures in the range of 6 μK to 60 μK has been achieved for Li and K atoms [Rio Fernandes et al., 2012; Salomon et al., 2013; Grier et al., 2013; Burchianti et al., 2014; Gerken, 2016]. In future experiments gray molasses cooling of ^{6}Li is expected to be a key component for the realization of a double superfluid mixture of ^{6}Li-^{133}Cs.

Concept of gray molasses cooling

Gray molasses cooling is based on the following idea: An atom moving in a blue detuned light field with spatially dependent polarization experiences a spatially and state dependent light shift. The light field couples to the atomic states and splits the ground state manifold into dark $|\psi_D\rangle$ and bright $|\psi_B\rangle$ dressed states. While the dark states do not couple to the light field and hence do not experience any light shift, the bright states are subject to a spatially-varying energy shift. The bright state $|\psi_B\rangle$ and dark state $|\psi_D\rangle$ energy in such a light field along the beam propagation axis z is depicted in Fig. 1.7.

In our simple picture an atom is moving along the z direction with a velocity v. When the atom is in state $|\psi_B\rangle$ it will transform its kinetic energy into potential energy when climbing the potential hill. At the top of the hill, where the light-shift is the largest, also the probability to absorb a photon is maximized. The atom gets excited and subsequently either decays to the bright or dark state. If the atom is pumped into $|\psi_B\rangle$, it will again absorb photons until it finally decays to the dark state. In each of these cooling cycles, the atom loses kinetic energy on the order of the bright-state light shift.

Coherent dark state and Λ configuration The emergence of the bright $|\psi_B\rangle$ and dark $|\psi_D\rangle$ states, required for the gray molasses cooling process, can be understood from the three level Λ configuration. A general Λ three-level system is depicted in Fig. 1.8. Here, the two ground states $|1\rangle$ and $|2\rangle$ are coupled to the excited state $|3\rangle$ via light fields with Rabi frequencies $\Omega_1 = \Gamma\sqrt{I_1/2I_{sat}}$ and $\Omega_2 = \Gamma\sqrt{I_2/2I_{sat}}$, where Γ is the inverse of the life-time of $|3\rangle$ and I_1, I_2 the intensities of the two light fields.

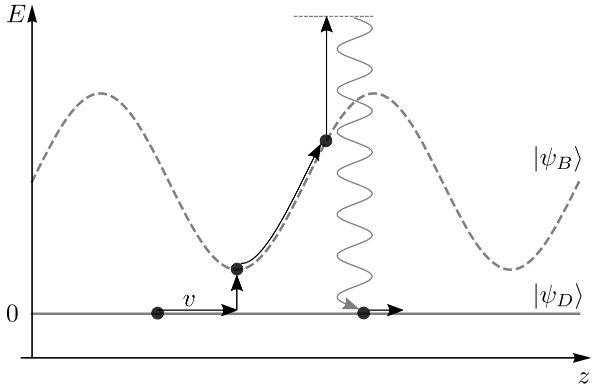

Figure 1.7.: Basic principle of gray molasses cooling. A blue detuned light field with respect to a $f \to f' = f$ or $f \to f' = f - 1$ transition splits the ground state into a bright state $|\psi_B\rangle$ and dark state $|\psi_D\rangle$ manifold. The positive detuning leads to a positive energy shift of the bright state. A spatially varying polarization along z results in a bright-state energy which is spatially modulated. The cooling process occurs, when an atom in $|\psi_B\rangle$ climbs the potential hill and is pumped back into the dark state. The transfer from the dark to the bright state is ensured by velocity selective coupling preferably occurring at the potential minimum of the bright state.

$I_{sat} = \Gamma\hbar\omega_0^3/12\pi^2c^2$ is the saturation intensity of the atomic transition. The two light fields are positively detuned from resonance by δ_1 and δ_2 and $\Delta = \delta_1 - \delta_2$ is their relative detuning.

Under the assumption of equal energies of $|1\rangle$ and $|2\rangle$ and fulfilling the Raman condition $\Delta = 0$, we find the two eigenstates in the dressed-state picture to be:

$$|\psi_D\rangle = \frac{1}{\sqrt{\Omega_1^2 + \Omega_2^2}}(\Omega_2 |1\rangle - \Omega_1 |2\rangle), \tag{1.2}$$

$$|\psi_B\rangle = \frac{1}{\sqrt{\Omega_1^2 + \Omega_2^2}}(\Omega_1 |1\rangle + \Omega_2 |2\rangle). \tag{1.3}$$

We can immediately see, that the eigenstate $|\psi_D\rangle$ does not couple to the interaction Hamiltonian $V = \hbar\Omega_1/2\,|1\rangle\langle 3| + \hbar\Omega_2/2\,|2\rangle\langle 3| + c.c.$ and hence does not experience any light shift. Accordingly, this state is the dark state. The bright state $|\psi_B\rangle$ experiences a positive energy shift (in case of blue detuning $\delta_1 > 0$) of $(\Omega_1^2 + \Omega_2^2)/\delta_1$.

For the gray molasses cooling, however, we require a spatial modulation of the bright-state energy. This can be achieved in a real atomic system, not only consisting of three energy levels, where the coupling between different hyperfine states $|f, m_f\rangle$ and $\left|f', m_f'\right\rangle$ depends on the polarization of the coupling field. While π polarized light drives transitions between levels with $\Delta m_f = 0$, $\sigma^\pm$ polarized light couples levels with $\Delta m_f = \pm 1$. The Rabi frequency for a transition between levels l and m is altered to

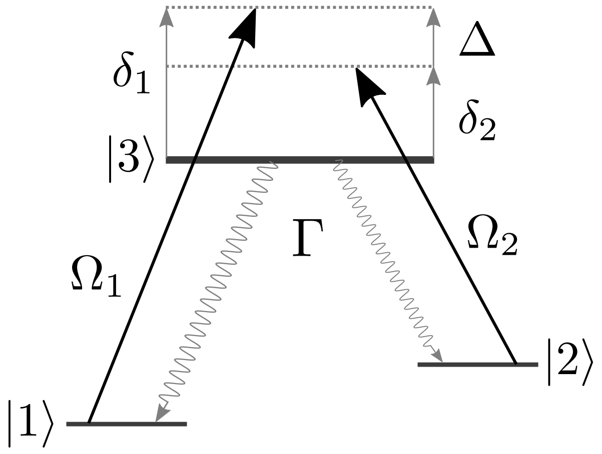

Figure 1.8.: Λ three-level scheme with two ground states $|1\rangle$ and $|2\rangle$ coupled to the excited state $|3\rangle$ by two light fields with Rabi frequencies Ω_1 and Ω_2 with a detuning of δ_1 and δ_2, respectively.

be $\Omega_{lm} = C_{lm}\Gamma\sqrt{I/2I_{sat}}$, where the Clebsch-Gordon coefficients C_{lm} are polarization dependent. This leads to an energy shift of the bright state, which depends not only on light intensity, but also on its polarization. Thus, by introducing polarization gradients, the light shift can be spatially modulated even for constant light intensity.

A spatially varying light polarization can be achieved by several beam configurations. The lin⊥lin configuration, characterized by two counter propagating beams with orthogonal linear polarizations, creates a polarization lattice with a period of $\lambda/2$, where the polarization changes from linear to σ^+ to linear orthogonal to the first one to σ^-. Another possibility is the standard configuration for realization of a MOT with counter propagating beams with σ^+ and σ^- polarizations. This configuration generates a more complex three dimensional polarization lattice, which was implemented in our experiment.

Velocity selective coupling In order to perform multiple cooling cycles the atoms need to be transferred form the dark to the bright state. The transition is ensured by velocity selective coupling. For an atom with momentum p Papoff et al. [1992] found the following transfer probability,

$$P_{|\Psi_D\rangle\rightarrow|\Psi_B\rangle} = 2\left(\frac{\Omega_1\Omega_2}{\Omega_1^2+\Omega_2^2}k\frac{p}{\hbar}\right)^2\delta_1\frac{\delta_1}{(\Omega_1^2+\Omega_2^2)}, \tag{1.4}$$

where k is the wave number of the atomic transition. P is inversely proportional to the light shift of the bright state and hence the coupling will preferably take place where the energy difference of bright and dark state is minimal, i.e. at the valley of the bright state energy.

The transfer probability is furthermore proportional to the velocity v^2 [Dalibard and Cohen-Tannoudji, 1989], leading to VSCPT [Arimondo, 1991], in which the slow atoms accumulate in the dark state $|\psi_D\rangle$. By successive repetitions of this process, the atom is cooled until it reaches almost zero velocity. In principle this process is neither limited to the Doppler temperature nor the single photon recoil temperature [Esslinger et al., 1996]. However, imperfections in the polarization of the light field and off-resonant couplings to other atomic states lead to deviations from the ideal scenario of Fig. 1.7 and thus limit the achievable temperatures. In contrast to Sisyphus cooling, gray molasses cooling does not rely on a hyperfine structure in the excited state and is also efficient even if all levels in the excited state are addressed [Sievers et al., 2015]. Additionally, gray molasses cooling operates at positive detuning, while standard sub-Doppler cooling on the D_2 requires negative detuning and does not exhibit VSCPT.

Implementation and characterization

In the following we describe the specific requirements for gray molasses cooling on the D_1-line of ^{6}Li and describe our experimental setup. In the last part a detailed characterization of the molasses cooling process is presented.

Gray molasses of ^{6}Li The energy level scheme of the D_1 transition of ^{6}Li is depicted in Fig. 1.9. We apply gray molasses cooling on the D_1-line, since the $j = 1/2 \rightarrow j' = 3/2$ transition (D_2-line) does not allow the process of gray molasses cooling. The two ground states $|f = 1/2\rangle$ and $|f = 3/2\rangle$ are coupled to the excited state manifold by the repumping and cooling beam, respectively. Their detunings from resonance are labeled δ_{cool}, δ_{rep} and their difference is given by $\Delta = \delta_{cool} - \delta_{rep}$. In order to fulfill the Raman condition $\Delta = 0$ that is necessary for efficient performance of gray molasses cooling, we need two laser frequencies separated by the hyperfine splitting of the ground state $\delta_{hfs} = 228.2$ MHz at a wavelength of approximately 670.992 nm.

Setup The setup for the gray molasses cooling, which has recently been improved with respect to the system presented in Gerken [2016], is divided into four separable parts and schematically shown in Fig. 1.10. The required light is provided by a Toptica DLC TA pro 670 laser system, delivering up to 500 mW around a wavelength of 671 nm. An electro-optic phase modulator (Qubig EO-Li6-3M), operating at a frequency of 228.2 MHz, is used to generate the necessary repumping light by means of frequency sideband modulation. This ensures, that the Raman condition $\Delta = 0$ is met. A small part of the laser power (approx. 15 mW) is amplified by a homebuilt tapered amplifier system. After collimation and passing a dual stage optical Faraday isolator (Qioptiq FI-670-5TVC) we achieve a linearly polarized beam with a power of around 450 mW. Two AOMs are used for frequency tuning and switching on and off of the laser beams.

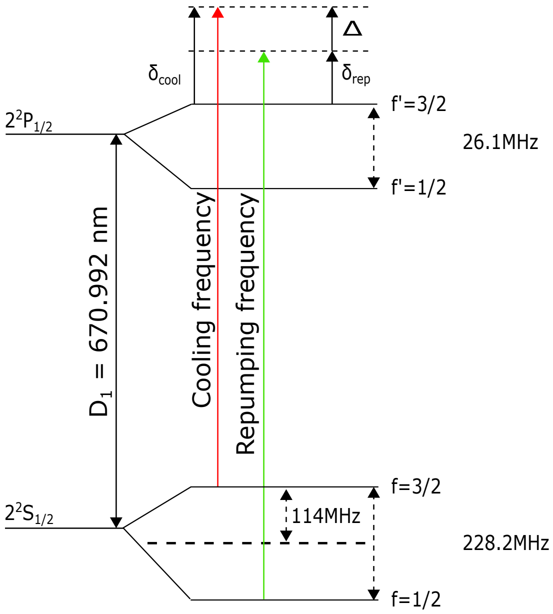

Figure 1.9.: Level scheme of the D_1 transition of ^{6}Li and realization of gray molasses cooling. Cooling and repumping frequencies couple both ground states to an excited state manifold with a blue detuning. The detunings for the cooling and repumping beam are labeled by δ_{cool} and δ_{rep}, respectively. The relative detuning is $\Delta = \delta_{cool} - \delta_{rep}$. Figure adapted from Gerken [2016].

The laser light is coupled in three optical fibers and is guided to the experimental chamber. The beams are circular polarized and back reflected after twice passing a $\lambda/4$ wave plate, as shown in Fig. 1.6. We achieve intensities of $I_{cool} = 15 I_{sat}$ and $I_{rep} = 0.75 I_{sat}$, where the ratio has been experimentally optimized [Gerken, 2016]. The laser frequency is stabilized by modulation transfer spectroscopy on the D_1-line of ^{6}Li [McCarron et al., 2008; Gerken, 2014]. The light passes an acoustic-optic modulator in double pass configuration before it enters the spectroscopy cell. This allows us to adjust the overall detuning of cooling and repumping light $\delta_{cool} = \delta_{rep}$. More details of the experimental setup can be found in Gerken [2016].

Experimental sequence A typical experimental sequence for gray molasses cooling of ^{6}Li is shown in Fig. 1.11. We start with the MOT loading phase for a typical duration of 1.5 s. Subsequently, the Zeeman slower coils and beams are switched off and the MOT loading process is stopped. In the next step we transfer the MOT from the large MOT coils to the curvature coils (see Sec. 1.1.2), by linearly ramping down the current in the MOT coils and simultaneously increasing the current through the curvature coils within 30 ms. The atomic cloud is compressed by increasing the magnetic field gradient while decreasing the power and detuning of the MOT laser beams within

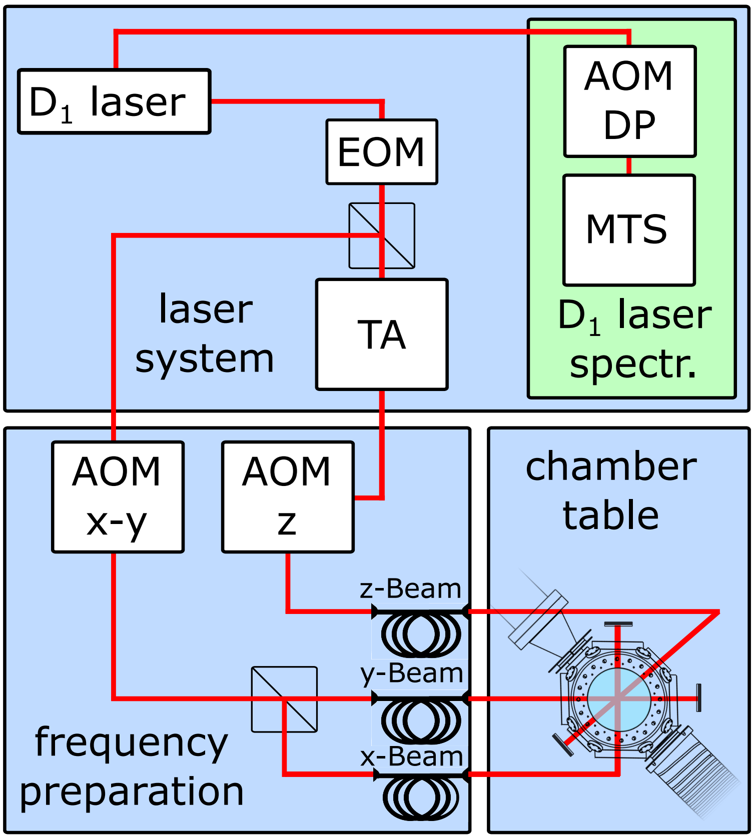

Figure 1.10.: Schematic setup for gray molasses cooling of ^{6}Li, consisting of the four parts: laser system, frequency preparation, frequency stabilization, and cooling beams at the experimental chamber. Figure adapted from Gerken [2016].

70 ms. At this stage the sample typically consists of 4×10^7 Li atoms at a temperature of 240 μK. The MOT beams and curvature coils are turned off and after a time Δt a short gray molasses cooling phase with a typical duration of $\tau = 1$ ms is applied. The atomic cloud is imaged by absorption imaging after a variable time-of-flight (TOF) and we deduce the number of atoms, cloud widths σ_x and σ_y, and temperature of the gas (see Sec. 1.4).

The exchange phase between the MOT and Curvature coils proved to be essential for efficient gray molasses cooling. The high sensitivity of the molasses with respect to magnetic fields was investigated in detail in Gerken [2016]. It was found, that even fields of a couple of 100 mG lead to severe heating of the sample, because of breakup of the Raman condition due to Zeeman shifts. Therefore, it is required that no magnetic fields are present during the gray molasses cooling phase. The magnetic gradient fields, generated by the MOT coils, display a characteristic switch-off time of 10 ms (see Sec. 1.1.2). During this time the Li cloud will have expanded and will no longer be captured in the molasses. Therefore, we use the curvature coils, which

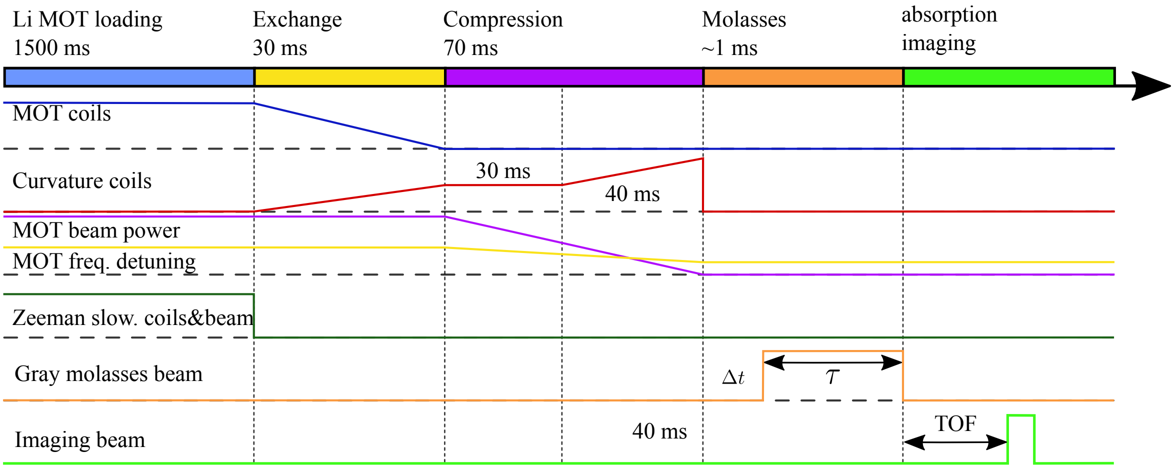

Figure 1.11.: Experimental sequence for gray molasses cooling of ^{6}Li. After loading of the MOT, the atomic cloud is transfered from the magnetic gradient fields of the MOT coils to the curvature coils and finally compressed. A gray molasses cooling pulse with a duration of τ is applied after a waiting time Δt. Finally, the cloud is imaged via absorption imaging after a variable time-of-flight (TOF).

feature a much faster switch-off due to their vicinity to the atoms and their small inductance.

Characterization The most important parameter for gray molasses cooling is the relative detuning Δ. We measure temperature and number of atoms in dependence of the detuning between repumping and cooling frequency Δ in a range from -2.5Γ to 2Γ and present the results in Fig. 1.12. The other parameters have been optimized in other measurements and are kept constant: intensities $I_{cool} = 15 I_{sat}$, $I_{rep} = 0.75 I_{sat}$, detuning $\delta_{cool} = 4\Gamma$, duration $\tau = 1$ ms and time delay $\Delta t = 0$.

For large detuning $|\Delta| > \Gamma$, the number of atoms is at a constant level of 2.5×10^7, corresponding to roughly 60% of the initial atom number, while the temperature is decreased to about 150 μK. Here, the states are not well separated into dark and bright states and the cooling process is perturbed. In case of small positive detuning $\Delta \approx 0.5\Gamma$ the temperature is dramatically increased and all atoms are lost from the molasses. For this detuning the bright states are energetically lower than the dark states. During each optical pumping cycle, the atoms gain kinetic energy and can escape the molasses. At a detuning of about $\Delta = -0.25\Gamma$ all atoms can be captured. However, the achievable temperatures are slightly elevated to roughly 80 μK due to a larger energy spacing between dark and bright states, resulting in a reduced velocity selective coupling and hence a slow-down of the cooling process. The best cooling performance is observed at the the Raman condition $\Delta = 0$. We achieve a minimal temperature of 42 μK with a captured number of atoms of 3.2×10^7, corresponding to a capture efficiency of 80%. During the gray molasses cooling phase the phase-space

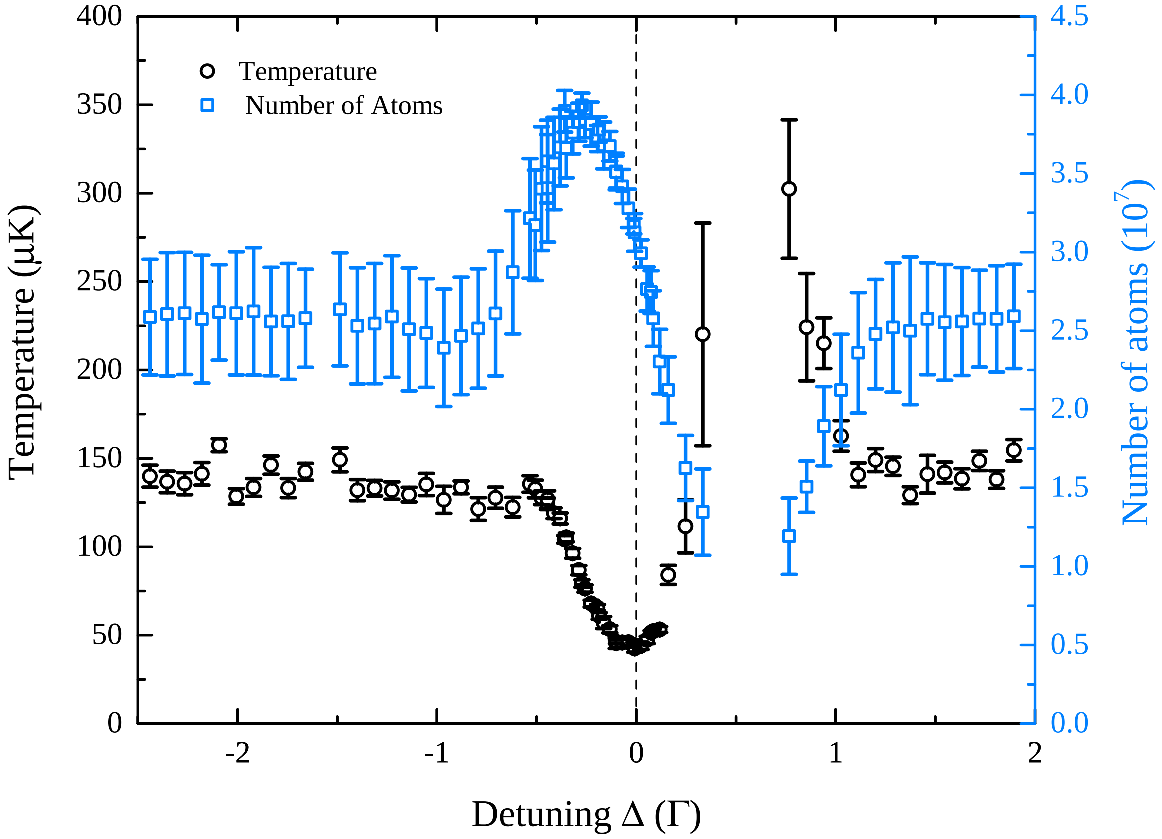

Figure 1.12.: Temperature (black circles) and number of atoms (blue squares) after $\tau = 1$ ms of gray molasses cooling as a function of the relative detuning Δ in units of Γ with $\delta_{cool} = 4\Gamma$, $I_{cool} = 15 I_{sat}$ and $I_{rep} = 0.75 I_{sat}$. The lowest temperature $T = 42$ μK is reached at the Raman condition $\Delta = 0$ (dashed vertical line). The highest number of atoms is captured at $\Delta \approx -0.25\Gamma$, where we trap 100% of the atoms of the initial sample at slightly higher temperatures of ≈ 80 μK. Figure adapted from [Gerken, 2016].

density is increased by one order of magnitude, offering improved starting conditions for subsequent loading in an optical dipole trap. By further adaption to our experimental setup, i.e. by fast modulation of the dimple optical dipole trap (see Sec. 1.3.1) in order to increase its trapping volume, we expect to increase the transfer efficiency by up to one order of magnitude [Burchianti et al., 2014] and thus obtain better starting conditions for subsequent evaporative cooling.

1.3. Trapping

The realization of atomic gases at ultracold temperatures relies on the capability of capturing neutral atoms in a confining potential for a certain time. Optical dipole traps (ODTs) are a widely used method to create such potentials [Grimm et al., 2000].

We introduce the basic principle of optical dipole traps and their implementation in our experiment for simultaneous confinement of ^{6}Li and ^{133}Cs atoms in Sec. 1.3.1. We discuss the challenges of simultaneous trapping posed by the large mass imbalance of this mixture and present the solution, a bichromatic optical dipole trapping scheme, described in Sec. 1.3.2. Combining the methods of slowing, cooling, and trapping presented in the previous parts, we describe our preparation scheme for an ultracold Bose-Fermi mixture of ^{133}Cs and ^{6}Li at temperatures of down to 100 nK in Sec. 1.3.3.

1.3.1. Optical dipole potentials

Optical dipole traps are a convenient tool to provide trapping potentials for neutral atoms, which are (almost) independent of their internally occupied state. They are based on the interaction of an induced electric dipole moment with the oscillating electric field of the light. The dipole potential for a neutral particle with a frequency-dependent, complex polarizability $\alpha(\omega)$ interacting with a light field with intensity distribution $I(\vec{r})$ and angular laser frequency ω can be expressed by [Grimm et al., 2000]:

$$U_{\mathrm{dip}}(\vec{r}) = -\frac{1}{2\epsilon_0 c}\Re(\alpha(\omega))I(\vec{r}) \approx -\frac{3\pi c^2}{2\omega_0^3}\left(\frac{\Gamma}{\omega_0-\omega}+\frac{\Gamma}{\omega_0+\omega}\right)I(\vec{r}), \qquad (1.5)$$

where ω_0 is the resonance frequency of the atomic transition, Γ the natural linewidth, c the speed of light, and ϵ_0 the vacuum permittivity. Thus the dipole potential is proportional to $-\Re(\alpha)$ and intensity $I(\vec{r})$ of the light field. In the approximation on the right hand side, a large detuning $|\omega_0 - \omega| \gg \Gamma$ and negligible saturation is assumed. For positive polarizabilities (usually the case for red detuning) the dipole potential is negative and atoms are attracted into the light field. The potential minima are at positions of maximum intensity. For $\Re(\alpha) < 0$ the atoms are repelled from the light field and trapped in minima of the light intensity. A plot of the polarizability $\Re(\alpha)$ of ^{6}Li and ^{133}Cs in their electronic ground state in dependence of the laser wavelength can be found in Fig. 1.13(a). The polarizability of Li atoms shows one[1] pronounced resonance feature at a wavelength of 671 nm and is positive for longer wavelengths. In Cs two resonances at the D_1 (894.6 nm) and D_2 (852.3 nm) line are clearly visible. Above 894.6 nm the dipole potential is attractive, while below 852.3 nm it is repulsive. At a wavelength of 880.25(4) nm [Arora et al., 2011] the polarizability of Cs is zero, and thus Cs atoms in their ground state do not experience any light force. This wavelength is called tune-out wavelength [LeBlanc and Thywissen, 2007] and offers the possibility for species selective trapping. Another special wavelength for the trapping of Li-Cs

---

[1] In fact we expect two resonance features located at the D_1 and D_2-lines. However, the small hyperfine splitting in ^{6}Li of only ≈ 10 GHz, or equivalently 0.015 nm, is not resolved in Fig. 1.13.

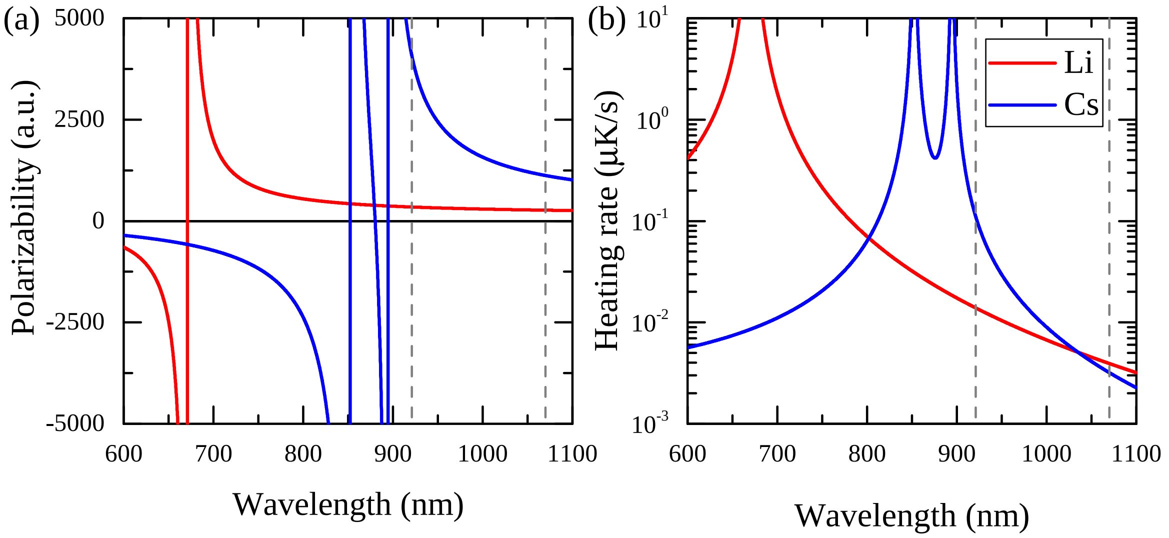

Figure 1.13.: (a) Polarizability $\Re(\alpha)$ and (b) heating rate for a typical intensity of 10^4 Wcm^{-2} in dependence of wavelength λ for ^{6}Li (red) and ^{133}Cs (blue). The wavelengths of the dimple and tunable dipole traps are indicated by the vertical dashed lines.

mixtures is 879.23 nm, where the polarizabilities are equal and thus the dipole trapping potential is the same for both species [Häfner, 2013].

Another crucial property of dipole traps is off-resonant scattering of photons from the trapping light. The scattering rate is given by [Grimm et al., 2000]

$$\Gamma_{\mathrm{sc}} = \frac{1}{\hbar\epsilon_0 c}\Im(\alpha(\omega))I(\vec{r}) \approx \frac{3\pi c^2}{2\hbar\omega_0^3}\left(\frac{\omega}{\omega_0}\right)^3\left(\frac{\Gamma}{\omega_0-\omega}+\frac{\Gamma}{\omega_0+\omega}\right)^2 I(\vec{r}), \tag{1.6}$$

where $\hbar$ is the reduced Planck constant. For a single atomic resonance, the scattering rate scales as I/Δ^2, where $\Delta = \omega - \omega_0$ is the detuning from resonance. Continuous absorption and re-emission of photons leads to heating of the sample. The heating rate in a three-dimensional harmonic trap is given by $\dot{T} = T_{\mathrm{rec}}\bar{\Gamma}_{\mathrm{sc}}/3$, where $T_{\mathrm{rec}} = \hbar^2 k^2/m$ is the recoil temperature, defined by the energy transfer during emission of a photon with wavenumber k [Grimm et al., 2000], and $\bar{\Gamma}_{\mathrm{sc}}$ is the trap averaged scattering rate. The wavelength dependent heating rate of Li and Cs is shown in Fig. 1.13(b) for a typical trapping light intensity of 10^4 Wcm^{-2}. Close to the resonances, the heating rates are severely enhanced, limiting the lifetime and achievable temperature of the atomic samples. Thus it is beneficial to choose large detunings from the atomic resonances, while at the same time increasing the intensity to achieve sufficient trapping potentials.

Optical dipole traps are conveniently realized by focusing Gaussian laser beams. In the vicinity of the bottom of the potential ($x = y = z = 0$), which is probed by the confined atoms in thermal equilibrium, it can be approximated by a three-dimensional harmonic potential

$$U_{\text{dip}}(x, y, z) = \frac{1}{2} m \left(\omega_x^2 x^2 + \omega_y^2 y^2 + \omega_z^2 z^2 \right) , \tag{1.7}$$

where ω_x, ω_y, and ω_z are the trapping frequencies. For a thermal Boltzmann distribution $n(x, y, z) = n_0 \exp\left(-U(x, y, z)/k_B T\right)$ with temperature T, peak density n_0, and Boltzmann constant k_B, the density distribution in the trap is given by

$$n(x, y, z) = n_0 \exp\left(-\frac{x^2}{2\sigma_x^2}\right) \exp\left(-\frac{y^2}{2\sigma_y^2}\right) \exp\left(-\frac{z^2}{2\sigma_z^2}\right) , \tag{1.8}$$

with the corresponding widths of the distribution

$$\sigma_i = \sqrt{k_B T / m\omega_i^2}. \tag{1.9}$$

The peak density in the trap is calculated as

$$n_0 = N \bar{\omega}^3 \left(\frac{m}{2\pi k_B T} \right)^{3/2} , \tag{1.10}$$

where $\bar{\omega} = \sqrt[3]{\omega_x \omega_y \omega_z}$ is the mean trapping frequency and N the total number of atoms. For a given dipole potential the trapping frequency ω_i scales as $1/\sqrt{m}$ and is a factor of about five different for Li and Cs. However, the width σ_i of the density distribution and its peak density n_0 are solely determined by the parameter $m\omega_i^2 = \partial^2 U_{\text{dip}}(x, y, z)/\partial x_i^2|_{x=y=z=0} \propto \Re(\alpha(\omega))$, which is determined by the curvature of the potential around the minimum. Thus, these properties do not show any mass scaling, but depend on the given intensity distribution of the laser beams and the strength of the potential. The width of the atomic distribution varies as $\sqrt{\Re(\alpha(\omega))}$, which might vary considerably for different atomic species.

The ratio between potential depth and heating rate for each species can be tuned by the wavelength of the trapping light, while the absolute trap depth and the shape of the potential is controlled by the intensity distribution of the trapping light.

In the following we describe the optical dipole traps implemented in our experimental setup. Their configuration with respect to the main chamber is depicted in Fig. 1.14:

- The **dimple trap** is formed by two intersecting beams from a 200 W fiber laser with a wavelength of 1070 nm focused to a beam waist of 62 μm. The two beams are crossed under an angle of 8.5° and are linearly polarized. At the maximal power of approximately 100 W per beam a maximal trap depth of 1.2 mK for Li is achieved, which is necessary in order to transfer the Li atoms from the MOT to the dipole trap. The large trapping frequencies on the order of 10 kHz ensure fast thermalization during loading and evaporative cooling. This trap is

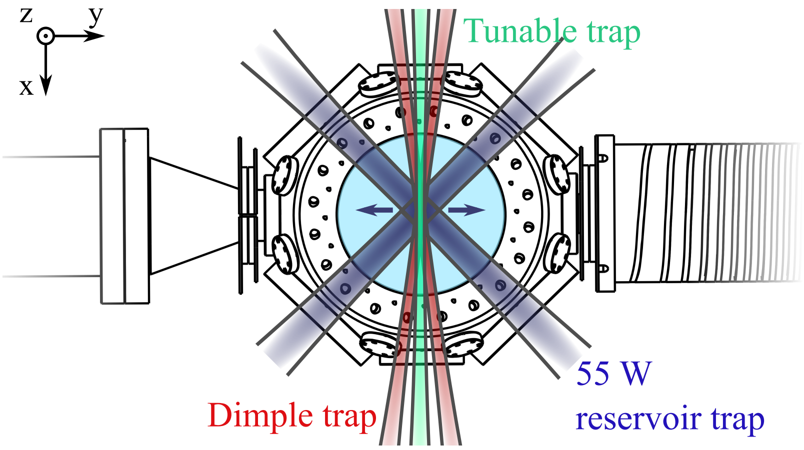

Figure 1.14.: Configuration of the three optical dipole traps in our experiment. The position of the reservoir trap (blue) can be shifted with a piezo mirror. This allows to optically transport Cs atoms to the dimple trap (red). The wavelength tunable trap (green) is implemented as single beam along the long axis of the cigar shaped dimple trap and offers almost independent control over the Li and Cs trapping potentials. Figure adapted from Repp [2013].

used also for combined trapping of Li and Cs atoms (see Sec. 1.3.3). A detailed description of the design and implementation can be found in Heck [2012].

- **Reservoir trap.** Since ^{133}Cs atoms are optically cooled routinely to temperatures below 1 μK, we only require trapping depths on the order of 10 μK during the capture process. On the other hand, the large background scattering length of $\approx 2000\ a_0$ leads to large three-body loss rates [Weber et al., 2003], which scale as n^3 [see Eq. (3.36) and (3.37)]. Thus, it is beneficial to keep the Cs density low. We achieve this by trapping the Cs atoms in a large volume optical dipole trap, which reduces the Cs density to roughly 10^{11}atoms/cm^3. A suitable trapping potential is realized by crossing two laser beams with 300 μm beam waist crossed under an angle of 90°. The light is provided by a Nd:YAG solid-state laser with a wavelength of 1064 nm and 55 W output power. The position of the crossing region can be moved by a piezo-driven mirror which is used for mixing of the two species, as described in Sec. 1.3.3. The design considerations, implementation and characterization of the trap are given in Arias [2014].

- **Tunable trap.** The optical trapping potentials for ^{6}Li and ^{133}Cs provided by the dimple trap, operating at a wavelength of 1070 nm, differ by a factor of four, as can be seen in Fig. 1.13(a), leading to different trap depths and sizes of the atomic clouds. Individual control over the trapping potentials for each species can be gained by adding an additional optical dipole trap with a different wavelength. This procedure was introduced by LeBlanc and Thywissen [2007] and is known as species-selective trapping. In order to be able to implement different possible trapping scenarios, we design the trap to be wavelength tunable. This is achieved by usage of a titanium sapphire laser (Coherent MBR-100 pumped by a Coherent Verdi V-18), delivering up to 3 W in the wavelength range from 700 nm to 1030 nm. The trap is realized by a single beam, aligned along the long axis of the cigar shaped dimple trap, with a beam waist of 60 μm. This ensures nearly harmonic potentials in combination with the dimple trap. The complete design and implementation in our experiment can be found in Häfner [2013].

1.3.2. Combined trapping of Li-Cs

For experiments with ultracold mixtures several challenges arise for the combined trapping of different atomic species. As outlined above, the trap depth and the density distribution depend on the real part of the wavelength dependent atomic polarizability [see Fig. 1.13(a)]. For a mixture confined in a single-wavelength optical dipole trap, this leads to different trap depths and consequently different temperatures of the two species[2]. When we let the two species collide with each other, this leads to sympathetic evaporation of one species by the other one and may result in complete loss of one species from the trap.

Another challenge arises for mixtures with large mass imbalance, such as Li-Cs, due to the significantly different gravitational potentials. The gravitational potential tilts the trapping potential causing anharmonicity of the trapping potential and a species dependent shift of the potential minimum, commonly referred to as gravitational sag. In a combination with large mass imbalance, e.g. Li-Cs with a mass ratio of $m_{\mathrm{Cs}}/m_{\mathrm{Li}} \approx 22$, this leads to a large differential gravitational sag and eventually complete spatial separation of the two species [Fig. 1.16(e)].

Gravity can in principle be compensated by applying a magnetic field gradient in vertical direction, which generates a force proportional to the magnetic moment μ of the atom. The necessary field gradient for magnetic levitation depends on the magnetic-moment-to-mass ratio μ/m and in general is different for each species and internal state. The magnetic field dependent magnetic moments $\mu(B)$ and the magnetic-moment-to-mass ratio $\mu(B)/m$ for alkali-species in their lowest hyperfine state are shown in Fig. 1.15. From the plot we see that the magnetic-moment-to-mass ratio is almost equal for the combinations of Rb-Cs and Na-K, which makes simultaneous levitation feasible in these mixtures [Debatin, 2013]. For combinations, where one atom does not possess any magnetic moment, e.g. Yb or Sr, external magnetic fields can be employed for species-selective manipulation [Roy et al., 2017]. However, ^{6}Li and ^{133}Cs

---

[2] The temperature obtained after evaporative cooling is typically proportional to the trap depth [Ketterle and van Druten, 1996].

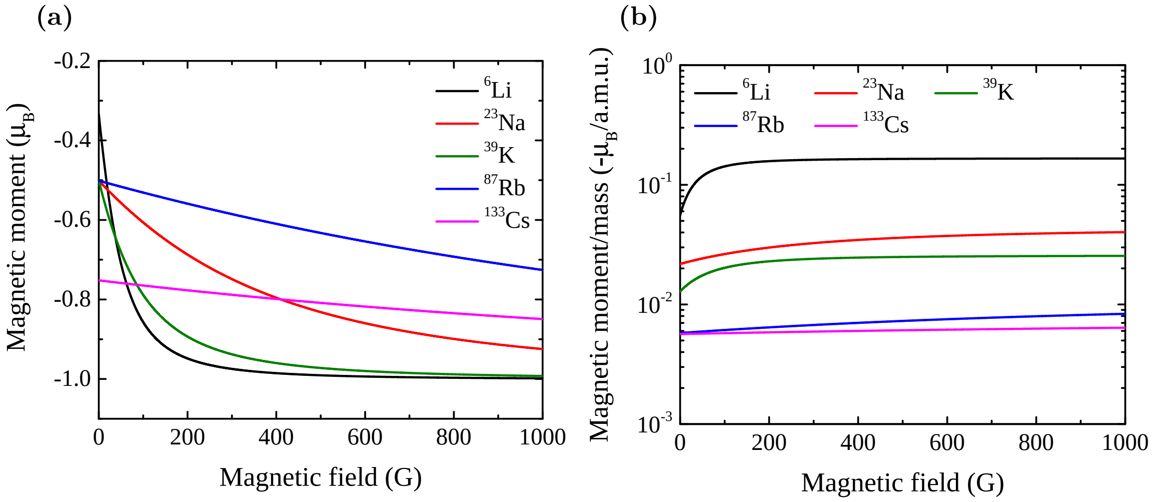

Figure 1.15.: (a) Magnetic moment μ dependence on the magnetic field for the hyperfine groundstate of alkali-metal atoms. (b) Magnetic moment divided by atomic mass. Atomic parameters taken from [Gehm, 2003; Steck, 2010; Tiecke, 2011; Steck, 2015, 2008].

atoms require magnetic field gradients differing by a factor of ≈ 30 in the interesting magnetic field region around 900 G, and thus simultaneous levitation is impossible.

In the following, we present the approach realized in our experiment for simultaneous trapping of Li and Cs atoms at temperatures of down to 100 nK, while still maintaining sufficient spatial overlap. We start with the potential generated by the dimple trap with a wavelength of 1070 nm. As long as the dipole potential dominates over the gravitational potential $U_{\mathrm{dip}} \gg mgw_0$, where w_0 is the extension of the ODT potential, the difference of atomic polarizabilites of a factor of four results in potential depths differing by the same factor $U_{\mathrm{dip}}^{\mathrm{Cs}} \approx 4U_{\mathrm{dip}}^{\mathrm{Li}}$. When the intensity of the dimple trap is further reduced, the influence of the gravitational potential becomes significant and eventually dominates over the ODT potential. The trapping potentials and the corresponding normalized density distributions for two different beam intensities are illustrated in Fig. 1.16(a,b,d,e). The two trapping situations are chosen to yield Li-Cs mixtures at temperatures of 400 nK [Fig 1.16(a,b)] and 100 nK [Fig. 1.16(d,e)][3]. Along the x axis, corresponding to the long axis of the dimple trap (see Fig. 1.14), the trapping potentials are simply proportional to the beam intensity. If the temperature of the gas is assumed to be proportional to the total trap depth U_{dip}, the density distributions are even unaffected when lowering the intensity as can be seen in Fig. 1.16(a,d)[4]. Along the direction of gravity (the z direction) the total potentials are

---

[3] We assume, that the temperature is approximately related to the trap depth via $U_{\mathrm{dip}} = \eta k_B T$ [Ketterle and van Druten, 1996] and choose $\eta_{\mathrm{Li}} \approx 10$ [Heck, 2012] and $\eta_{\mathrm{Cs}} \approx 5$ [Pires, 2014].

[4] For the plotting of Fig. 1.16(d) we did not include the gravitational potential in our model.

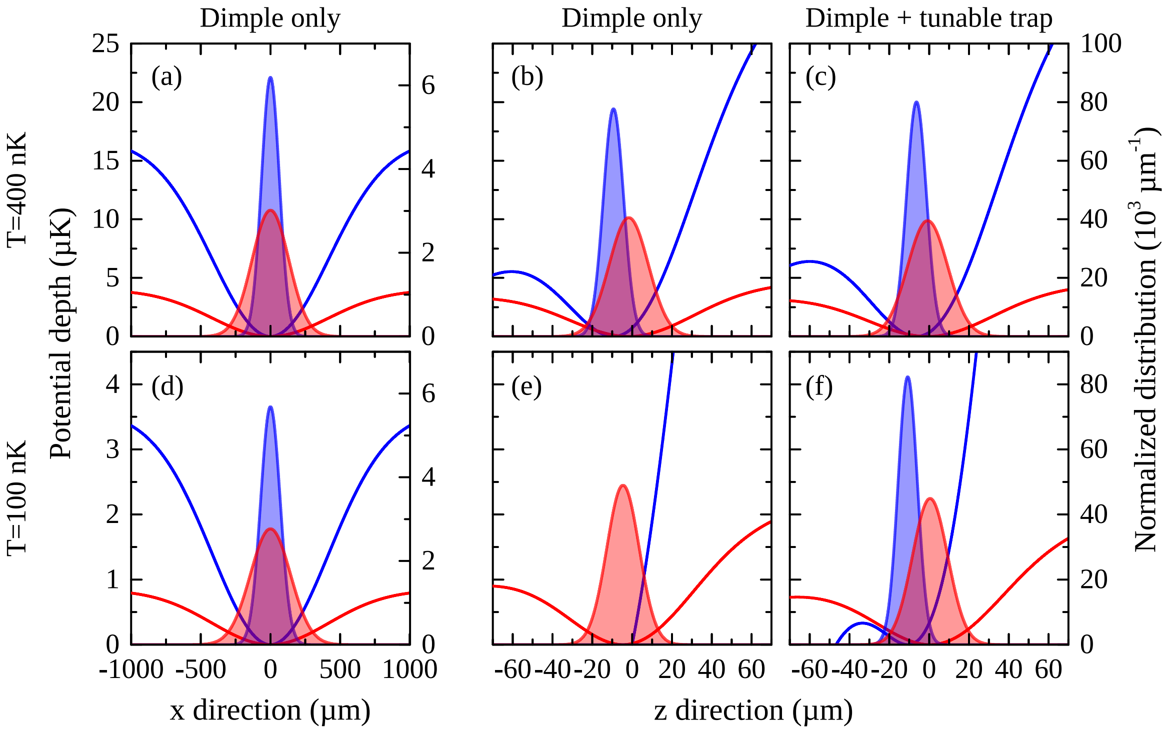

Figure 1.16.: Trapping potential for Li (red) and Cs (blue) atoms in their ground state together with the corresponding atomic distributions for temperatures of 400 nK (top) and 100 nK (bottom). (a) and (d): Along x axis (long symmetry axis of dimple trap, Fig. 1.14) for confinement in the dimple only. The spatial distributions overlap, irrespective of the trap depth. (b) and (e): Along the vertical z axis (direction of gravity) for confinement with the dimple. The potentials are tilted due to gravity and the species start to spatially separate. At 400 nK the overlap decreases to 80% and at 100 nK the Cs atoms can no longer be held against gravity. (c) and (f): Combined trapping potentials of the bichromatic optical dipole trap. The configuration corresponds to a vertical displacement of 25 μm and dipole trap powers of $P_{\text{dimple}} \approx P_{\text{tunable}} \approx 40$ mW, which restores the Cs trapping potential. The differential sag amounts to 16 ± 5 μm yielding an estimated spatial overlap of 45%. Figure adapted from Ulmanis et al. [2016a].

tilted. Especially for Cs this leads to a drastic reduction in effective trap depth and an evident shift in the position of the potential minimum. At the same time the position of the Li atoms is almost unchanged and thus the spatial overlap of the two species is drastically reduced. When further decreasing the trap intensity, corresponding to the potentials shown in Fig. 1.16(e), the ODT can no longer confine the Cs atoms. The single-wavelength trapping configuration, used for the experiments presented in Sec. 2.2 and partially for Sec. 3.4, is thus limited to trap Li-Cs mixtures of down to 200 nK before the atomic clouds separate completely and the Cs atoms are lost from the trap.

The gravitational sag and loss of Cs confinement at low laser intensities is overcome by combining dimple and tunable dipole trap. As seen above, this trap is employed to increase the trapping potential for Cs in order to restore confinement of Cs atoms against gravity. At the same time, the potential depth of Li should only experience minor changes. Therefore we choose a wavelength of 921.2 nm for the tunable trap, where the polarizability for Cs ($\alpha_{\mathrm{Cs}} = 4060$ a.u.) is a factor of 12 larger than for Li ($\alpha_{\mathrm{Li}} = 345$ a.u.), and thus we gain almost independent control over the individual trapping potentials and atomic density distributions. This wavelength was optimized experimentally as a compromise between differential polarizability and sufficiently small heating rates of Cs. The differential gravitational sag is reduced by shifting the center of the tunable trap slightly above the dimple trap position and thereby "pulling" up the Cs atoms to the position of the Li atoms [cf. Fig. 1.16(f)]. The relative trap depths and residual gravitational sag can be controlled by the relative shift and intensities of the two dipole traps. For our experiments on the Efimov effect, presented in Ch. 3, we require similar trap depths of approx. 500-700 nK and a finite spatial overlap of the atomic clouds. This situation can be achieved by a vertical displacement of the tunable trap of 25 μm and powers of $P_{\mathrm{dimple}} \approx P_{\mathrm{tunable}} \approx 40$ mW. The corresponding potentials and atomic density distributions are shown in Fig. 1.16(c,f), yielding a differential gravitational sag of 16 ± 5 μm resulting in an estimated spatial overlap of 45% and temperatures of down to 100 nK.

1.3.3. Preparation of ultracold Li-Cs mixtures

In this section, we describe our approach to prepare ultracold Li-Cs mixtures using the experimental apparatus described in Sec. 1.1. Details of the MOT loading sequences and further optical cooling and spin-polarization techniques are provided in Repp [2013] and Pires [2014]. We start with a discussion of the preparation of mixed samples in the single-wavelength dimple trap, where the minimal achievable temperature is limited to roughly 200 nK, and proceed with our bichromatic trapping approach allowing to produce Li-Cs mixtures at temperatures of 100 nK.

Single wavelength trapping

A schematic overview of our experimental sequence is given in Fig. 1.17. Each experimental cycle starts by loading a Cs MOT for a typical duration of 1 s, followed by a 35 ms long compression and a sub-Doppler cooling phase [Drewsen et al., 1994], where temperatures on the order of 10 μK are reached. The Cs atoms are further cooled and spin-polarized in the energetically lowest Zeeman state $|3, +3\rangle$ by degenerate Raman sideband cooling (DRSC) [Vuletić et al., 1998; Kerman et al., 2000; Treutlein et al., 2001]. After switching on the reservoir trap (see Fig. 1.14) to approximately 25 W, the

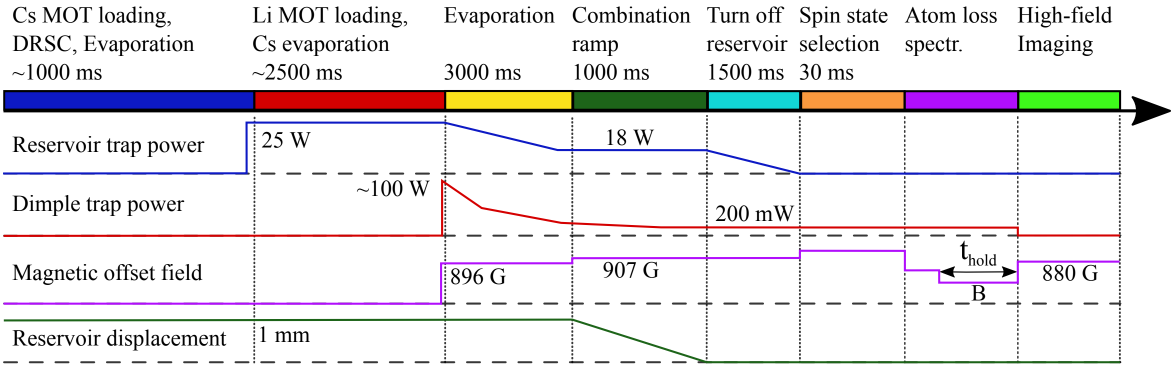

Figure 1.17.: Experimental sequence for preparation of ultracold Li-Cs mixtures at temperatures down to 200 nK. Schematic time series of reservoir and dimple trap beam powers, as well as the magnetic offset field and reservoir displacement. Details are given in the text.

atoms in the wings of the dipole trap are heated due to conversion of potential into kinetic energy. After one quarter of the reservoir trapping period, the atoms accumulate in the center of the trap, where the kinetic energy is maximal. At this time a second 1.5 ms long DRSC pulse is applied, removing the excess kinetic energy. The beam powers of the Raman lattice and polarizer, as well as the magnetic fields are ramped down in order to achieve temperatures of less than 1 μK and a spin polarization of 90%. We apply a homogeneous external magnetic field of ≈ 4.5 G to keep the ^{133}Cs sample spin polarized.

In the next step we load ^{6}Li atoms in a spatially separated MOT for 2.5 s. During a compression phase the temperature is reduced to ≈ 300 μK and the Li atoms are transferred into the dimple trap, located approx. 1 mm away from the position of the Cs atoms confined in the reservoir trap. At the same time, we perform optical pumping into the $f = 1/2$ hyperfine manifold, where the Li atoms equally populate the two sub-levels Li$|1/2, 1/2\rangle$ and Li$|1/2, -1/2\rangle$.

We perform simultaneous forced evaporative cooling of the two separated atomic samples at a magnetic offset field of ≈ 896 G, where the large intraspecies scattering length $a_{\mathrm{Li}} \approx -8000$ a_0 and $a_{\mathrm{Cs}} \approx 400$ a_0 ensure fast thermalization of both species. After 3 s the two traps are overlapped within 1 s by moving the beams of the reservoir trap with help of a piezo-driven mirror. The slow shifting speed ensures approximately adiabatic merging of the two traps. The combination process is performed at a magnetic field of 907 G, where a the large scattering length between the Li$|1/2, 1/2\rangle$ and Cs$|3, +3\rangle$ states leads to sympathetic cooling of the Cs atoms, i.e. we evaporate the atoms in the Li$|1/2, 1/2\rangle$ spin state out of the trap and thereby cool the Cs atoms. Afterwards the power of the reservoir trap is linearly ramped down and turned off within 1.5 s. At this point, the mixture is confined in the single-wavelength dimple trap and consists of Cs atoms in their energetically lowest spin state $|3, +3\rangle$ and Li atoms in the states $|1/2, 1/2\rangle$ and $|1/2, -1/2\rangle$. Either of the two Li spin-states is selected by removing the other one with a 80 μs long resonant light pulse. The final number of Li and Cs atoms, temperatures, and trapping frequencies are subject to the exact trapping conditions and can be tuned in a certain regime. Thus, we list these parameters individually for the measurements of *s*-, *p*-, and *d*-wave Feshbach resonances presented in Sec. 2.2.3-2.2.5 and the Efimov measurements at the higher temperature discussed in Sec. 3.4.1 and 3.4.2.

Atom-loss spectroscopy, as it is used in almost all of the experiments presented in this thesis, is performed by setting the magnetic field a couple of G away from the Feshbach resonance being studied. We wait for 100 ms to 150 ms in order to let the magnetic field stabilize before we set the final field value. After a hold time t_{hold} the atomic samples are typically detected using high field imaging at magnetic fields of 880 G.

Bichromatic trapping

The previously described experimental procedure, based on trapping in the dimple trap, is limited to a temperature of approximately 200 nK for simultaneous trapping of Li and Cs. Further reduction of the dimple trap power leads to spatial separation of the two species in vertical direction due to the different gravitational potentials and finally loss of Cs confinement, as can be seen in Fig. 1.16(e). Therefore, we implement a bichromatic trapping scheme in the combined dimple and tunable dipole trap as outlined in Sec. 1.3.2.

A typical experimental sequence for the preparation of Li-Cs mixtures at temperatures of 100 nK, as used for the experiments described in Ch. 3, is illustrated in Fig. 1.18. The MOT loading and further cooling stages of Cs and Li, as well as the initial forced evaporation ramps are similar to the experiments performed only in the dimple trap. Therefore, we start our discussion with the combination sequence. Mixing of Li and Cs is performed by moving the reservoir trap in a linear ramp of 1 s at a magnetic field of 907 G. Once the traps are superimposed, the tunable trap is turned on to 32 mW within 400 ms. Forced evaporation is performed by ramping off the reservoir trap within 1 s, during which the remaining Cs and Li atoms in the reservoir trap are used as cooling agent. The final evaporation phase is executed at 920 G while we linearly decrease (increase) the dimple (tunable) trap power to 42 mW (37 mW). This procedure ensures good spatial overlap and similar trap depths for Li and Cs during evaporation, as shown in Fig. 1.16(c,f).

At this point, the mixture consists of Cs atoms in the $|3, +3\rangle$ state and the majority of Li atoms populating the $|1/2, -1/2\rangle$ state. Again, we spin polarize the Li sample by

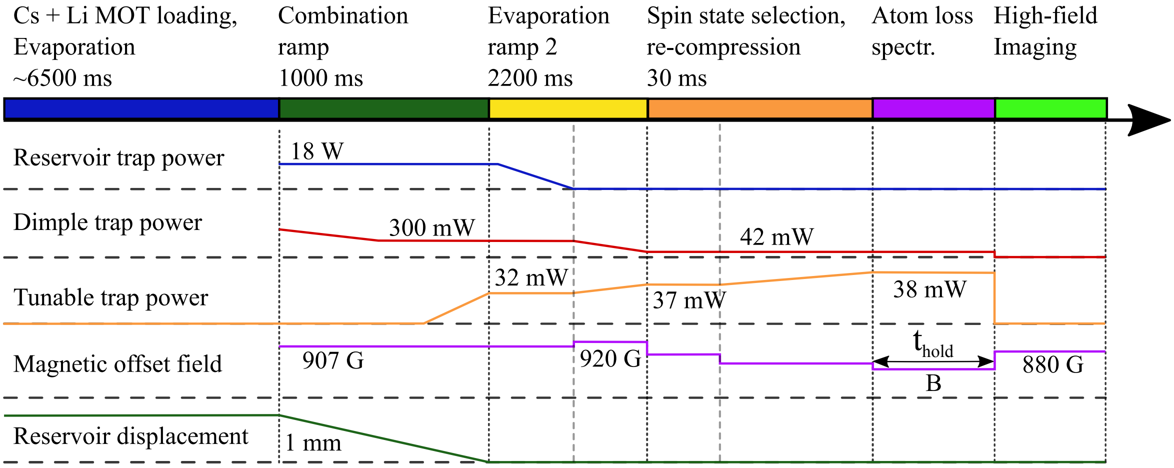

Figure 1.18.: Schematic experimental sequence for the preparation of Li-Cs mixtures at a temperature of 100 nK. The temporal evolution of reservoir, dimple, and tunable trap powers and the magnetic field values, as well as the displacement of the reservoir trap are illustrated. The first part of the preparation procedure is similar to the one illustrated in Fig. 1.17 and not shown here.

removing the atoms in $|1/2, 1/2\rangle$[5]. We perform a slight re-compression of the tunable trap in order to stop persistent plain evaporation. During this time, the magnetic field is set to roughly +4 G away from the pole of the Feshbach resonance and we let the field stabilize. Finally, we obtain samples of 7×10^3 Li and 1×10^4 Cs at a temperature of 100 nK in either of the two spin-channels. The trapping frequencies are determined to be $\omega_{\mathrm{Cs}} = 2\pi \times (5.7, 115, 85)$ Hz and $\omega_{\mathrm{Li}} = 2\pi \times (25, 160, 180)$ Hz. The final magnetic field value is set by a fast ramp and after a variable interaction time both atomic species are imaged at high magnetic fields.

1.4. Detection

The relevant information, i.e. the number density distribution, about the ultracold atomic samples are obtained by means of absorption imaging [Ketterle et al., 1999] at the end of each experimental cycle. The method is destructive and relies on recording the shadow cast by the atoms when illuminated by resonant laser light. For each species three images are recorded with one of three CCD cameras, as illustrated in Fig. 1.6. The first image displays the intensity distribution $I_{\mathrm{abs}}(x, y)$ after illuminating the atoms with resonant laser light. The intensity distribution of the illuminating laser light $I_{\mathrm{div}}(x, y)$ without atoms is recorded on a second image. The background

---

[5] During the preparation process we lose almost all Li atoms in state $|1/2, 1/2\rangle$ due to the previously described sympathetic colling of Cs atoms. We produce mixed samples containing Li in the $|1/2, 1/2\rangle$ state by rapid adiabatic passage, where we apply a 2 ms long rf-pulse at a frequency of 76.3189 MHz during a 4 ms magnetic field ramp to 847 G.

intensity $I_{\text{back}}(x, y)$, caused by readout or thermal noise, can be subtracted by taking a third picture without laser light present. From the three images, we calculate the transmission $T(x, y)$ at each pixel of the image:

$$T(x,y) = \frac{I(x,y)}{I_0(x,y)} = \frac{I_{\text{abs}}(x,y) - I_{\text{back}}(x,y)}{I_{\text{div}}(x,y) - I_{\text{back}}(x,y)} = \exp\left[-\sigma \int n(x,y,z)dz\right], \tag{1.11}$$

where $I_0(x, y)$ is the intensity of the incident beam and $I(x, y)$ after passing the atomic cloud. The transmission is related to the absorption cross section σ and the atomic column density $n(x, y) = \int n(x, y, z)dz$, representing the density distribution integrated along the direction of propagation of the imaging beam, via Beer's law. The column density at each pixel is given by

$$n(x,y) = -\sigma^{-1} \ln T(x,y). \tag{1.12}$$

The total number of atoms and the $1/e^2$ cloud radii σ_x, σ_y are typically obtained by fitting a two-dimensional Gaussian function to $n(x, y)$. The temperature T of a thermal cloud is deduced from the ballistic expansion, studied by varying the time-of-flight t between switching off the trapping potential and performing absorption imaging

$$\sigma_i(t) = \sqrt{\sigma_i(t=0) + \frac{k_B T}{m} t^2}. \tag{1.13}$$

In our experiment absorption imaging of Li and Cs atoms can either be performed at zero or high magnetic fields of up to 1000 G and along both horizontal and vertical direction (see Fig. 1.6). The necessary laser frequencies for high-field imaging of ^{6}Li are provided by an additional ECDL (Toptica DL pro 670), frequency offset locked to the main Li laser [Schünemann et al., 1999]. Its frequency can be tuned over a wide range in order to provide resonant light on the ^{6}Li D_2-line at high magnetic fields. Two additional diode lasers, Radiant Dyes NarrowDiode 852 and a homebuilt DBR laser, locked with a tunable frequency offset with respect to the main cooling lasers, are used for imaging and repumping of ^{133}Cs atoms at high magnetic fields [SchÃ¶nhals, 2013]. The high-field imaging technique offers the possibility of spin-selective detection via frequency tuning of the imaging light, due to the Zeeman splitting between different m_f states in presence of a magnetic field (Fig. 1.2). Additionally, the Li high-field imaging system can be used to prepare a spin-polarized Li sample in either of the two lowest hyperfine states (see Sec. 1.3.3).

Recently, the imaging systems have been improved and extended with respect to the setups presented by Repp [2013] and Pires [2014]. The camera for imaging in the horizontal plane was replaced by a Ximea MD028MU-SY CCD camera, featuring roughly twice the quantum efficiency at 852 nm, lower noise characteristics, and increased pixel

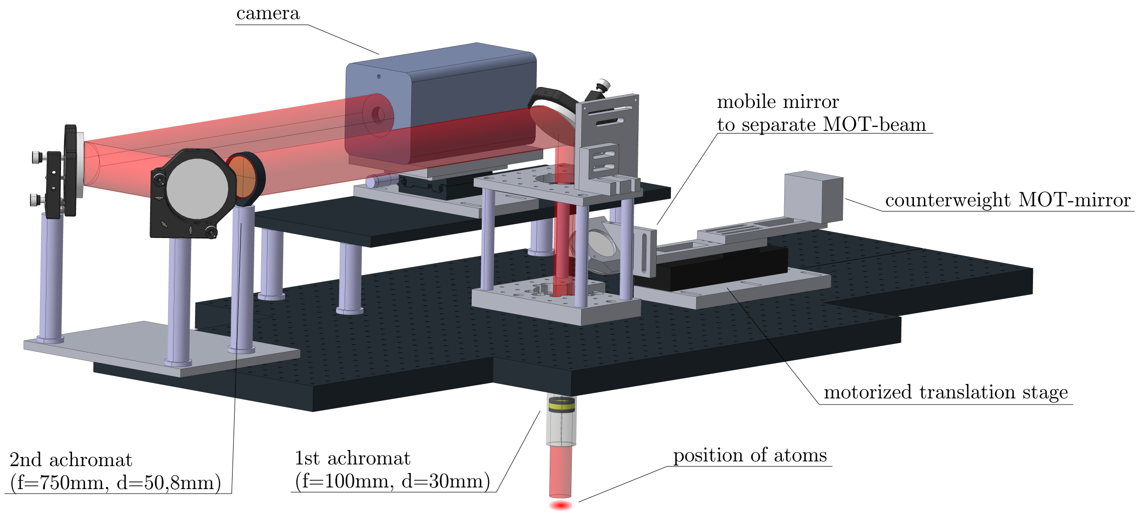

Figure 1.19.: High-resolution imaging setup for imaging along the vertical direction: the image of the atoms is magnified by a factor of roughly 8 with a 4f setup, consisting of two lenses with focal lengths of 100 mm and 750 mm, and recorded on a CCD camera. The imaging light can be separated from the MOT light by a movable mirror. Reprinted from Renner [2014].

bit depth in comparison to the previously used AVT Guppy-38B. The imaging system in the vertical direction has been extended by a new setup for high-resolution imaging shown in Fig. 1.19. The design follows a 4f setup, consisting of an achromatic lens with focal length $f = 100$ mm and diameter $D = 30$ mm placed inside the Feshbach and curvature coils and a second lens of focal length $f = 750$ mm imaging the atoms onto a high quantum efficiency CCD camera. The optics were chosen to minimize the chromatic focal shifts for imaging of Li and Cs atoms at wavelengths of 671 nm and 852 nm, respectively. The imaging system exhibits a resolution of 5.4 μm (Li) and 6.1 μm (Cs) at a magnification factor of approx. 8 [Renner, 2014]. The light is detected on an Andor iKon-M back illuminated Deep Depletion CCD Sensor (DU934P-BEX2-DD) with quantum efficiencies exceeding 75% for both resonant wavelengths. By making use of Andor's fast kinetics mode, we can image both atomic species within a minimum time frame of 2 ms on a single detector. For this purpose we mask 4/5 of the chip with a razor blade to ensure, that the imaging beams only illuminate the top part of the chip. After illumination of each image, the charges are quickly shifted down and stored in the non-illuminated part of the chip. At the end, the accumulated charges are read out from the chip and we obtain the five images [Eberhard, 2016]. In order to perform imaging of Cs at high magnetic fields along the vertical direction we implement a movable mirror (see Fig. 1.19). This mirror, mounted on a translation stage (Festo EGC-50-100-TB-KF-10H-GK), is moved out of the MOT beams while the atoms are trapped in the ODTs and directs the light towards the high-resolution imaging setup. This is necessary, since the Cs atoms are imaged with σ^+ polarized light, which can not be separated from the MOT light with a polarizing beam splitter. A detailed description and characterization of this setup can be found in Renner [2014]. The new high-resolution imaging setup enables us to precisely map out the density distribution of the atomic clouds, allowing for determination of temperature and the degree of quantum degeneracy in a single experimental cycle [Eberhard, 2016; Ketterle and Zwierlein, 2008].

Summary

In summary, we have introduced our experimental apparatus for slowing, cooling, trapping, and detecting of ultracold mixtures of ^{6}Li and ^{133}Cs atoms. We have presented our ultra-high vacuum setup in which the atoms are prepared and manipulated by magnetic and light fields. The interaction of *one* atom with external magnetic fields, building the foundation for the Feshbach tuning of the inter- and intraspecies two-body interactions, is studied. A description of our laser cooling techniques on the D_2-lines is given. Gray molasses cooling on the D_1-line of ^{6}Li has been introduced and implemented as a new sub-Doppler cooling technique. We demonstrated our approach for combined trapping of the highly mass imbalanced mixture and outlined the preparation procedure for ultracold mixtures of Li and Cs atoms at temperatures of down to 100 nK. Finally, we present our system for absorption imaging, which has been improved significantly by a new high-resolution imaging setup. The setup and techniques presented in this chapter are the starting point for further investigations of scattering phenomena of *two-*, *three-*, and *many*-body physics in the Li-Cs system.

Two

2

This chapter is partially based on the following manuscript and publication, from which parts of the text are reproduced verbatim:

Spin-rotation coupling in higher partial wave Feshbach resonances
S. Häfner, B. Zhu, B. Tran, M. Gerken, J. Ulmanis, E. Tiemann, and
M. Weidemüller
Manuscript in preparation

Universality of weakly bound dimers and Efimov trimers close to Li-Cs Feshbach resonances
J. Ulmanis, S. Häfner, R. Pires, E.D. Kuhnle, M. Weidemüller, and
E. Tiemann
New Journal of Physics **17**, 055009 (2015)

After the study of single particles and their interactions with magnetic and light fields, we investigate the scattering properties of *two* atoms. In dilute ultracold atomic gases collisions between particles are determined by pure *two*-body interactions. At ultralow collisional energies[1] the scattering properties are greatly simplified and can be described by a single parameter, the so-called s-wave scattering length a. It has the unit of a length and gives the approximate distance at which the particles scatter. Since this distance is usually much larger than the extension of the interaction potential, the details of the two-body interaction potential are not probed. In fact, their interactions are well approximated by contact-like interactions described by δ-function pseudo potentials, the so-called zero-range potentials [Dalibard, 1999; Dalfovo et al., 1999].

One of the great breakthroughs in the field of ultracold gases was the discovery of Feshbach resonances [Inouye et al., 1998; Courteille et al., 1998; Chin et al., 2010]. Their magnetic field dependent resonance behavior allows to change the magnitude and sign of the scattering length a in a controlled way. This means one can tune the two-body interaction from non-interacting to strongly interacting and repulsive to attractive interaction by exposing the atoms to certain magnetic field strengths.

---

[1] The ultracold regime is defined by thermal collision energies that are much smaller than the centrifugal barrier.

Feshbach resonances have become a standard tool in the manipulation of ultracold atomic gases and are one of the driving forces for ongoing studies in the field.

Ultracold atoms have provided remarkable insight in physical systems from seemingly very different fields, characterized by vastly different energy scales and densities. The study of the behavior of strongly interacting fermions is important for the understanding of the quark-gluon plasma of the early universe, strongly correlated electron systems in solid-state physics, the inside of atomic nuclei, and even neutron stars [Ketterle and Zwierlein, 2008]. Furthermore, the tunable interactions were exploited in the study of few- and many-body physics, e.g. ultracold molecules [Quéméner and Julienne, 2012], Efimov physics [Braaten and Hammer, 2007], and the Bardeen-Cooper-Schrieffer (BCS) superfluid (SF) to Bose-Einstein condensate (BEC) crossover regime [Giorgini et al., 2008]. While these studies only involved isotropic s-wave interactions, also anisotropic interactions can be engineered by letting the atoms interact at *finite* angular momentum ($l > 0$)[2]. In systems with anisotropic interactions intriguing effects such as the super-Efimov effect [Naidon and Endo, 2017] and a much richer SF phase diagram, e.g. p-wave SF and d-wave high-T_C superconductivity [Scalapino, 1995], with phase transitions between different SF phases [Gurarie et al., 2005; Cheng and Yip, 2005] may be studied. A possible candidate for the realization of p-wave SF are spin-polarized fermionic atoms interacting via p-wave FRs [Ho and Diener, 2005; Ohashi, 2005; Botelho and Melo, 2005], where the observed splitting into $m_l = 0$ and $m_l = \pm 1$ components [Ticknor et al., 2004] can give rise to a phase transition between a topologically trivial and non-trivial SF phase [Gurarie et al., 2005; Cheng and Yip, 2005]. However, observation of p-wave SF in these systems remains elusive due to the short lifetime of p-wave Feshbach molecules [Gaebler et al., 2007].

An ultracold gas consisting of multiple atomic species features in general different interactions for each atom-pair combination. For the Li-Cs system this means that we have to consider three different scattering lengths: the intraspecies scattering lengths between two Li atoms or two Cs atoms and the interspecies scattering length of one Li atom interacting with one Cs atom. Thus, one can for example realize situations, where the atoms of one species do not interact directly with each other but only by means of an interaction mediated through the second species. The magnetic field dependent interactions for ^{6}Li atoms and ^{133}Cs atoms have been studied by Zürn et al. [2013] and Berninger et al. [2013a] and are among the most well known.

In this chapter we experimentally and theoretically study the scattering properties of fermionic ^{6}Li atoms and bosonic ^{133}Cs atoms at ultracold temperatures. The precise understanding of the magnetic field dependent scattering length builds the foundation for the later performed studies on few-body (Ch. 3) and many-body (Ch. 4) systems of the Li-Cs combination. We perform high-precision measurements on 23 Feshbach

---

[2] We label the partial waves according to the angular momentum of the closed-channel molecule $l_Q = 0, 1, 2, ...$ as s-,p-,d-,... waves.

resonance features in the s-, p-, and d-wave channels. For the first time we observe a splitting of the p-wave FRs into a triplet structure, resolving all three projections $m_l = -1, 0, +1$ of the rotational angular momentum $l = 1$ at high magnetic fields. We attribute this splitting to electronic spin-rotation coupling known from molecular spectroscopy of Σ-states with non-zero spin S [Hund, 1927; Kramers, 1929; Van Vleck, 1929; Lefebvre-Brion and Field, 1986], which lifts the near-degeneracy of the $m_l = \pm 1$ states at high magnetic fields. In the Li-Cs system this interaction is particularly large due to the small reduced mass and large spin-orbit interaction in Cs leading to a significant second order contribution. The triplet splitting provides full control over the angular momentum l and its projection m_l in the scattering process by the external magnetic field. Extending previous studies of Li-Cs FRs [Repp et al., 2013; Tung et al., 2013; Pires et al., 2014a] with measurements of d-wave FRs gives access to the rotational ladder of $l = 0, 1, 2$ states of the least bound vibrational state and allows us to improve the long-range description of the LiCs molecular potential curves.

This chapter is structured as follows: In Sec. 2.1 we recapitulate the basic scattering theory in ultracold atomic gases (Sec. 2.1.1), introduce the scattering Hamiltonian describing the binary collision of atoms (Sec. 2.1.2) and the concept of a magnetically tuned Feshbach resonance (Sec. 2.1.3). Sec. 2.2 describes the coupled channels modeling of the Li-Cs Feshbach resonances (Sec. 2.2.1), the measurement procedure (Sec. 2.2.2) and the characterization of s-, p-, and d-wave Li-Cs Feshbach resonances in Sec. 2.2.3-2.2.5.

2.1. Collisions

We start our discussion of the scattering properties at ultralow kinetic energies by introducing the basic scattering theory in Sec. 2.1.1 followed by the Hamiltonian describing the collision process in ultracold atomic gases in Sec. 2.1.2. This is the prerequisite for the understanding of the origin of magnetic Feshbach resonances that are introduced in Sec. 2.1.3.

2.1.1. Basic scattering theory

In this section we recapitulate the most important concepts of scattering theory, following the review article by Dalibard [1999]. A rigorous treatment of two-body low energy scattering can be found in many textbooks and lecture notes, e.g. [Joachain, 1984; Ketterle et al., 1999; Landau and Lifshitz, 1991; Schwabl, 2007; Sakurai and Napolitano, 2010].

We start our discussion with the time-independent Schrödinger equation in the center-off-mass reference frame for two colliding particles with masses m_1 and m_2, interacting via the potential $V(\vec{r})$

$$\left[-\frac{\hbar^2}{2\mu}\vec{\nabla}^2 + V(\vec{r})\right]\psi(\vec{r}) = \frac{\hbar^2 k^2}{2\mu}\psi(\vec{r}) \tag{2.1}$$

with the interparicle separation $\vec{r}$, the reduced mass $\mu = m_1 m_2/(m_1+m_2)$, and the wavevector $k = \sqrt{2\mu E}/\hbar$ determined by the positive energy E. We assume, that the interaction potential $V(\vec{r})$ vanishes for sufficiently large interatomic separations $|\vec{r}| = r \gg r_0$, where r_0 is the characteristic length scale of $V(\vec{r})$. In this regime, the wavefuction $\psi(\vec{r})$ can be expressed as a superposition of an incoming plane wave with momentum k and an outgoing spherical wave with scattering amplitude $f(k,\theta)$:

$$\psi(\vec{r}) = e^{ikr} + f(k,\theta)\frac{e^{ikr}}{r} \tag{2.2}$$

from which the differential scattering cross-section $d\sigma(k)/d\Omega = |f(k,\theta)|^2$ into the solid angle Ω can be computed.

The assumption of isotropic interaction potentials $V(r)$, as it is well fulfilled in case of neutral atoms interacting via isotropic, short-ranged Born-Oppenheimer molecular potentials[3], allows one to considerably simplify the problem by expanding the wavefunction in spherical harmonics $Y_l^m(\theta,\phi)$:

$$\psi(\vec{r}) = \sum_{l=0}^{\infty}\sum_{m=-l}^{l} Y_l^m(\theta,\phi)\frac{\chi_{k,l,m}(r)}{r}, \tag{2.3}$$

where $\chi_{k,l,m}(r)$ is the radial wavefunction depending on wavenumber k, the quantum number of the relative angular momentum l, and its projection m. The scattering amplitude for large r is obtained by inserting the expansion Eq. (2.3) into the Schrödinger Eq. (2.1)

$$f(k,\theta) = \frac{1}{2ik}\sum_{l=0}^{\infty}(2l+1)(e^{2i\delta_l(k)}-1)P_l(\cos\theta), \tag{2.4}$$

where P_l are the Legendre polynomials, which determine the angular dependence of the scattering amplitude. The angular distribution of the scattering amplitude thus only depends on the angular momentum l in the collision process. In case of s-wave ($l=0$) scattering, the Legendre polynomial P_0 is constant, resembling an isotropic scattering cross-section and consequently the introduced phase shift $\delta_l(k)$ between the incoming and outgoing waves incorporates all information about the interatomic interaction.

---

[3] Note that this assumption is not justified in systems exhibiting dipole-dipole interactions [Aikawa et al., 2012, 2014; Stellmer et al., 2009; Stuhler et al., 2005; Lu et al., 2012].

Inserting the solution of the angular part [Eq. (2.4)] back into the Schrödinger equation (2.1) results in the radial wavefunctions[4] $R_l(r) = \chi_l(r)/r$. The result reads [Schwabl, 2007; Petrov, 2010]:

$$\frac{\partial^2}{\partial r^2}R_l(r) + \frac{2}{r}\frac{\partial}{\partial r}R_l(r) + \frac{2\mu}{\hbar^2}[E - V_l(r)]R_l(r) = 0\ , \tag{2.5}$$

where $V_l(r) = V(r) + \frac{\hbar^2 l(l+1)}{2\mu r^2}$ contains the interaction potential and the centrifugal term due to the angular momentum l. By the substitution $\chi_l(r) = r \cdot R_l(r)$ and redifinition of $\epsilon = 2\mu E/\hbar^2$ and $\tilde{V}(r) = 2\mu V_l(r)/\hbar^2$ we arrive at the simplified equation

$$\frac{\partial^2}{\partial r^2}\chi_l(r) + [\epsilon - \tilde{V}(r)]\chi_l(r) = 0. \tag{2.6}$$

For s-wave ($l = 0$) scattering the potential $\tilde{V}(r)$ corresponds to the two-body interaction potential $V(r)$. In case of higher partial waves ($l > 0$) a centrifugal barrier arises in the potential of the Schrödinger equation as depicted in Fig. 2.1(b). For collision energies E much smaller than the height of the centrifugal barrier, the particle will be reflected from the barrier and will not sense the interaction potential $V(r)$. From the Wigner threshold law [Wigner, 1948] we obtain the scaling of the phase shift $\delta_l \propto k^{2l+1}$ in the low energy limit $k \to 0$. Therefore, at sufficiently low energies the effect of all partial waves but $l = 0$ goes to zero. We define the s-wave scattering length a by

$$a = -\lim_{k\to 0}\frac{\tan\delta_0(k)}{k}. \tag{2.7}$$

It is the only parameter that describes the collision process at ultracold temperatures, because all other partial waves are “frozen” out.

So far, we did not take the quantum statistics of the particles into consideration. In case of indistinguishable particles we need to obey the (anti)symmetrization principle of the wavefunction. The differential cross-section thus reads $d\sigma(k)/d\Omega = |f(k,\theta) \pm f(k,\pi-\theta)|^2$, where the plus and minus sign is used for bosons and fermions, respectively. The (anti)symmetrization leads to a doubling of the contribution of (odd)even and a cancellation of (even)odd partial waves in the total scattering cross-section

$$\sigma(k) = \frac{8\pi}{k^2}\sum_l (2l+1)\sin^2\delta_l(k), \tag{2.8}$$

where the summation is only performed over (odd)even l for identical (fermions)bosons.

---

[4] We omit the indices k and m for clarity.

With the definition of the scattering length [Eq. (2.7)] the s-wave scattering cross-section can be written as

$$\sigma(k) = \begin{cases} \frac{4\pi a^2}{1+k^2a^2} & \text{for distinguishable particles,} \\ \frac{8\pi a^2}{1+k^2a^2} & \text{for identical bosons,} \\ 0 & \text{for identical fermions.} \end{cases} \tag{2.9}$$

An important consequence of this result is, that spin-polarized identical fermions do not interact with each other at low temperatures. Their scattering process can only occur in the odd partial waves $l = 1, 3, ...$ for which the cross-section approaches zero as $k \to 0$ [Wigner, 1948]. In the limiting case of $k^2a^2 \gg 1$ the scattering cross-section becomes independent of the scattering length and is solely determined by the thermal wavevector k. This limit is commonly called unitary limit, where the cross-section becomes $4\pi/k^2$ for distinguishable particles and $8\pi/k^2$ for identical bosons. Thus, for $k^2a^2 > 1$ the cross-section flattens off to the unitary limit, which can not be exceeded. In order to increase the maximal scattering cross-section the thermal wavevector k, or equivalently the temperature of the sample, needs to be reduced.

2.1.2. The scattering Hamiltonian

In the previous section we have recapitulated the basic principles of scattering theory and introduced the s-wave scattering length and scattering cross-section. So far, we did not consider the explicit form of the interaction term $V(r)$ in our discussion. We introduce the scattering Hamiltonian describing the binary collision process of two atoms A and B [Stoof et al., 1988; Moerdijk et al., 1995; Timmermans et al., 1999; Köhler et al., 2006] and discuss each of its terms. In comparison to previous work [Repp et al., 2013; Pires et al., 2014a; Ulmanis et al., 2015] we extend the Hamiltonian H in Eq. 2.1 by the spin-rotation interaction H_{SR}:

$$H = T + \sum_{S=0,1} P_S V_S(r) + H_{\mathrm{hf}} + H_Z + H_{\mathrm{dd}} + H_{\mathrm{SR}} \ , \tag{2.10}$$

where $T = -\vec{\nabla}^2/(2\mu)$ is the relative kinetic energy with the reduced mass μ of the vibrational and rotational motion[5] containing the centrifugal barrier as discussed in Sec. 2.1.1. The interatomic interaction is described by the Born-Oppenheimer potentials $V_S(r)$ of the singlet ($S = 0$) and triplet ($S = 1$) states and P_S are their projection operators. H_{hf} is the hyperfine interaction of the atoms A and B, H_Z the magnetic Zeeman interaction for electrons and nuclei, and H_{dd} the magnetic dipole-dipole interaction term. We add the spin-rotation Hamiltonian H_{SR} in order to describe our

---

[5] For clarity, we omit factors of $\hbar$ in the description of the scattering Hamiltonian.

observations. The individual terms are explained in the following starting with the interaction potential.

Molecular potential curves The molecular potentials are typically described in the Born-Oppenheimer approximation, assuming that the large mass difference between electrons and nuclei allows for the separation of electronic and nuclear motion. At large internuclear separations r, exceeding the size of the individual electron clouds, the induced dipole-dipole interactions generate a attractive potential, which is commonly written as power series of $1/r$:

$$V_{\mathrm{LR}}(r) = -C_6/r^6 - C_8/r^8 - C_{10}/r^{10} \pm ... \,, \tag{2.11}$$

where C_6, C_8, and C_{10} are the dispersion coefficients, which depend on the details of the electronic configurations and are often obtained from either *ab initio* calculations (see, for example, [Derevianko et al., 2001; Porsev and Derevianko, 2003; Porsev et al., 2014]), photoassociation [Jones et al., 2006] or Feshbach spectroscopy [Köhler et al., 2006; Chin et al., 2010]. The long-range behavior of the molecular potential curves allows one to introduce characteristic van der Waals length and energy scales r_{vdW} and E_{vdW}, respectively, which are given by

$$r_{\mathrm{vdW}} = \frac{1}{2}\left(\frac{2\mu C_6}{\hbar^2}\right)^{1/4}, \tag{2.12}$$

and

$$E_{\mathrm{vdW}} = \frac{\hbar^2}{2\mu r_{\mathrm{vdW}}^2}. \tag{2.13}$$

In case of Li and Cs atoms these amount to $r_{\mathrm{vdW}}^{\mathrm{LiCs}} = 45\ a_0$, $r_{\mathrm{vdW}}^{\mathrm{Cs}} = 101\ a_0$, $E_{\mathrm{vdW}}^{\mathrm{LiCs}} = h \times 156$ MHz, and $E_{\mathrm{vdW}}^{\mathrm{Cs}} = h \times 2.7$ MHz. The Bohr radius is denoted by $a_0 = 0.5292 \times 10^{-10}$ m.

At intermediate distances, where the individual electronic clouds overlap, the valence electrons' spins $\vec{s}_A$ and $\vec{s}_B$ of the two atoms couple to a total spin $\vec{S} = \vec{s}_A + \vec{s}_B$. For alkali atoms in the ground state, for which $s = 1/2$, either singlet ($S = 0$) or triplet ($S = 1$) configurations are possible. The fermionic nature of the electrons requires anti-symmetrization of the wavefunction. Since the singlet (triplet) state is anti-symmetric (symmetric) under particle exchange, this requires a symmetric (anti-symmetric) spatial wavefunction. Thus, the probability of finding the electron between the nuclei is greatly enhanced (reduced) for the singlet (triplet) case. For the singlet state this leads to a screening of the Coulomb repulsion of the positively charged atom cores and therefore results in deeper molecular potential curves than in the triplet case. The energy difference between singlet and triplet states is usually described by

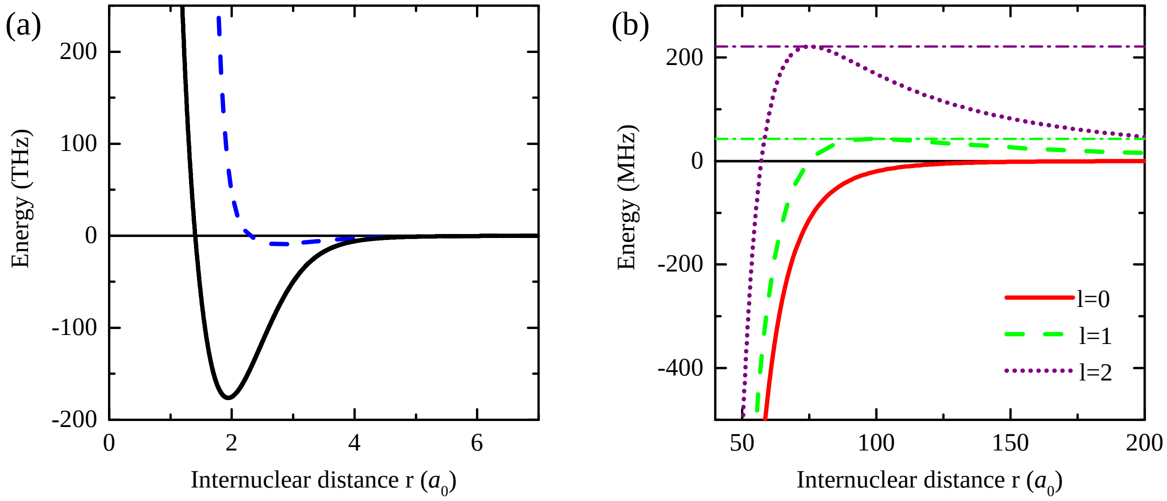

Figure 2.1.: LiCs molecular potential curves: (a) full singlet $X^1\Sigma^+$(black line) and triplet $a^3\Sigma^+$(blue dashed line) ground state Born-Oppenheimer potentials obtained from a coupled channels calculation, (b) long range van der Waals potential including the centrifugal term from the kinetic energy operator T for $l = 0$ (red line), $l = 1$ (green dashed line), and $l = 2$ (purple dotted line). The horizontal dash-dotted lines represent the respective rotational barrier heights given by Eq. (2.15).

an exchange term

$$E_{ex}(r) = \pm A_{ex} r^{\gamma_{ex}} \exp\left(-\beta_{ex} r\right), \tag{2.14}$$

which is negative for the singlet and positive for the triplet potential. The parameters A_{ex}, γ_{ex}, and β_{ex} depend on the details of the electronic and nuclear configurations.

At even shorter distances the molecular potentials are purely repulsive due to Pauli blocking of the electrons and Coulomb repulsion between the positively charged atomic cores. The LiCs molecular potential curves of the singlet ground state $X^1\Sigma^+$ and the triplet one $a^3\Sigma^+$are shown in Fig. 2.1(a).

In Fig. 2.1(b) we show the long-range behavior of the potential including the centrifugal term for $l = 0, 1, 2$. The height of the rotational barrier can be expressed as

$$U_{\text{rot}} = \frac{1}{\sqrt{2C_6}} \left(\frac{\hbar^2 l(l+1)}{3\mu} \right)^{3/2}. \tag{2.15}$$

This barrier is on the order of 2 mK for p-wave ($l = 1$) collisions and 11 mK for d-wave ($l = 2$) collisions in ^{6}Li-^{133}Cs, which is well above the temperatures used in current experiments. Thus, it is often sufficient to describe the scattering process with the s-wave components of the partial-wave expansion.

Hyperfine interaction The hyperfine term couples the electronic angular momentum $\vec{j_\beta}$ of each atom to its nuclear spin $\vec{i_\beta}$. In case of alkaline atoms in their electronic ground state ($\vec{l} = 0$), the total electronic angular momentum $\vec{j_\beta}$ equals the spin $\vec{s_\beta}$. Thus, the hyperfine interaction is given by

$$H_{\mathrm{hf}} = \sum_{\beta=A,B} \alpha_\beta(r)\vec{s_\beta} \cdot \vec{i_\beta}, \tag{2.16}$$

where the functions $\alpha_\beta(r)$ describe the molecular hyperfine coupling and approach the atomic hyperfine constants $a_{\beta,\mathrm{hf}}$ in the limit of large internuclear separations r [Strauss et al., 2010]. Their r dependence accounts for distortion of the electronic distributions and the coupling of the electronic spin of one atom to the nuclear spin of the other one.

Zeeman term The coupling of the electron spins $\vec{s_\beta}$ and nuclear spins $\vec{i_\beta}$ to an external magnetic field $\vec{B}$ is contained in the Zeeman interaction Hamiltonian

$$H_Z = \sum_{\beta=A,B} (g_{s,\beta}\vec{s_\beta} + g_{i,\beta}\vec{i_\beta})\mu_B\vec{B}, \tag{2.17}$$

with the electronic (nuclear) gyromagnetic ratio $g_{s,\beta}$ ($g_{i,\beta}$) and the Bohr magneton μ_B. In presence of an external magnetic field this term leads to an energy splitting in the different projections m of the electronic and nuclear spins. We have plotted the magnetic field dependent energy of ^{6}Li and ^{133}Cs atoms in their respective electronic ground state in Fig. 1.2 of the previous chapter.

The Dipole-dipole interaction is used in its effective form [Strauss et al., 2010]

$$H_{\mathrm{dd}} = \frac{2}{3}\lambda(r)(3S_Z^2 - S^2), \tag{2.18}$$

where S_Z is the projection of the total electronic spin onto the molecular axis Z. The function

$$\lambda(R) = -\frac{3}{4}\alpha^2 \left(\frac{1}{r^3} + \sum_{i=1,2} a_{\mathrm{SO}i} \exp(-b_i r)\right) \tag{2.19}$$

includes direct magnetic spin-spin interaction [Stoof et al., 1988; Moerdijk et al., 1995] with its $1/r^3$ functional form for the dipole-dipole interaction and the second-order spin-orbit interactions with exponential r-functions [Mies et al., 1996; Kotochigova et al., 2000]. α is the fine-structure constant and the parameters of the second-order spin-orbit coupling $a_{\mathrm{SO}i}$ and b_i are adjustable parameters, typically obtained by fitting to the experimentally observed p-wave Feshbach resonances. This term in the Hamiltonian causes the observed doublet splitting of p-wave resonances between $|m_l| = 0$ and 1 [Repp et al., 2013] of the overall rotation of the atom pair l.

Spin-rotation coupling The very last term couples the electron spins of the two atoms to the pair rotation by either the direct coupling between the electron spin moment and the magnetic field produced by the rotating nuclear charges [Kramers, 1929] or the second-order spin-orbit interaction [Van Vleck, 1929]. Typically the latter dominates and the spin-rotation coupling takes the form

$$H_{\mathrm{SR}} = \frac{\gamma}{2\mu r^2} \sum_{\beta=A,B} \vec{s_\beta} \cdot \vec{l}, \tag{2.20}$$

with the dimensionless spin-rotation coupling constant γ with respect to the rotational constant represented by the inverse of the moment of inertia of the atom pair about an axis perpendicular to the molecular axis. Similar to the spin-spin interaction, only the diagonal matrix elements make significant contributions and $\langle l, m_l | H_{\mathrm{SR}} | l, m_l \rangle \propto m_l$. Thus, the spin-rotation interaction lifts the near-degeneracy of the $|m_l| = 1$ components.

Scattering channels The Hamiltonian Eq. (2.10) allows one to define a number of channels with a certain projection of the total angular momentum m_f of the atom pair. Since Feshbach resonances typically originate from the vibrational states close to the atomic asymptote, it is convenient to express the scattering state in Hund's coupling case (e)

$$|\xi\rangle \equiv |(s_A, i_A), f_A, m_{f,A}; (s_B, i_B), f_B, m_{f,B}; f, m_f, l, m_l\rangle \,, \tag{2.21}$$

where the electron spin $s_{A/B}$ and nuclear spin $i_{A/B}$ of each atom are coupled to the atomic angular momentum $f_{A/B}$ with its projection $m_{f,A/B}$ on the space fixed axis. f is the total angular momentum and m_f its projection. Furthermore, we label a state by the rotation l and its projection m_l of the atom pair. In the field-free case, the individual $f_{A/B}$ are good quantum numbers, while at high magnetic fields, where the Zeeman energy is larger than the hyperfine coupling, f_A and f_B are only approximate quantum numbers. In our experiments, we prepare the two species in their asymptotic atomic states given by $\left| f_{A/B}, m_{f,A/B} \right\rangle$, where the f quantum number labels the state at zero magentic field. The scattering channel is thus defined as a sum state of atomic states $A\,|f_A, m_{f,A}\rangle \oplus B\,|f_B, m_{f,B}\rangle$ and characterized by a total angular momentum $m_f = m_{f,A} + m_{f,B}$.

2.1.3. Feshbach resonances

We introduce the concept of a magnetically tunable Feshbach resonance, following the approach of Moerdijk et al. [1995]. In general it is convenient to write the effective Hamiltonian given in Eq. (2.10) as a sum of the internal part H_0 with eigenstates $|\{\alpha\beta\}\rangle$, asymptotically corresponding to a product state of single-atoms in internal states $|\alpha\rangle$ and $|\beta\rangle$, and an interaction part, which couples the different channels $|\{\alpha\beta\}\rangle$. We expand the scattering state Ψ in the basis of $|\{\alpha\beta\}\rangle$ with $\vec{r}$ dependent coefficients:

$$\Psi = \sum_{\{\alpha\beta\}} \psi_{\{\alpha\beta\}}(\vec{r})|\{\alpha\beta\}\rangle. \tag{2.22}$$

By insertion into the Schrödinger equation [Eq. (2.1)] one arrives at a coupled channels problem with a set of coupled differential equations for the wavefunction $\psi_{\{\alpha\beta\}}(\vec{r})$. The scattering energy E allows for the classification of the channels into two groups: if the asymptotic energy is lower than E the channel is referred as "open", otherwise it is "closed" (see Fig. 2.2). We subdivide the Hilbert space into an open channel subspace $\mathcal{P}$ and a corresponding closed channel subspace $\mathcal{Q}$. Projecting the Hamiltonian from Eq. (2.10) onto $\mathcal{P}$ and $\mathcal{Q}$ via the projection operators $\hat{P}$ and $\hat{Q}$ leads to a set of coupled equations:

$$(E - H_{PP})\Psi_P = H_{PQ}\Psi_Q \tag{2.23}$$

$$(E - H_{QQ})\Psi_Q = H_{QP}\Psi_P, \tag{2.24}$$

where the projection onto the respective open and closed subspaces is denoted by subscripts P and Q with $\Psi_{\hat{I}} \equiv \hat{I}\Psi$ and $H_{\hat{I}\hat{J}} \equiv \hat{I}H\hat{J}$.

Eq. (2.24) can be solved by introducing the Green's operator $1/(E^+ - H_{QQ})$, where $E^+ = E + i\delta$ with δ approaching zero from positive values. Applying it to Eq. (2.24) yields:

$$\Psi_Q = \frac{1}{E^+ - H_{QQ}} H_{QP}\Psi_P. \tag{2.25}$$

Insertion into Eq. (2.23) gives an effective equation describing the scattering process in the the open channel:

$$\left(H_{PP} + H_{PQ}\frac{1}{E^+ - H_{QQ}}H_{QP}\right)\Psi_P = E\Psi_P. \tag{2.26}$$

This effective Schrödinger equation contains the basic mechanism of Feshbach resonances. The first term can be interpreted as bare scattering in the open $\mathcal{P}$ channel, giving rise to the so-called background scattering length a_{bg}. The second term describes a transition from the open $\mathcal{P}$-subspace to $\mathcal{Q}$-subspace, subsequent propagation in $\mathcal{Q}$-space, and re-emission back into $\mathcal{P}$-space. The accumulated phase shift during

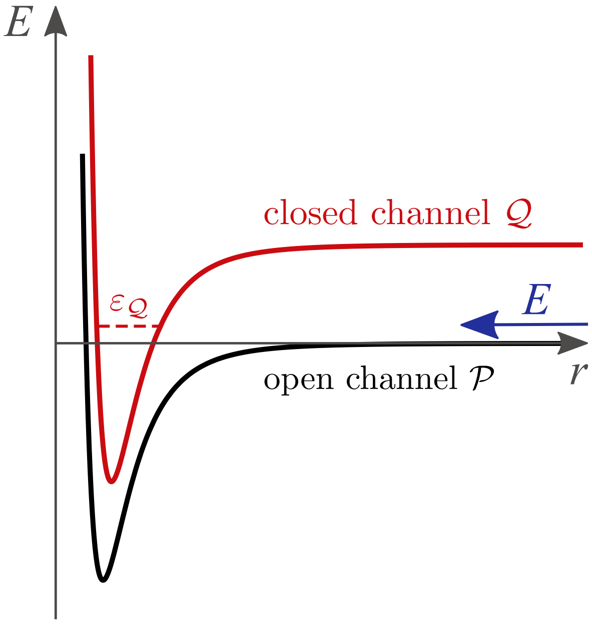

Figure 2.2.: Basic principle of a Feshbach resonance: The incoming atoms in the open channel $\mathcal{P}$ with energy E are coupled to a near-degenerate molecular bound state ϵ_Q in the closed channel $\mathcal{Q}$-subspace.

the propagation in the closed channels determines the s-wave scattering length, defined in Eq. (2.7).

The collision event is characterized by the unitary scattering matrix S, whose elements S_{ji} describe the scattering probability from channel i into j. In our experiments the atoms are typically prepared in their energetically lowest states. Thus, there is only one open channel in the system. If the total energy E is close to a bound state in the closed channel with energy ϵ_Q, as depicted in Fig. 2.2, we reduce the S-matrix to

$$S = S_{\mathcal{P}} \left(1 - \frac{i\Gamma}{E - \epsilon_Q - \mathcal{A}(E)} \right), \tag{2.27}$$

where $\Gamma = 2\pi \left| \langle \psi_Q | H_{PQ} | \zeta^+ \rangle \right|^2$ describes the coupling between the molecular state $|\psi_Q\rangle$ in $\mathcal{Q}$ and the incoming scattering state $|\zeta^+\rangle$ and the direct matrix of the $\mathcal{P}$-subspace is denoted by $S^0_{ii} = S_{\mathcal{P}}$. The S-matrix element is related to the scattering phase shift $\delta(k)$ via the relation $S(k) = e^{2i\delta(k)}$. This approach is known as single resonance, two-channel approach [Moerdijk et al., 1995; Timmermans et al., 1999; Mies and Raoult, 2000; Köhler et al., 2006]. The complex energy shift is given by

$$\mathcal{A}(E) = \langle \psi_Q | H_{QP} \frac{1}{E - H_{PP} + i0} H_{PQ} | \psi_Q \rangle, \tag{2.28}$$

and contains the energy shift of the bare molecular state state $|\psi_Q\rangle$ due to its coupling to the open channel. $\mathcal{A}(E) = \Delta(E) + i/2\Gamma(E)$ is decomposed into its real part, the resonance shift $\Delta(E)$, and its imaginary part, the width $\Gamma(E)$. In case of energies above the threshold ($E > 0$), the molecular state can be interpreted as a quasi-bound state that is shifted by $\Delta(E)$ from its unperturbed energy ϵ_Q and has a finite width $\Gamma(E)$. For negative energies $\mathcal{A}(E)$ is real and $\Gamma(E) = 0$, thus describing an actual energy shift of the bare molecular state $|\psi_Q\rangle$.

In ultracold atomic gases the closed and open channel consist of a pair of atoms in different hyperfine states, Eq. (2.21). In general the two hyperfine states have different electronic and nuclear spin quantum numbers and thus the channels will possess different magnetic moments (cf. Fig. 1.2). As a consequence the energy difference between ϵ_Q and E can be controlled by the applied magnetic field. If a bound-state in the closed channel is close to the energy of the incoming channel (the threshold energy), one can bring both in degeneracy by applying a specific magnetic field. In this case the S-matrix, Eq. (2.27), diverges due to a zero in the denominator and hence, a resonance occur that is referred to as Fano-Feshbach resonance [Feshbach, 1958, 1962; Fano, 1961].

At ultracold temperatures, where the scattering can be reduced to pure s-wave collisions, the S-matrix [Eq. (2.27)] is directly related to the scattering length via $S(k) = e^{-2ika}$:

$$S(k) = e^{-2ika_{bg}} \left(1 - \frac{2iCk}{iCk - \epsilon_{res}(B)}\right), \tag{2.29}$$

where the effect of the open $\mathcal{P}$-subspace defines the so-called background scattering length a_{bg}. C is a positive constant, which describes the coupling between the open and closed channels, and $\epsilon_{res} = \epsilon_Q(B) - \delta(B)$ is the energy of the bound state relative to the threshold energy. We take the explicit B-dependence of $\epsilon_{res}(B) = (\mu_P - \mu_Q)(B - B_{\mathrm{FR}})$ into account, where μ_P denotes the magnetic moment of the atom pair in the scattering channel and μ_Q that of the bound molecular state in $\mathcal{Q}$. We finally arrive at the well-known dispersive behavior

$$a(B) = a_{bg} \left(1 - \frac{\Delta}{B - B_{\mathrm{FR}}}\right), \tag{2.30}$$

where B_{FR} is the Feshbach resonance position. The width Δ is the distance between scattering pole and zero crossing of the scattering length and is determined by the coupling strength between open and closed channels. The resonance behavior of the scattering length and the binding energy of the weakly-bound dimer state in the vicinity of a Feshbach resonance is depicted in Fig. 2.3.

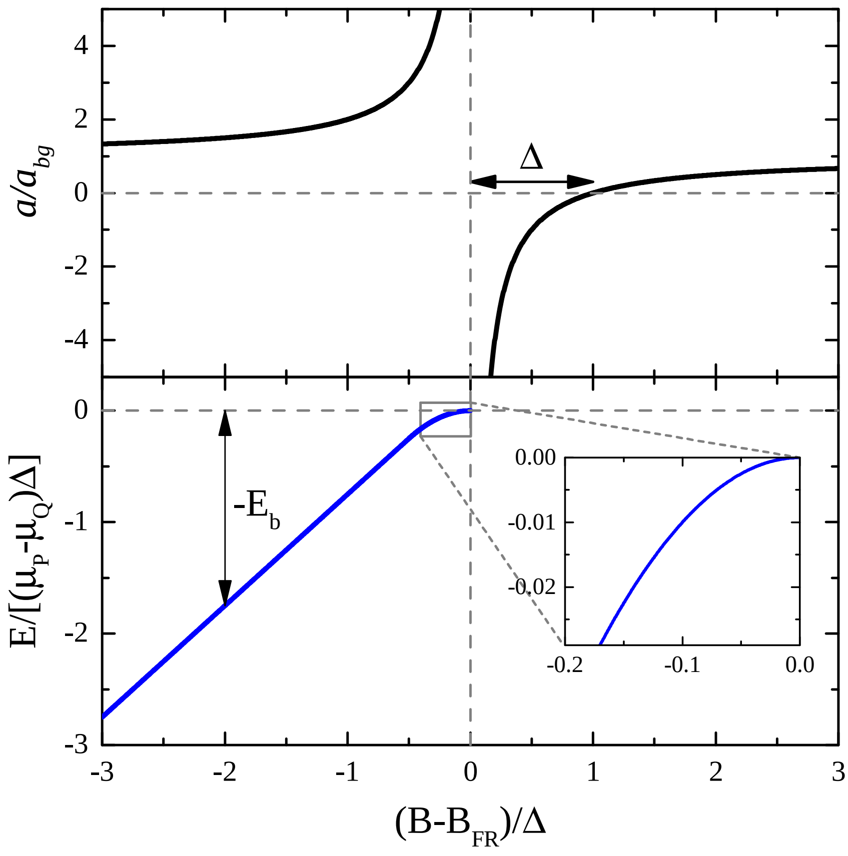

Figure 2.3.: Behavior of scattering length and binding energy close to a Feshbach resonance. Upper panel: scattering length a versus the magnetic field according to Eq. (2.30). The zero-crossing is located at a distance of one resonance width Δ from the resonance position B_{FR}. Lower panel: energy of the weakly-bound molecular state. The inset depicts the universal regime, where the binding energy is given by the universal formula Eq. (2.32). Replotted from Chin et al. [2010].

In the vicinity of the Feshbach resonance pole, the energy of the bound molecular state is given by [cf. Eq. (2.27)]:

$$E_b = \epsilon_Q + \mathcal{A}(E_b), \tag{2.31}$$

which consists of the unperturbed energy ϵ_Q of the closed subspace $\mathcal{Q}$ which is "dressed" by the incoming channel in the open subspace $\mathcal{P}$. In the vicinity of the resonance pole $B \to B_{\mathrm{FR}}$, where the binding energy E_b approaches zero, the closed-channel admixture of the Feshbach molecule is negligible and vanishes at the resonance position [Köhler et al., 2006]. In this regime, typically referred to as universal regime, the molecular state and its energy can be described solely by the entrance channel, and thus the scattering length a. From a rigorous treatment of the energy dependent complex energy shift $\mathcal{A}(E_b)$ [GÃ³ral et al., 2004; Köhler et al., 2006] we arrive at the universal formula of the binding energy

$$E_b = \frac{\hbar}{2\mu a^2}. \tag{2.32}$$

Coupling and classification of Feshbach resonance

Having introduced the basic concept of a Feshbach resonance, we now turn our discussion to the coupling between the entrance channel and the closed channels. Coupling between the different channels can be either achieved by the electronic interaction V, described by the molecular potential curves, or the spin-spin interaction H_{dd} contained in the scattering Hamiltonian Eq. 2.10. The isotropic electronic interaction V is diagonal in the angular momentum l and its projection m_l but has off-diagonal elements for quantum numbers $f_{A/B}$ and $m_{f,A/B}$. Thus, it can only provide coupling between the entrance channel and molecular bound states that have the same angular momenta $l = l_Q$ and $m_l = m_{l,Q}$[6]. This term, usually gives rise to a large interaction between the channels and leads to large resonance strengths. The spin-spin interaction H_{dd}, however, is anisotropic and has off diagonal elements in $f_{A/B}$,$m_{f,A/B}$, and l, and thus can couple channels with different l and l_Q. This term has only non-zero diagonal elements for $l > 0$ and typically leads to weak couplings and narrow resonances.

Feshbach resonances are classified by the quantum numbers of the entrance channel and of the closed channel bound state. It is important to note that the labeling of s, p, d, ...-wave Feshbach resonances does not correspond to the angular momentum l in the entrance channel of the colliding atom pair, but to the angular momentum l_Q of the closed-channel molecule. The angular momenta l and l_Q do not necessarily have to be the same and coupling between different partial waves is ensured by off-diagonal terms in the Hamiltonian. However, parity conservation requires $|l - l_Q|$ to be even [Chin et al., 2010].

For the Feshbach resonances observed in Li-Cs this means the following: the s-wave Feshbach resonances dominantly occur in the $l = 0$ entrance channel and the coupling is ensured by the V term in the Hamiltonian. At the experimental temperatures higher partial waves are frozen out due to the occurrence of the centrifugal barrier, which is much larger than the ultralow collision energies.

For the p-wave FRs the situation is considerably different as shown in Fig. 2.4. Here, also the entrance channel has to have odd l. Thus, even in the lowest possible $l = 1$ partial wave a rotational barrier exists in the entrance channel leading to a drastic reduction in the cross-section for low temperatures as $\sigma \propto T^2$ [Wigner, 1948]. However, at resonance the particles can resonantly tunnel through the potential barrier and the p-wave cross-section is considerably enhanced. In addition, the energy of the

---

[6] l and m_l characterize the open entrance channel and the bound molecular state in the closed channel is characterized by angular momentum l_Q and projection $m_{l,Q}$.

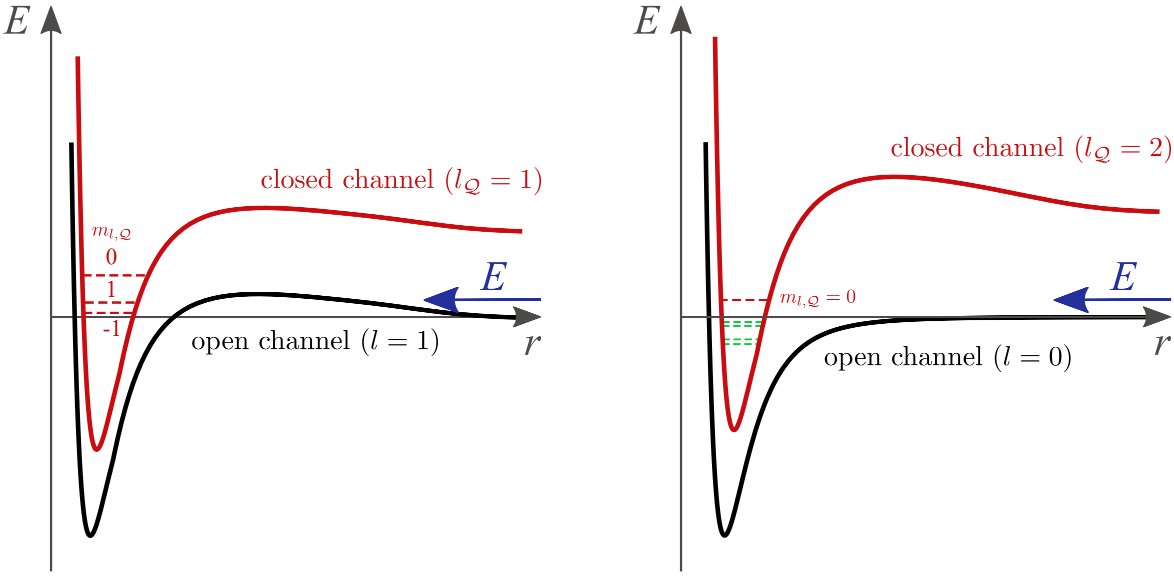

Figure 2.4.: Schematic p- and d-wave Feshbach resonances. The open and closed channel potentials are depicted by the black and red lines. The dashed lines give the bound state energies with different quantum numbers $m_{l,\mathcal{Q}}$. Left panel: p-wave FR occurring in the p-wave entrance channel. At resonance the particles can tunnel through the rotational barrier and couple to the $m_{l,\mathcal{Q}} = -1, 0, 1$ bound states in the $l_{\mathcal{Q}} = 1$ closed channel. The energy difference of the three $m_{l,\mathcal{Q}}$ leads to occurrence of a multiplet splitting of p-wave FRs. Right panel: d-wave FR from a s-wave entrance channel. There is no rotational barrier in the entrance channel. The coupling to the closed channel $m_{l,\mathcal{Q}} = 0$ molecule is provided by magnetic spin-spin interaction H_{dd}. Coupling to other $m_{l,\mathcal{Q}}$ is not allowed due to conservation of total m. For better representation the energies are not drawn in scale.

closed channel bound states depends on the magnetic quantum number $m_{l,\mathcal{Q}}$. Thus, the states with different $m_{l,\mathcal{Q}}$ will become resonant with the entrance channel at different magnetic fields. This will be reflected in a multiplet splitting of the FR. While the spin-spin interaction leads to a splitting according to $|m_{l,\mathcal{Q}}|$, the near-degeneracy of the $|m_{l,\mathcal{Q}}| = 1$ states is lifted by the spin-rotation interaction that couples differently to the $m_{l,\mathcal{Q}} = \pm 1$ states. Thus, we expect to observe the p-wave FRs as a triplet structure.

The d-wave Feshbach resonances in Li-Cs, however, predominantly result from s-wave entrance channel collisions, for which no rotational barrier is present. Thus, in contrast to p-wave FRs, d-wave FRs even persist in the limit of zero kinetic collision energy. The coupling between the different partial waves is due to the spin-spin Hamiltonian H_{dd}, which usually gives weak couplings and small resonance widths. d-wave FRs occurring in a s-wave entrance channel are observed as a single resonant feature, since the s-wave channel can only couple to one of the $m_{l,\mathcal{Q}}$ bound states. This is due to the conservation of the total quantum number $m_{l,\mathcal{Q}} + m_f = m_{f,A} + m_{f,B}$ in the collision process. Coupling to $m_{l,\mathcal{Q}} \neq 0$ would require $m_f \neq m_{f,A} + m_{f,B}$, which has an energy difference on the order of the Zeeman splitting being orders of magnitude larger than the splitting between the different $m_{l,\mathcal{Q}}$ bound states. Thus, for the d-wave resonances observed in our experiment, we do not expect to observe any multiplet splitting. A triplet splitting has recently been detected in a broad d-wave FR occurring from the d-wave open channel [Cui et al., 2017].

2.2. Li-Cs Feshbach resonances

Precise understanding of the magnetic field dependent interatomic scattering properties is essential for the study of Efimov physics, presented in Ch. 3, and many-body physics (Ch. 4) in the Li-Cs mixture. With the Hamiltonian from Eq. (2.10) it is in principle possible to calculate the Li-Cs scattering properties by a coupled channels calculation (see Sec. 2.2.1). However, these ab initio calculations did not prove to be accurate enough, since conventional molecular spectroscopy, such as laser-induced fluorescence Fourier-transform spectroscopy, does not provide precise enough long-range molecular potentials, whose understanding is crucial for predicting Feshbach resonances. Therefore, it is essential to characterize Feshbach resonances in the experiment and use the results as an input for the theoretical modeling of the Hamiltonian and the molecular potential V.

In order to achieve a more precise mapping of the scattering length on the magnetic field, we remeasure the previously observed Li-Cs s-wave and p-wave Feshbach resonances [Repp et al., 2013; Tung et al., 2013] and extend it by the first observation of d-wave resonances. These experiments are performed at one order of magnitude lower temperature and improved magnetic field stability. We experimentally explore the scattering properties of Li-Cs in the two energetically lowest scattering channels

$$\begin{aligned} |\alpha\rangle &= \mathrm{Li}\left|\frac{1}{2}, +\frac{1}{2}\right\rangle \oplus \mathrm{Cs}\left|3, +3\right\rangle , \\ |\beta\rangle &= \mathrm{Li}\left|\frac{1}{2}, -\frac{1}{2}\right\rangle \oplus \mathrm{Cs}\left|3, +3\right\rangle \end{aligned} \tag{2.33}$$

in the magnetic field range from 0 G to 1000 G. The two scattering channels are characterized by different projections m_f of the total angular momentum $m_f^{\alpha} = 7/2$ and $m_f^{\beta} = 5/2$.

In the following, the general measurement procedure with two complementary techniques, trap-loss spectroscopy and binding energy measurements, are introduced. In Sec. 2.2.3-2.2.5 we present the measurement results and their modeling with a coupled channels calculation for the s-, p-, and d-wave Li-Cs Feshbach resonances. The performed experiments allow for the construction of precise Li-Cs molecular singlet and triplet potentials, from which we calculate the s-wave scattering length, Feshbach resonance positions and widths. The outcomes agree well with previous measurements [Repp et al., 2013; Tung et al., 2013] and further theoretical modeling [Pires et al., 2014a], but feature almost one order of magnitude improvement in precision and accuracy.

2.2.1. Coupled channels model calculation

The coupled channels (cc) calculation is a numerical approach to solve the Schrödinger equation with the scattering Hamiltonian given by Eq. 2.10. In order to limit the number of coupled equations, the basis is truncated in the close-coupling approximation. In our approach this means, that the truncation is performed in the rotational quantum number l and by using only the electronic singlet $X^1\Sigma^+$ and triplet $a^3\Sigma^+$ ground state potentials. The coupling to higher electronic states is to some degree effectively contained in H_{dd}. In the case of ground state alkali atoms at ultra-cold temperatures, higher partial waves l components are strongly suppressed by the rotational barrier [see Eq. (2.15)]. In the present analysis, this means that we only consider the lowest possible partial waves, namely $l = 0$ for the s- and d-waves and $l = 1$ in case of p-waves, in the analysis of the Feshbach resonances. For $l > 1$ the respective rotational barrier is incorporated in the Hamiltonian. Inclusion of higher partial waves did not show any significant contribution and improvement in the theoretical description. We include all allowed spin channels for a given combination of spins s_A, s_B, i_A, and i_B and the projection m_f of the total molecular angular momentum.

The measured s-, p-, and d-wave Feshbach resonances (see Sec. 2.2.3-2.2.5), as well as previously measured Li-Cs FRs in spin channels involving Cs atoms in state Cs$|3, +3\rangle$, are modeled by a coupled channels calculation[7] [Dulieu and Julienne, 1995; Tiesinga et al., 1998] of the Li(2s)+Cs(6s) asymptote in a similar manner than in other alkaline-metal systems, e.g., as presented in Marzok et al. [2009] and Schuster et al. [2012]. In contrast to previous analysis in the Li-Cs system [Repp et al., 2013; Pires et al., 2014a; Ulmanis et al., 2015] we extend the scattering Hamiltonian with the spin-rotation term [see Eq. (2.10)]. We use atomic hyperfine constants and g-factors of Li and Cs from Arimondo et al. [1977] and atomic masses from tables by Audi et al. [2003]. Because of missing data of hyperfine splittings of deeply bound levels we keep the functions α_β constant at their respective atomic values. The parameters a_{SOi} and b_i of the second-order spin-orbit coupling in Eq. (2.19), as well as the spin-rotation coupling constant γ, are determined from the observed $m_l = -1, 0, 1$ splitting of the p-wave FRs and are given in the Appendix B.

---

[7] The coupled channels calculations were performed by Prof. E. Tiemann from Leibniz Universität Hannover, Germany.

The precise determination of FR resonance positions and scattering lengths relies on the knowledge of accurate LiCs molecular potential curves of the electronic singlet $X^1\Sigma^+$ and triplet $a^3\Sigma^+$ ground states. The molecular potentials are expanded in a power series of internuclear separation R similar to NaK ground state potential curves [Gerdes et al., 2008] and are given in Appendix B. The coefficients are fitted to simultaneously reproduce 6498 rovibrational transitions from laser-induced fluorescence Fourier-transform spectroscopy [Staanum et al., 2007] as well as all known Li-Cs Feshbach resonances, meaning, we not only include the measurements of *s*-,*p*- and *d*-wave Feshbach resonances in the two energetically lowest scattering channels presented in Sec. 2.2.3-2.2.5, but also previous measurements of *s*- and *p*-wave resonances in the $\text{Li}|1/2, \pm 1/2\rangle \oplus \text{Cs}|3, +2\rangle$ entrance channel [Repp et al., 2013] in our analysis. From the model we extract the theoretical resonance positions B^t as the peak positions of the two-body collision rate at a kinetic energy corresponding to the measured atomic cloud temperature for each resonance and compare them to the experimental findings.

2.2.2. Measurement of Feshbach resonances

In our experiments, we gain information about the Li-Cs FRs by two complementary techniques: Atom-loss spectroscopy and radio-frequency spectroscopy of the weakly bound dimer state. In the following we discuss the two methods and outline their assets and drawbacks.

Trap-loss spectroscopy

Trap-loss spectroscopy is a commonly applied method for the experimental observation of Feshbach resonances [Chin et al., 2010]. The technique relies on the resonant enhancement of ineleastic collisions in the vicinity of a Feshbach resonance. In order to understand the procedure, we describe the main processes responsible for loss from an ultracold atomic sample:

- **One-body losses.** In ultracold atomic experiments there a two main sources of one-body losses: Either the trapped atoms collide with remaining particles from the background gas and thus gain sufficient kinetic energy to leave the trap, or they absorb photons from the optical dipole trap. One-body losses are independent of the atomic density and typically lead to lifetimes of the trapped atoms on the order of tens of seconds to minutes.

- **Two-body losses.** Inelastic two-body collisions occur when the internal state of the atoms changes in the binary collision event. For atoms polarized in their energetically lowest channel, i.e. $|\alpha\rangle = {}^6\text{Li}|1/2, 1/2\rangle \oplus {}^{133}\text{Cs}|3, +3\rangle$, such processes are excluded. For all other channels these losses are possible. However, for the

$|\beta\rangle$=^{6}Li$|1/2,-1/2\rangle\oplus{}^{133}Cs|3,+3\rangle$ channel the inelastic two-body rate is negligible [Tung et al., 2013]. Additional two-body losses might occur due to sympathetic evaporation of one species by the other. This means, if the trap depths, and consequently the temperatures, of the two species are largely different one of the species is heated by the other one and evaporates. Since the elastic scattering cross-section scales as a^2 [Eq. (2.9)], we expect an enhancement of elastic losses close to the Feshbach resonance.

- **Three-body losses.** In our experiments three-body recombination is the dominating loss process. During this event, the three colliding atoms form a diatomic molecule and a free atom. The molecular binding energy is released as kinetic energy, which typically exceeds the trapping potential and leads to immediate loss of the constituents from the trap. The three-body loss coefficient L_3 scales as [Fedichev et al., 1996; Esry et al., 1999; Nielsen and Macek, 1999]

$$L_3 \propto C(a,T)a^4, \tag{2.34}$$

where $C(a,T)$ contains the modulation due to the Efimov effect (see Sec. 3.1.3). L_3 exhibits a loss maximum at the Feshbach resonance position B_{FR}, where the scattering length a diverges and a minimum can be found close to the zero crossing of the s-wave scattering length. This procedure allows for the determination of Feshbach resonance positions and widths. However, the loss mechanisms in Bose-Fermi mixtures are considerably different, due to the interplay between inter- and intraspecies scattering lengths [D'Incao and Esry, 2009] and Pauli suppression effects. Additionally, the shape of the loss feature might be highly asymmetric and might include additional loss processes, e.g. due to weakly-bound dimer formation and subsequent atom-dimer recombination on the positive scattering length side of the Feshbach resonance. These effects can lead to a shift between the Feshbach resonance position B_{FR} and the maximum of the losses [Dieckmann et al., 2002; Bourdel et al., 2003; Zhang and Ho, 2011; Weber et al., 2008; Machtey et al., 2012a; Khramov et al., 2012] as has been observed for the broad Li-Cs s-wave resonances, cf. Fig. 2.7. In general one can state that a Feshbach resonance is accompanied by a loss maximum.

Using the knowledge of the leading trap-loss processes, we use magnetic field dependent trap-loss spectroscopy to detect Feshbach resonances. This means, we record the remaining number of Li and Cs atoms after a holding time t_{hold} as a function of the magnetic field. The holding time is chosen such that the relative atom loss signal on resonance is between 30% and 50%. This time varies strongly between different Feshbach resonances and depends on the strength of the FR. A typical measurement is performed as follows: the mixture is prepared at a constant magnetic field, the pre-set field, interacts at the measurement field B for a time t_{hold} and is then imaged at the high-field imaging field. Special care in the measurement sequence has to be taken in order to avoid additional loss processes that could mimic the loss behavior of a Feshbach resonance or lead to asymmetric line-shapes of the loss features. Such processes include for example magneto-association of Feshbach dimers (see Fig. 5.1) by ramping over a Feshbach resonance from negative to positive scattering lengths when setting the measurement field. This might lead to enhanced losses on the positive-a-side of the FR. Additional losses may occur at the pre-set field, high-field imaging field and during the ramps. However, the measurements were performed with holding times much larger than the ramp times for setting the magnetic field strength and thus these effects can be neglected. Atom-loss spectroscopy is a simple and straightforward technique for the detection of Feshbach resonances. It relies on an indirect measurement of the two-body Feshbach physics via three-body loss processes and thus might be prone to misinterpretation of its results. Therefore, it is desirable to directly study the two-body interaction.

Binding energy measurement

A second method for the detection of Feshbach resonances is the measurement of the binding energy of the weakly-bound dimer state shown in Fig. 2.3. This technique is complementary to atom-loss spectroscopy, but provides a more accurate and direct way to infer FR properties such as resonance position and width. In the vicinity of a FR the binding energy is approximately related to the scattering length via the universal relation given in Eq. (2.32). Therefore, the study of the binding energy gives direct access to the two-body physics governing the Feshbach resonance. The s-wave scattering length, Feshbach resonance positions, and widths can be precisely determined in combination with theoretical modeling. This technique especially proved to be valuable in case of broad s-wave resonances, where atom-loss features might be ambiguous and hard to interpret, and has led to the most precise measurements of ultracold scattering properties. The energy of the weakly-bound dimer was probed either by the magnetic field oscillation technique [Thompson et al., 2005; Papp and Wieman, 2006; Weber et al., 2008; Fuchs et al., 2008; Lange et al., 2009; Thalhammer et al., 2009; Gross et al., 2010; Dyke et al., 2013; Berninger et al., 2013a] or radio-frequency (rf) and microwave (mw) spectroscopy [Regal et al., 2003; Bartenstein et al., 2005; Ospelkaus et al., 2006a; Mark et al., 2007; Zirbel et al., 2008; Maier et al., 2010; Wu et al., 2012; Zürn et al., 2013; Huang et al., 2015b]. In our experiments, we perform rf spectroscopy by associating the weakly bound dimer state from the colliding atom pair. Such a transition is called “free-bound” transition.

2.2.3. s-wave Li-Cs Feshbach resonances

We remeasure the five s-wave Feshbach resonances in the two energetically lowest scattering channels $|\alpha\rangle$ and $|\beta\rangle$ [Repp et al., 2013; Tung et al., 2013] in the magnetic field range between 800 G and 1000 G. In comparison to their previous determination our experiments are performed with one order of magnitude lower temperature and improved magnetic field stability. We distinguish the resonances by their width Δ and group them into narrow and broad ones. For the narrow resonances ($\Delta < 5$ G) close to 816 G, 892 G, and 943 G we perform atom-loss spectroscopy. Their small width allows to determine the resonance position with high accuracy. In case of the broad s-wave resonances close to 843 G and 889 G we employ binding energy measurements of the Feshbach dimer, which allows us to solely access the two-body physics leading to the Feshbach resonance, and thereby being less prone to false interpretation of the connection between scattering length and atomic loss.

Radio-frequency spectroscopy of LiCs Feshbach dimers

We prepare an ultracold Li-Cs mixture consisting of 4×10^4 Li and 4×10^4 Cs atoms at a temperature of 400 nK as described in Sec. 1.3.3. The measured trapping frequencies are $\omega_{\mathrm{Li}} = 2\pi \times (33, 275, 308)$ Hz and $\omega_{\mathrm{Cs}} = 2\pi \times (11, 114, 123)$ Hz, where the external magnetic field and gravity are parallel to the z-axis. The mixture is initially produced in the non-resonant state at a variable magnetic field slightly below the FR position in the interacting state (cf. Fig. 2.5). In case of the study of the 843 G Feshbach resonance, shown in Fig. 2.5(a), the mixture is initially prepared in the $|\beta\rangle$ state and subsequently associated into dimer states coupled to the $|\alpha\rangle$ scattering channel. Accordingly, for the 889 G resonance is prepared in $|\alpha\rangle$ and associated into the molecular state coupled to $|\beta\rangle$ which is depicted in Fig. 2.5(b). We perform rf spectroscopy by shining in a rectangular rf pulse and scanning its frequency E_{rf}/h in the vicinity of the resonance frequency $E_0/h \approx 76$ MHz between the two energetically lowest Li spin states and observing the remaining fraction of Li atoms in the initially-prepared non-resonant state.

In the spectroscopy measurements, we observe two loss features in the population of Li atoms in the non-resonant state. Close to the frequency E_0/h we observe a broad resonance feature corresponding to the nuclear spin flip transition to the other Li spin state. We refer to this transition as “free-free”. This feature is considerably broadened in comparison to a typical nuclear spin flip transition due to high rf-powers and might be shifted with respect to the unperturbed free-free transition due to mean-field shifts caused by the interaction with Cs atoms. Therefore we do not consider this transition in the determination of the dimer binding energies or magnetic field calibration. A second loss feature is found for detunings of up to 600 kHz from the free-free transition, which can be ascribed to the formation of weakly bound LiCs dimers.

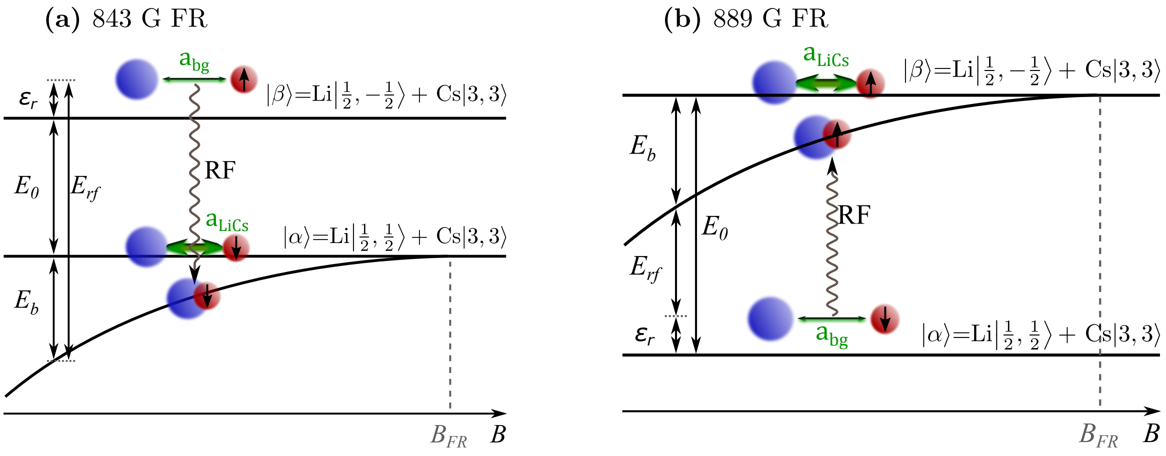

Figure 2.5.: Radio-frequency spectroscopy of Li-Cs Feshbach molecules close to the two broad Li-Cs Feshbach resonances close to (a) 843 G and (b) 889 G. We prepare an ultracold mixture in the non-resonant channel $|\beta\rangle$ ($|\alpha\rangle$) at a magnetic field slightly below the resonance position of the Li-Cs 843 G (889 G) s-wave FR. At this fields a weakly bound dimer state exists, that is coupled to the resonant channel. We perform spectroscopy by varying the energy E_{rf} of the rf field and observe the free-free transition at an energy of E_0 and the free-bound transition shifted by energies of $\pm E_b$ (the plus and minus sign apply for the 843 G and 889 G FR, respectively). The relative collision energy ε_r of the colliding atom pair is typically much smaller than the other energy scales. The energy spacings are not to scale and have been changed for better representation. Figure adapted from [Ulmanis, 2015].

This transition originating from the scattering state into the weakly-bound dimer state is called "free-bound" transition. Typical rf-association spectra are shown in Fig. 2.6. The atom loss is originating from the association of LiCs Feshbach molecules and subsequent recombination with the remaining Li and Cs atoms in the initial non-resonant state. Therefore, we observe a similar loss feature in the remaining number of Cs atoms. The length and power of the applied rf pulses are experimentally optimized such that at most 30% of the atoms are lost after association in order to avoid saturation effects. The pulse lengths are in the range between 0.5 s in the vicinity of the Feshbach resonance up to 7 s away from the resonance.

The association lineshape can be model by a rate equation model and the dimer binding energy dependent two-body association rate [Chin and Julienne, 2005; Klempt et al., 2008]. By assuming a quasi-stationary state, where each molecule is immediately lost through atom-dimer recombination, the time evolution of the number of Li atoms in the non-resonant state can be described by the following equation [Ulmanis et al., 2015]

$$N_{\mathrm{Li}} = N_{\mathrm{Li}}^{0} e^{-n_{\mathrm{Cs}} K_2^M \tau}, \tag{2.35}$$

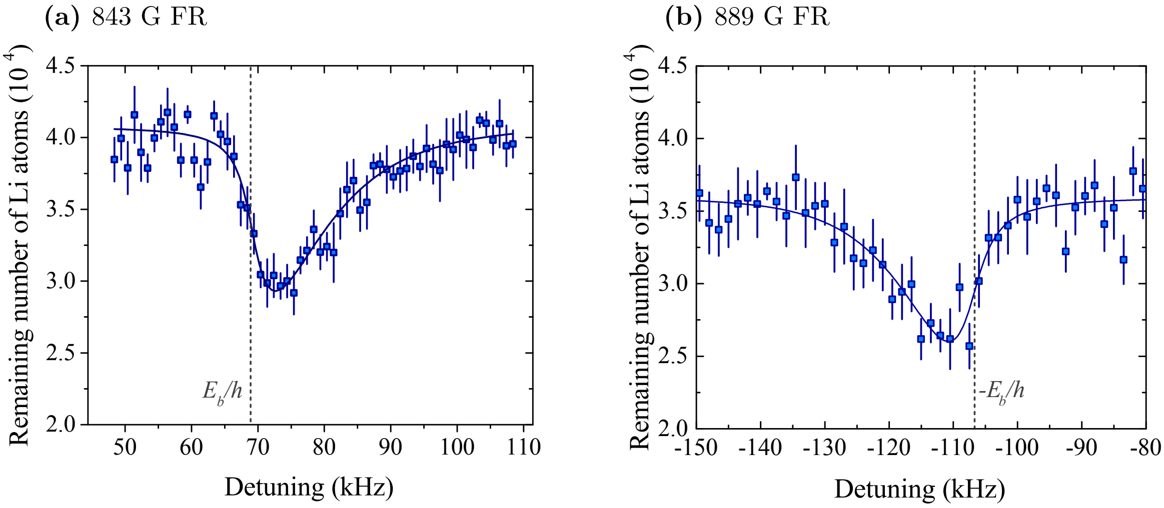

Figure 2.6.: Remaining number of Li atoms in the initially-prepared, non-resonant state after rf association of LiCs Feshbach dimers versus the detuning $(E_{rf} - E_0)/h$. (a) spectrum at a magnetic field of 842.04 G and (b) at 887.599 G close to the broad s-wave resonances in $|\alpha\rangle$ and $|\beta\rangle$ scattering channel, respectively. The experiments were performed at a temperature of 400 nK. Each point is an average of at least three measurements, where the error bars represent the standard error of the mean. The solid lines show a fit of the theoretic line-shape function Eq. (2.36) to the data from which the binding energy is obtained (vertical dashed lines). Figure adapted from [Ulmanis, 2015].

where N_{Li}^0 is the initial number of Li atoms, n_{Cs} the density of the Cs atoms, τ the length of the rf-pulse, and K_2^M the molecular association rate modeled by[8]

$$K_2^M(E_{rf}) = C\int_0^\infty h(\varepsilon_r)F(\varepsilon_r, E_b)L_\gamma(E_{rf}, E_0 + E_b + \varepsilon_r)d\varepsilon_r. \tag{2.36}$$

Here $h(\varepsilon_r) \propto e^{-\varepsilon_r/k_bT}$ is the number density of colliding atom pairs with relative energy ε_r and temperature T containing the information about the energy distribution in the initial state. $L_\gamma(E_{rf}, E_0 + E_b + \varepsilon_r)$ is a Lorentzian profile. The energy dependent Franck-Condon overlap between the scattering wave function of a Li-Cs atom pair in the non-resonant channel and the bound Feshbach dimer is

$$F(\varepsilon_r, E_b) \propto \left(1 - \sqrt{\frac{E_b}{E_b'}}\right)^2 \frac{\sqrt{\varepsilon_r E_b}E_b'}{(\varepsilon_r + E_b)^2(\varepsilon_r + E_b')}\ , \tag{2.37}$$

---

[8] Note: For the case of the 889 G resonance occurring in state $|\beta\rangle$ the necessary frequency for dimer association is smaller than E_0/h (cf. Fig 2.5). Therefore, in the expression of K_2^M we make the substitution $L_\gamma(E_{rf}, E_0 + E_b + \varepsilon_r) \rightarrow L_\gamma(E_{rf}, E_0 - E_b - \varepsilon_r)$ in the analysis of the rf-spectra close to the 889 G Feshbach resonance.

where E_b is the binding energy of the bound dimer state and $E_b' = \hbar^2/(2\mu a'^2)$ is given by the scattering length a' in the non-resonant channel. The asymmetry of the observed lineshapes (see Fig. 2.6) originates from the distribution of the relative collision energy $h(\varepsilon_r)$ at the finite temperature of the atomic samples.

The dimer binding energy E_b for each magnetic field is extracted by fitting Eq. (2.35) to the rf loss spectra of Li atoms as shown in Fig. 2.6, where the fitting parameters are E_b, N^0_{Li}, γ, and C. The temperature is determined from single species experiments under the same conditions, and the non-resonant scattering length is fixed to $a' = -28.5\ a_0$ [Repp et al., 2013; Tung et al., 2013; Pires et al., 2014a]. A detailed analysis of possible systematic shifts in the determination of the binding energy, including variations of a', uncertainties in temperature determination, mean-field shifts, differential AC-Stark shifts, confinement induced shifts, and corrections due to non-separability of relative and center-of-mass coordinates, has been performed in Ulmanis [2015]. These effects have been included in the total systematic error.

The measured binding energy of the LiCs Feshbach dimer in the vicinity of the two broad s-wave Feshbach resonances located at 843 G and 889 G are shown in Fig 2.7, together with the theoretical prediction of the coupled channels calculation, Sec. 2.2.1, and a plot of the universal formula $E_b = \hbar^2/2\mu a^2$ using the parameters obtained from the cc calculation given in Table 2.1. The measured binding energies are very well described by the universal formula in the shown magnetic field range. We do not expect large deviations from the $1/a^2$ behavior, since in the shown magnetic field range the scattering length a is much larger than the background scattering length a_{bg} and the Li-Cs van der Waals length scale $r^{\mathrm{LiCs}}_{\mathrm{vdW}} = 45\ a_0$. In addition the different Feshbach resonances in the same scattering channel separate clearly from each other and thus one can treat them independently.

For binding energies $E_b \lesssim 10$ kHz the molecular association feature overlaps with the free-free transition. Therefore, a reliable and precise determination of the binding energy is not possible and strongly dependent on the exact functional form of the assumed combined fitting model. Thus, we exclude these data points in the theoretical analysis of the Feshbach resonance parameters. At the observed maximum in the atomic loss [Pires et al., 2014b; Tung et al., 2014] represented by the green data points in Fig. 2.7, however, we clearly observe molecular formation. Hence, the atom-loss maximum does not coincide with the pole of the Feshbach resonance. As outlined previously in Sec. 2.2.2, this points out that atom-loss spectroscopy may be ambiguous in the precise determination of the resonance position in case of broad s-wave resonances, where the width is much larger than the experimental uncertainties. Additional loss processes may lead to increased losses away from the pole of the Feshbach resonance. Therefore, the total loss maximum can be shifted with respect to the maximum in the three-body recombination [Dieckmann et al., 2002; Bourdel et al., 2003; Zhang and Ho, 2011] and Feshbach resonance position.

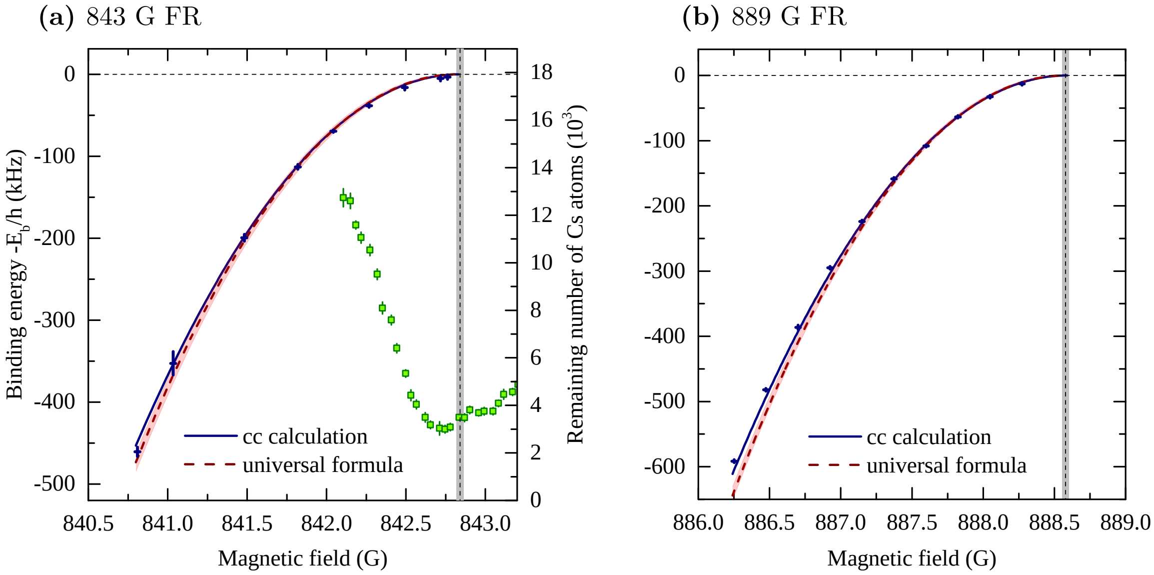

Figure 2.7.: LiCs dimer binding energies close to (a) the 843 G and (b) the 889 G Feshbach resonance. The corresponding atom-loss spectroscopy data are given by the green data points. The blue symbols represent the measured binding energy of the Feshbach molecules extracted by fitting Eq. (2.35) to the rf association spectrum at each magnetic field. The error bars represent one standard deviation of the total error, resulting from statistical and systematic uncertainties. The blue line represents the calculated molecular energies from the coupled channels model and the red dashed line is a plot of the universal binding energy from Eq. (2.32) for the resonance parameters given in Table 2.1. The red shaded region corresponds to the uncertainty of the FR parameters. The green squares show the remaining number of Cs atoms, and the error bars correspond to one standard error of the mean. The vertical dashed line displays the resonance pole position from the coupled channels calculation and the shaded region represents its uncertainty. Adapted from [Ulmanis et al., 2015].

Atom-loss spectroscopy at narrow s-wave resonances

The remaining three narrow s-wave Feshbach resonances are detected via standard atom-loss spectroscopy. The atom-loss spectra of Cs atoms are displayed in Fig. 2.8. Similar features are observed in the remaining number of Li atoms. The experimental resonance positions B^e are obtained by fitting Gaussian profiles to the loss features and are listed in Table 2.1. The improved magnetic field stability and lower temperatures allow us to determine them with a roughly five-fold better precision than in previous measurements [Repp et al., 2013]. In contrast to the two broad s-waves, where we observed a shift of the atom-loss maximum with respect to the resonance position, we do not expect large deviations between the Feshbach resonance position and the loss maximum for these resonances. From our observations at the broad s-waves, where

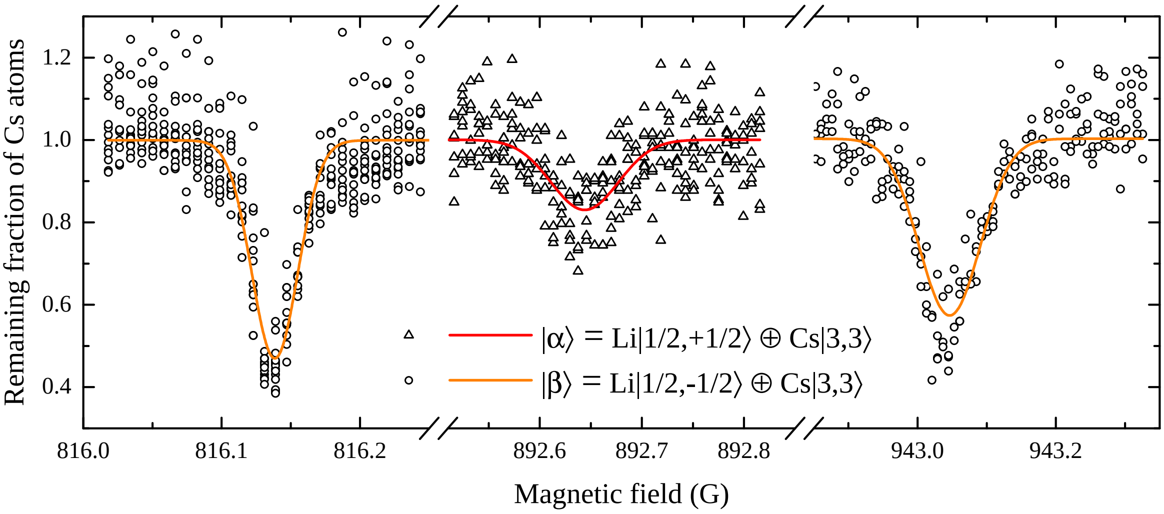

Figure 2.8.: Atom-loss spectroscopy of three narrow Li-Cs s-wave Feshbach resonances in the two lowest scattering channels $|\alpha\rangle$ and $|\beta\rangle$. The remaining fraction of Cs atoms after holdtimes of 100 ms (816 G and 892 G resonance) and 200 ms (943 G resonance) is plotted in dependence of the magnetic field. The red and orange lines are fits of Gaussian profiles from which the experimental resonance positions B^e are extracted (see Table 2.1).

this shift is on the order of a couple of permill of the Feshbach resonance width Δ, we estimate a shift of $\sim$ 10 mG for the narrow resonances, which is on the order of our experimental uncertainty.

Li-Cs s-wave scattering length and Feshbach resonances

The experimental resonance positions B^e and the results of the cc modeling B^t are listed in Table 2.1. In case of the two broad s-wave resonances B^e gives the extrapolated resonance position from the calculated binding energies. The theoretical Feshbach resonance positions B^t are the maxima of the calculated total two-body collision rate for the experimental kinetic energy and are listed as deviation $\delta = B^e - B^t$ from the experimental value. These results provide almost an order of magnitude improvement over the previous determination of the FR positions through trap-loss measurements [Repp et al., 2013; Tung et al., 2013] and rf spectroscopy [Pires et al., 2014b], and are consistent with an extensive theoretical analysis by Pires et al. [2014a], if the differences in determining the resonance positions and experimental accuracy are taken into account.

Finally, we calculate the magnetic field dependent s-wave scattering length from the coupled channels model at a kinetic energy of $k_B \times 1$ nK for both scattering channels

Entrance channel	B^e (G)	δ (mG)	T (nK)	B_{FR} (G)	Δ (G)	a_{bg} (a_0)
$\lvert\alpha\rangle$=Li$\lvert 1/2, +1/2\rangle$ $\oplus$Cs $\lvert 3, +3\rangle$	842.845(16)*	-0	100	842.829	-58.21	-29.4
	892.655(30)†	5	100	892.629	-4.55	-29.4
$\lvert\beta\rangle$=Li$\lvert 1/2, -1/2\rangle$ $\oplus$Cs $\lvert 3, +3\rangle$	816.128(20)	-5	300	816.113	-0.37	-29.6
	888.595(16)*	2	100	888.578	-57.45	-29.6
	943.020(50)	-33	400	943.033	-4.22	-29.6

---

[*] Extrapolated from rf-association spectroscopy. The temperature shown is only used for the calculation of the scattering resonance and selected sufficiently low to reduce its influence to less than 5 mG. The error reflects the uncertainty of the field calibration.

[†] This measurement was performed in the bichromatic dipole trap with species selective optical potentials, as described in Sec. 1.3.3.

Table 2.1.: Feshbach resonance positions of the LiCs s-wave Feshbach resonances in the two energeticall lowest scattering channels $\lvert\alpha\rangle$ and $\lvert\beta\rangle$. The experimental resonance positions B^e are extracted either by fitting Gaussian profiles to the atom-loss spectra or extrapolation from the binding energy measurements. The numbers in brackets represent the total error, including the uncertainty of the magnetic field calibration, statistical and systematic errors in the determination of the resonance center. The resonance positions obtained from the coupled channels calculation B^t are given as deviations $\delta = B^e - B^t$ to the experimental observations. B_{FR}, Δ, and a_{bg} are the fitted resonance pole position, width, and background scattering length, respectively, from the calculation of the scattering length at a kinetic energy of $k_B \times 1$ nK. The scattering length is given in units of the Bohr radius $a_0 = 0.5292 \times 10^{-10}$ m.

$\lvert\alpha\rangle$ and $\lvert\beta\rangle$. We fit their dependence with the conventional functional form

$$a(B) = a_{bg}\left(1 - \sum_i \frac{\Delta_i}{B - B_{\mathrm{FR},i}}\right) \tag{2.38}$$

with as many terms i as there are resonances in the given channel. The resonance position $B_{\mathrm{FR},i}$, its width Δ_i, and background scattering length a_{bg} are used as fitting parameters, and listed in Table 2.1. The simultaneous fit of all observed resonances in Eq. (2.38) allows to define a single effective background scattering length for each channel. The fitted values reproduce the calculated s-wave scattering length to better than 2% in the entire magnetic field range between 500 G and 1000 G, which we also use for the evaluation of the Efimov resonance positions in Ch. 3. We observe a slight difference between the two theoretically obtained resonance pole positions B^t and B_{FR}. One might suspect that it originates from the different types of numerical calculations that were used to extract these parameters, however, further investigation is necessary to find the exact reason behind this difference. Therefore we estimate the error for the resonance pole positions from the systematic error from the magnetic field uncertainty

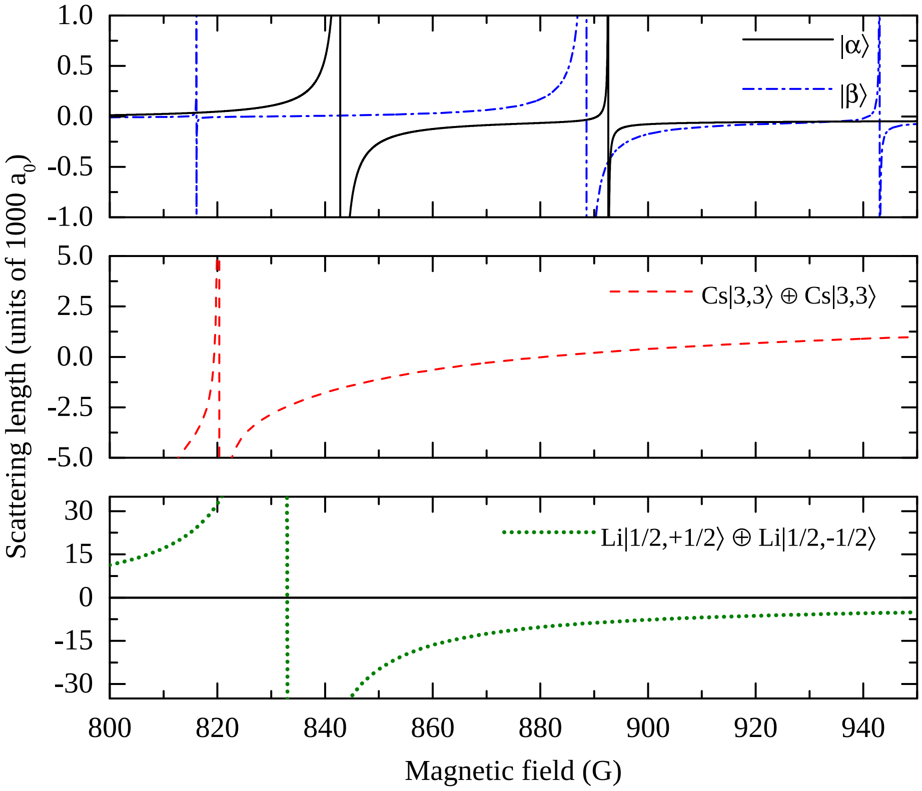

Figure 2.9.: Interspecies scattering lengths a_{LiCs} for the channels $|\alpha\rangle = \mathrm{Li}|1/2, 1/2\rangle \oplus \mathrm{Cs}|3,3\rangle$ (upper panel, black line), $|\beta\rangle = \mathrm{Li}|1/2, -1/2\rangle \oplus \mathrm{Cs}|3,3\rangle$ (upper panel, blue dash dotted line) and intraspecies scattering length a_{Cs} for Cs atoms in the ground state $\mathrm{Cs}|3,3\rangle \oplus \mathrm{Cs}|3,3\rangle$ (middle panel, red dashed line). The lowest panel (green dotted line) shows the scattering length between the two energetically lowest ^{6}Li spin states $\mathrm{Li}|1/2, 1/2\rangle \oplus \mathrm{Li}|1/2, -1/2\rangle$. Scattering lengths taken from Table 2.1, Berninger et al. [2013a] and Zürn et al. [2013].

and the difference between the theoretical values, which yields ± 23 mG.

The Li-Cs s-wave scattering length dependence for channels $|\alpha\rangle$ and $|\beta\rangle$ on the magnetic field is shown in Fig. 2.9 together with the intraspecies scattering lengths between Cs atoms in their energetically lowest spin state $\mathrm{Cs}|3,3\rangle \oplus \mathrm{Cs}|3,3\rangle$ [Berninger et al., 2013a] and between the two energetically lowest ^{6}Li spin states $\mathrm{Li}|1/2, 1/2\rangle \oplus \mathrm{Li}|1/2, -1/2\rangle$ [Zürn et al., 2013]. In the range between 800 G and 1000 G the system offers in total five interspecies s-wave Feshbach resonances, out of which two are intermediately broad ($s_{\mathrm{res}} \approx 0.7$ [Tung et al., 2013]) and three are narrow resonances characterized by $s_{\mathrm{res}} \leq 0.03$ [Tung et al., 2013].

The Cs-Cs scattering length in this magentic field region is dominated by a broad s-wave FR located at 787 G [Berninger et al., 2013a] and displays a zero-crossing at about 880 G. The Li-Li scattering length shows a very broad Feshbach resonance at 832 G [Zürn et al., 2013] and, in most of the field range, is large and negative.

The inter- and intraspecies scattering lengths in the Li-Cs system offer several interesting regimes. The two intermediately broad Li-Cs FRs are characterized by a different sign and magnitude of the Cs-Cs scattering length a_{Cs}: while close to the 843 G resonance the intraspecies scattering length is large and negative $a_{\mathrm{Cs}} \approx -1500\ a_0$, the 889 G resonance is characterized by a small and positive intraspecies scattering length $a_{\mathrm{Cs}} \approx +190\ a_0$ [Berninger et al., 2013a]. Since the 889 G Li-Cs FR is close to the zero-crossing in a_{Cs} we can create situations in which the bosons do not interact with each other, but at the same time strongly interact with the lithium. Thus, there might be interactions between them which are mediated by the presence of the fermionic Li atoms.

2.2.4. p-wave Li-Cs Feshbach resonances

In order to obtain a full understanding of the Li-Cs scattering properties, we perform high-precision atom-loss spectroscopy on the five Li-Cs *p*-wave FR multiplets of the $|\alpha\rangle$ and $|\beta\rangle$ scattering channels [see Eq. (2.33)] in the magnetic field range between 650 and 770 G [Repp et al., 2013]. The ultracold mixture is prepared as described in Sec. 1.3.3 with approx. 5×10^4 Cs in state $|3,+3\rangle$and 3×10^4 Li atoms either in state $|1/2, 1/2\rangle$ or $|1/2, -1/2\rangle$ are trapped at a temperature of 430 nK. The Li and Cs atomic loss signals for the *p*-wave Feshbach resonances are shown in Fig. 2.10. The numbers of atoms are measured after variable interaction times between 0.4 s and 10 s and have been normalized to the values far off the interspecies FR. These values can be considerably different from the initial number of atoms due to competing loss processes such as three-body recombination of Cs atoms. Each point is an average of at least four measurements and the error bars resemble the standard deviation.

In addition to the well-known doublet structure of *p*-wave FRs due to magnetic dipole-dipole and second order spin-orbit interactions [Ticknor et al., 2004; Repp et al., 2013], we observe a further splitting of the $m_l = \pm 1$ components for the resonances close to 658 G, 663 G, and 708 G [see Fig. 2.10(e), 2.10(a), and 2.10(c)]. However, this triplet structure is not resolved for the 714 G and 764 G Feshbach resonances [Fig. 2.10(b) and 2.10(d)], even if the magnetic field step-size was reduced to 2 mG close to the resonance.

We obtain the experimental resonance positions B_i^e by fitting a sum of Gaussian functions

$$N = N_0 \left(1 - \sum_i \frac{A_i}{\sigma_i \sqrt{2\pi}} \exp\left[-\frac{1}{2}\left(\frac{B - B_i^e}{\sigma_i}\right)^2\right]\right) \tag{2.39}$$

with widths σ_i to the Li and Cs loss spectra with as many summands i as loss features observed. The off-resonant number of atoms N_0 and amplitudes A_i are additional fitting parameters. The resonance positions attained from Li and Cs data are averaged and their difference (<2 mG) is included in the statistical uncertainty. The observed

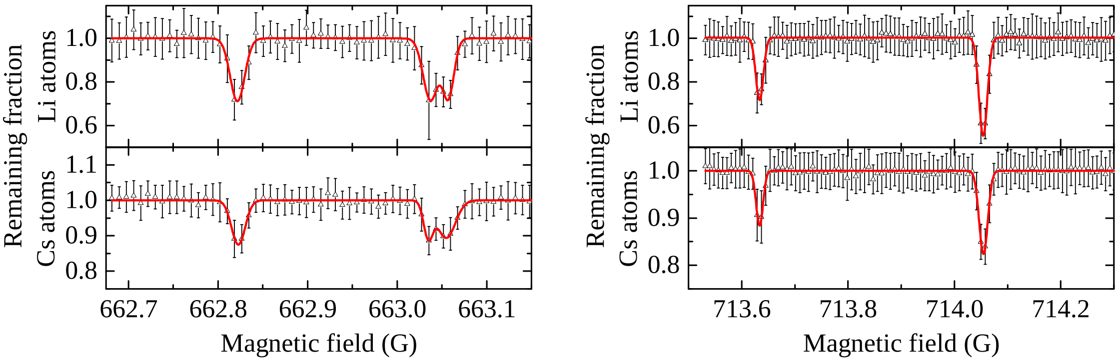

(a) 663 G p-wave FR in channel $|\alpha\rangle$ **(b)** 714 G p-wave FR in channel $|\alpha\rangle$

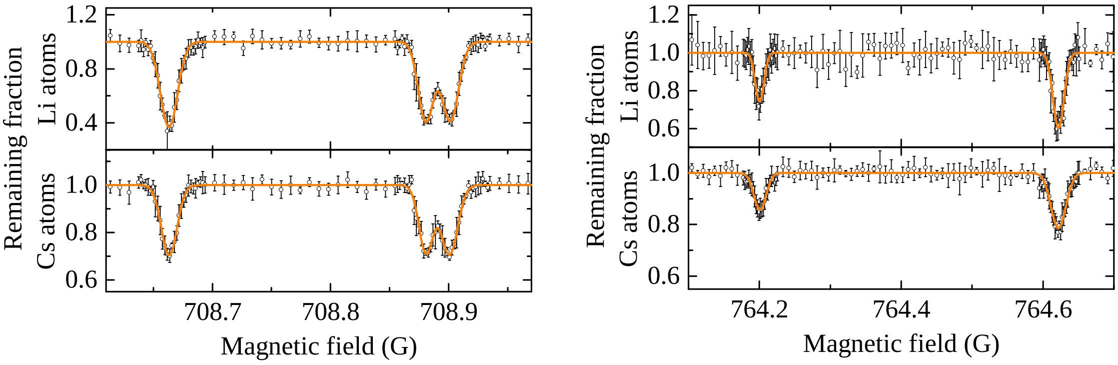

(c) 708 G p-wave FR in channel $|\beta\rangle$ **(d)** 764 G p-wave FR in channel $|\beta\rangle$

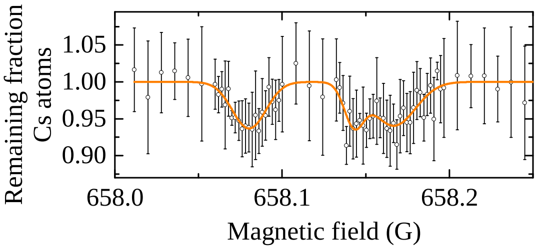

(e) 658 G p-wave FR in channel $|\beta\rangle$

Figure 2.10.: Feshbach spectroscopy of the five Li-Cs p-wave Feshbach resonances in the (a)-(b) $|\alpha\rangle$=Li$|1/2,+1/2\rangle \oplus$Cs$|3,3\rangle$ and (c)-(e) $|\beta\rangle$=Li$|1/2,-1/2\rangle \oplus$Cs$|3,3\rangle$ channels in the magnetic field range between 658 G and 765 G. The upper panels show the remaining fraction of Li atoms in either of the $|1/2,\pm 1/2\rangle$ states and the lower panel shows Cs atoms in the $|3,3\rangle$ state after optimized holding times ranging from 0.4 s to 10 s. Each point is the average of at least four measurements and the error bars represent the standard deviation. While the resonances at 658 G, 663 G, and 708 G split into a triplet, the 714 and 764 G resonances are observed as a doublet. The red and orange curves are fits of a sum of 3 (2) Gaussian functions. The fitted resonance positions B^e and widths σ are listed in Table 2.2.

Entrance channel	B^e (G)	σ (mG)	δ (mG)	m_l
$\lvert\alpha\rangle$=Li$\lvert 1/2, +1/2\rangle$ $\oplus$ Cs$\lvert 3, +3\rangle$	662.822(3)(16)	8	22	0
	663.036(4)(16)	7	16	+1
	663.056(4)(16)	8	19	-1
	713.632(4)(16)	8	-4	0
	714.054(4)(16)§	8	3	+1
	714.054(4)(16)§	8	-6	-1
$\lvert\beta\rangle$=Li$\lvert 1/2, -1/2\rangle$ $\oplus$ Cs$\lvert 3, +3\rangle$	658.080(10)(16)	10	46	0
	658.143(10)(16)	6	40	+1
	658.167(10)(16)	13	39	-1
	708.663(3)(16)	7	15	0
	708.881(3)(16)	6	9	+1
	708.901(3)(16)	7	12	-1
	764.201(1)(16)	8	-21	0
	764.622(1)(16)§	9	-18	+1
	764.622(1)(16)§	9	-28	-1

§ No splitting of $m_l = \pm 1$ is resolved in the experiment.

Table 2.2.: Resonance positions of the Li-Cs p-wave FRs. The experimentally obtained resonance positions B^e and widths σ are extracted by fitting Gaussian profiles to the atomic loss spectra. The numbers in brackets give the statistical and systematic uncertainty of the determination of the resonance positions. The theoretical resonance positions B^t are given as deviations $\delta = B^e - B^t$. They are obtained from the coupled channels calculation performed at a relative kinetic energy of 430 nK, matching the experimentally measured temperature. In addition the magnetic quantum number m_l of the rotation l of the atom pair is given.

widths of the loss features of $\sigma \lesssim 10$ mG are much larger than the width of the calculated two-body collision rates $\ll 1$ mG from our coupled channels calculation and can be attributed to the thermal energy distribution of the atoms, magnetic field variations over the size of the cloud, and short-term field fluctuations.

The experimental Li-Cs p-wave FR positions B^e, their widths σ, and the deviations from theory $\delta = B^e - B^t$ are listed in Table 2.2. While no triplet splitting was observed for the p-wave FRs close to 714 G and 764 G, we observe a splitting of the $m_l = \pm 1$ partial waves of roughly 20 mG for the three FRs at approx. 663 G, 658 G, and 708 G. Such splittings were only observed until now at fairly low fields [Park et al., 2012], where the manifold of the pair rotation $l = 1$ is almost degenerate and the non-diagonal term of the spin-spin interaction results in the splitting of its projection m_l. However, at high fields the non-diagonal parts in m_l of the spin-spin interaction, Eq. (2.19), are too small to lead to a significant splitting of the $m_l = \pm 1$ components.

We attribute this splitting to electronic spin-rotation coupling and add the spin-rotation interaction term [cf. Eq. (2.20)] in the Hamiltonian in Eq. (2.10) describing the collision process. This term lifts the near-degeneracy of the $m_l = \pm 1$ states at high magnetic fields. From our fit we determine the spin-rotation coupling constant $|\gamma| = 0.00056$, to be about 0.06% of the effective rotational constant. In the Li-Cs system this interaction is particularly large due to the small reduced mass, resulting in fast rotational motion, and large spin-orbit interaction in Cs, leading to a significant second order contribution.

The spin-rotation splittings are reproduced within less than 3 mG, even though there are deviations of up to $\delta = 43$ mG between experiment and theory for the total triplet. For the two FRs at 714 G and 764 G our model predicts a smaller splitting of only ≈ 10 mG, which is of the same size as the width of the observed loss features. Therefore, the two loss features overlap and can not be resolved in the current experiment. In future experiments at lower temperatures and possible increased magnetic field homogeneity and stability this splitting might become observable.

We can not determine the sign of the m_l quantum numbers for the two $m_l = \pm 1$ components. Changing the sign of all m_l, and simultaneously the sign of γ, did not change the overall quality of the fit and hence we cannot determine the sign of γ from our measurements. The signs of m_l given in Table 2.2 correspond to a positive value of γ. We calculated the binding energies for the hyperfine manifold of the levels directly below the atom pair asymptote $2s^2S_{1/2}(f_{\mathrm{Li}} = 1/2)+$ $6s^2S_{1/2}(f_{\mathrm{Cs}} = 3)$ at zero magnetic field and found that the spin-rotation contribution for rotational angular momentum up to $l = 2$ is below 300 kHz and strongly dependent on the total angular momentum. Measuring these binding energies for example with high precision rf-spectroscopy would allow to determine the sign of this interaction. The extrapolation to higher l values and especially to more deeply-bound levels will lead to significant uncertainties because of missing experimental data in that range.

We checked if other extensions of the Hamiltonian could be important for describing the observed FRs, e.g. the rotational Zeeman effect or the molecular anisotropy of the electron g-tensor with respect to the molecular axis as discussed for other molecules (see example O_2 [Tischer, 1967]). Fitting such contributions led to unphysical large magnitudes of the coupling parameters and showed severe correlations between each other. Thus we assume that our present data set is insufficient to study such interactions.

Finite temperature and AC-Stark effect on Feshbach resonance positions

In order to systematically characterize the influence of finite temperature and intensity of the optical dipole trap on the atom-loss spectra of p-wave Feshbach resonance, we prepare the mixture at different ensemble temperatures ranging from 0.21 μK to 0.84 μK by stopping the evaporation process at varying power of the dipole trap

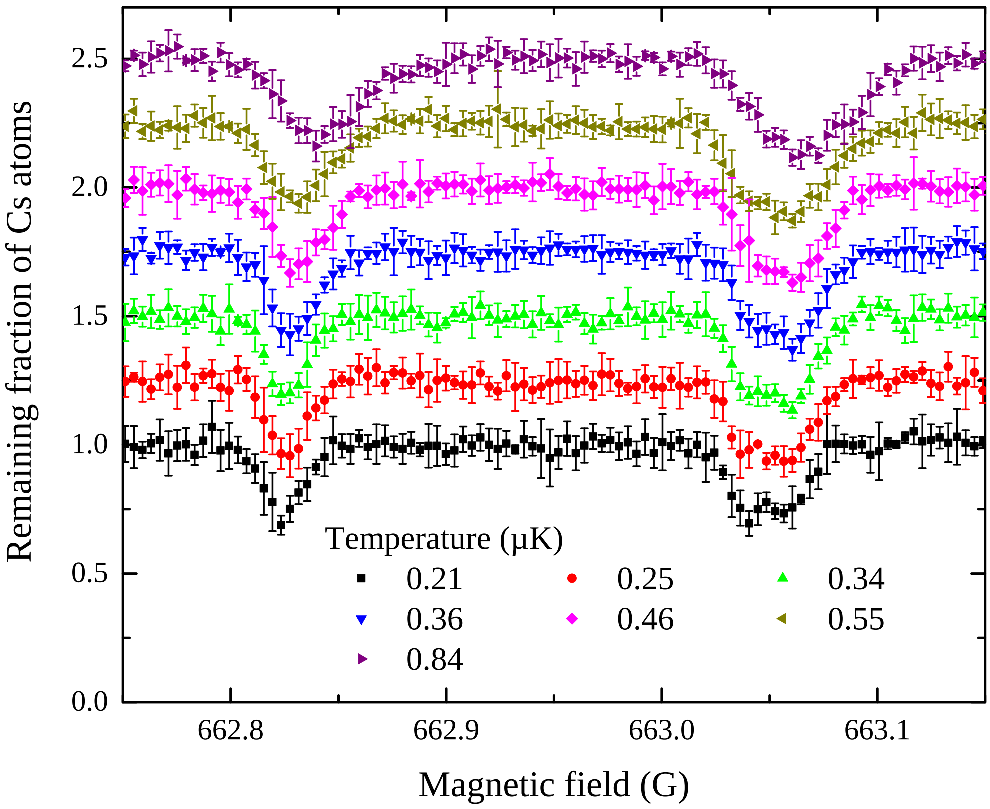

Figure 2.11.: Atom-loss spectroscopy of the p-wave Feshbach resonance multiplet close to 663 G for different temperatures between 0.21 μK and 0.84 μK. The remaining fraction of Cs atoms has been vertically shifted by 0.25 for the different measurements. Each data point is averaged over at least four measurements and the error bars display the standard deviation.

beams. The atom-loss spectra are shown in Fig. 2.11. For increasing temperature the loss features are broadened due to a widening of the thermal energy distribution and the $m_l = \pm 1$ splitting can no longer be resolved. Thus, it is essential to measure at ultralow temperatures to observe the splitting, even though, for low temperatures, the rotational barrier greatly suppresses the p-wave scattering cross-section $\sigma_p \propto T^2$ [DeMarco et al., 1999] and the observed losses might be dominated by the finite s-wave cross-section or single species loss mechanisms such as Cs three-body recombination or lifetime in the optical dipole trap. In the measurements presented in Fig. 2.10 the experimental parameters were chosen such that the $m_l = \pm 1$ splitting is well resolvable while maintaining sufficient interspecies loss rates.

In addition to the broadening of the loss features, we observe a shift of the resonance positions towards higher magnetic fields for increasing temperature. In order to quantify this resonance shift, we extract the resonance position of the $m_l = 0$ component by fitting with a Gaussian profile, for each sample temperature. The relative shift is obtained with respect to the resonance position obtained from the measurement per-

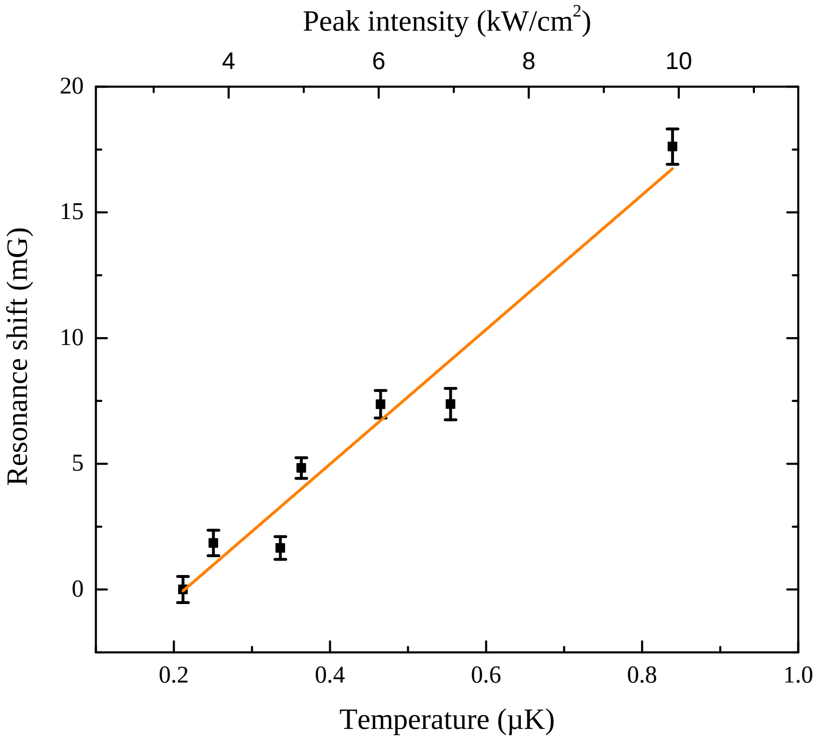

Figure 2.12.: Influence of temperature and dipole trap power on the resonance position. The relative shift of the 663 G p-wave Feshbach resonance position with respect to the measurement at 0.21 μK in dependence of the ensemble temperature and dipole trap intensity. The orange line is a linear fit to the data and the error bars are the standard errors from the determination of the resonance position.

formed at the lowest sample temperature of 0.21 μK. The resonance shift is plotted in dependence of the sample temperature and peak intensity of the dipole trapping light in Fig. 2.12. We fit a linear function to the data and obtain a slope of +27 mG/μK.

The observed shift of the resonance position can be partially attributed to the increase in relative kinetic energy in the scattering event. From the differential magnetic moment between the least-bound vibrational state and the free atoms of $\delta\mu = \mu_{\mathrm{mol}} - \mu_{\mathrm{at}} \approx h \times 3$ MHz/G in this magnetic field range, we estimate the shift to be $\Delta B/\Delta T = k_B/\delta\mu \approx 7$ mG/μK. A similar shift is obtained in our coupled channels model (Sec. 2.2.1), when calculating the maximum of the two-body collision rate for different relative kinetic energies. However, we measure a much larger resonance shift of the resonance position, which can not be described by the increase in temperature alone. The major part of the observed shift, namely +20 mG/μK, needs to have a different origin.

A probable explanation is a differential AC Stark shift between the molecular state and the atomic state, which is caused by the trapping light. When changing the intensity of the trapping light this will result in relative energy shifts between the two states and consequently in a shift of the FR position. Expressing the remaining resonance shift in dependence of the trapping light intensity yields a slope of 2 mG/(kW/cm^2). A shift towards higher magnetic fields can be explained by a down-shifting of the molecular energy with respect to the atomic threshold. This in turn shifts the intersection point of the molecular state with the atomic threshold, where the Feshbach resonance occurs, to higher magnetic fields. Thus, we estimate a differential AC Stark effect of $-h \times 6$ kHz/(kW/cm^2) between the molecular and scattering state at the wavelength $\lambda = 1070$ nm of our trapping laser. This shows that the resonance position is influenced by the trapping light. For the determination of the p-wave resonance positions B^e listed in Table 2.2 this shift amounts to 8 mG. On the other hand the AC Stark effect may be employed to manipulate Feshbach resonance positions and eventually the scattering length by the trapping light. This effect has indeed been used for ultra-fast switching of the interaction strength in an ultracold ^{6}Li-^{40}K mixture [Jag et al., 2014; Cetina et al., 2016] via switching between different dipole trap configurations.

2.2.5. d-wave Li-Cs Feshbach resonances

Motivated by a systematic shift between the experimental observations of p-wave FR positions and their theoretical description with the molecular potential curves obtained in Ulmanis et al. [2015], we have searched for d-wave Li-Cs FRs in the field range around 400 G. In combination with the measurements of s- and p-wave FRs our measurements corresponds to high-precision spectroscopy of the rotational ladder of the least bound vibrational state and should enable us to refine the long-range part of the molecular ground-state potentials.

We start our measurements with a mixture of approx. 3×10^4 Cs and 3×10^4 Li atoms in one of the two energetically lowest states at a temperature of 300 nK. The secular trapping frequencies are $\omega_{\mathrm{Cs}} = 2\pi \times (11, 147, 133)$ Hz and $\omega_{\mathrm{Li}} = 2\pi \times (37, 325, 325)$ Hz, where the external magnetic field and gravity are parallel to the z-axis[9]. The remaining fraction of Li and Cs atoms after a interaction time of 5 s (resonances at 341.9 G and 388.6 G) and 8 s (resonance at 426.1 G) is shown in Fig. 2.13. Again, we fit Gaussian functions to the loss features in order to extract their positions B^e and widths σ listed in Table 2.3. We found three d-wave resonances a couple of hundred mG away from the initial predictions. Since the collisions occur predominantly in the s-wave ($l = 0$) entrance channel, no multiplet splitting is expected. We start our theoretical modeling with the molecular potentials from Ulmanis et al. [2015] and adapt the C_6, C_8, and C_{10} coefficients, describing the potentials for large internuclear distances, as has been explained in Sec. 2.2.1. The observed d-wave resonance positions B^e and widths σ are

---

[9] The trapping frequencies in y-direction are deduced from our model potentials, as described in [Ulmanis et al., 2016a].

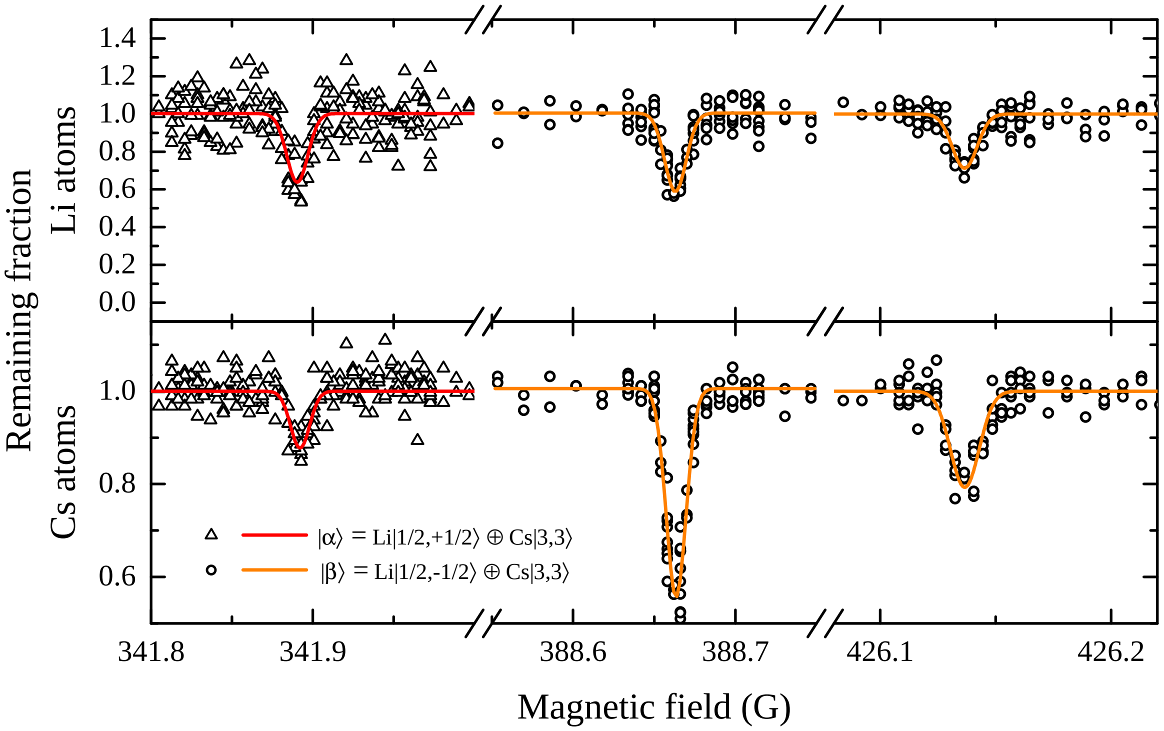

Figure 2.13.: Feshbach spectroscopy of three Li-Cs d-wave resonances in the $|\alpha\rangle$ channel (triangles and red line) and $|\beta\rangle$ channel (circles and orange lines) in the magnetic field range of 340 G to 430 G. The remaining fraction of Li and Cs atoms after a holdtime of 5 s (resonances at 341.9 G and 388.6 G) and 8 s (resonance at 426.1 G) are plotted as a function of the magnetic field. The red and orange curves are fits of Gaussian profiles to the data. Their resonance positions B^e and widths σ are listed in Table 2.3.

listed in Table 2.3 together with their deviations from theory $\delta = B^e - B^t$ with the improved long range function. For two predicted but unobserved FRs in the inspected field range, we give theoretical resonance positions instead of B^e.

As all previously observed Li-Cs FRs, the observed d-wave FRs originate from the least bound vibrational levels below the atomic asymptote $2s^2S_{1/2}(f_{\mathrm{Li}} = 1/2)+ 6s^2S_{1/2}(f_{\mathrm{Cs}} = 3)$ [Repp et al., 2013]. The total angular momentum f (excluding pair rotation l) at zero magnetic field, its projection m_f and the rotational angular momentum l are fairly good quantum numbers. Also the angular momentum $G = S + i_{\mathrm{Cs}}$ is a good quantum number due to the large Cs hyperfine interaction. We assign quantum numbers to the d-wave FRs and list them in Table 2.3.

We only observed three of the expected five d-wave FRs. In the region around the two unobserved resonances we measure Li-Cs loss rates of $\leq 0.02\ s^{-1}$, which are about a factor of five smaller than at the resonance positions of the observed ones. This observation agrees with the calculated collision rates around the resonances. The atomic loss signal is dominated by the CsCsCs three-body recombination loss rates

Entrance channel	B^e (G)	σ (mG)	δ (mG)	m_f	f	G
Li$\|1/2,+1/2\rangle$	341.891(10)(16)	7	8	7/2	9/2	7/2
$\oplus$ Cs$\|3,+3\rangle$	375.367‡	-	-	7/2	7/2	7/2
Li$\|1/2,-1/2\rangle$	357.920‡	-	-	5/2	9/2	7/2
$\oplus$ Cs$\|3,+3\rangle$	388.663(5)(16)	6	5	5/2	7/2	7/2
	426.137(5)(16)	6	-36	5/2	5/2	7/2

---

‡ Not observed in the experiment. Instead we give the theoretical resonance position B^t.

Table 2.3.: Resonance positions of the Li-Cs *d*-wave Feshbach resonances. The experimentally obtained resonance positions B^e and widths σ are extracted by fitting Gaussian profiles to the atomic loss spectra. The numbers in brackets give the statistical and systematic uncertainty of the determination of the resonance positions. The theoretical resonance positions B^t obtained from the coupled channels calculation performed at a relative kinetic energy of $k_B \times 300$ nK, matching the experimentally measured temperature, are given as deviations $\delta = B^e - B^t$. We assign the quantum numbers m_f, f, and $G = S + i_{\mathrm{Cs}}$ to the Feshbach resonances.

of approx. 0.15 s^{-1} in this magnetic field range. In addition, close to the predicted Li-Cs *d*-wave FR at 357.92 G, we find a Cs-Cs *g*-wave FR [Berninger et al., 2013a] (see Appendix A), which leads to enhanced Cs three-body recombination.

2.2.6. Molecular potential curves

With the help the high-precision remasurements of *s*- and *p*-wave FRs and the first observation of *d*-wave FRs new measurements we refine the LiCs molecular potential curves. The potential parametrization for the $\mathrm{X}^1\Sigma^+$and $\mathrm{a}^3\Sigma^+$are given in Appendix B. With the improved molecular potential curves and inclusion of the spin-rotation coupling we achieve a total weighted RMS error of 16 mG for all 32 FR features, which is an improvement by a factor of two compared to previous theoretical analysis [Pires et al., 2014a]. The significant improvements in the overall fit originate from the combination of the precise characterization of the *s*-wave FRs via the binding energy measurements (Sec. 2.2.3) in combination with the narrow *p*- and *d*-resonances. A list of the previously observed Li-Cs *s*- and *p*-waves FRs in the scattering channels Li$|1/2,\pm1/2\rangle$ $\oplus$Cs$|3,+2\rangle$ and a comparison to our current coupled channels calculations can be found in Appendix A.

From the new molecular potentials we calculate the singlet and triplet scattering lengths for both Li isotopologues and list them in Table 2.4. They are slightly different to former reported values [Pires et al., 2014a], which reflects the largely extended data set. Because of missing observation of Feshbach resonances for ^{7}Li-^{133}Cs, the

state	a (^{6}Li-^{133}Cs)	a (^{7}Li-^{133}Cs)
$X^1\Sigma^+$	30.147(50) a_0	45.28(30) a_0
$a^3\Sigma^+$	-34.97(15) a_0	846.4(200) a_0

Table 2.4.: Scattering lengths a for states $X^1\Sigma^+$ and $a^3\Sigma^+$ for the isotoptic combinations of ^{6}Li-^{133}Cs and ^{7}Li-^{133}Cs.

uncertainties for the corresponding values extrapolated by mass scaling and Born-Oppenheimer correction are larger compared to the ^{6}Li-^{133}Cs isotopologue.

Summary

In summary, we have performed high-precision scattering experiments in an ultracold ^{6}Li-^{133}Cs sample. We determined s-, p-, and d-wave FRs and modeled their resonance positions by a full coupled channels calculation on the $2s^2S_{1/2}(f_{\mathrm{Li}} = 1/2)+ 6s^2S_{1/2}(f_{\mathrm{Cs}} = 3)$ asymptote. For the precise determination of s-wave FR positions we employed two complementary techniques: binding energy measurements via radio-frequency association of the colliding atom pair into the weakly-bound dimer state and atom-loss spectroscopy. The new measurements represent an almost ten-fold improvement in precision in comparison to earlier studies [Repp et al., 2013; Tung et al., 2013; Pires et al., 2014a], which proved to be essential for the quantitative study of the three-body Efimov scenario, presented in the following chapter. Furthermore, the precise knowledge of the Li-Cs *two*-body physics will be beneficial for the study of many-body phenomena (see Ch. 4) as well as the production of ultracold polar molecules (cf. Fig. 5.1).

For the first time we observe a triplet splitting of p-wave FRs at high magnetic fields for the $m_l = -1, 0, 1$ components of the scattering channel at high magnetic fields. By our coupled channels calculation we attribute this effect to spin-rotation coupling. Comparison with the experimental resonance positions allows to determine the magnitude of the spin-rotation coupling constant $|\gamma| = 0.000566(50)$ with respect to the effective rotational constant of the asymptotic levels. The observed splitting at high fields provides full control over the angular momentum l and its projection m_l in the scattering process by the external magnetic field. The initial detection of Li-Cs d-wave FRs proved to be beneficial for the refinement of the molecular potentials at large internuclear distances.

Three

3

This chapter is partially based on the following publications, from which parts of the text are reproduced verbatim:

Role of the intraspecies scattering length in the Efimov scenario with large mass difference
S. Häfner, J. Ulmanis, E.D. Kuhnle, Y. Wang, C.H. Greene, and M. Weidemüller
Physical Review A **95**, 062708 (2017)

Heteronuclear Efimov scenario with positive intraspecies scattering length
J. Ulmanis, S. Häfner, R. Pires, E.D. Kuhnle, Y. Wang, C.H. Greene, and M. Weidemüller
Physical Review Letters **117**, 153201 (2016)

Universal three-body recombination in an ultracold Li-Cs mixture
J. Ulmanis, S. Häfner, R. Pires, F. Werner, D. Petrov, E.D. Kuhnle, and M. Weidemüller
Physical Review A **93**, 022707 (2016)

Observation of Efimov Resonances in a Mixture with Extreme Mass Imbalance
R. Pires, J. Ulmanis, S. Häfner, M. Repp, A. Arias, E.D. Kuhnle, and M. Weidemüller
Physical Review Letters **112**, 250404 (2014)

What distinguishes the quantum mechanical *three*-body from the two-body system? Intuitively one could think that the third particle binds to an already existing dimer state, thus forming a three-body bound state. However, in the 1970's the Russian physicist V. Efimov discovered a bizarre and seemingly counterintuitive property of the quantum mechanical three-body problem, in which a binding of three particles is possible although the two-body system is unbound. In the limit of resonant pairwise interactions, where the two-body scattering length a exceeds by far the characteristic

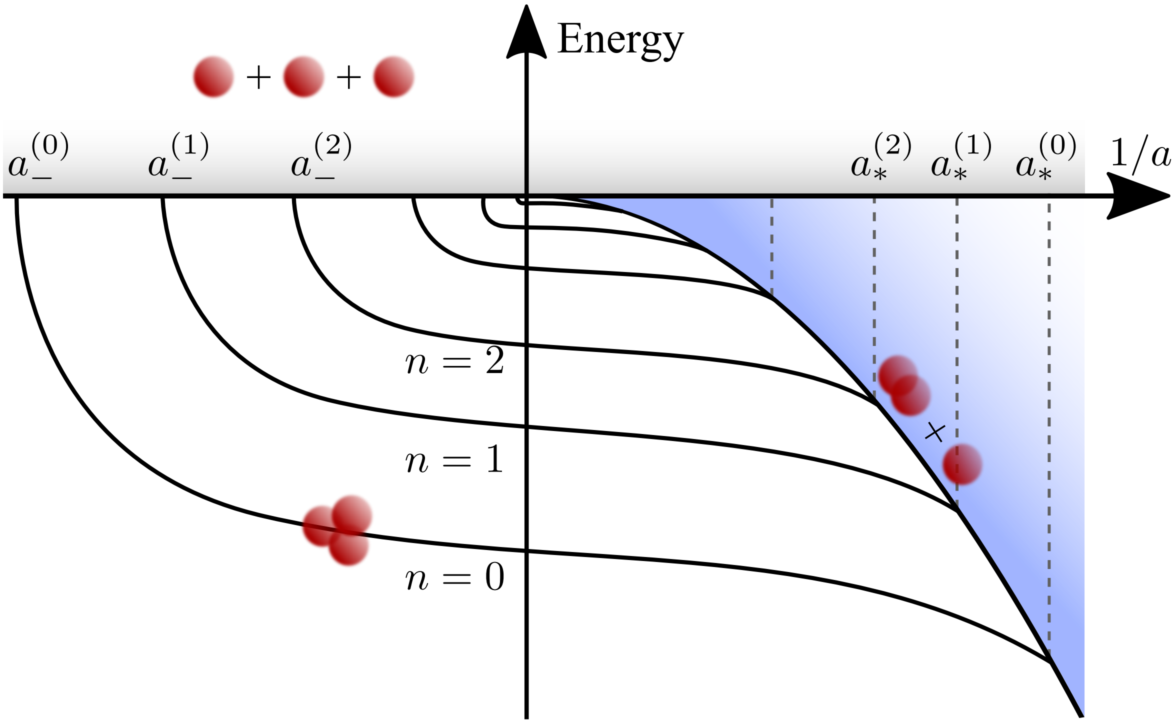

Figure 3.1.: Efimov's scenario: the three-body energy diagram is plotted as a function of inverse scattering length $1/a$. The gray shaded and blue shaded areas represent the scattering continua for three atoms and a dimer plus an atom, respectively. The Efimov states are connecting the three-body to the atom-dimer threshold, even existing in regions where no dimer state can be formed. Positions $a_-^{(n)}$ and $a_*^{(n)}$ indicate where the trimers intersect with the three atom and atom-dimer thresholds.

length scale of the interaction potential r_0, i.e. $|a| \gg r_0$, Efimov found the three-body energy diagram depicted in Fig. 3.1. He predicted an infinite series of weakly-bound three-body states at the two-body resonance $a \to \infty$ [Efimov, 1970, 1971, 1973]. The so-called Efimov states connect the three-body threshold at $a < 0$ to the atom-dimer threshold at positive scattering lengths $a > 0$. These three-body bound states, exist even at negative scattering lengths where the two-body potential is not strong enough to support a bound dimer state. As a result, if only one of the constituents of an Efimov state is removed the whole system falls apart into three separate particles. This intriguing property of a bound N-body system that is built up on $N-1$ subsystems which are unbound is commonly referred to as "Borromean" binding, in close analogy to the three intertwined circles in the coat of arms of the Borromeo family.

Another interesting property of the Efimov effect is its discrete scale invariance, reflected in the geometric progression of the trimer binding energies. The energy of the n^{th} trimer is given by $E_n = e^{-2\pi n/s_0} E_0$, and s_0 is a universal constant. Thus, if the energy of only one state is known, we know the energy of all Efimov states. Moreover, the positions $a_-^{(n)}$ and $a_*^{(n)}$, where the Efimov trimers either dissociate into the three-body or atom-dimer continuum, are also log-periodically spaced, with $a_-^{(n)} = e^{\pi n/s_0} a_-^{(0)}$ and $a_*^{(n)} = e^{\pi n/s_0} a_*^{(0)}$. The universal factor s_0 depends only on the mass ratio, number of resonant interactions, and quantum statistics of the three particles.

Remarkably, the Efimov effect exists irrespective of the specific details of the two-body interaction potential, as long at it is sufficiently short-ranged, making the Efimov effect a prime example of universal few-body physics, that occurs in microscopically vastly different systems spanning many orders of magnitude in energy and length scales (for reviews of Efimov physics in different systems see [Nielsen et al., 2001; Braaten and Hammer, 2006, 2007; Greene, 2010; Ferlaino et al., 2011; Wang et al., 2013; Greene et al., 2017; Naidon and Endo, 2017]). Examples in the realm of nuclear physics are the three-nucleon system, initially studied by Efimov based on early studies of the triton by Thomas [1935] and Skorniakov and Ter-Martirosian [1957], hypernuclei [Lim, 1986], and halo nuclei [Fedorov et al., 1994]. In the field of atomic physics the Helium trimer $^4He_3$ was proposed to be a prime candidate for the observation of the Efimov effect [Lim et al., 1977; Nakaichi-Maeda and Lim, 1983; Esry et al., 1996; Nielsen et al., 1998; Blume and Greene, 2000]. Due to accidental fine tuning of nature, the two-body interaction is just resonant enough to only support a single weakly bound dimer state and two three-body bound states [Blume and Greene, 2000; Blume et al., 2000; Hiyama and Kamimura, 2012a,b; Blume et al., 2014]. Finally, almost forty years after the initial prediction of the Efimovian He trimer it was observed by Kunitski et al. [2015]. Recently, Efimov states of strongly interacting photons in quantum nonlinear media of highly excited Rydberg atoms have been observed [Liang et al., 2017; Gullans et al., 2017].

The prosperity in the field of laser cooled atomic gases has established a new testbed for the study of universal few- and many-body physics. The full control over the s-wave scattering length via magnetic Feshbach resonances, allows to study the Efimov energy diagram from $-\infty \leq a \leq \infty$ with a single atomic system. Several groups predicted Efimov states to appear as periodic enhancements of the three-body loss coefficient, due to the appearance of shape-resonances, the so-called Efimov resonances, in these systems [Esry et al., 1999; Nielsen and Macek, 1999; Bedaque et al., 2000]. In fact, the first evidence of Efimov physics was found in the group of R. Grimm [Kraemer et al., 2006] in an ultracold sample of ^{133}Cs atoms. The initial observation has triggered the exploration of the Efimov effect in many *homonuclear* systems at ultralow temperatures, e.g. ^{6}Li [Ottenstein et al., 2008; Wenz et al., 2009; Lompe et al., 2010a; Huckans et al., 2009; Williams et al., 2009; Nakajima et al., 2010; Naidon and Ueda, 2011; Huang et al., 2014a], ^{7}Li [Gross et al., 2009, 2010, 2011; Pollack et al., 2009; Dyke et al., 2013; Machtey et al., 2012b], ^{39}K [Zaccanti et al., 2009; Roy et al., 2013], ^{85}Rb [Wild et al., 2012], and ^{133}Cs [Kraemer et al., 2006; Esry and D'Incao, 2007; Lee et al., 2007; Ferlaino et al., 2008; Ferlaino and Grimm, 2010; Ferlaino et al., 2011; Berninger et al., 2011; Knoop et al., 2009b,a; Zenesini et al., 2013, 2014; Huang et al., 2014b, 2015a] by observation of three-body recombination resonances and via direct radio-frequency association from the scattering continuum into the weakly-bound Efimov states in ^{6}Li [Lompe et al., 2010b; Nakajima et al., 2011] and ^{7}Li [Machtey et al., 2012b]. With these tremendous achievements even unexpected universal behavior was found, e.g. the discovery of the so-called van der Waals universality of the three-body parameter [Berninger et al., 2011; Wang and Julienne, 2014; Naidon et al., 2014b,a].

The discrete scale invariance, being a central feature of the Efimov effect, however, requires the observation of at least three consecutive Efimov resonances. In the case of homonuclear atomic gases the relatively large scaling factor of $\lambda = 22.7$ poses serious experimental challenges, e.g. a high control over the scattering length and very low temperatures, for the observation of the excited state resonances and thus only two experiments could reveal the first excited Efimov state [Williams et al., 2009; Huang et al., 2014b]. These obstacles can be overcome by use of mass-imbalanced systems [D'Incao and Esry, 2006a; Greene, 2010], where the scaling factor is drastically reduced. The experimental exploration of the *heteronucelar* Efimov scenario, however, has been limited (for a recent review see [Ulmanis et al., 2016b]). To date, only one isolated Efimov resonance was observed in a ^{7}Li-^{87}Rb [Maier et al., 2015] mixture and atom-dimer recombination resonances in different K-Rb combinations [Bloom et al., 2013; Hu et al., 2014; Wacker et al., 2016]. Possible Efimov resonances in this system [Barontini et al., 2009, 2010] are highly questionable and could not be reproduced by other groups [Wacker et al., 2016].

The Li-Cs system, studied in this thesis, is a prototypical system for the exploration of the *heteronuclear* Efimov effect. Due to its high mass imbalance the scaling factor is reduced to only 4.9 [Braaten and Hammer, 2006; D'Incao and Esry, 2006a]. Indeed a series of three successive Li-Cs-Cs Efimov resonances has been observed [Pires et al., 2014b; Tung et al., 2014], allowing for a test of the discrete scale invariance of Efimov's scenario. Further studies in this system revealed the influence of finite-range effects [Ulmanis et al., 2016a; Ulmanis et al., 2016], the effect of the intraspecies scattering length [Ulmanis et al., 2016; Häfner et al., 2017] as well as the strength of the two-body Feshbach resonance [Johansen et al., 2017].

In this chapter we extend the studies of heteronuclear Efimov physics in the Li-Cs system, by investigating the role of the intraspecies scattering length. We juxtapose the heteronuclear Efimov scenario in a BBX system, consisting of two heavy bosons B and one distinguishable particle X, for positive and negative intraspecies scattering lengths. We start with a general introduction to the solution of the quantum mechanical three-body problem in Sec. 3.1 during which we introde key features of the adiabatic hyperspherical formalism in Sec. 3.1.1, followed by analytically solving the three-body problem for the simplest two-body interaction potential, the zero-range delta potential, in Sec. 3.1.2. In Sec. 3.1.3 we introduce the concept of a three-body recombination resonance being the main observable of Efimov trimers in ultracold atomic gases. We apply these concepts to the BBX system within the zero-range theory in the adiabatic hyperspherical formalism (Sec. 3.2.1) and derive an analytic description of the three-body loss rate in Sec. 3.2.2. For a more realistic modeling of the three-body loss rates, we employ the spinless van der Waals (vdW) theory (Sec. 3.2.3), which models pairwise interactions with single-channel Lennard-Jones potentials [Wang et al., 2012c]. The experimental procedure for the extraction of the three-body recombination rate L_3 in the Cs-Cs-Li system is given in Sec. 3.3. A comparison between experiment and theory for negative and positive intraspecies scattering lengths is given in Sec. 3.4.1 and 3.4.2, respectively. Finally, by comparing experimental three-body loss rates close to the two different Li-Cs Feshbach resonances in Sec. 3.4.4 we find two distinct scaling behaviors, in agreement with previous predictions [D'Incao and Esry, 2009]. Such distinct scaling properties can be used, for example, to tune and significantly increase the three-body lifetime due to Cs-Cs-Li collisions, which is an important step towards studies of strongly-interacting Bose-Fermi mixtures.

3.1. Efimov effect

In order to understand the occurrence of the Efimov effect we take a closer look into the three-body problem. The quantum mechanical three-body problem can in general not be solved analytically. Several methods have been employed, including different simplifications of the problem, e.g. effective field theory [Bedaque and van Kolck, 2002; Kaplan, 2005; Platter, 2009; Hammer et al., 2013], renormalization group theory [Wilson, 1983; Fisher, 1998; Hammer and Platter, 2011], and the hyperspherical formalism [Macek, 1968; Zhen and Macek, 1988; Lin, 1995; Nielsen et al., 2001; Greene, 2010; Rittenhouse et al., 2011] as well as further simplifications such as reformulating the Schrödinger equation as Faddeev equations [Faddeev, 1961] or Alt-Grassberger-Sandhas equations [Alt et al., 1967]. An extensive overview over the different techniques is given in [Wang et al., 2013; Greene et al., 2017] and they are described in detail by Braaten and Hammer [2006]. Here, we focus on the adiabatic hyperspherical treatment of the three-body problem since it delivers an intuitive, potential based description.

3.1.1. The hyperspherical formalism

We introduce the hyperspherical formalism, following the extensive reviews by Braaten and Hammer [2006] and Wang et al. [2013], by starting our discussing with the time-independent three-body Schrödinger equation determining the wavefunction $\Psi(\vec{r}_1, \vec{r}_2, \vec{r}_3)$ of three particles i with masses m_i

$$\left[-\sum_{i=1}^{3} \frac{\hbar^2}{2m_i} \nabla_i^2 + V(\vec{r}_1, \vec{r}_2, \vec{r}_3)\right] \Psi(\vec{r}_1, \vec{r}_2, \vec{r}_3) = E\Psi(\vec{r}_1, \vec{r}_2, \vec{r}_3), \tag{3.1}$$

where $V(\vec{r}_1, \vec{r}_2, \vec{r}_3)$ is the three-body interaction potential for particles at positions $\vec{r}_i$. Without an external potential, the center-of-mass motion can be separated, reducing the number of degrees of freedom to six. A convenient choice are the Jacobi coordinates [Delves, 1958, 1960]. We define the mass-scaled Jacobi vectors

$$\vec{\rho}_{ij} = \sqrt{\frac{\mu_{ij}}{\mu_3}} (\vec{r}_i - \vec{r}_j), \tag{3.2}$$

$$\vec{\rho}_{ij,k} = \sqrt{\frac{\mu_{ij,k}}{\mu_3}} \left(\vec{r}_k - \frac{m_i \vec{r}_i + m_j \vec{r}_j}{m_i + m_j} \right), \tag{3.3}$$

with the positions $\vec{r}_{i,j,k}$ of the atoms in the laboratory frame. The indices i, j, k represent permutations of $1, 2, 3$. The two- and three-body reduced masses are given by [Wang et al., 2013]:

$$\mu_{ij} = \frac{m_i m_j}{m_i + m_j}, \quad \mu_{ij,k} = \frac{m_k (m_i + m_j)}{m_i + m_j + m_k}, \quad \mu_3 = \sqrt{\frac{m_i m_j m_k}{m_i + m_j + m_k}}. \tag{3.4}$$

A further simplification is gained by combining the two Jacobi vectors to a single vector and parametrization in six-dimensional spherical coordinates, consisting of one hyperradius and five hyperangles. The hyperradius R, being the only remaining length scale, describes the overall size of the system and is defined as[1]

$$R^2 = \rho_{ij}^2 + \rho_{ij,k}^2. \tag{3.5}$$

The hyperradius is only small if all three particles are in close vicinity. One possible definition of the hyperangles is given by [Delves, 1958, 1960]

$$\tan\phi = \frac{\rho_{ij,k}}{\rho_{ij}}, \tag{3.6}$$

which range between 0 and $\pi/2$ and are commonly combined in the vector Ω. The Schrödinger equation, Eq. (3.1), can be reformulated in the hyperspherical formalism

---

[1] In fact the hyperradius is not defined uniquely. However, the quantity $\mu_3 R^2$ is invariant for different definitions of μ_3 and R [Wang et al., 2013]. Thus, a different choice in the definition of R implies a different definition of μ_3.

as

$$\left(-\frac{\hbar}{2\mu_3}\frac{\partial^2}{\partial R^2}+\frac{\Lambda^2+15/4}{2\mu_3 R^2}+V(R,\Omega)\right)\psi(R,\Omega)=E\psi(R,\Omega), \tag{3.7}$$

where the wavefunction has been rescaled by $\psi = R^{5/2}\Psi$ and Λ is the general angular momentum operator.

The Schrödinger equation is conveniently solved within the adiabatic hyperspherical representation introduced by Macek [1968]. The approach is based on the assumption, that the hyperradial and hyperangular motions can be separated in close analogy to the Born-Oppenheimer approach of molecular physics. We treat R as an adiabatic variable and solve the angular part of the Schrödinger equation for fixed hyperradius R

$$\left(\frac{\Lambda^2}{2\mu_3 R^2}+V(R,\Omega)\right)\Phi_\nu(\Omega;R)=U_\nu(R)\Phi_\nu(\Omega;R), \tag{3.8}$$

with the channel functions $\Phi_\nu(\Omega;R)$ and adiabatic potentials $U_\nu(R)$. We expand the total wavefunction $\psi(R,\Omega)$ on the complete basis set

$$\psi(R,\Omega)=\sum_\nu F_\nu(R)\Phi_\nu(\Omega;R). \tag{3.9}$$

The Schrödinger equation finally reduces to a coupled set of eigenvalue equations of the hyperradial functions $F_\nu(R)$

$$\begin{aligned}&\left[-\frac{\hbar^2}{2\mu_3}\frac{d^2}{dR^2}+U_\nu(R)-E\right]F_\nu(R)\\ &-\frac{\hbar^2}{2\mu_3}\sum_{\nu'}\left[P_{\nu,\nu'}\frac{d}{dR}+\frac{d}{dR}P_{\nu\nu'}(R)+Q_{\nu,\nu'}(R)\right]F'_\nu(R)=0,\end{aligned} \tag{3.10}$$

where $P_{\nu\nu'}(R)$ and $Q_{\nu\nu'}(R)$ are the non-adiabatic couplings between different hyperangular functions $\Phi_\nu(\Omega;R)$. In case of well-separated adiabatic potentials $U_\nu(R)$, the system can be described by single-channel solutions $F_\nu(R)$ of the effective potential $W_{\nu\nu}(R)=U_\nu(R)-\hbar/2\mu_3 Q_{\nu\nu}(R)$. Thus, the initial multidimensional problem has been reduced to a one-dimensional problem with a set of effective potentials.

3.1.2. The zero-range model

So far we did not consider the interaction potential $V(\vec{r}_1,\vec{r}_2,\vec{r}_3)$ in our discussion. We make the assumption that the potential can be simplified and expressed as a sum of isotropic two-body interactions

$$V(\vec{r}_1,\vec{r}_2,\vec{r}_3)=V(r_{12})+V(r_{13})+V(r_{23}), \tag{3.11}$$

which only depend on the separation r_{ij} of the atom pairs. This assumption seems to be restrictive, but is indeed justified in ultracold atom systems, where the large de Broglie wavelength allows to describe the two-body wavefunction by its long-range properties. Thus, the scattering length a is the only relevant parameter in the system and any choice of the interaction potential giving the right value of a should be good to describe the system. In order to obtain the exact three-body potentials short range three-body interactions have to be included [Braaten and Hammer, 2006; Wang et al., 2013; Hammer et al., 2013].

A convenient choice is the modeling of the two-body interactions with pseudo-potentials whose range of interactions r_0 is going to zero. We call such interaction potentials zero-ranged. In this way all types of non-universal behavior, that usually depend on the exact interactions at short range, are not contained in this model and only the universal properties of three-body systems are studied. One of the simplest zero-range potentials in three dimensions is the contact potential with radial derivative

$$V_{zr}(r_{ij}) = \frac{2\pi a}{\mu}\delta(\vec{rij})\frac{\partial}{\partial r_{ij}}r_{ij}, \tag{3.12}$$

which is equivalent to imposing the Bethe-Peierls boundary condition

$$\Psi = 1/r_{ij} - 1/a, \quad r_{ij} \to 0 \tag{3.13}$$

on the wavefunction Ψ. The description in the zero-range model is valid in the limit of $r_0/a \to 0$. Here, r_0 represents the characteristic length scale of the two-body potential, which is typically given by the van der Waals length r_{vdW} for atoms in their electronic ground state. The zero-range potential comprises the weakly-bound universal dimer state with binding energy $E_b = \hbar/2\mu a^2$, which accounts for the Feshbach resonance as discussed in Sec. 2.1.3, and is only present for $a > 0$. Thus, the zero-range potential is expected to be well applicable to the situation, where the three-body physics is dominated by the weakly-bound dimer, i.e. for $a \gg r_0$.

Using the simple zero-range interaction potential, the Schrödinger equation, Eq. (3.1), may even be solved analytically within various theoretical frameworks [Braaten and Hammer, 2006; Wang et al., 2013]. For three identical bosons, we find the adiabatic hyperspherical potentials

$$U_\nu(R) = \frac{\hbar^2}{2\mu_3}\frac{s_\nu^{*2} - 1/4}{R^2}, \tag{3.14}$$

where the parameters s_ν^* are solutions of the following transcendental equation

$$s_\nu^* \cos\left(\frac{\pi}{2}s_\nu^*\right) - \frac{8}{\sqrt{3}}\sin\left(\frac{\pi}{6}s_\nu^*\right) = 12^{-1/4}\sin\left(\frac{\pi}{2}s_\nu^*\right)\frac{2R}{a}. \tag{3.15}$$

In the resonant limit $a \to \infty$, the transcendental equation becomes independent of R

and the original Efimov scenario is obtained. In this limit there is only one imaginary solution to Eq. (3.15), namely $s_0^* = is_0 = 1.00624i$, which leads to an attractive $-1/R^2$ potential. Additionally, there is an infinite number of real solutions, giving rise to repulsive potentials $U_{\nu>0}(R)$ [Efimov, 1971].

Inserting the hyperspherical potential $U_0(R)$ in Eq. (3.10) and neglecting non-adiabatic couplings yields

$$\frac{\hbar^2}{2\mu_3}\left[-\frac{d^2}{dR^2} - \frac{s_0^2 + 1/4}{R^2}\right] F_0(R) = EF_0(R). \tag{3.16}$$

The solution of this equation is an exponentially decaying Bessel function with imaginary index. The energy spectrum of the Efimov states can be expressed as

$$E_n = \left(e^{-2\pi/s_0}\right)^{n-n_*} \frac{\hbar^2 k_*^2}{\mu_3}, \tag{3.17}$$

where k_* is the binding wavenumber of the Efimov state labeled by $n = n_*$. The energy spectrum in Eq. (3.17) displays an infinite geometric progression of bound states, where the binding energy ratio of successive states is given by $\lambda^2 = e^{2\pi/s_0} \approx 515.03$. Thus, if only the binding energy of a single trimer state n_* is known, the whole energy spectrum is defined. This property is the essence of the Efimov effect and is a direct consequence of the attractive $-1/R^2$ potential [Landau and Lifshitz, 1991; Coon and Holstein, 2002; Essin and Griffiths, 2006].

Another remarkable feature of the Schrödinger equation (3.16) with the attractive $-1/R^2$ potential is its scale invariance under transformations of $R \to \lambda R$. Because of this scale invariance its solutions, the three-body wavefunctions, are self similar. However, in such a system the energy spectrum is not bounded from below and the three-body system collapses. This property is well known in quantum physics as “Thomas collapse” or “fall to the center” [Thomas, 1935]. The problem can be solved either by regularization of the potential with a hard-sphere wall at a hyperradius R_0, or by imposing the value of the logarithmic derivative of $F_0(R_0)$, reminiscent of the Bethe-Peierls boundary condition [Naidon and Endo, 2017]. These are two possible implementations of the so-called three-body parameter (3BP), which is artificially introduced in order to reproduce three-body observables known from experiment. In a real physical system, however, the energy spectrum is well defined due to the short-range behavior of the potential which is strongly repulsive. At asymptotically large scattering lengths, where the specific details of the short-range interactions are not resolved, their effect can be incorporated in the 3BP. As a big surprise it was found experimentally that the ground state Efimov resonances do not occur at random values of a, but are correlated to the van der Waals length r_{vdW} by a species-independent constant [Berninger et al., 2011; Roy et al., 2013; Wild et al., 2012; Gross et al., 2009, 2010; Huang et al., 2014a]. Apart from slight modifications due to short-range effects [Huang et al., 2014a, 2015a], this general scaling constitutes an example of the so-called vdW universality [Wang et al., 2012a; Schmidt et al., 2012b; Sørensen et al., 2012; Naidon et al., 2014b,a], where a deformation in the trimer configuration at distances of the van der Waals length prevents the atoms from probing the short-range behavior of the potentials.

3.1.3. Efimov resonances

We now turn our attention to the observation of the Efimov effect in ultracold atom experiments. Two complementary methods have been employed in experiments in order to provide evidence of Efimov states: The first method relies on direct radio-frequency association of the Efimov trimers and measurement of their binding energies. This method has until now only been employed for three component spin mixtures of fermionic ^{6}Li [Lompe et al., 2010b; Nakajima et al., 2011] and bosonic ^{7}Li [Machtey et al., 2012b]. The other method comprises the detection of three-body recombination close to the three-atom or atom-dimer thresholds. Close to the values of the scattering length $a_-^{(n)}$ and $a_*^{(n)}$, where the Efimov states cross the dissociation threshold (see Fig. 3.1), an enhancement in the three-body loss is expected [Esry et al., 1999; Nielsen and Macek, 1999; Bedaque et al., 2000]. This method has been widely used in experiments to detect Efimov states in hetero- and homonuclear systems and will be used in the studies throughout this thesis.

In order to get an intuitive understanding of the recombination process we take a closer look at the adiabatic hyperspherical potentials. For the following we limit our discussion to the case of two identical bosons B and one distinguishable particle X, since this is the relevant case for the experiments discussed in Sec. 3.4. For simplification, we discuss the case of negative scattering length $a < 0$, where no weakly bound dimer states exist. The hyperspherical potentials are schematically shown in Fig. 3.2 together with the main pathway of three-body recombination. We divide the potential into three regions:

- In the asymptotic region, $R \gg |a|$, the potential is repulsive and given by [D'Incao and Esry, 2005]

  $$U(R) = \frac{\hbar^2}{2\mu_3}\frac{\xi(\xi+4)+15/4}{R^2}, \tag{3.18}$$

  where ξ is a non-negative integer. The hyperradial wavefunctions in this region are Bessel functions.

- The scale invariant region, $r_0 \ll R \ll |a|$, is governed by the Efimov potential $U_0(R)$ defined in Eq. (3.14). The Efimov trimers (red dashed lines in Fig. 3.2) are located in this region.

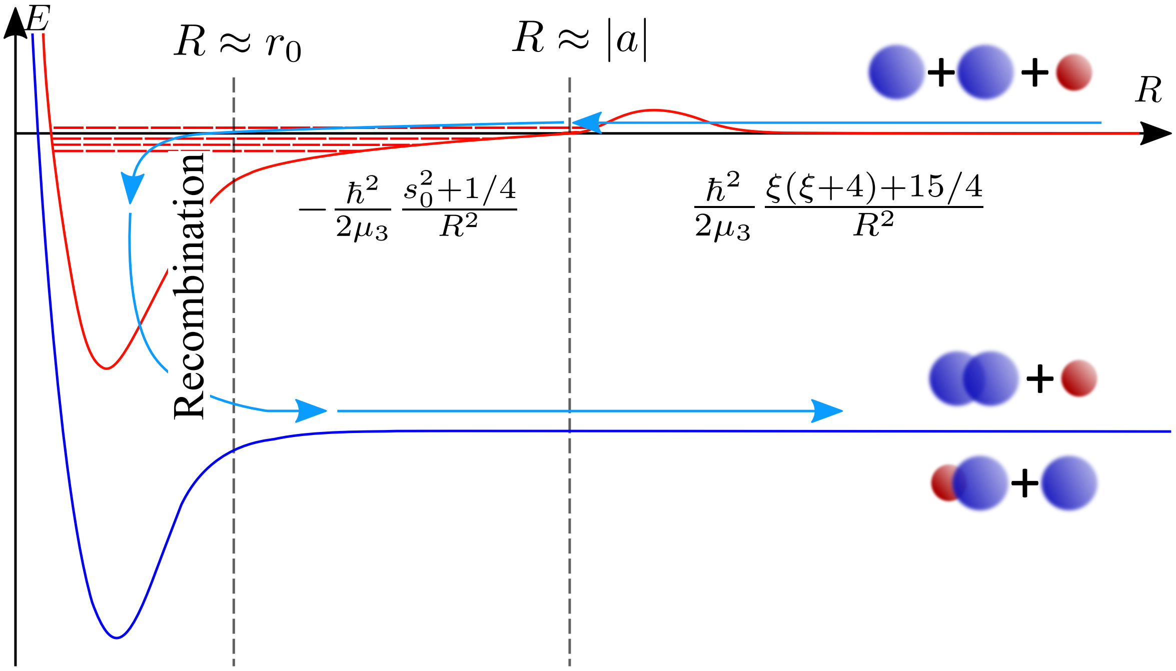

Figure 3.2.: Schematic illustration of the adiabatic hyperspherical potentials and the recombination process for negative scattering length $a < 0$. The three colliding atoms tunnel through the repulsive potential at $R \approx |a|$ to reach the Efimov region $r_0 \ll R_0 \ll |a|$. In the short-range region $R < r_0$ the three atoms recombine into various deeply-bound dimer and atom states. The released binding energy allows the constituents to leave the trap. The energy of the Efimov states are depicted as red dashed lines.

- The short-range region, $R < r_0$, where the non-adiabatic couplings are not negligible and drive transitions to deeply bound molecules. This region is non-universal and strongly depends on the exact shape of the three-body potential.

The adiabatic hyperspherical potential develops a potential barrier between the asymptotic region and the scale invariant region at around $R \approx |a|$. In an recombination event, the three particles, approaching each other from the asymptotic region $R \gg |a|$, have to tunnel through the potential barrier in oder to reach $R \approx |a|$. The wavepacket propagates through the scale-invariant region, dominated by the Efimov potential, and finally arrives at the short-range region $R < r_0$. In this region the three-particles recombine into various deeply-bound dimer and atom channels. It is clear, that the amplitude of the three-body wavefunction at r_0 together with the transition probability to all the lower lying channels will determine the recombination rate. Three-body recombination may result in many different deeply-bound states with various transition probabilities. The total recombination probability is typically modeled by the single parameter η (see Sec. 3.2.2). The binding energy, which is typically much larger than the trap depth, is distributed among the constituents as kinetic energy and thus the atoms can leave the trap. Thus, in our experiments, the recombination process is observed as loss of atoms from the trap.

As the scattering length a is varied, the position changes as $\propto |a|$ and the height of the potential barrier as $\propto a^{-2}$. For increasing scattering length this leads to an increase in tunneling probability and thus an enhancement of the recombination rate. It was found that the three-body recombination rate $L_3 \propto a^4$ in a three-boson system [Esry et al., 1999]. In addition, when $|a|$ is increased, the energy of the Efimov states (red dashed lines in Fig. 3.2) decreases and at some specific a will be resonant with the energy E of the incoming particles, significantly enhancing the tunneling probability through the barrier and thus giving rise to an increase of the wavefunction amplitude in the scale invariant and short-range regions. This, again, increases the decay to deeply-bound atom-dimer channels and leads to an enhancement in the recombination rate. Efimov resonances occur as such three-body shape resonances [Esry and D'Incao, 2007]. In a spectrum of the three-body recombination rate L_3 the Efimov resonances arise as modulations on top of the increasing inelastic collision rate.

In addition, the three-body loss rate can not take arbitrarily large values, but is limited by the thermal de Broglie wavelength. For values of $k^2a^2 \gtrsim 1$ the collisional cross section [Eq. (2.9)] deviates from the proportionality $\sigma \propto a^2$. In the limit $a \to \infty$ it becomes independent of the scattering length and saturates to its maximum value $\sigma = 4\pi/k^2$. In turn, the three-body loss rate L_3 departs from the general $\propto a^4$ scaling and approaches its unitary limit, given by an order of magnitude estimate [D'Incao and Greene, 2014; Petrov and Werner, 2015]

$$L_3^{\max} = \frac{4\pi\hbar^5}{\mu_3^3(k_B T^2)}. \tag{3.19}$$

Variations in L_3 can thus only be resolved for $k^2a^2 \lesssim 1$. By lowering the temperature T, which is equivalent to lowering k, the maximum value of $|a|$, at which modulations due to Efimov resonances can be observed, is increased. Therefore, a larger number of Efimov sates might be accessible in experiment. We define the so-called *window of universality* as the range where the scattering length can be well separated from the length scale r_0 of the interaction potential and the thermal de-Broglie wavelength λ_T, i.e. $r_0 \ll |a| \ll \lambda_T$.

3.2. Heteronuclear Efimov effect

Our discussion of the Efimov effect was limited to systems of three identical bosons so far. We turn our attention to general three-body systems in which the Efimov effect has been first discussed by Amado and Noble [1972] and Efimov himself [Efimov, 1971, 1973]. Although the Efimov effect in ultracold *heteronuclear* systems is based on the

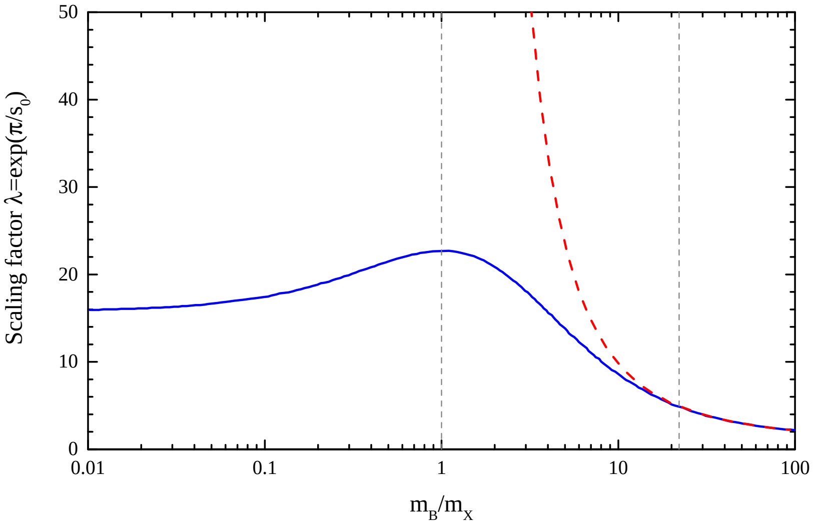

Figure 3.3.: Efimov scaling factor $\lambda = e^{\pi/s_0}$ in dependence of the mass ratio m_B/m_X of two identical bosons B with mass m_B and one distinguishable particle X of mass m_X. The blue and red dashed lines correspond to three and two resonant interactions, respectively. The vertical dashed lines indicate a mass ratio of one and the mass ratio of the Cs-Cs-Li combination.

same physical principles as in homonuclear systems, its signatures are much richer. In general three-body systems the three bodies can exhibit different masses, different quantum statistics and interact through in general three distinct pairwise interaction potentials and consequently different scattering lengths that complicate the simple picture. The existence of the Efimov effect and the factor s_0 depend on the mass ratio, number of resonant interactions, and quantum statistics of the involved particles. The possible combinations of three particles are extensively reviewed and investigated with respect to exhibiting the Efimov effect in Braaten and Hammer [2006] and Wang et al. [2013]. In the following we limit our discussion to a system of two indistinguishable bosons B and one distinguishable particle X, as this is the case for the Li-Cs mixture studied in this thesis. We refer to this system as BBX.

The mass ratio

The BBX system can be described by the same hyperspherical Schrödinger equation (3.16) with one single attractive hyperspherical potential characterized by s_0. However, the masses of the particles have to be included in the transcendental equation, Eq. (3.15), from which we obtain the scaling factor $\lambda = e^{\pi/s_0}$. This scaling factor is shown as a function of the mass ratio m_B/m_X in Fig. 3.3 for the case of either three or two resonant interactions.

For a mass ratio $m_B/m_X = 1$ and three resonant interactions, we recover the case of three equal bosons with $\lambda = 22.7$. However if the number of resonant interactions is reduced to two, the scaling factor is drastically increased to $\lambda = 1986.1$. For mass ratios $m_B/m_X < 1$ the scaling factor tends to 16 for three resonant interactions and diverges in case of only two resonant interactions. As the mass ratio is increased to $m_B/m_X > 1$, the scaling factor, in both cases, monotonically decreases and approaches 1 for infinite mass ratios. The reduced scaling factor for $m_B/m_X > 1$ results in a denser spectrum of Efimov states and recombination resonances as discussed in Sec. 3.1.3. From an experimental point of view, this behavior is favorable for the observation of a series of consecutive Efimov states. The excited Efimov states are observed at lower scattering lengths or respectively larger binding energies, and thus are not masked by the unitary limit. The reduced spacing relaxes the requirements for the precise tuning of the scattering length, and consequently the necessary stability and accuracy of the magnetic field control and knowledge of the two-body interaction properties. Therefore, we call to such systems “Efimov favored”. The Li-Cs system is a prototypical example for the study of the Efimov effect, due to its large mass ratio of $m_B/m_X = 22.1$. The scaling factor in this system is reduced to 4.88 and 4.80 for two and three resonant interactions, respectively.

Inter- and intraspecies scattering lengths

Besides the experimentally desirable mass ratio heteronuclear BBX systems exhibit not only different inter- and intraspecies interaction potentials V_{BX} and V_{BB}, respectively, but also two distinct scattering lengths a_{BX} and a_{BB}. This defines in total eight different regimes depending on the signs of each of the scattering lengths and their relative magnitudes $|a_{BX}|/|a_{BB}| \gtrless 1$. Thus BBX systems feature much richer Efimov physics compared to the homonuclear three-atom case. In view of the experiments discussed in Sec. 3.4, we concentrate on the case of negative interspecies scattering length $a_{BX} < 0$ and both signs of the intraspecies scattering length $a_{BB} \gtrless 0$ in a highly mass imbalanced combination. We extend the concepts introduced in Sec. 3.1.1-3.1.3 to the case of two different scattering lengths. In Sec. 3.2.1 we derive the adiabatic hyperspherical potentials for a BBX system and observe significant alterations to the Efimov scenario in presence of a weakly-bound BB dimer state. An analytic expression of the three-body recombination rate L_3 for $a_{BB} < 0$, which can be directly compared to the measurements, is presented in Sec. 3.2.2. The spinless van der Waals theory, introduced in Sec. 3.2.3, uses more realistic two-body interaction potentials in comparison to the zero-range theory. It is expected to describe the experimental observations even in the region, where the scattering length is on the same order as the extension of the interaction potential $|a_{BX}| \approx r_0$. In this region the zero-range theory is no longer applicable and deviations from it are expected.

3.2.1. Zero-range theory

We extend the universal zero-range theory[2] in the hyperspherical adiabatic approximation, presented in Sec. 3.1.2, to the case of two different inter- and intraspecies scattering lengths for a system constisting of two heavy bosons B and one light particle X. Again, we assume pairwise contact interactions [Eq. (3.12)] and derive the adiabatic hyperspherical potentials. We introduce the relevant reduced mass factors:

$$\mu_{BB} = \frac{m_B}{2}, \quad \mu_{BX} = \frac{m_X m_B}{m_X + m_B}, \quad \mu_3 = \sqrt{\frac{m_X m_B^2}{2m_B + m_X}}, \tag{3.20}$$

and further relevant factors that relate to mass ratios:

$$\begin{gathered} d_{BB} = \sqrt{\frac{m_X(2m_B)}{\mu_3(2m_B + m_X)}}, \quad d_{BX} = \sqrt{\frac{m_B(m_X + m_B)}{\mu_3(2m_B + m_X)}}, \\ \beta_{BB} = \arctan\left[\sqrt{\frac{m_X(2m_B + m_X)}{m_B^2}}\right], \quad \beta_{BX} = \arctan\left[\sqrt{\frac{(2m_B + m_X)}{m_X}}\right]. \end{gathered} \tag{3.21}$$

The following functions are also required as additional preliminaries, before we can state the transcendental equation, that determines the adiabatic hyperspherical potentials, in a compact form,

$$f(s,\alpha) \equiv \sqrt{\frac{2}{\cos\alpha}}\frac{\Gamma(\frac{3}{2})}{\sin\alpha}P_{s-1/2,-1/2}(\sin\alpha), \tag{3.22}$$

where $\Gamma(z)$ is the gamma function and $P_{n,m}$ is the associated Legendre function of the first kind and

$$W(s) = \frac{\pi\Gamma(\frac{2+s}{2})\Gamma(\frac{2-s}{2})}{2\Gamma(\frac{3}{2})^2\Gamma(\frac{1+s}{2})\Gamma(\frac{1-s}{2})}, \tag{3.23}$$

$$X(s) = \frac{\Gamma(\frac{2+s}{2})\Gamma(\frac{2-s}{2})}{2\Gamma(\frac{3}{2})^2}f(s,\beta_{BX}), \tag{3.24}$$

$$Y(s) = \frac{\Gamma(\frac{2+s}{2})\Gamma(\frac{2-s}{2})}{2\Gamma(\frac{3}{2})^2}f(s,\beta_{BB}). \tag{3.25}$$

Then the roots $s_\nu(R)$, which determine the hyperradial potential curves

$$U_\nu(R) = \frac{\hbar^2}{2\mu_3}\frac{s_\nu(R)^2 - 1/4}{R^2} \tag{3.26}$$

---

[2] The zero-range theory in the hyperspherical formalism has been developed and provided to us by Prof. C.H. Greene from Purdue University, West Lafayette, Indiana, USA.

are solutions of the following transcendental equation:

$$\left(W(s_\nu)\frac{\mu_3 a_{BB}}{\mu_{BB} d_{BB}^3} - R\right)\left(\frac{\mu_3 a_{BX}}{\mu_{BX} d_{BX}^3}(W(s_\nu) - Y(s_\nu)) - R\right) \\ -2X(s_\nu)^2 \frac{\mu_3^2 a_{BX} a_{BB}}{\mu_{BX} d_{BX}^3 \mu_{BB} d_{BB}^3} = 0. \tag{3.27}$$

Note that in general there could be real solutions $s_\nu(R)$ corresponding to hyperspherical potential curve energies higher than $\frac{-\hbar^2}{8\mu_3 R^2}$, which is the critical coefficient to support an infinite number of three-body bound states, and imaginary solutions for $s_\nu(R)$ that correspond to potential curve energies below $\frac{-\hbar^2}{8\mu_3 R^2}$.

The two energetically lowest heavy-heavy-light adiabatic hyperspherical potential curves are shown in Fig. 3.4 for the case of positive and negative intraspecies scattering length a_{BB}. Here, a mass ratio of $m_B/m_X = 22.1$ and different values of $a_{BX} < 0$ are assumed. If both scattering lengths are negative, the original Efimov scenario with an $\propto -1/R^2$ hyperspherical potential is recovered for $a_{BX} \to -\infty$, supporting an infinite number of bound states (Fig. 3.4, left panel). For finite interspecies scattering lengths a potential barrier at $R \approx 2|a_{BX}|$ leads to quasi-bound states, generating three-body recombination resonances, when passing the dissociation threshold. Since there is no repulsive short-range potential in this case, a three-body parameter is indispensable to regularize the energy spectrum.

For positive intraspecies scattering lengths ($a_{BB} > 0$) the situation is considerably altered by the existence of a dimer BB with binding energy E_{BB} (Fig. 3.4, right panel). The channel $BB + X$, splits the potential curves into two Efimov branches. The lower branch, which is asymptotically connected to the $BB + X$ channel, recovers the original Efimov scenario with a potential that is proportional to $-1/R^2$. In this case regularization with a three-body parameter is required to avoid a diverging binding energy of the ground state. Note that there is no potential barrier arising for finite values of a_{BX}, and thus there are no recombination resonances expected in the $BB + X$ channel. However, the upper Efimov branch with energies $E > E_{BB}$ shows a different behavior. It exhibits a potential barrier at $R \approx 2a_{BB}$, roughly independent of a_{BX}. Therefore, even for resonant interactions ($a_{BX} \to -\infty$), where the $\propto -1/R^2$ potential is restored for large interpaticle separations, the energy spectrum is well defined and no regularization with a three-body parameter is necessary. For finite a_{BX} an effective potential barrier forms at $R \approx 2|a_{BX}|$, leading to recombination resonances. An extension to this model, now offering an analytic expression of L_3, has recently been developed by Giannakeas and Greene [2017].

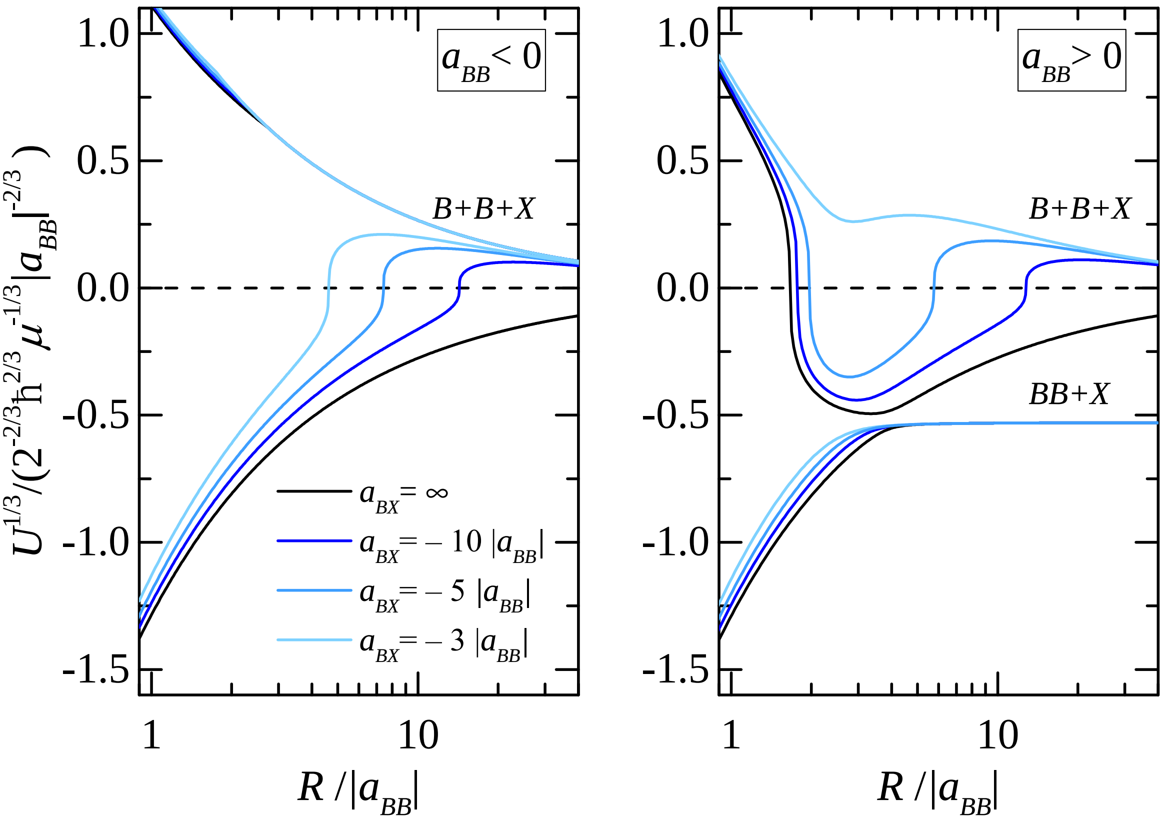

Figure 3.4.: First two adiabatic hyperspherical potentials U_ν for a BBX system with a mass ratio of $m_B/m_X = 22.1$ and $a_{BB} < 0$ (left panel) and $a_{BB} > 0$ (right panel) in the universal zero-range model. The curves correspond to interspecies scattering lengths a_{BX} with respective values ∞, -10, -5, -3 in units of $|a_{BB}|$. Figure adapted from [Ulmanis et al., 2016].

3.2.2. Recombination within the zero-range theory

In order to directly compare the universal zero-range theory with the experimental measurements, we calculate three-body loss rates from the S-matrix formalism [Rem et al., 2013; Efimov, 1979; Braaten and Hammer, 2006; Braaten et al., 2008], which was generalized to BBX systems by Petrov and Werner [2015][3]. The model is applicable in the range of negative scattering lengths $a_{BX} < 0, a_{BB} < 0$, where no weakly-bound dimer states exists. Thus, the loss process is entirely described by recombination into deeply-bound dimer plus atom channels.

The wavefunctions in the asymptotic and scale-invariant region, defined in Fig. 3.2,

---

[3] The theoretical calculations of the three-body loss rate L_3 within the hyperspherical formalism with zero-range potentials and negative intraspecies scattering lengths have been performed by D. Petrov from LPTMS, CNRS, Univ. Paris Sud, Université Paris-Saclay, Orsay, France and F. Werner from Laboratoire Kastler Brossel, ENS-PSL, UPMC-Sorbonne Université, Collège de France, CNRS, Paris, France.

are characterized by incoming and outgoing waves with amplitudes $A_3^{\text{in,out}}$ and $A_1^{\text{in,out}}$, respectively. The reflection and transmission probabilities, connecting the different amplitudes, and the loss at short distances are illustrated in Fig. 3.5. The behavior of the wavefunction in the short-range region $R \lesssim r_0$ is influenced by the non-universal interaction potentials at short internuclear distances. We incorporate this in the three-body contact condition [Petrov and Werner, 2015]

$$A_1^{\text{in}} = \mathcal{A} A_1^{\text{out}}, \tag{3.28}$$

where the reflection amplitude $\mathcal{A}$ from the point $R = 0$ is given by

$$\mathcal{A} = -(kR_0)^{-i2s_0} e^{-2\eta}. \tag{3.29}$$

The parameter R_0 serves as three-body parameter and defines the phase of the reflection amplitude. Equivalently R_0 can be interpreted as fixing a hyperradial node of the three-body wavefunction and thereby determining the whole Efimov energy spectrum. The modulus of the reflection probability $|\mathcal{A}| = e^{-4\eta}$ is characterized by a single quantity, the inelasticity parameter η. It contains the non-universal loss to all deeply-bound atom-dimer channels and is usually obtained by comparison to experiment. The total flux lost at short-range is thus given by

$$\varphi_{\text{loss}} = (1 - e^{-4\eta}) |A_1^{\text{out}}|^2. \tag{3.30}$$

Now we turn our attention to the transition region between the scale-invariant and asymptotic regimes, where a repulsive potential barrier forms (see Fig. 3.2). The amplitudes of the incoming and outgoing wavefunctions in the scale-invariant and asymptotic regions are connected by the unitary S-matrix

$$\begin{pmatrix} A_1^{\text{out}} \\ A_3^{\text{out}} \end{pmatrix} = \begin{pmatrix} s_{11} & s_{13} \\ s_{31} & s_{33} \end{pmatrix} \begin{pmatrix} A_1^{\text{in}} \\ A_3^{\text{in}} \end{pmatrix}. \tag{3.31}$$

Its elements s_{ij} are the transition amplitudes between channel j and i and can be easily calculated [Petrov and Werner, 2015]. Combining Eq. (3.28) and (3.31) and using the property of the unitary S-matrix, $|s_{13}|^2 = 1 - |s_{11}|^2$, we rewrite the total lost flux

$$\varphi_{\text{loss}} = (1 - e^{-4\eta}) \frac{1 - |s_{11}|^2}{|1 - s_{11}\mathcal{A}|^2} |A_3^{\text{in}}|^2. \tag{3.32}$$

The amplitude of the incoming wavepacket A_3^{in} at large hyperradius is obtained by the k-dependent projection of the incoming plane wave onto the Efimovian hyperradial wavefunction $\Phi_0(\Omega; R)$ [see Eq. (3.8)]. We arrive at the energy dependent three-body recombination rate $L_3(k) = \cos\phi \langle \varphi_{\text{loss}} \rangle_{\hat{k}} / 2$ after averaging over the direction of $\hat{k}$ and

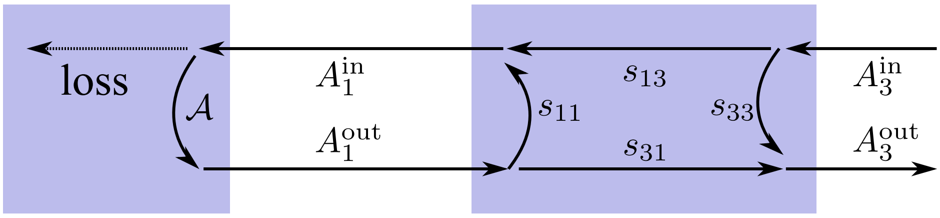

Figure 3.5.: Illustration of possible three-body collision pathways. A wavepacket with amplitude A_3^{in} approaching from large R can either be lost at $R = 0$ or return again to large hyperradii R. The different pathways are determined by the reflection and transmission probabilities s_{ij} and $\mathcal{A}$.

the hyperangular coordinates:

$$L_3(k) = \frac{64\pi^2 \cos^3\phi}{2\mu_{BX}k^4}(1 - e^{-4\eta})\frac{1 - |s_{11}|^2}{|1 - s_{11}\mathcal{A}|^2}, \tag{3.33}$$

where $\mu_{BX} = m_B m_X/(m_B + m_X)$ is again the two-body reduced mass and the angle ϕ is defined through the masses by $\sin\phi = m_B/(m_X + m_B)$. After thermal averaging, assuming a Boltzmann distribution with temperature T, we arrive at the loss rate constant

$$L_3 = 4\pi^2 \cos^3\phi \frac{\hbar^7}{\mu_{BX}^4 (k_B T)^3}(1 - e^{-4\eta}) \times \int_0^\infty \frac{1 - |s_{11}|^2}{|1 + (kR_0)^{-2is_0} e^{-2\eta} s_{11}|^2} e^{-\hbar^2 k^2/2\mu_{BX} k_B T} k dk. \tag{3.34}$$

We apply this formalism to the Li-Cs system by replacing the masses $m_B \to m_{\text{Cs}}$ and $m_X \to m_{\text{Li}}$ in the relevant mass factors and setting the quantity s_0 related to the Cs-Cs-Li Efimov scaling factor $\exp(\pi/s_0) \approx 4.799$ for resonant Li-Cs and Cs-Cs interactions. The universal function s_{11} depends on ka_{LiCs}, ka_{Cs}, and the mass ratio m_B/m_X. We use the known magnetic field dependence of a_{LiCs} and a_{Cs} from Table 2.1 and Berninger et al. [2013a] and tabulate s_{11} as a function of k and the magnetic field in vicinity of the 843 G FR (see Ref. [Petrov and Werner, 2015] for details on the calculation). By this approach, we obtain an analytic expression of the three-body loss rate L_3, which only depends on temperature T, three-body parameter R_0, and inelasticity parameter η. Thus the model can be directly compared and fitted to the experimental observations and allows one to extract the non-universal parameters, i.e. R_0 and η, as introduced in Sec. 3.4.1.

In Fig. 3.6 the thermally averaged three-body loss rate L_3 from Eq. (3.34) in dependence of the Li-Cs scattering length is shown. The recombination rate generally increases for increasing scattering length roughly as a_{LiCs}^2 (see Sec. 3.4.4). We observe a modulated enhancement of the L_3 rate due to the occurrence of Efimov resonances. In the unitarity limit $a_{\text{LiCs}} \to -\infty$ the loss rate approaches a constant value corresponding to the unitary limit L_3^{max}, Eq. (3.19). This limit increases $\propto T^{-2}$ when temperature

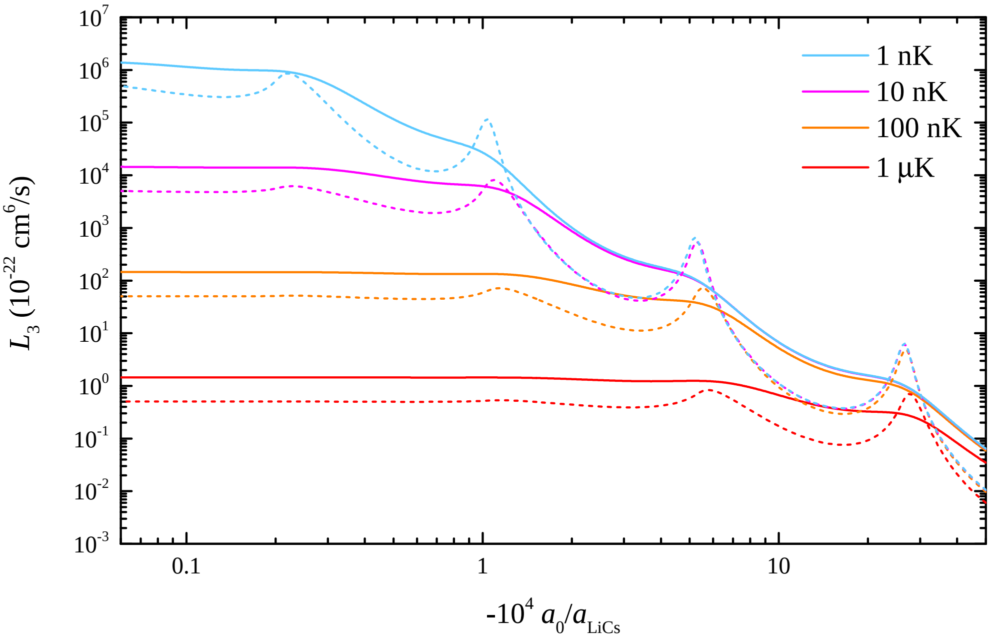

Figure 3.6.: Cs-Cs-Li three-body recombination rate L_3 in dependence of the inverse of the intraspecies scattering length a_{LiCs} close to the 843 G Feshbach resonance. We exemplarily plot L_3 for four different temperatures and two inelasticity parameters $\eta = 0.75$ (solid lines) and $\eta = 0.1$ (dashed lines). The three-body parameter was kept constant at $R_0 = 130\ a_0$.

is reduced. Thus the maximal scattering length at which variations in L_3 are still resolvable increases with decreasing temperature and, as a consequence, a larger number of Efimov resonances can be observed. While at 1 μK only two Efimov features are visible, four features are resolvable at a temperature of 1 nK. The inelasticity parameter η, which determines the total loss into energetically lower channels, determines the width and height of the peaks in the L_3 rate. For large values of η, the resonance features are considerably broadened and become less pronounced, thus impeding their observation in experiments. Similar results have been obtained by a formalism based on optical potentials [Mikkelsen et al., 2015] and from effective field theory [Helfrich et al., 2010; Helfrich and Hammer, 2010; Acharya et al., 2016].

3.2.3. Spinless van der Waals theory

Additionally we solve the three-body problem within the spinless van der Waals theory [Wang et al., 2012c][4]. The approach consists of numerically solving the three-body Schrödinger equation in the full hyperspherical formalism, where the two-body inter-

---

[4] All calculations of L_3 based on two-body Lennard-Jones potentials have been performed by Y. Wang, Kansas State University, Manhattan, Kansas, USA, and Prof. C.H. Greene from Purdue University, West Lafayette, Indiana, USA.

action potentials $V_{BB/BX}$ within equal bosons or between bosons and the third particle separated by distance $r_{BB/BX}$ are modeled by single-channel Lennard-Jones potentials with vdW tails [Jones, 1924a,b]

$$V_{BB/BX}(r_{BB/BX}) = -\frac{C_{6,BB/BX}}{r_{BB/BX}^{6}}\left[1-\left(\frac{r_{c,BB/BX}}{r_{BB/BX}}\right)^{6}\right], \tag{3.35}$$

where $C_{6,BB/BX}$ are the dispersion coefficients. The scattering lengths a_{BX} and a_{BB} are reproduced by tuning the short-range cut-offs $r_{c,BB/BX}$. We assume that the hyperradial and hyperangular motions are approximately separable [Macek, 1968] and treat the hyperradius as adiabatic parameter. Thus, the Schrödinger equation is reduced to a set of coupled 1D equations [Wang, 2010]. We include the non-adiabatic couplings between the hyperspherical potentials and assume a $J^{\Pi} = 0^{+}$ symmetry[5], the dominant contribution at ultracold temperatures, where J is the total angular momentum and Π the total parity.

This formalism is applied to the Cs-Cs-Li system and allows us to compare the theoretical predictions directly to our experimental observations. The interaction potentials are tuned such that the scattering lengths a_{LiCs}, a_{Cs} and their functional dependence $a_{\mathrm{Cs}}(a_{\mathrm{LiCs}})$ are reproduced for the experimentally employed field ranges (see Fig. 2.9). The adiabatic hyperspherical potentials are plotted in Fig. 3.7 for intraspecies scattering lengths of $a_{\mathrm{Cs}} = -1500\,a_0$ and $a_{\mathrm{Cs}} = +200\,a_0$ resembling the two cases of the 843 G and 889 G Li-Cs FRs. The interspecies scattering length $a_{\mathrm{LiCs}} = -400\,a_0$ is tuned close to the value where the ground state Efimov resonance is expected [Pires et al., 2014b]. For positive intraspecies interactions an avoided crossing originating from the coupling between the attractive three-body potential and a repulsive atom-dimer channel leads to an effectively repulsive Efimov potential. This prevents the scattering wavefunction from probing short-range parts of the potential and, consequently, recombination. Such an avoided crossing is not present for the case of $a_{\mathrm{Cs}} = -1500\,a_0$, where the original Efimov effect is recovered.

The adiabatic potentials calculated within the spinless vdW theory closely resemble those within the zero-range theory when R, $|a_{BB}|$, and $|a_{BX}|$ are all significantly greater than $r_{\mathrm{vdW}}^{\mathrm{Cs}}$ and $r_{\mathrm{vdW}}^{\mathrm{LiCs}}$. The universal condition $|a_{BB}|$, $|a_{BX}| \gg r_{\mathrm{vdW}}^{\mathrm{Cs}}$, $r_{\mathrm{vdW}}^{\mathrm{LiCs}}$ is satisfied or approximately satisfied in both cases of the 843 G and 889 G Feshbach resonances, therefore the zero-range theory is still helpful for understanding the scaling behavior of the three-body losses observed in our experiment, as discussed above. The quantitative

---

[5] The absence of the Efimov effect in higher partial waves for our mass ratio of $m_B/m_X = 22.1$ [D'Incao and Esry, 2006b], leads to a substantial suppression of $J > 0$ contributions to the recombination rate in the ultracold regime with $k_B T \ll E_{\mathrm{vdW}}$. The suppression is estimated to be $(kr_{\mathrm{vdW}})^{2p_0} \ll 1$ for $a_{\mathrm{Cs}} < 0$ and $(ka_{\mathrm{Cs}})^{2p_0} \ll 1$ for the $a_{\mathrm{Cs}} \approx +190a_0$ case [Wang and Esry, 2011], where $p_0 > 1$ is a universal constant for the given mass ratio [D'Incao and Esry, 2006b] and k the thermal wavevector.

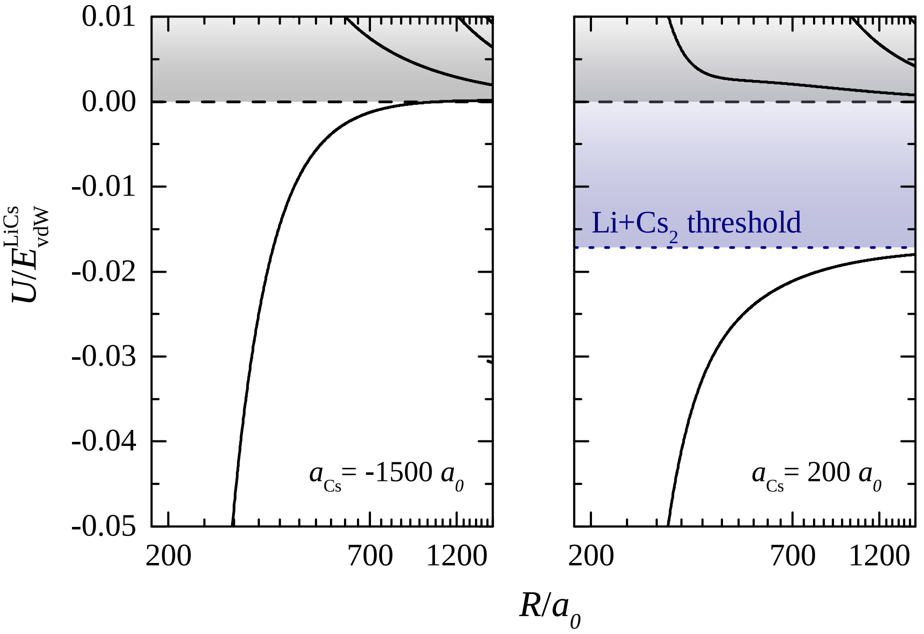

Figure 3.7.: Cs-Cs-Li adiabatic hyperspherical potentials U within the spinless vdW theory for intraspecies scattering lengths $a_{\mathrm{Cs}} = -1500\,a_0$ (left panel) and $a_{\mathrm{Cs}} = +200\,a_0$ (right panel) in units of the Li-Cs vdW energy $E_{\mathrm{vdW}}^{\mathrm{LiCs}}$. In both cases the interspecies scattering length is $a_{\mathrm{LiCs}} = -400\ a_0$. Reproduced from Häfner et al. [2017].

determination of the observables, especially of the 3BP, requires the knowledge of the three-body dynamics when R is smaller than or comparable with the van der Waals lengths, which needs the spinless van der Waals theory to resolve.

We calculate the energy dependent three-body recombination rate from the S-matrix [Mehta et al., 2009; Wang, 2010] and perform thermal averaging [Suno et al., 2003], assuming Boltzmann distributions with the experimentally determined temperatures. The width of the experimentally observed recombination features is reproduced by adding a heuristic hyperradial loss channel that assumes near unity loss at short distances, without modifying the resonance positions [Wang et al., 2015]. The obtained three-body recombination rates are plotted together with the energy spectrum of the three energetically lowest Efimov states in Fig. 3.10 and 3.11. For the case of the 843 G Li-Cs FR, where $a_{\mathrm{Cs}} \approx -1500\ a_0$, the classical Efimov scenario is recovered (Fig. 3.10). By lowering a_{LiCs} the Efimov states successively disappear by crossing the three-body scattering threshold. For positive intraspecies scattering length $a_{\mathrm{Cs}} \approx +190\ a_0$, as it is the case for the 889 G Li-Cs FR, the Efimov sates split into two branches (Fig. 3.11). While the lowest state predissociates into a Cs_2+Li state (blue dashed line) before reaching the three-body threshold and consequently does not lead to a recombination resonance at the three-body threshold, the higher-lying states recover the original Efimov scenario.

3.3. Three-body loss rates

In ultracold atomic gases, Efimov states can be observed at the three-body scattering threshold as enhanced losses due to recombination into deeply-bound atom-dimer channels. This leads to an increase of the three-body loss rate L_3 as described in Sec. 3.1.3. However, for an unambiguous observation of Efimov resonances it is not enough to perform standard atom loss spectroscopy as performed in Ch. 2, since this method is not sensitive to the particles involved in the loss process and can not distinguish between different loss channels. Therefore, we need to experimentally determine the three-body loss rate L_3 for recombination from the Cs-Cs-Li scattering channel, which is described in the following.

The experimental preparation sequence is described in Sec. 1.3.3. For the measurements at the higher sample temperatures of 450 nK (843 G FR) and 320 nK (889 G FR) we employ the single optical dipole trapping scheme and achieve samples of 1.6×10^4 Cs atoms in state $|3, +3\rangle$ and 4×10^4 Li atoms in either of the $|1/2, 1/2\rangle$ or $|1/2, -1/2\rangle$ states. We measure trapping frequencies of $\omega_{\mathrm{Cs}} = 2\pi \times (11, 114, 123)$ Hz and $\omega_{\mathrm{Li}} = 2\pi \times (33, 275, 308)$ Hz. By usage of the bichromatic trapping scheme we prepare samples of 1×10^4 Cs and 7×10^3 Li atoms at temperatures as low as 120 nK. The spatial overlap of the two atomic clouds is approximately 45% and assumed to be constant within the investigated magnetic field range. The measured trapping frequencies are $\omega_{\mathrm{Cs}} = 2\pi \times (5.7, 115, 85)$ Hz and $\omega_{\mathrm{Li}} = 2\pi \times (25, 160, 180)$ Hz.

In order to obtain the three-body recombination rates we record the time evolution of the atom number densities n_{Li} and n_{Cs}. They are related by the set of coupled rate equations

$$\dot{n_{\mathrm{Li}}} = -L_1^{\mathrm{Li}} n_{\mathrm{Li}} - L_3 n_{\mathrm{Li}} n_{\mathrm{Cs}}^2 \,, \tag{3.36}$$

$$\dot{n_{\mathrm{Cs}}} = -L_1^{\mathrm{Cs}} n_{\mathrm{Cs}} - 2L_3 n_{\mathrm{Li}} n_{\mathrm{Cs}}^2 - L_3^{\mathrm{Cs}} n_{\mathrm{Cs}}^3 \,, \tag{3.37}$$

where $L_1^{\mathrm{Li,Cs}}$ correspond to the single-body loss rates of Li and Cs atoms from the trap and L_3^{Cs} is the three-body loss rate associated to recombination of three Cs atoms. The three-body loss rate L_3 describes inelastic Cs-Cs-Li collisions and is the quantity of interest, since it contains the signatures of Cs-Cs-Li Efimov resonances. The factor of 2 in the rate equation of the Cs density [Eq. (3.37)] indicates, that in each recombination process two Cs atoms and one Li atom are lost from the trap. In principle also inter- and intraspecies two-body processes have to be considered. However, since we prepare the atoms in their energetically lowest scattering states, only elastic two-body collisions are possible and thus we do not include loss terms involving two particles. In addition, we neglect inelastic three-body processes involving more than one Li atom, e.g. Li-Li-Li or Cs-Li-Li collisions, since the probability of finding multiple Li atoms close to each other is strongly suppressed due to Pauli blocking. In general a third differential

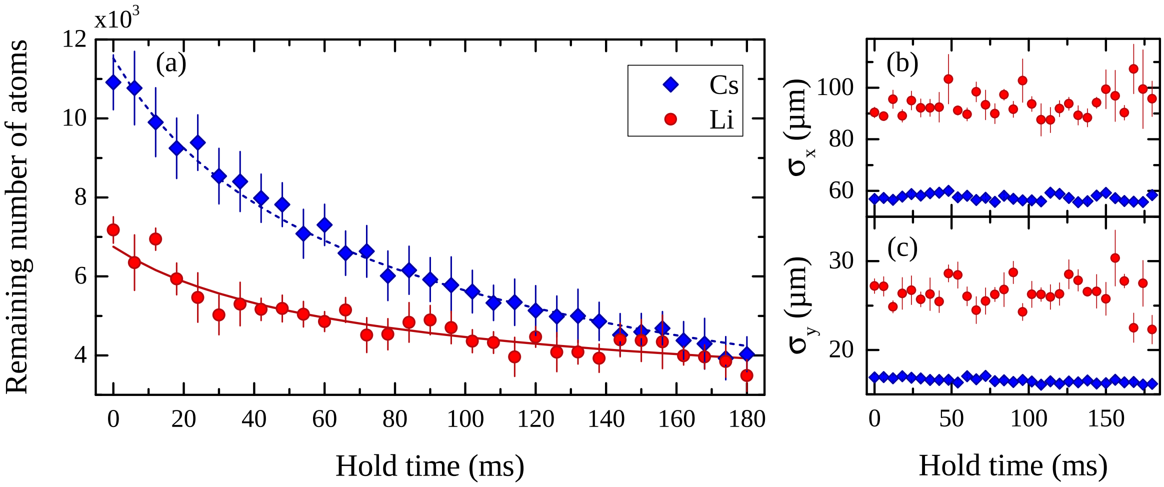

Figure 3.8.: Temporal evolution of a Li-Cs mixture at a magnetic field of 843.049 G and a temperature of 120 nK. (a) Remaining number of Li (red circles) and Cs (blue diamonds) atoms. The red solid (Li) and blue dashed (Cs) lines represent a simultaneous fit of the coupled rate equations (3.38) and (3.39) to the data. (b) and (c) Respective fitted σ widths of the Li and Cs atom clouds in two directions after a time of flight of 0.3 ms and 5 ms, respectively. Each data point is an average of at least three independent measurements and the error bars represent the standard error of the mean. Figure adapted from Ulmanis et al. [2016a]

equation, representing recombinational heating [Weber et al., 2003; Roy et al., 2013; Bloom et al., 2013] has to be included. However, we do not observe any increase in the recorded Gaussian widths $\sigma_i(t)$ [see Eq. (1.9)] of the atomic clouds during the atomic loss [see Fig. 3.8(b) and 3.8(c)] after 5 ms and 0.3 ms of time of flight for Cs and Li, respectively. The widths of both species stay constant within 10%, which corresponds to temperature variations of ≈20% for our experimental parameters. Thus, we consider the temperature to be time independent and do not include it in our analysis.

The densities $n_{\mathrm{Li,Cs}}$ are not directly accessible in our experiments, but we can only record the total number of atoms $N_{\mathrm{Li,Cs}}$ in dependence of the interaction time and magnetic field value. We spatially integrate Eq. (3.36) and (3.37) over the density distributions and arrive at the equivalent system of differential equations:

$$\dot{N}_{\mathrm{Li}} = -L_1^{\mathrm{Li}} N_{\mathrm{Li}} - \mathcal{L}_3 N_{\mathrm{Li}} N_{\mathrm{Cs}}^2, \tag{3.38}$$

$$\dot{N}_{\mathrm{Cs}} = -L_1^{\mathrm{Cs}} N_{\mathrm{Cs}} - 2\mathcal{L}_3 N_{\mathrm{Li}} N_{\mathrm{Cs}}^2 - \mathcal{L}_3^{\mathrm{Cs}} N_{\mathrm{Cs}}^3, \tag{3.39}$$

where the rates $\mathcal{L}_3$ and $\mathcal{L}_3^{\mathrm{Cs}}$ are related to the three-body loss rates defined in Eq. (3.36) and (3.37) by constants of unit volume squared. We assume Gaussian density distributions [see Eq. (1.8)] of the atomic clouds and arrive at the following relations

$$L_3 = 8\pi^3 \exp\left(\frac{z_0^2}{2\sigma_{z,\mathrm{Li}}^2 + \sigma_{z,\mathrm{Cs}}^2}\right)\mathcal{L}_3 \prod_{i=x,y,z} \sigma_{i,\mathrm{Cs}}\sqrt{2\sigma_{i,\mathrm{Li}}^2 + \sigma_{i,\mathrm{Cs}}^2}\ , \tag{3.40}$$

$$L_3^{\mathrm{Cs}} = 24\sqrt{3}\pi^3 \mathcal{L}_3^{\mathrm{Cs}} \prod_{i=x,y,z} \sigma_{i,\mathrm{Cs}}^2\ , \tag{3.41}$$

where $\sigma_{i,\mathrm{Li},\mathrm{Cs}}$ are the widths of the atomic clouds defined in Eq. (1.9). The displacement z_0 between the centers of the Li and Cs distributions reduces the experimentally observable loss rate $\mathcal{L}_3$ and stems from the differential gravitational sag of the two species. The value of z_0 is estimated from our modeled trapping potential as described in Sec. 1.3.2.

A typical time evolution of the remaining number of Li and Cs atoms at a magnetic field of 843.049 G is shown in Fig. 3.8(a). the temporal evolution of Li and Cs atom numbers is numerically fitted with the coupled equations Eq. (3.38) and (3.39), from which the rate coefficient $\mathcal{L}_3$ is extracted. The single-body $L_1^{\mathrm{Li},\mathrm{Cs}}$ and single-species three-body rates $\mathcal{L}_3^{\mathrm{Cs}}$ are determined from independent single species measurements under the same experimental conditions. Hence, $\mathcal{L}_3$ and the initial number of atoms $N_{0,\mathrm{Li}}$ and $N_{0,\mathrm{Cs}}$ are the only fitting parameters. Finally, the quantities L_3 and L_3^{Cs}, which are independent of the atomic number densities and can therefore be directly compared to theory, are computed via Eq. (3.40) and (3.41). The systematic error for the determination of the absolute value of L_3 is estimated to be a factor of 3 (120 nK data) and 0.8 (450 nK and 320 nK data), respectively, and are mainly caused by uncertainties in the determination of atom cloud temperatures, densities, overlap and trapping frequencies. Recording the temporal evolution allows us to demonstrate clearly, that the three-body loss is dominated by Cs-Cs-Li and Cs-Cs-Cs collisions. Replacing the interspecies three-body loss by a process involving two Li and one Cs atom can not explain the measured atom number decay curves. Thus, we conclude, that the Efimov resonances occur in the Cs-Cs-Li channel.

The recombination rate spectra discussed in Sec. 3.4.1 and 3.4.2 are obtained by recording the holding-time dependent atom numbers for each magnetic field value. Since the loss rates close to the Feshbach resonance are much faster than away from it, the maximum hold time was adapted for the different magnetic field regions, while the number of time steps is kept constant at 30. We estimate the errors in determination of $\mathcal{L}_3$ by standard bootstrapping techniques [Wu, 1986; Efron and Tibshirani, 1993], where we resample the residuals for 1000 repetitions of the fitting procedure [Ulmanis, 2015]. We assume the mean and the standard deviations to be the best estimates for the determination of $\mathcal{L}_3$ and its uncertainty.

The extraction of the three-body loss rate L_3 however is limited by intraspecies losses.

For small scattering lengths the atomic loss is dominated by single-species losses, such as $2L_3 n_{\mathrm{Li}} n_{\mathrm{Cs}} \ll L_1^{\mathrm{Cs}} + L_3^{\mathrm{Cs}} n_{\mathrm{Cs}}^2$ or $L_3 n_{\mathrm{Cs}} \ll L_1^{\mathrm{Li}}$. Under the experimental conditions during our measurements, the intraspecies losses of Cs are the limiting factor. We estimate the extraction to be unreliable when the interspecies loss rate is on the order of 1/10 of the intraspecies one. This limits our minimal measurable L_3 to be

$$L_3^{\mathrm{min}} \approx 1/20 (L_1^{\mathrm{Cs}} n_{\mathrm{Li}}^{-1} n_{\mathrm{Cs}}^{-1} + L_3^{\mathrm{Cs}} n_{\mathrm{Li}}^{-1} n_{\mathrm{Cs}}) \tag{3.42}$$

This limit depends on the Li and Cs densities and the intraspecies loss rates and is thus varies for each of our measurements performed at different temperatures and Feshbach resonances. In case this limit is reached, the given three-body loss rates represent an upper bound of the actual L_3 and are indicated by error bars extending to the lower axis. This limit is due to pure technical reasons and could be further reduced by adapting the relative densities of Li and Cs, i.e. increasing n_{Li} and decreasing n_{Cs}, by reducing the single-body loss rates $L_1^{\mathrm{Li,Cs}}$, or by reducing the shot-to-shot fluctuations in our experiments.

3.4. Role of the intraspecies scattering length in the Efimov scenario

The Cs-Cs-Li system offers the unique possibility to study the influence of the intraspecies scattering length on the heteronuclear Efimov scenario. As has been seen in Sec. 3.2, the intraspecies scattering length a_{BB} has a decisive impact on the Efimov spectra on both trimer binding energies and resonance positions. It may lead to vanishing of Efimov resonances at the three-body dissociation threshold or even serve as a universal three-body parameter, defining the whole energy spectrum. The experimentally adjustable interspecies and intraspecies scattering lengths a_{LiCs} and a_{Cs} are shown in Fig. 2.9. Two intermediately broad ($s_{\mathrm{res}} \approx 0.7$ [Tung et al., 2013]) Li-Cs Feshbach resonances, located at approx. 843 G and 889 G, are well suited for the study of the heteronuclear Efimov scenario [Repp et al., 2013; Tung et al., 2013; Pires et al., 2014a; Ulmanis et al., 2015]. They are characterized by different sign and magnitude of the Cs-Cs scattering length a_{Cs}: while close to the 843 G resonance the intraspecies scattering length is large and negative $a_{\mathrm{Cs}} \approx -1500\ a_0$, the 889 G resonance is characterized by a small and positive intraspecies scattering length $a_{\mathrm{Cs}} \approx +190\ a_0$ [Berninger et al., 2013a]. These two Feshbach resonances are used in the following to verify the decisive influence of the Cs-Cs scattering length on the Efimov scenario as predicted in Sec. 3.2. Furthermore, by investigating the narrow resonances located at approximately 816 G, 889 G and 943 G characterized by $s_{\mathrm{res}} \leq 0.03$ [Tung et al., 2013], the Cs-Cs-Li system offers the possibility to investigate the influence of the multichannel nature of Feshbach resonances on the universal Efimov scenario [Wang and Julienne, 2014] which has been studied recently [Johansen et al., 2017].

3.4.1. Negative intraspecies scattering length

Zero-range model

The observed Cs-Cs-Li three-body recombination rates L_3 versus the magnetic field and the interspecies scattering length a_{LiCs} close to the broad Li-Cs FR at 843 G at temperatures of 450 nK and 120 nK are shown in Fig. 3.9. The experimental data and theoretical recombination rates are plotted in the magnetic field range between 842.6 G and 852 G, where the magnitude of the interspecies scattering length $|a_{\mathrm{LiCs}}| > 200\ a_0$. As the absolute value of the scattering length is increased in the vicinity the FR, indicated by the vertical dashed line, we observe a general increase of the recombination rate towards the temperature dependent unitary limited loss rate L_3^{max}. As explained previously, the interspecies loss rate can not be reliably determined for small scattering lengths. For these datasets the minimal L_3 amount to $L_3^{\mathrm{min},120} \approx 2 \times 10^{-22}$ cm^6/s and $L_3^{\mathrm{min},450} \approx 1 \times 10^{-25}$ cm^6/s. This limits the determination to magnetic field values below 850 G or equivalently $|a_{\mathrm{LiCs}}| \gtrsim 1000\ a_0$ for our data at 120 nK, while for the 450 nK data the limit is well outside the range where our measurements were performed. In this range, the data points represent an upper limit of the actual L_3, which is indicated by error bars ranging to zero. In the studied magnetic field range the intraspecies scattering length is negative and in the range $-1560\ a_0 \lesssim a_{\mathrm{Cs}} \lesssim -1000\ a_0$.

In the measured three-body recombination rate spectra we observe three consecutive Efimov resonances by additional modulations on top of the inclining L_3 rate. The position of the enhanced losses correspond to the scattering legnths $a_-^{(n)}$, where the nth crosses the scattering threshold (see Fig. 3.1). While the ground state Efimov resonance, located at around 848.9 G or equivalently $a_{\mathrm{LiCs}} \approx -300\ a_0$, is only visible in the data set with a temperature of 450 nK, we observe a common enhancement in both data sets at about 843.8 G. This corresponds to a scattering length of $a_{\mathrm{LiCs}} \approx -1800\ a_0$. For even larger scattering lengths a third loss feature is clearly visible in the low temperature data, while it cannot be resolved in the 450 nK data due to the unitary limited interspecies loss rate at these temperatures. It is approximately located at 843.0 G or $a_{\mathrm{LiCs}} \approx -9210\ a_0$. Note that the maximum of the three-body recombination rate is not at the Feshbach resonance position (vertical dashed line in Fig. 3.9). This may be explained by contributions from other recombination processes, e.g. weakly-bound dimer formation and subsequent recombination in the atom-dimer channel, which may lead to increased loss on the positive scattering length side of the Feshbach resonance.

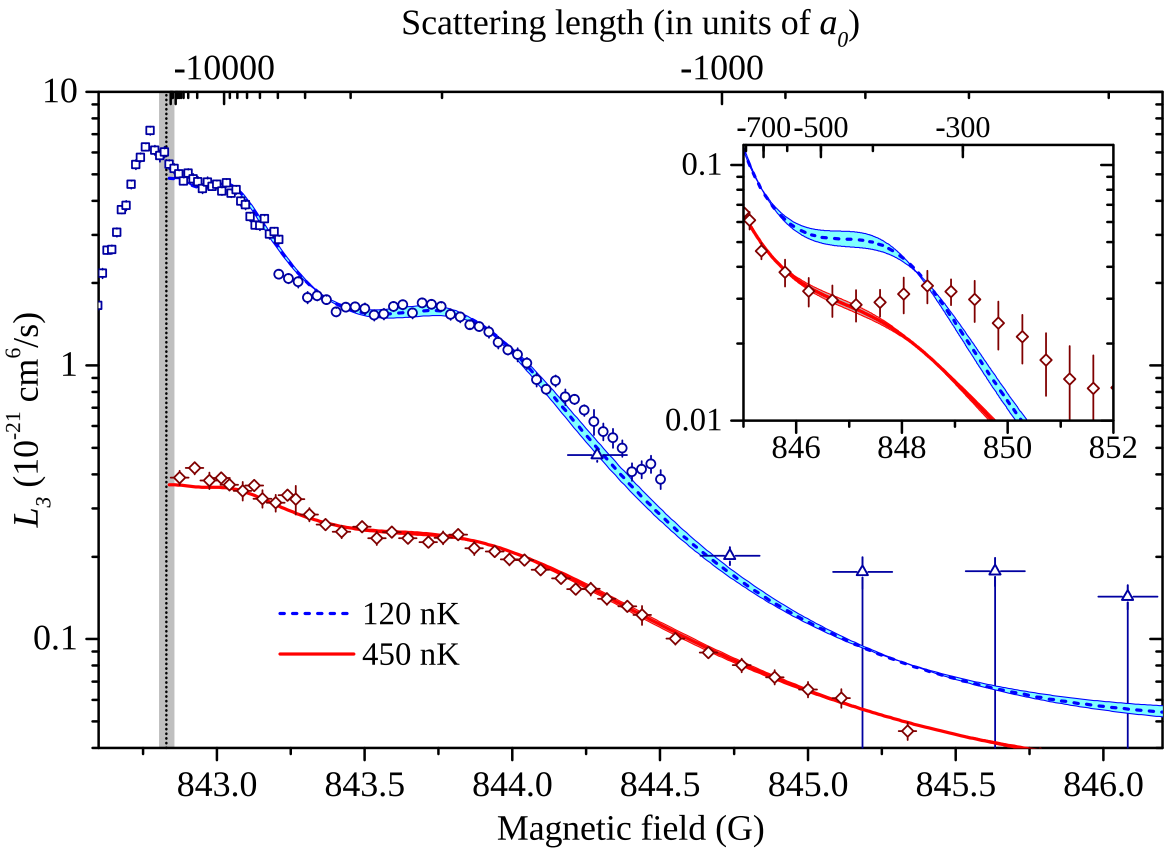

Figure 3.9.: Cs-Cs-Li three-body loss rate L_3 at temperatures of 450 nK (red) and 120 nK (blue). The experimental data (red diamonds and blue squares, circles, triangles) are rescaled by factors γ employing a fit to the zero-range theory (solid red lines and dashed blue lines) close to the 843 G Li-Cs Feshbach resonance. The corresponding interspecies scattering length a_{LiCs} is given on the upper axis. The shaded region around the fits represent the uncertainty of the Feshbach resonance position. Note that the maximum of L_3 does not correspond to the Feshbach resonance position indicated by the vertical gray dotted line and its uncertainty by the gray shade. The spectra clearly show three Efimov resonances at ≈ 848.9 G, ≈ 843.8 G, and ≈ 843.0 G. The zero-range theory clearly deviates from the Efimov ground state (see inset). Figure reproduced from Ulmanis et al. [2016a].

The experimental L_3 spectra are analyzed with the zero-range S-matrix formalism introduced in Sec. 3.2.2. We employ Eq. (3.34) to fit each of the data sets and obtain the parameters $\eta^{(120)} = 0.61$, $\eta^{(450)} = 0.86$, $R_0^{(120)} = 125a_0$, and $R_0^{(450)} = 130a_0$. In addition we rescale the experimentally measured rates L_3^{expt} to the theoretical ones by introducing the prefactors γ, such that $L_3 = \gamma L_3^{\mathrm{expt}}$. The rescaling constants are determined to be $\gamma^{(120)} = 1.9, 1.2, 0.6$ for the data set at colder temperatures and $\gamma^{(450)} = 0.7$ and are well within the experimental uncertainty of the absolute determination of L_3. The dataset at 120 nK consists of three measurements with varying maximal hold time and are taken on different days, and therefore slightly different trapping conditions (indicated in Fig. 3.9 by the blue squares, circles, and triangles). Thus each subset was scaled with an appropriate factor γ. The temperature is taken to be fixed at the experimentally determined values of 120 nK and 450 nK.

In order to estimate the uncertainty of the fit parameters, we repeat the fitting for two different Feshbach resonance pole positions 842.829 ± 0.023 G (which corresponds to the uncertainty in its determination presented in Sec. 2.2.3), and see that all fit parameters change by less than 2%. These two additional fits are indicated in Fig. 3.9 as the shaded areas around the theoretical curves. Also excluding the data points above 847 G of the 450 nK dataset, where the model clearly deviates from the measurements, gives only minor changes of less than 2%.

The experimentally determined three-body loss rate L_3 can be well described by the zero-range model, as shown in Fig. 3.9. The model reproduces the temperature dependence fully and a large range of the Efimov spectrum. While excellent agreement is found for the two excited Efimov resonances, deviations for the ground state become apparent (see inset of Fig. 3.9). For large scattering lengths, close to the pole of the FR, the Efimov resonances follow the universal behavior. Since the model incorporates the non-zero and non-constant Cs scattering length, the deviations at low a_{LiCs} are most likely due to finite-range corrections. Such a correction is not surprising, since the ground state resonance is located at scattering lengths only 3.5 times larger than the Cs-Cs van der Waals range, $|a_-^{(0)}| \approx 3.5 r_{\mathrm{vdW}}^{\mathrm{Cs}}$. Deviations from the universal zero-range theory have already been observed in the homonuclear case [Huang et al., 2014b], where the first resonance is located at about ten times the van der Waals range [Wang et al., 2012a; Naidon et al., 2014a]. Thus, it is interesting to study our experimental findings with more realistic model potentials. The large value of η compared to previous studies [Kraemer et al., 2006; Gross et al., 2009; Pollack et al., 2009; Zaccanti et al., 2009; Gross et al., 2010; Berninger et al., 2011; Wild et al., 2012; Roy et al., 2013; Barontini et al., 2009; Bloom et al., 2013; Huang et al., 2014b; Williams et al., 2009; Eismann et al., 2016; Wenz et al., 2009] hints at efficient recombination into deeply bound molecular states.

Spinless van der Waals theory

Due to the apparent deviations between the experimentally determined three-body recombination rate and the zero-range model in the vicinity of the ground state Efimov resonance, we compare the same experimental data to the theoretical recombination rate from the spinless vdW theory in the upper panel of Fig. 3.10. Again, the measured L_3 rates of different data sets have been scaled by numerical constants $\gamma^{(120)} = 1.9, 1.2, 0.6$ and $\gamma^{(450)} = 0.7$, which are obtained by fitting to the universal

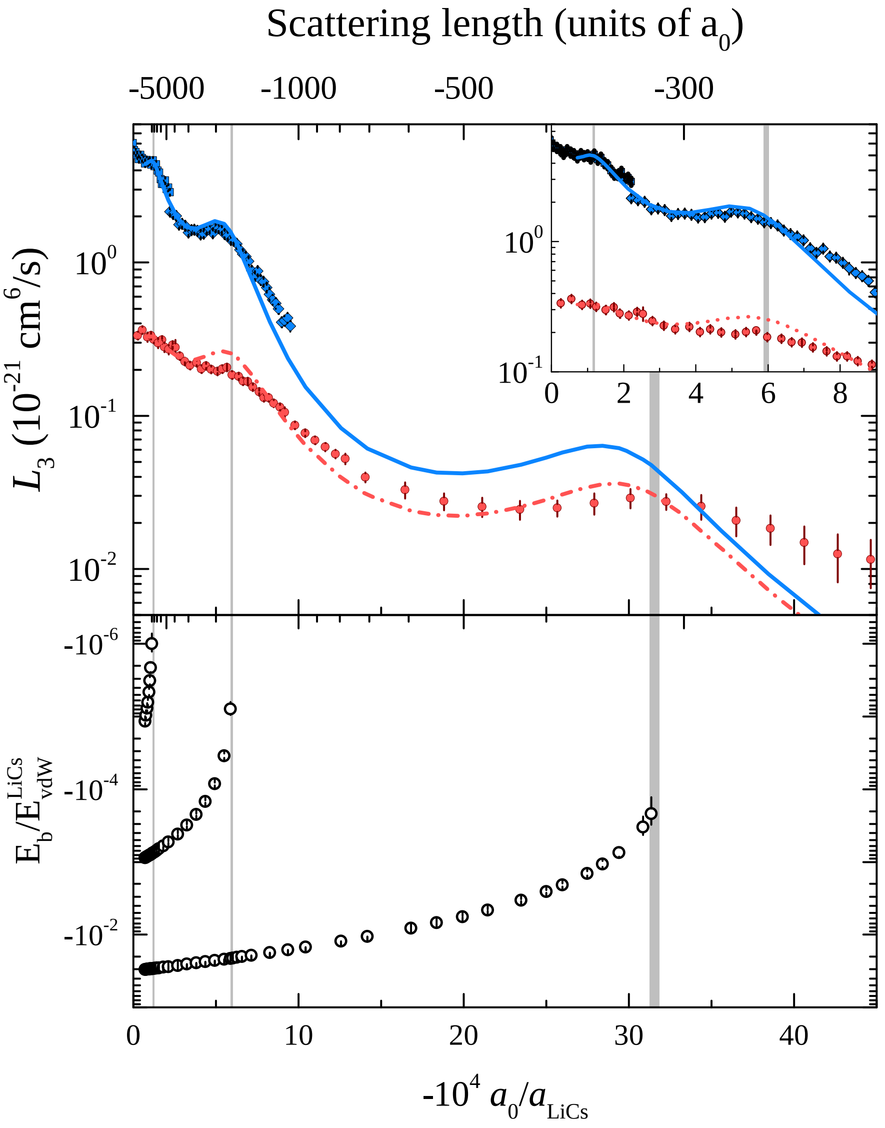

Figure 3.10.: Three-body recombination rates and energy spectra close to the 843 G Li-Cs Feshbach resonance, where $a_{\mathrm{Cs}} \approx -1500\ a_0$.

Upper panel: Experimental Cs-Cs-Li three-body recombination rate spectra at temperatures of 120 nK (blue diamonds and squares) and 450 nK (red circles). The inset shows a zoom into the region of the two excited Efimov resonances. The error bars represent statistical errors from bootstrapping and magnetic field uncertainties. The blue solid and red dash-dotted lines show the calculated three-body loss rates from the spinless vdW theory for a temperature of 120 nK and 450 nK, respectively. Experimental data have been scaled by a numerical constant, well within the absolute error, to fit the universal zero-range theory (see Fig. 3.9).

Lower panel: calculated CsCsLi energy spectra for the three deepest bound Efimov states. The error bars represent the width of the corresponding Efimov state. Missing error bars indicate a width that is smaller than the symbol size. The grayed areas correspond to the positions at which the Efimov states cross the Cs+Cs+Li scattering threshold and their widths represent their uncertainty. Figure adapted from Häfner et al. [2017].

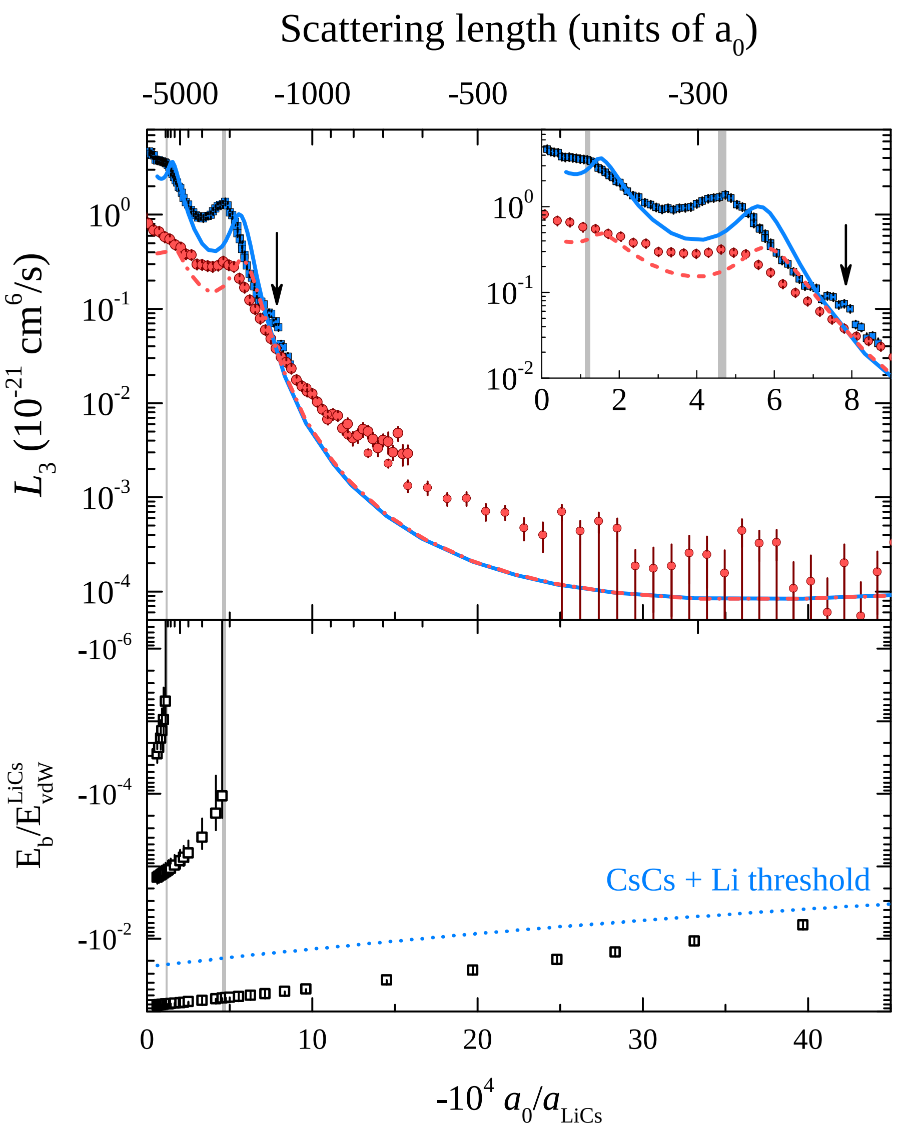

Figure 3.11.: Three-body recombination rates and energy spectra close to the 889 G Li-Cs Feshbach Resonance, where $a_{\mathrm{Cs}} \approx +190\ a_0$.
Upper panel: Experimental Cs-Cs-Li three-body recombination rate spectra at temperatures of 120 nK (blue squares) and 320 nK (red circles). The inset shows a zoom into the region of the two excited Efimov resonances. The error bars represent statistical errors from bootstrapping, magnetic field uncertainties, and the technical limit due to Cs-Cs-Cs three-body losses. The blue solid lines and red dash-dotted lines show the calculated three-body loss rates from the spinless vdW theory for a temperature of 120 nK and 320 nK, respectively. The arrow indicates a possible four-body resonance.
Lower panel: calculated CsCsLi energy spectra for the three deepest bound Efimov states. The atom-dimer scattering threshold CsCs+Li is shown as a dashed blue line. The error bars represent the width of the corresponding Efimov state. Missing error bars indicate a width that is smaller than the symbol size. The grayed areas correspond to the positions at which the Efimov states cross the Cs+Cs+Li scattering threshold and their widths represent their uncertainty. Figure adapted from Häfner et al. [2017].

zero-range theory in Fig. 3.9, but lie well within the experimental uncertainties. Three Cs-Cs-Li recombination resonances are evident, while the two excited ones are located in the universal regime (inset of Fig. 3.10). The spinless vdW theory is in excellent agreement with the experimental data. The theoretically calculated loss rate spectrum recovers not only the location of the two excited state resonances, but also the position of the ground state resonance. This is in stark contrast to the analysis with the universal zero-range theory (see Fig. 3.9), where no agreement between theory and experiment was observed for the ground state resonance. Since the essential difference from the zero-range theory is the inclusion of the vdW length scales that determine the short-range behavior of realistic pairwise potentials, we conclude that the previously observed deviation of the CsCsLi ground state resonance from the universal zero-range theory predominantly originates from the finite range of the interatomic vdW interaction. In addition we plot the energy spectrum of the three most-deeply bound trimer states in units of the characteristic vdW energy scale $E_{\mathrm{vdW}}^{\mathrm{LiCs}}$ as a function of scattering length. An excellent agreement is also found with the calculated energy spectrum show in the lower panel of Fig. 3.10, where the positions at which the three-body states become unbound (grayed areas in Fig. 3.10) perfectly align with the maxima of the measured recombination rates.

3.4.2. Positive intraspecies scattering length

We extend our studies of Efimov resonances to positive intraspecies scattering lengths $a_{\mathrm{Cs}} > 0$ in the vicinity of the 889 G Li-Cs Feshbach resonance. In the studied magnetic field range, the Cs-Cs scattering length is in the range $+180\ a_0 \lesssim a_{\mathrm{Cs}} \lesssim +360\ a_0$. The measured three-body recombination rate spectra at temperatures of 320 nK and 120 nK together with calculated recombination rates from the spinless vdW model are shown in Fig. 3.11. Again the extraction of L_3 is limited by the technical limit, which for this Feshbach resonance calculated as $L_3^{\mathrm{min},120} \approx 2 \times 10^{-23}$ cm^6/s and $L_3^{\mathrm{min},320} \approx 2.5 \times 10^{-25}$ cm^6/s. In terms of scattering length this limit corresponds to $|a_{\mathrm{LiCs}}| \gtrsim 1000\ a_0$ for our data at 120 nK and $|a_{\mathrm{LiCs}}| \gtrsim 400\ a_0$ for the data at a temperature of 320 nK. The given loss rates in this region represent an upper bound of the actual L_3, which is indicated by error bars extending to zero.

Here, only two Cs-Cs-Li Efimov resonances are observed, while the first recombination resonance is located at $a_{\mathrm{LiCs}} \approx -2000\ a_0$. This is about a factor of seven larger than in the case of negative a_{Cs} (see Fig. 3.10), which is consistent with the energy spectrum of the Efimov states (see lower panel of Fig. 3.11), where the most deeply bound state predissociates into a universal atom-dimer state before reaching the three-body continuum and hence does not generate a resonance at the scattering threshold. Such a behavior is already anticipated from the hyperspherical potentials obtained in the zero-range theory discussed in Sec. 3.2.1, where the existence of a Feshbach dimer

BB at positive intraspecies scattering lengths $a_{BB} > 0$ leads to a splitting into two Efimov branches asymptotically connecting to the three-atom and atom-dimer channels. The lowest Efimov state is situated in the lower branch and therefore dissociates into the $BB+X$ channel as $|a|$ is lowered. Therefore, we assign the first recombination feature to the first excited Efimov resonance and label it by $a_-^{(1)}$.

The calculated recombination spectra from the vdW model show qualitative agreement with the experimental observations. However, a shift between the experimental and theoretical resonance positions will require more detailed analysis and may be due to the multichannel nature of the employed FR [Wang and Julienne, 2014; Sørensen et al., 2012] for tuning a_{LiCs}. It is shown that significant deviation of the Efimov resonance positions from the spinless vdW theory has been observed near a FR with s_{res} about 35 times smaller than those in our current cases [Johansen et al., 2017]. However, the resonance positions obtained from the energy spectra (grayed areas) coincide very well with the experimental observations. Acharya et al. [2016] recently studied within the framework of an effective-field-theory corrections due to finite effective range and intraspecies scattering length on three-body recombination rates and Efimov resonance positions.

At a scattering length of $a_{\mathrm{LiCs}} \approx -1200\ a_0 \approx 0.6a_-^{(1)}$ we observe a slight increase in the three-body recombination rate indicated by arrows in Fig. 3.11. This increase might be a signature of a four-body Efimov resonance, which are predicted to appear at $0.55a_-^{(n)}$ and $0.91a_-^{(n)}$ [Blume and Yan, 2014]. The second feature would already be masked by the three-body Efimov resonance and might lead to an additional broadening of the resonant feature. However, the four-body resonance can not be unambiguously verified, since inclusion of corresponding Cs-Cs-Cs-Li loss rates in the coupled differential equations (3.38) and (3.39) did not improve the fitting of the observed loss curves and did not show any resonance features in the corresponding loss rate constant.

3.4.3. Efimov resonance positions and scaling factors

One of the most important properties of Efimov physics is the discrete scale invariance, which reflects itself in a geometric progression of the Efimov resonance positions. Therefore, we extract Efimov resonance positions $a_-^{(n)}$ and Efimov period dependent scaling factors $\lambda^{(n)} = a_-^{(n)}/a_-^{(n-1)}$ by four different methods:

1. The experimental resonance positions $\mathrm{B}_{\mathrm{exp}}^{(n)}$ are obtained by fitting a Gaussian profile with linear background to the three-body loss rate $L_3(\mathrm{B})$ and conversion to scattering length $a_{-,\mathrm{exp}}^{(n)}$ via the parametrization given in Tab. 2.1. Here the uncertainty consists of statistical, systematic and conversion errors.

2. The whole $L_3(\mathrm{B})$ spectrum in case of $a_{\mathrm{Cs}} < 0$, i.e. close to the 843 G Li-Cs FR, is fitted with the universal zero-range theory presented in Sec. 3.2.2 and the

three-body parameter R_0 as well as the inelasitcity parameter η are extracted, see Fig. 3.9. The resonance positions $a_{-,\mathrm{zr}}^{(n)}$ are obtained by fixing R_0 to the fitted value and setting the temperature T and inelasticity parameter η in the theory equal to zero and reading off the positions of the maxima in L_3. By this, finite temperature effects in their determination can be eliminated.

3. For the case of positive $a_{\mathrm{Cs}} > 0$, as it is the case around the 889 G Li-Cs FR, the resonance positions $a_{-,\mathrm{zr}}^{(n)}$ are calculated from the zero range model described in Sec. 3.2.1. We find the energy levels of the upper branch adiabatic hyperspherical potential curves (see Fig. 3.4) and search for the values of $a_{\mathrm{LiCs}}/a_{\mathrm{Cs}}$ where their energy intersects zero. The two largest ratios are determined to be -8.36 and -44.7. We calculate the resonance positions by the specific dependence of $a_{\mathrm{LiCs}}(a_{\mathrm{Cs}})$ close to the 889 G FR determined by the Li-Cs Feshbach resonance parameters given in Tab. 2.1 and the magnetic field dependent a_{Cs} given by Berninger et al. [2013a]. As opposed to the negative intraspecies scattering length case, there is no three-body parameter necessary.

4. The calculated trimer energy spectrum from the spinless vdW theory is employed to extract $a_{-,\mathrm{vdW}}^{(n)}$ as the average value of the two numerical grid points, between which the three-body state merges with the scattering continuum (see grayed areas in Fig. 3.10 and 3.11). The uncertainty is given by one-half of the step size of the local grid. In this way the influence of finite temperature can be safely neglected, since it modifies the three-body recombination rates, but not the energy spectrum below the scattering continuum.

For comparison, the resonance positions $a_{-}^{(n)}$ and scaling factors $\lambda^{(n)}$ obtained from experiment, both zero-range theories, and the spinless vdW theory are listed in Table 3.1.

843 G FR, $a_{\mathrm{Cs}} < 0$

Close to the 843 G Li-Cs FR, the experimental and vdW value of $a_{-}^{(0)}$ agree very well, while the zero-range theory deviates and predicts a much larger value. This deviation can be attributed to short-range effects and was observed as a deviation between the zero-range theory and the measured recombination rates for the ground state resonance in Fig. 3.10. Such a discrepancy in the zero-range model is not surprising since the scattering length of the ground state resonance is only a factor of 3.5 and 8 times larger than the Cs-Cs and Li-Cs van der Waals lengths $|a_{-}^{(0)}| \approx 3.5 r_{\mathrm{vdW}}^{\mathrm{Cs}} \approx 8 r_{\mathrm{vdW}}^{\mathrm{LiCs}}$ and thus, the influence of the molecular potentials can not be neglected. Therefore, the scaling factor from the spinless vdW model is larger by about 4% compared to the zero-range theory. An even larger deviation of about 7% is found when comparing to the zero-range theory for noninteracting bosons ($a_{BB} = 0$) [Braaten and Hammer, 2006; Helfrich et al., 2010]. The experiment gives an even larger value for $\lambda^{(1)}$ due to the larger value of $a_{-,\mathrm{exp}}^{(1)}$ in comparison to the zero-range and vdW models. Possible reasons for this discrepancy are the choice of the fitting function, which might not be appropriate and influence the fitted resonance position.

On the other hand, the vdW and zero-range theories predict a similar scaling factor between the first and second excited Efimov states $\lambda^{(2)}$, highlighting a behavior of the Cs-Cs-Li system that is independent of short-range effects in the limit of large $|a_{\mathrm{LiCs}}| \to \infty$. Here, a deviation from the universal scaling factor of approx. 4.88 [Braaten and Hammer, 2006; Helfrich et al., 2010; Helfrich and Hammer, 2010], assuming resonant interspecies interactions $|a_{\mathrm{LiCs}}| \to \infty$ and a negligible intraspecies scattering length $a_{\mathrm{Cs}} \to 0$, is already present in the universal zero-range theory. On the one hand, the condition $a_{\mathrm{LiCs}} \gg r_{\mathrm{vdW}}^{\mathrm{Cs/LiCs}}$ is well fulfilled, but the inter- and intraspecies scattering lengths are on the same order of magnitude. Furthermore, between the two Efimov resonances a_{Cs} changes by approx. 4% from -1490 a_0 to -1550 a_0 [Berninger et al., 2013a]. Thus, the non-zero and non-constant Cs-Cs scattering length has to be taken into account, which leads to a deviation from the universal scaling factor of 4.88 even in the zero-range theory.

The experimental values of $a_-^{(1)}$ and $a_-^{(2)}$ are consistent with the theories within their uncertainties. However, they should be taken with care, since they were determined by fitting a phenomenological peak function (Gaussian distribution with linear background). It is not clear how the choice of the fitting function influences the resulting resonance positions and scaling factors. In addition, the experimental positions might be influenced by finite temperature and the unitary limit, which both lead to a shift in the maximum position of the three-body loss rate. Thus, a comparison to the zero-temperature results from both theories is difficult.

889 G FR, $a_{\mathrm{Cs}} < 0$

In the vicinity of the 889 G Li-Cs FR we only observe two resonant Efimov features. As explained by both the zero-range theory (Sec. 3.2.1) and the spinless van der Waals theory (Sec. 3.2.3), the lowest Efimov state predissociates into the CsCs+Li channel before reaching the three-body threshold and hence does not lead to a three-body recombination resonance. For the higher lying resonances, we expect the system to be in the resonant limit, in which a_{LiCs} is by far the largest length scale. Here, $|a_{\mathrm{LiCs}}| \gtrsim 2000\ a_0$ is much larger than the van der Waals scales $a_{\mathrm{LiCs}} \gg r_{\mathrm{vdW}}^{\mathrm{Cs/LiCs}}$ and the intraspecies scattering length $a_{\mathrm{Cs}} \approx +190\ a_0$. Thus, we expect the system to possess a scaling factor close to 4.88 [Braaten and Hammer, 2006; Helfrich et al., 2010; Helfrich and Hammer, 2010], which is predicted in case of only two resonant interactions.

FR	n	$B_{\mathrm{exp}}^{(n)}$ (G)	$a_{-,\mathrm{exp}}^{(n)}$ (a_0)	$\lambda_{\mathrm{exp}}^{(n)}$	$a_{-,\mathrm{zr}}^{(n)}$ (a_0)	$\lambda_{\mathrm{zr}}^{(n)}$	$a_{-,\mathrm{vdW}}^{(n)}$ (a_0)	$\lambda_{\mathrm{vdW}}^{(n)}$
843 G	0	848.90(6)(3)*	-311(3)(1)(1)	-	-350†	-	-317(3)	-
	1	843.772(10)(16)	-1840(20)(30)(40)	5.9(1)(1)(1)	-1777†	5.08†	-1680(20)	5.3(1)
	2	843.040(10)(16)	-8140(380)(620)(880)	4.4(2)(3)(4)	-9210†	5.18†	-8570(250)	5.1(2)
889 G	1	889.389(4)(16)	-2130(10)(40)(70)	-	-1670§	-	-2150(50)	-
	2	888.787(4)(16)	-8170(160)(620)(890)	3.8(1)(3)(3)	-8200§	4.91§	-8500(500)	4.0(3)

---

[*] Fit to the L_3 spectrum at a temperature of 450 nK.

[†] Obtained from zero-range model presented in Sec. 3.2.2.

[§] Obtained from zero-range model with positive intraspecies scattering length presented in Sec. 3.2.1.

Table 3.1.: Cs-Cs-Li Efimov resonance positions $a_-^{(n)}$ and scaling factors $\lambda^{(n)} = a_-^{(n)}/a_-^{(n-1)}$ for the 843 G Li-Cs FR (upper lines) and the 889 G FR (lower lines) obtained by three different methods. The experimental positions $B_{\mathrm{exp}}^{(n)}$ are extracted by fitting a Gaussian profile with linear background to the three-body loss rate L_3(B) and conversion to scattering length $a_{-,\mathrm{exp}}^{(n)}$ via the parametrization given in Tab. 2.1. The values in brackets represent the statistical, systematic and conversion error. The theoretical values are extracted from the universal zero-range theory in Fig. 3.9 (843 G FR), the zero-range theory described in Sec. 3.2.1 (889 G FR) and the spinless vdW model. The values for the vdW model are extracted from trimer energy spectra (see lower panels of Fig. 3.10 and 3.11) and the quantities in the parentheses represent their uncertainty. Details are given in the text.

The experimental and vdW position of the first excited Efimov resonance $a_-^{(1)}$ close to the 889 G FR are shifted by $\approx$ 300 a_0 with respect to the 843 G FR, while it is nearly unchanged in the zero-range theory. The resonance positions $a_-^{(2)}$ extracted by all three methods agree very well with each other and are almost the same as for the negative a_{Cs} case. The deviation in $a_{-,zr}^{(1)}$ may be explained by neglect of nonadiabatic couplings in our single-channel zero-range theory. Additionally, the binding energy of the Cs_2 dimer is not reproduced in this model by disregard of effective range corrections. However, the quantitative influence of these limitations requires further detailed analysis. The scaling factor obtained from the zero-range theory agrees very well with the theoretically predicted scaling factor of 4.88 between consecutive Cs-Cs-Li Efimov resonances. The obtained scaling factors from experiment and vdW theory of 3.8(1)(3)(3) and 4.0(3) between the two excited Efimov resonances clearly deviate from the universal zero-range theory. The remarkably good agreement between zero-range and spinless vdW theory suggests, that indeed the boson-boson scattering length can serve as a three-body parameter even if the intraspecies scattering length is only a factor of two larger than the van der Waals range $a_{\mathrm{Cs}} \approx 2r_{\mathrm{vdW}}^{\mathrm{Cs}}$. The occurrence of a potential barrier in the hyperspherical potentials at approximately $R \approx 2a_{\mathrm{Cs}}$ prevents the system to probe the non-universal interaction potential at short range.

3.4.4. Scaling laws of three-body recombination rates

Besides the study and evidence of Efimov resonances, three-body recombination is an undesirable loss mechanism that limits the lifetime and stability of ultracold quantum gases. Therefore, it is crucial to research the absolute size of the loss rate as well as its dependence on the scattering lengths. The scaling behavior of three-body recombination in a heteronuclear system is expected to drastically depend on the sign and magnitude of the intra- and interspecies scattering lengths [D'Incao and Esry, 2009]. We study this behavior by comparing the three-body recombination spectra close to the 843 G and 889 G Li-Cs FRs for temperatures of 450 nK and 320 nK in Fig. 3.12. They feature approximate power law scaling behaviors with the scattering lengths a_{LiCs} and a_{Cs}, which qualitatively agree with the expected scaling laws near overlapping Feshbach resonances [D'Incao and Esry, 2009]. In certain ranges of a_{LiCs} each of the loss rate spectra corresponds to one of two distinct cases of three-body scattering: The one near the 889 G FR can be characterized by $|a_{\mathrm{LiCs}}| \gg a_{\mathrm{Cs}} \approx 190\ a_0$ for which $L_3 \propto a_{\mathrm{LiCs}}^4$ is expected, whereas the one near the 843 G FR for small a_{LiCs} approximately corresponds to the case of $|a_{\mathrm{LiCs}}| \ll |a_{\mathrm{Cs}}| \approx 1500\ a_0$ with an expected scaling of $L_3 \propto a_{\mathrm{LiCs}}^2 a_{\mathrm{Cs}}^2$ [D'Incao and Esry, 2009]. The scaling laws can be explained by tunneling trough effective three-body potential barriers within a simple Wentzel–Kramers–Brillouin (WKB) model. The power laws are displayed in the respective range in Fig. 3.12 as a guide to the eye. Since the experimentally employed

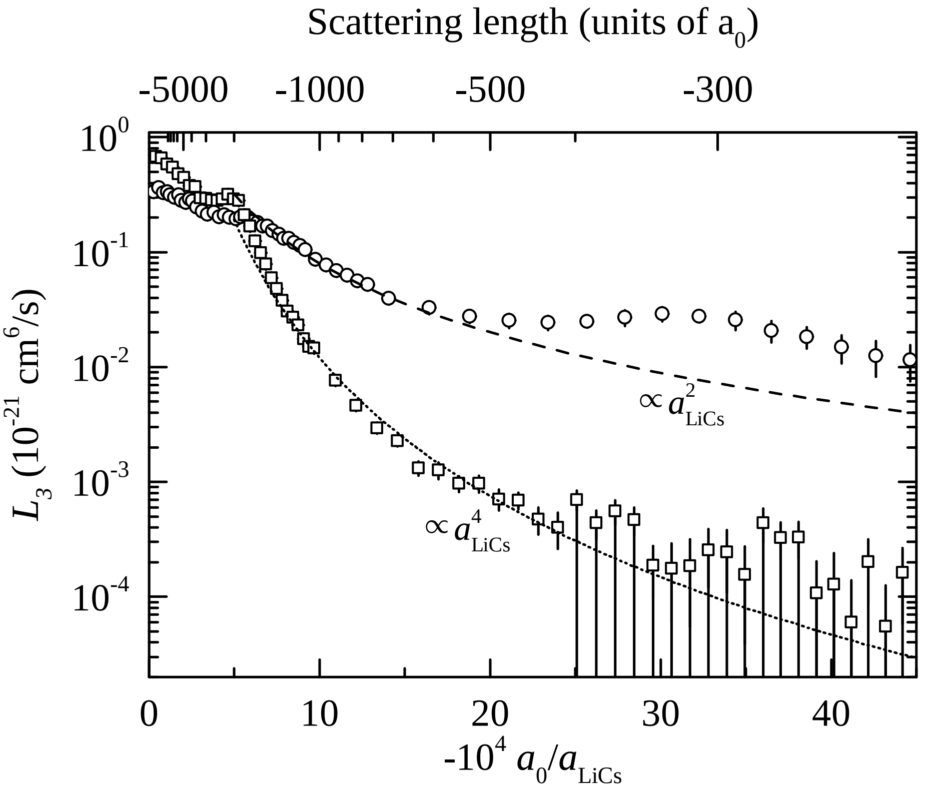

Figure 3.12.: Cs-Cs-Li three-body recombination rate spectra with positive (squares) and negative (circles) intraspecies interaction. The power laws $\propto a_{\mathrm{LiCs}}^4$ (dotted line) and $\propto a_{\mathrm{LiCs}}^2$ (dashed line) are drawn as guides to the eye. The error bars represent the statistical errors from bootstrapping, magnetic field uncertainties, and technical limit due to Cs-Cs-Cs three-body losses. The data were taken close to the 889 G Li-Cs Feshbach resonance at a temperature of 320 nK, where $a_{\mathrm{Cs}} \approx +190\, a_0$, and close to the 843 G Li-Cs Feshbach resonance at a temperature of 450 nK, where $a_{\mathrm{Cs}} \approx -1500\, a_0$. Figure reproduced from Häfner et al. [2017].

scattering lengths only approximately capture the inequalities imposed by the theory, especially in case of the 843 G FR, the power laws can only approximately recover the behavior of the actual Li-Cs system. Close to the pole of the FR the theoretical scaling does not apply anymore due to the unitary limit.

The shown power law for the 843 G FR does not account for varying a_{Cs}, which is tuned simultaneously with the magnetic field and changes by approximately a factor of 1.5 for the experimentally employed Feshbach resonance (see Fig. 2.9). For example, in the case of the 843 G Li-Cs Feshbach resonance, far away from the resonance the inequality $|a_{\mathrm{LiCs}}| \ll |a_{\mathrm{Cs}}|$ is fulfilled, whereas close to the pole of the resonance, the opposite is true, i.e. $|a_{\mathrm{LiCs}}| \gg |a_{\mathrm{Cs}}|$. In principle this should be reflected in a qualitative change in the power law from $L_3 \propto a_{\mathrm{LiCs}}^2 a_{\mathrm{Cs}}^2$ to $L_3 \propto a_{\mathrm{LiCs}}^4$ for small to large scattering lengths, respectively. Such a transition in the present data is masked by finite-temperature and short-range effects. However, it might become observable in samples with further reduced temperature. Similar behavior can be found in the universal zero-range theory with finite intraspecies scattering length [Petrov and Werner, 2015] and formalisms based on optical potentials [Mikkelsen et al., 2015].

The different observed power laws enable us to manipulate the three-body loss in a heteronuclear system. By choosing an appropriate FR, we can control the intraspecies scattering length between the heavy bosons and by this drastically influence the three-body loss rate. For scattering lengths $|a_{\mathrm{LiCs}}| \lesssim 500\ a_0$ the Cs-Cs-Li losses are reduced by approximately two orders of magnitude when changing from large and negative to small and postive intraspecies scattering lengths, paving the way to produce long-lived strongly-interacting Bose-Fermi mixtures.

Summary

In summary, we have observed in total five Efimov resonances in an ultracold mixture of Cs and Li atoms. The measurements have been performed in the vicinity of two Li-Cs Feshbach resonances, which are characterized by different sign and magnitude of the intraspecies scattering length a_{Cs}. For the 843 G FR, we have found for the first time a series of three consecutive Efimov resonances, which allowed to test the universality of the Efimov scenario. By detailed analysis and comparison to our measurements at the 889 G Li-Cs FR we confirm the decisive influence of the intraspecies scattering length on the heteronuclear Efimov effect. Experimentally, it manifests itself in resonance shifts and disappearance of Efimov resonances at the three-body scattering threshold.

Our experimental observations of Efimov resonances in a BBX system are analyzed with help of two different models: the universal zero-range theory and the spinless van der Waals theory. Within the hyperspherical adiabatic zero-range theory two qualitatively distinct cases of the heteronuclear Efimov scenario were shown. In case of $a_{BB} < 0$ we expect the original Efimov scenario with an infinite number of log-periodically spaced three-body states. However, the changing non-zero intraspecies scattering length leads to deviations of the Efimov scaling factor from its universal value. In addition, experiment-theory deviations are observed for the resonance of the Efimov ground state, since here the universal condition $|a| \gg r_0$ is not well fulfilled.

For positive intraspecies scattering lengths $a_{BB} > 0$ we find a considerably different situation. The existence of a weakly bound dimer BB splits the adiabatic hyperspherical potentials into two Efimov branches. Efimov states situated in the lower potential branch may not lead to Efimov resonances in the $B + B + X$ channel as observed in our measured three-body recombination rate spectra. For the upper branch a universal potential barrier at $R \approx 2a_{BB}$ makes the introduction of an artificial three-body parameter superfluous and allows for the determination of Efimov resonance positions.

However, the applied adiabatic approximation and the neglect of effective range corrections may effect the observed deviations from the experimentally determined resonance positions.

An encouraging level of understanding of the heteronuclear Efimov effect is provided by the spinless van der Waals theory in the adiabatic hyperspherical approximation, for both positive and negative intraspecies scattering lengths. We find excellent agreement between experiment and theory for negative a_{Cs}. For positive intraspecies interactions a good agreement between the observed resonances and the energy spectrum is observed. However, a shift between experimental and theoretical three-body recombination rates demands further analysis and may be due to the multichannel character of the Feshbach resonance. No Efimov resonance which can be assigned to the Efimov ground state is observed at the Cs+Cs+Li threshold for positive a_{Cs}. Before reaching the three-body continuum the most deeply bound state dissociates at the atom-dimer threshold.

Away from the two Li-Cs FRs we observe power law scalings of the three-body recombination rates, which can be attributed to two distinct cases of overlapping Feshbach resonances. We are able to suppress the three-body loss by up to two orders of magnitude via choosing a different Li-Cs Feshbach resonance and thus drastically increase the lifetime of the Bose-Fermi mixture.

Many

4

What happens if we add a fourth, fifth, ..., *many* particles to our system?

By adding more and more Cs atoms to the existing Cs_2Li state, larger and larger aggregates are formed. It was predicted that universal $B_{N-1}X$ states exist for system sizes of up to $N = 6$ [Wang et al., 2012b; Blume and Yan, 2014]. These cluster states are tied to Efimov states and are formed by attaching further particles to already existing trimer states. In homonuclear systems such universal four- and five-body states were observed in an ultracold ^{133}Cs gas [Ferlaino et al., 2009; Zenesini et al., 2013], while the observation in heteronuclear systems remains unsettled, although indications of a four-body resonance can be seen in Fig. 3.11.

When adding even more particles to the system, we arrive at the *many*-body scenario. In contrast to few-body systems, where it is possible to describe the behavior of each individual particle, in such systems any attempt of a microscopic description fails due to the large number of degrees of freedom. Instead, a different approach is taken by describing the system through its collective properties. It is an intriguing question how the many-body limit emerges from the few-body scenario. This transition was studied by immersing a single impurity in a one dimensional Fermi sea in which the atom number was varied by adding majority atoms one by one. Remarkably, the system already behaves as a many-body system in case of four particles in the Fermi sea [Wenz et al., 2013].

The behavior of a single impurity that is interacting with a many-body environment is an important paradigm of many-body quantum physics. The so-called impurity problem represents a simplified, yet highly nontrivial approach to many-body physics. When studying the movement of electrons in a polarizable medium, Landau and Pekar proposed to describe its properties by a quasi-particle termed *polaron* [Landau, 1933; Pekar, 1946; Landau and Pekar, 1948]. This quasi-particle can be understood as the interaction of the electron with the lattice phonons of the medium. The idea of the polaron has been elaborated on by Fröhlich, Feynman, and Holstein [Fröhlich, 1954; Feynman, 1955; Holstein, 1959a,b], describing the medium as a phononic bath. Immediate connections can be found to many other systems, such as ^3He impurities immersed in a ^4He bath [Baym and Pethick, 1991], and are of major interest for the understanding of solid state materials, such as ionic crystals and polar semiconductors [Mahan, 2000; Alexandrov, 2007; Alexandrov and Devreese, 2009; Devreese and Alexandrov, 2009; Devreese, 1972; Bogolubov and Bogolubov, 2000], and high temperature superconductivity [Dagotto, 1994]. Furthermore, the concept of a "dressed" impurity plays an important role in the understanding of conducting polymers [Bredas and Street, 1985] and charge transport in DNA [Conwell, 2005].

In ultracold atomic gases the impurity problem can be studied by immersing single impurities in either a Bose [Cucchietti and Timmermans, 2006; Tempere et al., 2009] or Fermi [Prokofev and Svistunov, 2008] gas, commonly referred to as *Bose* and *Fermi* polaron. Their realization in ultracold atoms with their tunable two-body interaction strength opens the possibility to access the strongly interacting regime, which is not possible in condensed matter systems [Devreese, 2007]. While the latter one has been extensively studied in experiments [Schirotzek et al., 2009; Koschorreck et al., 2012; Nascimbène et al., 2009; Kohstall et al., 2012; Cetina et al., 2016; Laurent et al., 2017], revealing both the attractive and repulsive polaron branches at tunable impurity bath interaction strength as well as the dynamics of the quantum impurities, the Bose polaron could only be observed recently by two groups in Aarhus [Jørgensen et al., 2016] and JILA [Hu et al., 2016].

In this chapter, we focus on the study of a low density Li gas interacting with a bosonic Cs gas. This scenario is reminiscent of the Bose polaron from solid state physics. We introduce the Bose polaron in the context of ultracold atoms and its connection to the few-body Efimov effect. In Sec. 4.1.1 we present our first attempt in the observation of the attractive Bose polaron in Li-Cs. We propose several changes in the experiment in order to experimentally realize the Bose polaron in Sec. 4.1.2. Further possible directions of many-body physics in the Li-Cs system are discussed in Sec. 4.2.

4.1. The Bose polaron and the Efimov effect

The impurity problem, in which the behavior of a single particle moving through a medium is studied, constitutes an intriguing topic of many-body physics. The physical properties of the polaron, namely its self-energy E_{pol}, effective mass m^*, and its mobility [Devreese and Alexandrov, 2009], are different from those of the bare impurity due to the interaction of the impurity with its self-induced polarization of the medium. In the 1950s, Fröhlich introduced the effective Hamiltonian, describing the behavior of an electron in a crystal lattice [Fröhlich, 1954]

$$H = \frac{\mathbf{p}^2}{2m_i} + \int d^3\mathbf{k}\,\omega_k \hat{a}^\dagger_{\mathbf{k}} \hat{a}_{\mathbf{k}} + \int d^3\mathbf{k}\, V_{\mathbf{k}} e^{i\mathbf{k}\;\mathbf{r}} \left(\hat{a}_{\mathbf{k}} + \hat{a}^\dagger_{-\mathbf{k}}\right), \tag{4.1}$$

which is nowadays called Fröhlich Hamiltonian. Here, $\mathbf{r}$ and $\mathbf{p}$ denote the position and momentum operators of the impurity with mass m_i. $\hat{a}^\dagger_{\mathbf{k}}$ and $\hat{a}_{\mathbf{k}}$ are the creation and annihilation operators of phonons with wavevector $\mathbf{k}$ and energy $\hbar\omega_k$. The impurity-phonon interaction is contained in the coupling constants $V_{\mathbf{k}}$ in the last term of the Hamiltonian. Depending on the impurity mass m_i and the impurity-phonon coupling strength the polaron in the Fröhlich model shows distinct behavior. For weak interactions, the polaron can be seen as a nearly free impurity loosely dressed by a screening cloud of phonons. This regime was first studied in a mean-field theory by Lee, Low and Pines [Lee et al., 1953] and is nowadays termed Fröhlich polaron. In the strong-coupling limit the impurity becomes self-trapped by its self-induced phonon cloud that was first studied by Landau and Pekar in an adiabatic approximation [Pekar, 1946; Landau and Pekar, 1948]. This situation is called Landau-Pekar polaron.

The possibility to tune the interaction in ultracold atomic systems has generated considerable interest in the study of the polaron problem. In these system the interaction of impurities with the excitations of a Bose gase, i.e. the Bogoliubov modes in a BEC, is an analog to the Fröhlich polaron described by Eq. (4.1) [Cucchietti and Timmermans, 2006; Sacha and Timmermans, 2006; Tempere et al., 2009].

In recent years, the so-called Bose polaron has been studied theoretically in great detail [Astrakharchik and Pitaevskii, 2004; Kalas and Blume, 2006; Grusdt and Demler, 2016; Christensen et al., 2015; Blinova et al., 2013] and has been extended to strong couplings where effects beyond the Fröhlich model are predicted [Rath and Schmidt, 2013; Li and Das Sarma, 2014; Ardila and Giorgini, 2015; Grusdt et al., 2017]. First experiments in ultracold atoms on the impurity problem have been limited to special cases, e.g. impurities in optical lattices [Ospelkaus et al., 2006b], single impurity interacting with an uncondensed Bose gas [Spethmann et al., 2012], localized impurities in a BEC [Scelle et al., 2013; Marti et al., 2014; Rentrop et al., 2016], and ions or electrons trapped and coupled to a BEC [Scelle et al., 2013; Marti et al., 2014; Rentrop et al., 2016]. In 2016, two groups almost simultaneously achieved the observation of a mobile impurity inside a BEC [Jørgensen et al., 2016; Hu et al., 2016]. By means of radio-frequency spectroscopy on the impurity atoms, they were able to detect the polaron energy for both attractive and repulsive interactions and from weak to strong coupling strengths.

It is an intriguing question how the many-body polaron physics builds up from the few-body system. In the three-body system, studied in Ch. 3, we observed the existence of peculiar three-body bound states, the Efimov states. Thus, it is a natural question to ask if Efimov states persist even in the many-body environment and if they lead to manifestations in many-body observables. This idea was first introduced and studied by Levinsen et al. [2015]. Within a variational Ansatz, including the dressing of the impurity by one or two Bogoliubov excitations, strong alterations in the polaron spectrum due to the existence of three-body states were found. The energy of the many-body ground state is influenced by an avoided crossing between the Bose polaron state and a dressed Efimov state. At the same time the character of the many-body ground states displays a crossover from a quasiparticle-like to a trimer-like state.

However, the two recent experiments on the Bose polaron [Jørgensen et al., 2016; Hu et al., 2016] did not show any indication of few-body correlation in the radio-frequency spectra of the many-body system.

What are favorable conditions for the observation of Efimov phyics in the Bose polaron? To answer this question we have to compare the characteristic size of the Efimov state l_T to the the mean distance d between the bath atoms. The characteristic size of the n^{th} Efimov state is roughly given by half of the scattering length at the resonance position, i.e. $l_T \approx |a_-^{(n)}|/2$, and thus varies for each atomic species or mixture of species. The mean distance between the majority atoms can be tuned by the atomic density $d \propto n^{-1/3}$. Depending on the ratio l_T/d we subdivide the systems into three groups which are pictorially presented in Fig. 4.1:

(a) When $l_T \gg d$ there are many majority atoms "inside" the Efimov state. Thus, the three-body effect can be easily washed out by two-body interactions between the impurity atoms and the many majority atoms in close vicinity. Consequently, we do not expect any signature of three-body correlations in the many-body environment. This situation usually occurs for very shallow Efimov trimers, which only exist close to the two-body resonance.

(b) If $l_T \ll d$ all other bath atoms are on average far away from the atoms that are bound to the trimer. Thus, the Efimov state is isolated from the many-body system and we do not expect any mutual influence between few-body and many-body states [Zinner, 2014]. This situation may be fulfilled for either very deeply bound trimer states or at low atomic densities.

(c) In the transition regime $l_T \approx d$ the average distance of the majority atoms is comparable to the distance between the atoms of the trimer state. Here, we expect strong modifications of the binding energy and character of both the Efimov and the polaron state, e.g. due to avoided level crossings. For this case Sun et al. [2017] pointed out, that the Efimov states will show signatures in the spectral response of the many-body system.

From this argument it becomes clear, why the influence of the Efimov effect was not observed so far. The two previously studied systems of ^{39}K-^{39}K [Jørgensen et al., 2016] and ^{40}K-^{87}Rb [Hu et al., 2016] are characterized by large Efimov scaling factors λ and only shallow Efimov states exist. Thus, they correspond to case (a) for which we do not expect any signatures of few-body correlations in the many-body observables. Case (c), for which we expect strong signatures, however, is easily realized in Efimov favored systems, e.g. the experimentally well studied combinations ^{7}Li-^{87}Rb [Maier et al., 2015] and ^{6}Li-^{133}Cs, where the large mass imbalance drastically reduces the Efimov scaling factor λ, thus leading to a dense spectrum of Efimov states and a large

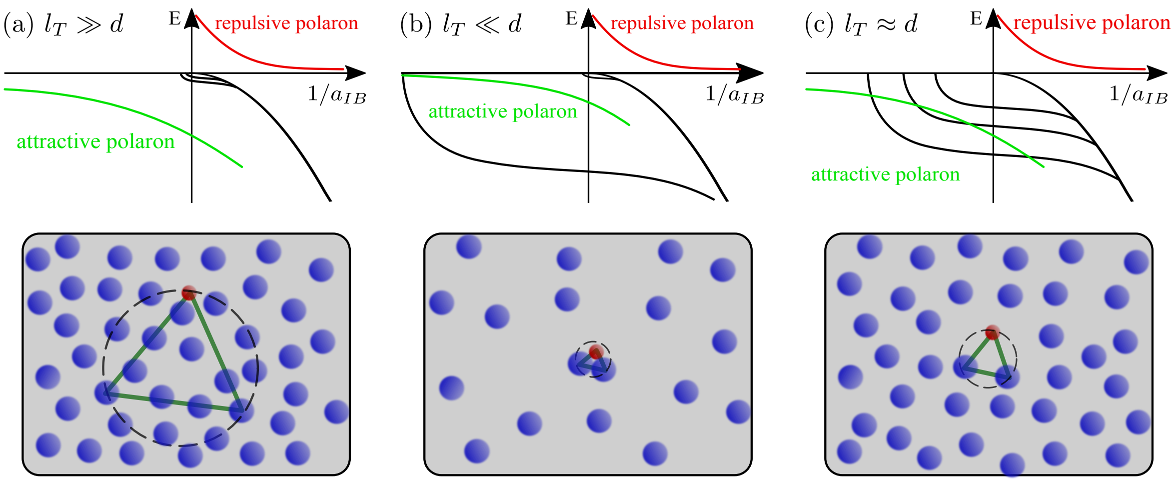

Figure 4.1.: The Bose polaron and the Efimov effect. The quasiparticle energy of the attractive (green line) and repulsive (red line) polaron in dependence of the impurity-boson interaction strength a_{IB} are pictorially shown together with the Efimov energy spectrum (black lines). We show the situation for three relative sizes of the Efimov trimer l_T and the average interpaticle spacing d between the majority atoms: (a) $l_T \gg d$: we do not expect sigantures of Efimov states in the many-body scenario, (b) $l_T \ll d$: the Efimov state is isloated from the many-body environment and thus we do not expect alterations in both the Efimov and polaron energies, and (c) $l_T \approx d$: the distance between the atoms in the trimer and to the majority atoms is comparable. We expect avoided level crossings between few- and many-body states and a large influence in the spectral response of the impurity atom is predicted [Levinsen et al., 2015; Sun et al., 2017; Sun and Cui, 2017].

binding energy of the ground state trimer. Hence, it is likely that one of the Efimov states fulfills the condition $l_T \approx d$ and manifests itself in the many-body spectrum.

A plot of the energy of the attractive polaron branch in Li-Cs versus the interaction strength is shown in Fig. 4.2 and compared to the binding energy of the first and second excited Efimov states in the vicinity of the 843 G Li-Cs Feshbach resonance (see lower panel of Fig. 3.10). The wavevector $k_n = (6\pi^2 n_{\mathrm{Cs}})^{1/3}$ and energy scale $E_n = \hbar^2 k_n^2/(2m_{\mathrm{Cs}})$ are defined by the atomic density of the Cs atoms, for which we assume $n_{\mathrm{Cs}} = 3 \times 10^{11}$ cm^{-3}. We estimate the self-energy E_{pol} of the Bose polaron by its mean-field energy

$$E_{\mathrm{MF}} = \frac{2\pi\hbar^2 n_{\mathrm{Cs}} a_{\mathrm{LiCs}}}{\mu}, \tag{4.2}$$

which describes the actual polaron energy very well in the limit of weak interactions $1/(k_n a_{\mathrm{LiCs}}) \to \pm\infty$ [Levinsen et al., 2015]. We find, that the polaron and first excited Efimov state intersect at $1/(k_n a_{\mathrm{LiCs}}) \approx -4$. The energy of the second excited Efimov trimer is very close to the mean-field polaron energy. However, for such strong inter-

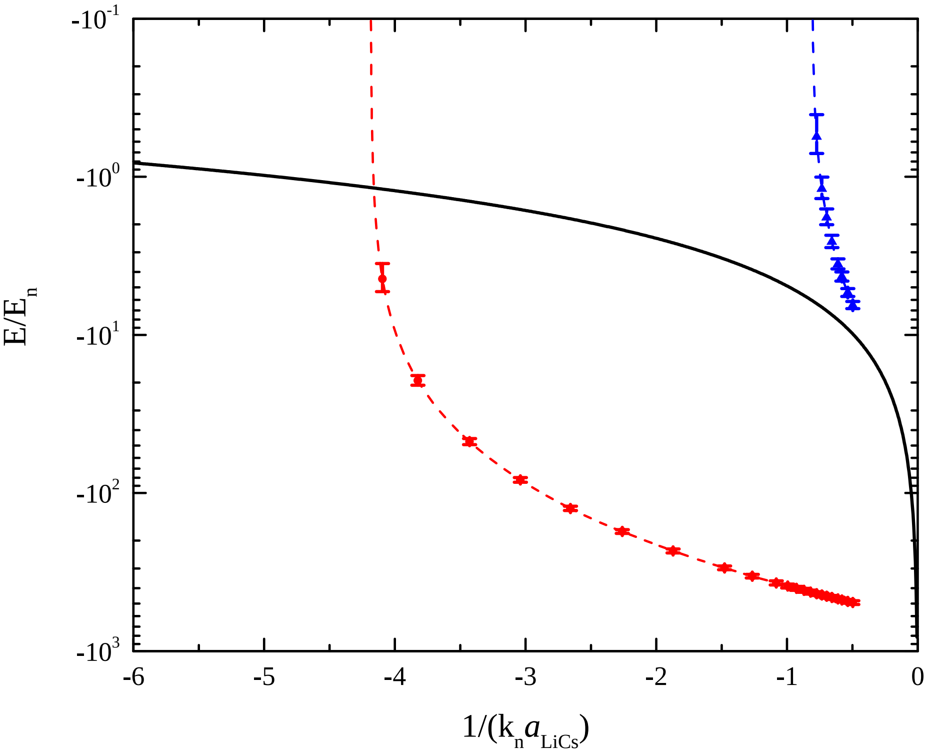

Figure 4.2.: Mean-field energy of the attractive Bose polaron (black solid line) and binding energy of the first (red) and second (blue) excited Efimov states close to the 843 G Li-Cs Feshbach resonance in dependence of the dimensionless interation parameter $1/(k_n a_{\mathrm{LiCs}})$. We assume an atomic Cs density of $n_{\mathrm{Cs}} = 3 \times 10^{11}$ cm^{-3} defining the wavevector $k_n = 3\ \mu\mathrm{m}^{-1}$ and respective energy scale $E_n = h \times 280$ Hz. The binding energy of the Efimov trimers is obtained from the spinless vdW model (Fig. 3.10) and the blue and red dashed lines are extrapolations of the calculated energies. The $\mathrm{Cs_2Li}$ ground Efimov state is out of the scale in this graph.

actions, we do not expect the mean-field approximation to be applicable and expect deviations of the polaron energy towards lower binding energies. Thus, there might be an additional crossing of these two states.

Within a high temperature virial expansion approach Sun and Cui [2017] calculated the spectral response of a ^{6}Li impurity inside an uncondensed gas of ^{133}Cs atoms. Besides the previously observed attractive and repulsive polaron branches signatures of Efimov states appear in the spectral response. These Efimov states can either undergo an avoided level crossing or come very close to the attractive polaron, thereby considerably altering the energy and width of the polaronic branches. Thus, it is highly desirable to study the manifestation of Efimov physics in the many-body system by an highly-mass imbalanced system such as ^{6}Li-^{133}Cs.

4.1.1. Radio-frequency spectroscopy in Li-Cs

Motivated by the predictions presented in the previous section, we perform radio-frequency spectroscopy on a small density ^{6}Li sample interacting with an uncondensed Bose gas of Cs atoms. The basic measurement procedure is shown in the inset of Fig. 4.3. We initially prepare the mixture in the non-interacting channel $|\beta\rangle{=}|1/2,-1/2\rangle{\oplus}|3,+3\rangle$ on the negative scattering length side of the 843 G Li-Cs Feshbach resonance. The spectral response of the ^{6}Li impurities is studied by spectroscopically probing their nuclear spin-flip transition with radio-frequency radiation and measuring the population in the interacting $|1/2,1/2\rangle$ state in dependence of the frequency. Signatures of the polaron are expected to be frequency (energy) shifted from the bare atomic transition of the Li impurity. In order to be able to observe the polaron the following conditions should be fulfilled:

- The frequency resolution of the rf-spectroscopy has to be large enough in order to clearly distinguish the polaron feature from the nuclear spin-flip transition of the bare Li atoms. The polaron is expected to have an energy shift E_{pol} with respect to the free-free transition at energy E_0. Due to the Fourier limit one requires the pulse length τ_{pulse} to be much longer than the time scale of the polaron $\tau_{pol} = \hbar/E_{pol}$.

- In addition we have to consider the lifetime τ_{loss} of the gas in the trap. This timescale is dominated by inter- and intraspecies three-body losses. We estimate τ_{loss} by the shortest of the timescales $1/(L_3 n_{\mathrm{Cs}}^2)$, $1/(L_3 n_{\mathrm{Li}} n_{\mathrm{Cs}})$, and $1/(L_3^{\mathrm{Cs}} n_{\mathrm{Cs}}^2)$, where we employ the magnetic field and temperature dependent three-body loss rates L_3 obtained in Ch. 3. τ_{loss} depends heavily on the magnetic field and the atomic densities of both species. The lifetime should be much longer than the pulse-length, which implies $\tau_{loss} \gg \tau_{pulse} \gg \tau_{pol} = \hbar/E_{pol}$.

- The concentration of the impurities needs to fulfill $n_{\mathrm{Li}}/n_{\mathrm{Cs}} \ll 1$ in order to be able to neglect interactions between the polarons. For impurity concentrations below 0.2 no effect of impurity interaction was observed by Cetina et al. [2016]. Furthermore, the impurities should not be quantum degenerate, such that one can consider them as single, independent particles.

The first condition can be fulfilled by applying rf-pulses with long pulse-length τ_{pulse}. In order to avoid side lobes (see Fig. 1.4) which may obscure a signal of the polaron, we apply rf-pulses that follow a Blackman shape [Blackman and Tukey, 1959]

$$\Omega(t) = \Omega_0 \left[0.42 + 0.5\cos\left(\frac{2\pi t}{\tau_{pulse}}\right) + 0.08\cos\left(\frac{4\pi t}{\tau_{pulse}}\right)\right] \text{ for } 0 \le t \le \tau_{pulse}, \qquad (4.3)$$

where Ω_0 is the maximum Rabi frequency. The other two conditions can be fulfilled by preparing the Li-Cs mixture at suitable densities and magnetic field.

We start our study by preparation of an ultracold mixture of 7×10^3 Li atoms in state $|1/2, -1/2\rangle$ and 6×10^3 Cs atoms in state $|3, +3\rangle$ at a temperature of 100 nK as described in Sec. 1.3.3. We calculate atomic peak densities of $n_{0,\mathrm{Li}} = 5 \times 10^{10}$ cm^{-3} and $n_{0,\mathrm{Cs}} = 3 \times 10^{11}$ cm^{-3} from which we obtain the wavevector $k_n = 3$ μm^{-1} and energy scale $E_n = h \times 280$ Hz. From the given temperature and densities we calculate $T/T_C \approx 4$ and $T/T_F \approx 2$ and thus both, the Bose gas and the Fermi gas, are far from quantum degeneracy. Furthermore, the impurity density is almost one order of magnitude smaller than that of the bosons, which allows to neglect interactions between them at such low impurity concentrations of $n_{\mathrm{Li}}/n_{\mathrm{Cs}} \approx 0.1$.

We choose a magnetic field of 844.20 G, which is slightly above the Efimov resonance position $B^{(1)}$ of the first excited Efimov trimer close to the 843 G resonance (cf. Table 3.1). Close to this point Sun and Cui [2017] predict the largest weight in the spectral response. At this magnetic field the interspecies scattering length amounts to $a_{\mathrm{LiCs}} \approx -1300\ a_0$ and we obtain the dimensionless interaction parameter $1/(k_n a_{\mathrm{LiCs}}) \approx -5$. For this scattering length and atomic densities we estimate a lifetime of $\tau_{loss} \approx 50$ ms and expect a polaron energy of roughly $E_{pol} \approx E_n = h \times 280$ Hz (see Fig. 4.2). Thus, we set the pulse-length to $\tau_{pulse} = 19.2$ ms, which corresponds to a 9π-pulse on the bare atomic transition, in order to fulfill the relation $\tau_{loss} > \tau_{pulse} > \tau_{pol} \approx 0.6$ ms.

We obtain radio-frequency spectra by recording the population of the Li atoms in the initially unoccupied, interacting $|1/2, 1/2\rangle$ state as a function of the frequency of the driving field. The obtained radio-frequency spectrum is shown in Fig. 4.3. At the frequency E_0/h of the Li nuclear spin-flip transition we transfer all of the Li atoms from the non-interacting state $|1/2, -1/2\rangle$ into the interacting state $|1/2, 1/2\rangle$. Thus, we observe a maximum in the number of Li atoms in state $|1/2, 1/2\rangle$. However, we do not notice any enhancement of the population in the state $|1/2, 1/2\rangle$ close to the expected polaron energy of $E_{\mathrm{rf}} - E_0 = E_{\mathrm{MF}} \approx E_n = h \times 280$ Hz, indicated by the arrow in Fig. 4.3. Experiments performed at different magnetic fields, i.e. different scattering length a_{LiCs}, pulse-length τ_{pulse}, and Rabi frequency Ω_0 of the radio-frequency pulse did not reveal any signatures of polarons so far. Thus, it remains an open question why the Bose polaron was not observed in the Li-Cs system. We discuss possible reasons in the following and suggest several prospects towards its observation.

In comparison to the observations in the combinations of ^{39}K-^{39}K [Jørgensen et al., 2016] and ^{40}K-^{87}Rb [Hu et al., 2016], we expect an even larger polaron energy due to the large mass imbalance. Furthermore, in our system the polaron feature should be much more pronounced, since the relative width in units of the binding energy are prediced to be much smaller [Sun and Cui, 2017]. However, the other experiments were performed with an impurity, which interacts with a BEC instead of a thermal

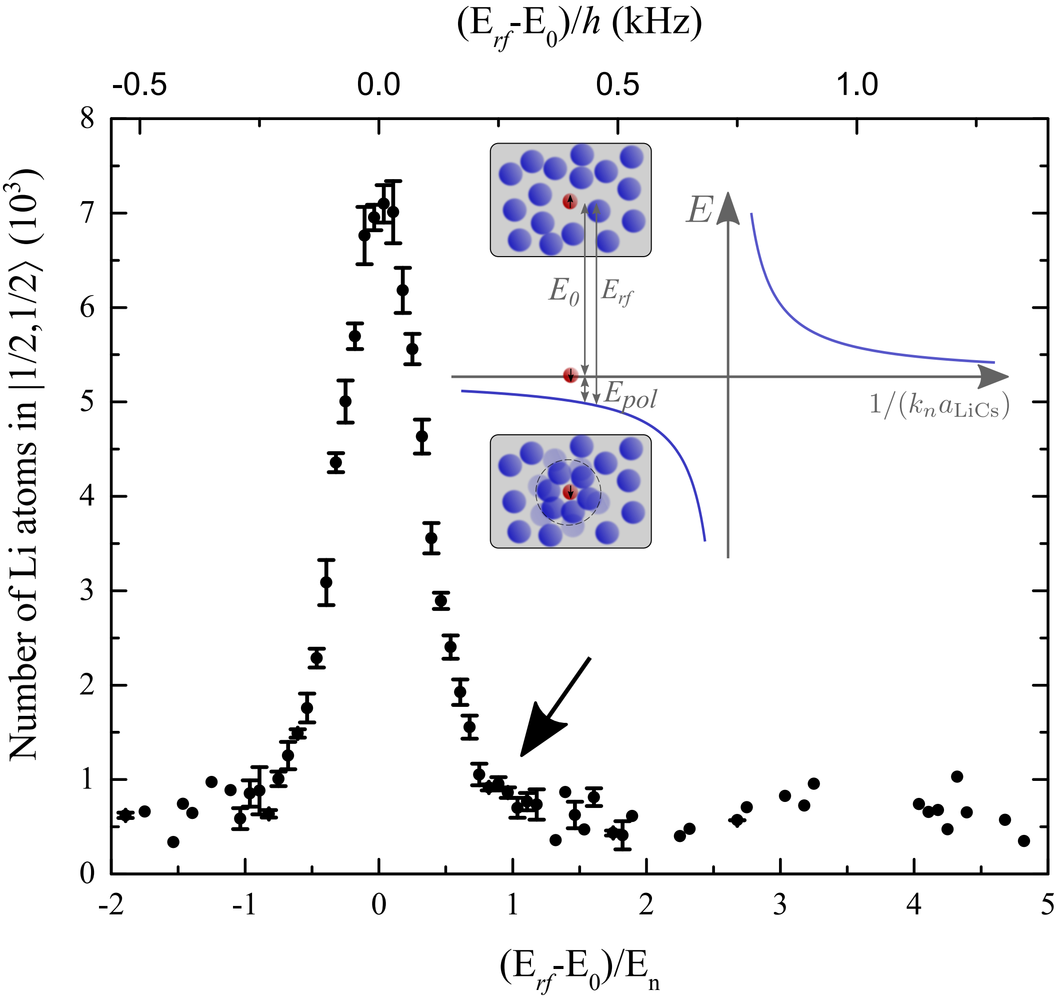

Figure 4.3.: Radio-frequency spectroscopy on Li atoms interacting with a uncondensed Cs gas: Number of Li atoms in state $|1/2, 1/2\rangle$ in dependence of the detuning $E_{\mathrm{rf}} - E_0$ from the nuclear spin-flip transition. The measurement is performed at a magnetic field 844.20 G, where $a_{\mathrm{LiCs}} \approx -1300\ a_0$ resulting in an interaction parameter of $1/(k_n a_{\mathrm{LiCs}}) \approx -5$ and energy scale $E_n \approx h \times 280$ Hz. The pulse-length of the Blackman-shaped rf-pulse amounts to 19.2 ms. We do not observe any feature at the expected polaron energy $E_{pol} \approx E_{\mathrm{MF}} \approx E_n$, which is indicated by the arrow. The inset shows the principle of the rf-spectroscopy, where the Li atoms are spin-flipped from the non-interacting into the interacting state at energy E_0 or into the polaron state with energy $E_0 + E_{pol}$.

gas, where the density of the bosonic bath is roughly three orders of magnitude higher than in our experiments. Thus, changes to our experimental setup or procedure are necessary in order to observe the Bose polaron.

4.1.2. Towards Bose polaron in Li-Cs

The Bose polaron has not been observed in our experiment so far. Thus we suggest the following improvements in order to experimentally study the Bose polaron.

Spatial overlap and gravitational sag A good spatial overlap of the two species is desired for the investigation of the Bose polaron via rf-spectroscopy. If the density distribution of the impurity atoms is much larger than that of the bath atoms, only a small part of the impurity atoms can form a polaron. Thus, the spectral weight in the rf-spectrum will be drastically reduced at the polaron energy $E_0 + E_{pol}$. On the other hand all of the impurity atoms can be spin-flipped at the energy E_0 and might obscure the polaron signal.

As pointed out in Sec. 1.3 and depicted in Fig. 1.16 our current bichromatic trapping scheme does lead to a situation where $\sigma_{i,\mathrm{Li}} > \sigma_{i,\mathrm{Cs}}$ and the gravitational sag between the Cs and Li atom clouds is not fully compensated. Due to the larger polarizability at the wavelengths of the two dipole traps with wavelengths of 1070 nm and 921 nm for Cs than for Li [see Fig. 1.13(a)], the width of the thermal Li cloud is larger than that of the Cs cloud. We have found previously that the width of the thermal density distribution scales as $\sigma_i \propto 1/\sqrt{\Re\alpha(\omega)}$. A further reduction in spatial overlap, and consequently in the rf-signal of the polaron, arises from the differential gravitational sag between the two species. In order to overcome these drawbacks, we suggest two changes in the bichromatic trapping scheme.

The beam waist of the optical dipole traps should be reduced along the direction of gravity. This will limit the influence of gravity onto the trapping potential on the extension of the dipole trap potential and consequently a smaller differential gravitational sag between Li and Cs will be present. Secondly, the wavelength of the tunable dipole trap should be changed to a wavelength, where it creates a repulsive potential for Cs atoms and an attractive potential for the Li atom, i.e. in the wavelength range between 671 nm and 852 nm. This will lead to a weakening of the Cs trapping potential in the horizontal direction and consequently to larger widths of the density distributions of the Cs atoms. At the same time, the gravitational sag can be overcome by positioning the tunable dipole trap slightly below the dimple trap at 1070 nm and thus “pushing” up the Cs atoms, while at the same time “pulling” down the Li atoms. The total potentials and density distributions for such a situation are shown in Fig. 4.4, where we give the parameters in the figure caption. This trapping scenario provides almost perfect compensation of the differential gravitational sag, while simultaneously the Cs potential is weakened in the horizontal directions, due to the blue detuning of the tunable dipole trap and thus the gas is expanded, resulting in similar widths of the density distribution of the Li and Cs atoms.

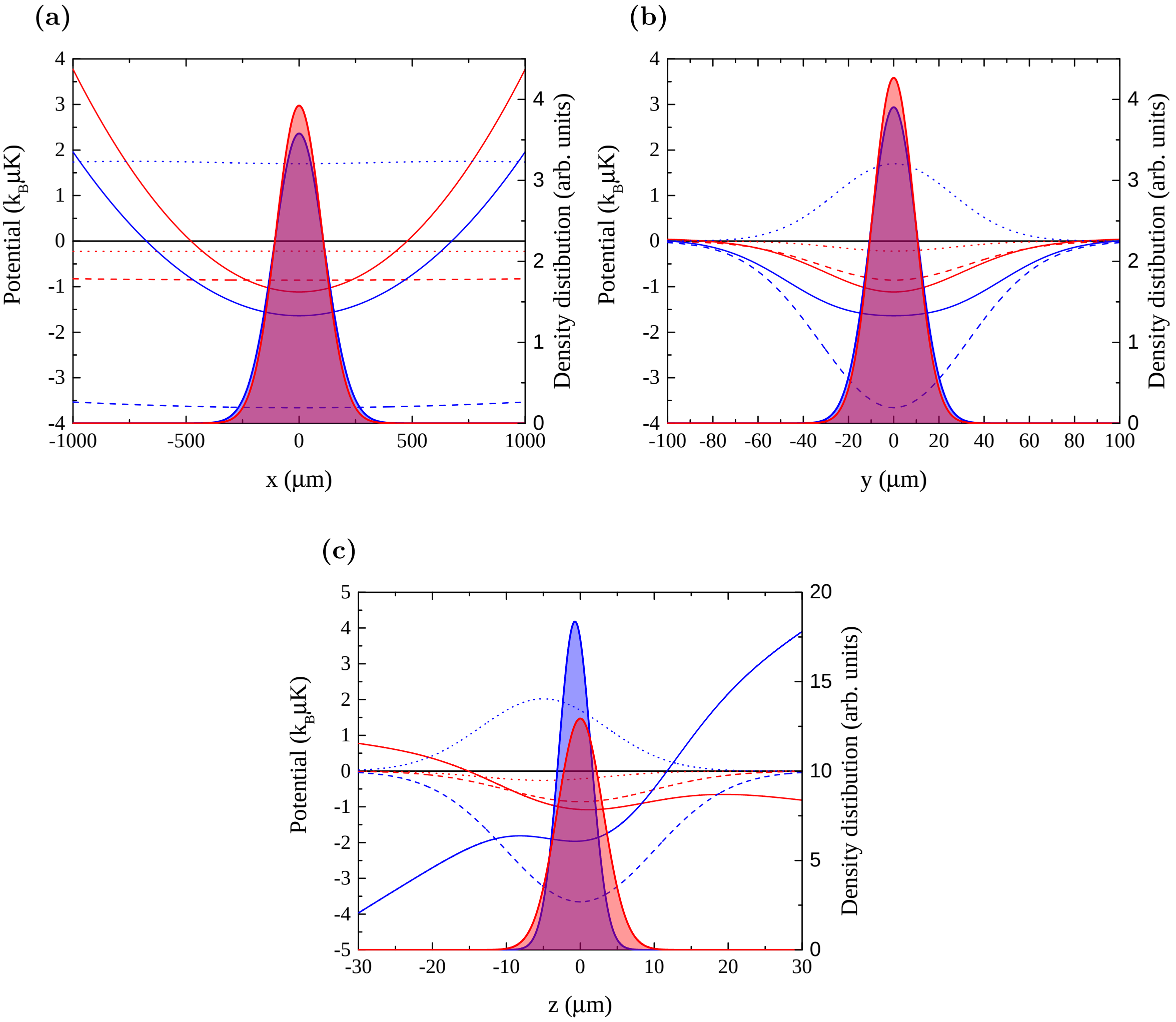

Figure 4.4.: Potentials and density distributions for Li (red) and Cs (blue) along the three axis defined in Fig. 1.14. Dashed lines represent the potential generated by the dimple trap, dotted lines are potentials of the tunable trap. The solid lines show the total potentials including optical, gravitational, magnetic confinement, and magnetic levitation potentials. For the plot we have chosen the following parameters: $P_{\mathrm{dimple}} = 40$ mW, beam waists $w_{y,\mathrm{dimple}} = 65$ μm and $w_{z,\mathrm{dimple}} = 20$ μm, $P_{\mathrm{tunable}} = 4$ mW, $w_{y,\mathrm{tunable}} = 52$ μm and $w_{z,\mathrm{tunable}} = 17$ μm, $\lambda_{\mathrm{tunable}} = 820$ nm, and a vertical displacement between dimple and tunable traps of 5 μm. The external magnetic field was set to 900 G, which provides the main confinement along the x-direction and a magnetic gradient field of $\partial B/\partial z = 5$ G/cm. The thermal density distributions (filled curves) are calculated for a temperature of 100 nK.

Inhomogeneous density distribution A further complication in the experiments results from the inhomogeneous density distribution of the Li and Cs atoms. Consequently the Li impurity atoms experience a position dependent density of the Cs bath atoms $n_{\mathrm{Cs}}(x, y, z)$, which in turn leads to a spatially varying polaron energy $E_{pol} \propto n_{\mathrm{Cs}}(x, y, z)$. In the rf-spectrum this will be reflected in a broadening around the polaron energy $E_0 + E_{pol}$ and the polaron feature will be less pronounced and may become indistinguishable from noise. A straight forward solution to this problem is provided by the realization of a homogeneous density distribution by trapping the atoms in a box potential. Homogeneous gases have been realized in experiments, e.g. for bosons in three dimensions [Gaunt et al., 2013] and two dimensions [Corman et al., 2014], as well as for fermions in three [Mukherjee et al., 2017] and two dimensions [Hueck et al., 2017]. In such a system all impurity atoms would probe a constant density of the bath atoms and thus the polaron energy is constant over the whole sample. Another possibility is to confine the atoms in a single layer of a two dimensional optical lattice, where the motion along the tightly confined direction is frozen out. The experiments on the Bose polaron would benefit in two ways: first the gravitational sag would be drastically reduced and second the absorption image does not contain an integration along one axis of the density profile and we get access to the full 2D density distributions $n_{\mathrm{Li}}(x, y)$ and $n_{\mathrm{Cs}}(x, y)$ of the atoms. Thus, one can assign a local density to each point in the 2D plane and consequently locally define the wavevector k_n and interaction parameter $1/(k_n a_{\mathrm{LiCs}})$. This means in a single experimental run, we can realize different values of $1/(k_n a_{\mathrm{LiCs}})$ at different spatial positions in the trap and thus we can access the full polaron spectrum in principle without changing the interspecies scattering length a_{LiCs}.

BEC The next step in our experiment is the creation of a BEC of ^{133}Cs atoms at magnetic fields close to the zero-crossing in the Cs scattering length at a magnetic field of 880 G and simultaneously trapping of Li atoms. Our experiments will benefit from the much higher densities of the BEC on the order of 10^{14} cm^{-2}, which is more than two orders of magnitude larger than in our current experiments. This in turn will lead to larger polaron energies E_{pol}, which can be probed with shorter rf-pulses. A Cs BEC at relatively low magnetic fields of 21 G has been achieved during this thesis work [Pires, 2014; Arias, 2014]. However, it was not possible to simultaneously trap Li atoms. Recently, the Chicago group has reported the achievement of simultaneous quantum degeneracy of ^{6}Li and ^{133}Cs atoms [DeSalvo et al., 2017]. It was shown, that a small number of Li atoms can be fully confined by the Cs BEC at moderate interaction strength. By this approach it is possible to achieve a good spatial overlap, even in the quantum degenerate regime at very low temperatures.

4.2. Further developments

Besides the study of the Bose polaron and its connections to few-body physics, the Li-Cs system is ideally suited for the investigation of various interesting many-body phenomena.

Realization of bubble polaron The question whether the single impurity self-localizes for strong coupling with the medium is an essential and ongoing problem of solid-state physics. Localized polarons can be divided into two classes based on their influence on the host medium: quasiparticles that merely distort the medium, such as electrons in dielectric crystals [Devreese, 1996], and the ones that greatly deform the medium. The first class is commonly termed Landau-Pekar polaron and the second category is the so-called “bubble” polaron, reminiscent of electron bubble formation in helium superfluids [Hernandez, 1991]. It has been shown, that in the field of ultracold atomic physics, both regimes are accessible [Blinova et al., 2013]. While the Landau-Pekar polaron leads to a small dent in the density of the BEC around the impurity, in the bubble polaron the impurity suppresses the BEC completely and creates a cavity - the “bubble” - around itself, as depicted in the insets in Fig. 4.5.

The bubble polaron has not been observed in the field of ultracold atomic gases so far. We investigate the realization of the bubble polaron in the ^{6}Li-^{133}Cs system by calculating the mass-scaled gas parameter α [Blinova et al., 2013]

$$\alpha = \left(\frac{m_{\mathrm{Cs}}}{m_{\mathrm{Li}}}\right)\sqrt{n_{\mathrm{Cs}} a_{\mathrm{Cs}}^3} \tag{4.4}$$

and the boson-impurity interaction parameter β [Blinova et al., 2013]

$$\beta = \sqrt{\pi n_{\mathrm{Cs}} \frac{a_{\mathrm{LiCs}}^4}{a_{\mathrm{Cs}}}}\left(1+\frac{m_{\mathrm{Li}}}{m_{\mathrm{Cs}}}\right)\left(1+\frac{m_{\mathrm{Cs}}}{m_{\mathrm{Li}}}\right) \tag{4.5}$$

for the ^{6}Li-^{133}Cs system close to the Li-Cs Feshbach resonance at 889 G. We calculate the accessible parameter space of α and β for different Boson densities n_{Cs} and plot them as lines together with the phase diagram of the polaron system [Blinova et al., 2013] in Fig. 4.5. The phase diagram of the BEC-impurity system shows distinct regions for different parameters α and β. In case of small β, the impurity is delocalized. For larger boson-impurity interaction, the polaron localizes either in the Landau-Pekar regime (small Boson-Boson interaction α) or in the bubble regime for large interactions between the bosons. Again, the large mass ratio of the Li-Cs system leads to an increase in both interaction parameters and thus allows to access the bubble polaron regime.

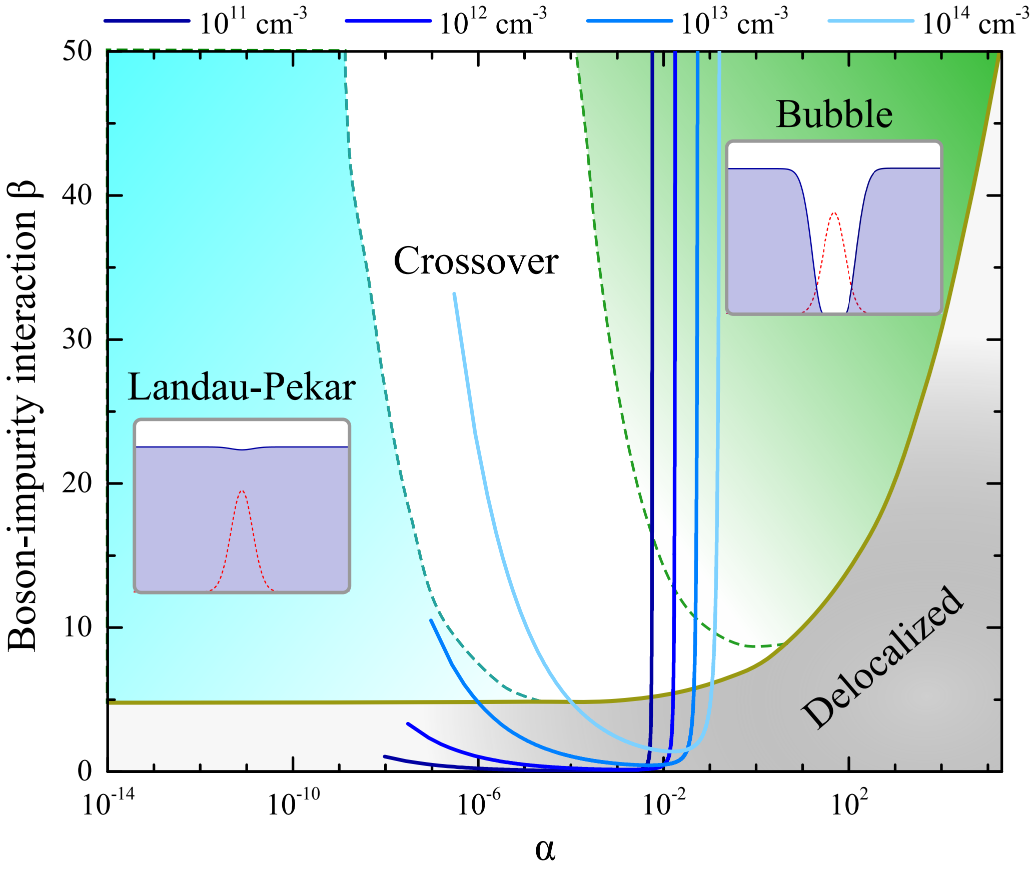

Figure 4.5.: Phase diagram of the polaron in a BEC according to Blinova et al. [2013]. For small boson-impurity interactions (below the yellow line) the impurity is delocalized. The borders of the Landau-Pekar and bubble polaron regime are depicted by the green and red dashed lines, respectively. The two regimes are connected by a smooth crossover. In the insets, we pictorially show the suppression of the BEC density (blue) around the localized impurity (red dashed line) for the two localized polaron cases. The blue lines represent the accessible parameter range of α and β for different BEC densities n_{Cs} in the vicinity of the 889 G Li-Cs Feshbach resonance.

Bragg spectroscopy A complementary approach to the measurement of the polaron energy via rf-spectroscopy is a measurement of the change in effective mass m^* of the impurity atoms due to their interaction with the bosonic bath. The effective mass of the impurities can be accessed by mapping out their dispersion relation $E(k) = \hbar^2 k^2/2m^*$. The dispersion relation can be obtained by performing Bragg spectroscopy on the impurity atoms [Casteels et al., 2011] for various transferred momenta k. An experimental setup for performing Bragg spectroscopy of ^{6}Li atoms has already been implemented in our experiment during the course of this thesis. Details of the experimental setup and measurement procedure can be found in Filzinger [2015].

The Fermi polaron In our experiment we can furthermore realize the other limiting case of a highly population imbalanced Li-Cs mixture, namely the Fermi polaron, where Cs impurities interact with a ^{6}Li Fermi sea. Such systems have been studied extensively in recent years both theoretically [Chevy, 2006; Combescot et al., 2007; Prokofev and Svistunov, 2008; Punk et al., 2009; Pilati et al., 2010; Massignan and Bruun, 2011; Schmidt and Enss, 2011; Schmidt et al., 2012a; Zöllner et al., 2011; Klawunn and Recati, 2011; Mathy et al., 2011; Nishida, 2015; Knap et al., 2012; Massignan et al., 2014; Yi and Cui, 2015] and in experiment [Schirotzek et al., 2009; Kohstall et al., 2012; Koschorreck et al., 2012; Scazza et al., 2017]. The measurements could reveal attractive and repulsive polaron branches in the weakly and strongly interacting regime, as well as the effective mass and quasiparticle residue. The real time evolution after a sudden quench of the impurity from the non-interacting in the interacting state has been studied [Cetina et al., 2016]. In contrast to the existing experiments, the large mass imbalance between the Li and Cs atoms allows to study the behavior of very heavy impurities coupled to a Fermi sea. When the impurity immersed in the Fermi sea is suddenly quenched into the interacting state we expect a decay of the quasiparticle residue, which is a measure of the wavefunction overlap with the initial noninteracting impurity. The long time dynamics are governed by a universal scaling function, which we aim to study experimentally. For large impurity mass the theoretical description is heavily simplified and even exact for static polaron (infinite mass). This regime is accessible in our system and will be studied in future experiments.

Double degeneracy of Li-Cs Besides the two limiting cases of Bose and Fermi polarons, realized with a highly population imbalanced mixture of Li and Cs atoms, it is intriguing to study the phase diagram of a Bose-Fermi mixture both in the thermal and superfluid regime. Due to the interaction between the bosonic and fermionic component, additional phases and phase separation are expected. However, both the theoretical description and the experimental realization of superfluid Bose-Fermi mixtures is challenging. It was long thought that simultaneous superfluidity can be achieved is the liquid ^{3}He-^{4}He system, where the double superfluid is predicted to exhibit a transition between s-wave and topological p-wave Cooper pairs [Rysti et al., 2012]. However, due to strong interactions between the two isotopes, the mixture becomes unstable for ^{3}He concentrations of more than 6%, which has prevented the realization of simultaneous superfluidity [Rysti et al., 2012; Tuoriniemi et al., 2002].

In the field of ultracold atomic gases simultaneous superfluidity of Bose-Fermi mixtures has been achieved for ^{7}Li-^{6}Li [Truscott et al., 2001; Schreck et al., 2001; Ferrier-Barbut et al., 2014], ^{6}Li-^{23}Na [Hadzibabic et al., 2002], ^{41}K-^{6}Li [Yao et al., 2016], ^{174}Yb-^{6}Li [Roy et al., 2017], and ^{6}Li-^{133}Cs [DeSalvo et al., 2017]. While the early realizations mainly employed the bosonic species for sympathetic cooling of the Fermions, recent experiments studied the damping and energy exchange between the two superfluids and the formation of coupled vortex lattices in ^{41}K-^{6}Li double superfluid mixture. DeSalvo et al. [2017] were able to confine a small number of fermionic ^{6}Li atoms by its attractive interactions with a ^{133}Cs BEC. It was found that the system is even stable for attractive interactions, where a collapse is expected in the mean-field theory [Ospelkaus and Ospelkaus, 2008]. Despite, the first experimental realizations of Bose-Fermi superfluidity, there are still many open questions.

With the improvements and extensions in the experimental apparatus (cf. Ch. 1 and Sec. 4.1.2) the preparation of a double superfluid Bose-Fermi mixture of ^{133}Cs and ^{6}Li atoms is within reach. This mixture offers particularly favorable properties for the study of double Bose-Fermi degeneracy, where the high mass imbalance is expected to change the interaction between the two superfluid components [Enss and Zwerger, 2009; Zhang et al., 2014]. The interspecies interaction can be tuned by the two broad magnetic Feshbach resonances located at around 843 G and 889 G (see Sec. 2.2.3) and are ideally suited for the study of the phase-diagram of mass-imbalanced Bose-Fermi mixtures from weak to strong interactions.

Summary and Outlook

5

In this work we have studied the scattering of *one, two, three,* and *many* particles of ultracold bosonic ^{133}Cs and fermionic ^{6}Li atoms.

For this purpose we have extended and improved the existing experimental apparatus for the production of ultracold mixed atomic samples. We have implemented and characterized gray molasses cooling of ^{6}Li atoms, which provides lower temperatures of the laser cooled Li atoms and thus will be beneficial for the creation of deeply degenerate Fermi gases and realization of simultaneous superfluidity in the Li-Cs mixture. The bichromatic optical dipole trapping scheme allows us to simultaneously confine the two mass-imbalanced species and control their differential gravitational sag. High-resolution absorption imaging of both species has been implemented and allows one to obtain information about the in-situ density distributions.

The *two*-body interactions in the Li-Cs system were studied by high-precision scattering experiments in the vicinity of interspecies Feshbach resonances. We employ two complementary experimental techniques: high-precision atom-loss spectroscopy and radio-frequency association of the colliding Li-Cs atom pairs into weakly bound dimers. A new effect, namely spin-rotation coupling in the Li-Cs p-wave FRs, is discovered, which manifests itself in a triplet splitting of the $m_l = -1, 0, 1$ components of the atom pair rotation l. This new effects offers full control over the angular momentum l and its projection m_l in the collision by tuning the external magnetic field. However, our investigations could not reveal the sign of the spin-rotation coupling and thus we can not distinguish the $m_l = \pm 1$ components. From possible future radio-frequency studies on the spin-rotation coupling, its sign could be determined. Making use of this splitting, one might speculate that new phases of superfluidity, reminiscent to the broken-axisymmetry phase in spinor BECs [Murata et al., 2007], and phase transitions or novel effects in the super-Efimov scenario in a highly mass imbalanced system [Moroz and Nishida, 2014] interacting through the p-wave channel can be found.

All experimentally observed Li-Cs Feshbach resonances are modeled by a full coupled channels calculation from which we determine the interspecies scattering length a_{LiCs}, improved LiCs molecular potential curves, and molecular interaction parameters. From the s-wave resonances we determine the magnetic field dependent s-wave scattering length with a ten-fold increase in precision in comparison to previous work [Repp et al., 2013; Tung et al., 2013; Pires et al., 2014a]. The observed triplet splitting of the p-wave resonances allows to determine the magnitude of the spin-rotation coupling constant

$|\gamma| = 0.000566(50)$ with respect to the effective rotational constant of the asymptotic levels. The improved understanding of the Li-Cs two-body interactions builds the foundation for studies of three-body and many-body problems.

In the scope of our work on *three*-body physics, we have observed in total five Cs-Cs-Li Efimov resonances and analysed them with help of the hyperspherical adiabatic approximation. We model the two-body interaction by either zero-range or Lennard-Jones type model potentials. The first observation of a series of three consecutive Efimov resonances allowed to test the universality in the Efimov scenario. In case of negative intraspecies scattering length $a_{\mathrm{Cs}} > 0$ (843 G FR), the experimentally determined three-body loss rates are fitted by an analytic zero-range theory, which appropriately treats the changing Cs-Cs scattering length and finite temperature. While the two excited Efimov resonances can be explained by the universal model, deviations are apparent for the ground state resonance. This discrepancy is not surprising, since the resonance is located at a scattering length that is only a factor of 7 and 3 larger than the Li-Cs and Cs-Cs van der Waals lengths. Thus, the ground state resonance is located outside the resonant regime and corrections due to the exact two-body interaction potential are expected. This discrepancy is resolved when the two-body interaction is modeled by more realistic potentials, as it is done in the spinless van der Waals theory.

The role of the intraspecies scattering length in the Efimov scenario has been studied by performing additional three-body loss rate measurements close to the Li-Cs Feshbach resonance at 889 G, where the scattering length between two Cs atoms is small and positive. In this case we only observe two Efimov resonances. The first feature is found at roughly the same scattering length as the first excited Efimov resonance close to the 843 G FR, hinting at a disappearance of the ground state resonance. This behavior can be intuitively understood from the hyperspherical adiabatic zero-range theory. The existence of a weakly bound dimer BB splits the adiabatic hyperspherical potentials into two Efimov branches. The lower branch, which asymptotically connects to the $BB+X$ threshold, may support rather deeply bound Efimov states, such as the energetically lowest Cs-Cs-Li Efimov state. As the magnitude of the scattering length is decreased, Efimov states situated in this lower potential branch may predissociate into the atom-dimer channel before reaching the three atom threshold. This leads to the disappearance of Efimov resonances in the three-body continuum when changing the intraspecies scattering length from negative to positive values.

Another interesting feature of the positive intraspecies scattering length case is found in the upper potential branch. A universal potential barrier at $R \approx 2a_{BB}$ develops, which uniquely defines the energy of Efimov states located in this branch. Thus, the intraspecies scattering length serves as a universal three-body parameter in such systems, which makes the introduction of an artificial boundary condition superfluous.

In the comparison with the spinless van der Waals theory, we observe a systematic shift between experiment and theory, which still remains an open question. One possible explanation is the single channel description in the theoretical model. However, the employed Li-Cs Feshbach resonances are intermediately broad [Tung et al., 2013] and thus a multichannel description would be appropriate. Such a description has been used in the investigation of three-body recombination in homonuclear systems [Mehta et al., 2008; Wang et al., 2011; Wang and Esry, 2011; Sørensen et al., 2013; Wang and Julienne, 2014]. Recently, this effect has been studied in the Li-Cs system, where large corrections were found for Efimov resonances close to narrow s-wave Feshbach resonances [Johansen et al., 2017].

We observe indications of *four*-body Cs-Cs-Cs-Li scattering resonances, that align well with theoretical predictions [Blume and Yan, 2014]. However, we were not able to identify the individual constituents of the tetramer and thus further studies in this direction are highly desirable.

Furthermore, the Li-Cs system is predestined for the study of the quantum *many*-body problem in a system with large mass imbalance. One interesting many-body phenomenon, is the Bose polaron problem in which the behavior of a single impurity interacting with a bosonic medium is studied. In the context of Li-Cs it is expected that not only two-body interactions but also enhanced three-body effects influence the many-body observables. Avoided crossings between Efimov states and the attractive polaron branch have been predicted for systems with large mass imbalance [Levinsen et al., 2015; Sun et al., 2017; Sun and Cui, 2017].

We performed radio-frequency spectroscopy on Li impurity atoms immersed in an uncondensed ensemble of bosonic Cs atoms. However, no indications of the poloaron were found in the spectra so far. With the proposed changes in the experimental setup, the observation of the Bose polaron is within reach. Besides the study of the connection between few- and many-body physics in the Bose polaron, the Li-Cs mixture provides many opportunities for the investigation of quantum many-body physics. The large mass ratio and the specific inter- and intraspecies scattering properties allow to access the “bubble” polaron regime, where the impurity completely depletes the medium and localizes in this self-created void. Complementary detection techniques, such as Bragg spectroscopy, may be used to access the dispersion relation of the quasi-particle and directly determine its effective mass. In addition to the Bose polaron, it will be interesting to study the Fermi polaron with a nearly infinite mass impurity and the phase diagram of a mass imbalance Bose-Fermi mixture in the quantum degenerate regime.

Besides the study of few- and many-body physics with contact interactions, the Li-Cs experiment will be employed to produce ultracold LiCs molecules in their ro-vibrational ground state. Such samples offer prospects in the study of the time variation of fundamental constants [Chin et al., 2009] and the permanent electronic dipole moment of the electron [DeMille et al., 2000]. The long-range and anisotropic nature of the dipolar

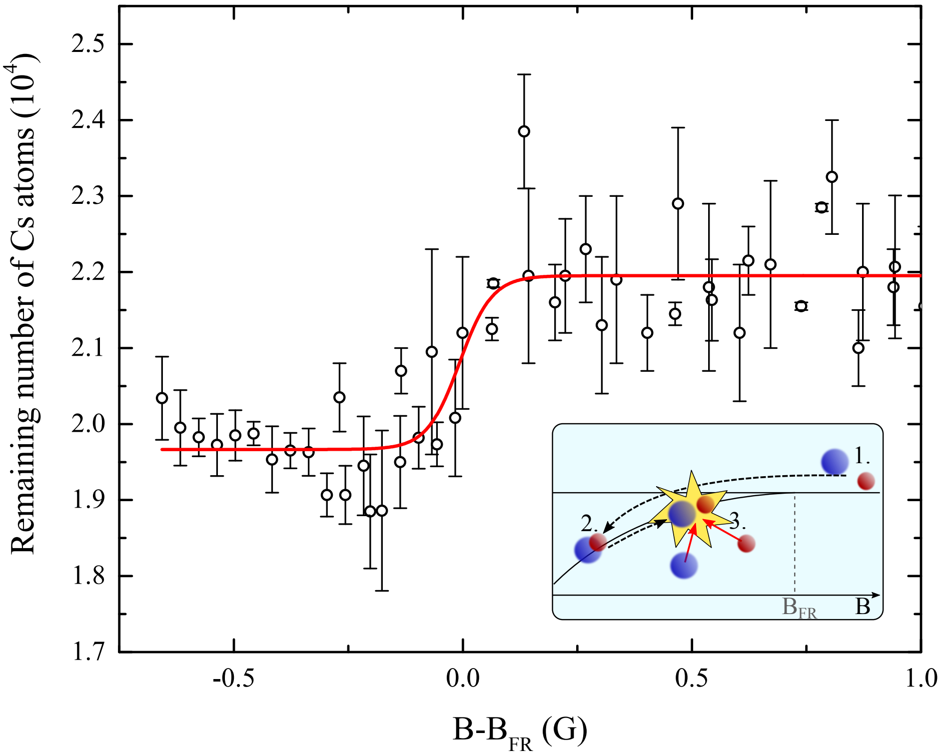

Figure 5.1.: Magneto-association and dissociation of LiCs Feshbach dimers close to the 943 G Feshbach resonance. The remaining number of Cs atoms is shown in dependence of the final magnetic field. The measurement procedure is shown in the inset: 1. a mixure of Li and Cs atoms on the negative scattering length side of a Feshbach resonance is prepared and 2. LiCs Feshbach molecules are associated by ramping the magnetic field over the Feshbach resonance to its positive side. 3. ramp-up to a variable magnetic field B, where the sample is hold for a few ms. In case the final field is above B_{FR} the dimers are dissociated and we obtain the initial number of Cs atoms. For $B < B_{\mathrm{FR}}$ the loosely-bound dimers inelastically collide with remaining free atoms in the trap and can leave the trap. From our measurements we estimate a number of 2×10^3 LiCs Feshbach dimers.

interaction allows to generate dipolar quantum gases exhibiting intriguing many-body phenomena [Baranov, 2008; Pupillo et al., 2008; Lahaye et al., 2009; Baranov et al., 2012]. They are expected to form novel crystalline phases [Büchler et al., 2007], used in simulation of condensed matter systems [Pupillo et al., 2008] and even quantum computing schemes [DeMille, 2002]. In this respect, deeply-bound LiCs molecules [Deiglmayr et al., 2008] are a particularly promising candidate due to their a large permanent electric dipole moment of 5.5 Debye [Aymar and Dulieu, 2005; Deiglmayr et al., 2010], the largest of all alkali metal combinations.

LiCs ground state molecules have already been studied extensively in our group [Deiglmayr et al., 2008, 2009b,a; Grochola et al., 2009; Deiglmayr et al., 2010, 2011c,a,b]. However, the phase-space density of the deeply-bound molecules produced by photoassiociation was not high enough to observe dipolar many-body physics. In future experiments, a different production scheme will be used. Making use of the Li-Cs s-wave Feshbach resonances (Ch. 2), the atomic sample will be adiabatically transferred into the weakly-bound molecular state by a magnetic field ramp [Herbig et al., 2003; Regal et al., 2003; Köhler et al., 2006]. Subsequently, these Feshbach dimers are transformed into the rovibrational ground state in a stimulated rapid adiabatic passage (STIRAP) [Bergmann et al., 1998; Ni et al., 2008; Danzl et al., 2008; Lang et al., 2008]. First indications of magnetoassiciation of Feshbach molecules were already found in our experiment and are shown in Fig. 5.1.

In conclusion, the Li-Cs experiment is looking into an exciting future. Based on the presented collisional studies, the realization and exploration of many-body physics either with contact or dipolar interactions is within reach.

A

Li-Cs Feshbach resonances in other scattering channels

In Table A.1 we give the experimental positions of the Li-Cs FRs occuring in spin-channels Li$|1/2, \pm 1/2\rangle \oplus$ Cs$|3, +2\rangle$ from previous work [Repp et al., 2013]. They have not been remeasured but included in the fitting and we compare them to our new evaluation. The experimentally obtained resonance positions B^e are extracted by fitting Gaussians to the atomic loss spectra. The numbers in brackets give the total uncertainty of the determination of the resonance positions. The theoretical resonance positions B^t obtained from the coupled-channels calculation performed at a relative kinetic energy $k_B \times T$, according to the experimentally measured temperature, are given as deviations $\delta = B^e - B^t$. The assignment of the FRs can be found in Repp et al. [2013].

Entrance channel	l	B^e (G)	δ (G)	T (μK)
Li$\|1/2, +1/2\rangle$	1	704.49(15)	0.159	2
$\oplus$ Cs$\|3, +2\rangle$	1	704.49(15)	0.078	2
	1	704.49(15)	0.053	2
	0	896.62(95)	0.72	2
Li$\|1/2, -1/2\rangle$	1	750.06(15)	0.148	2
$\oplus$ Cs$\|3, +2\rangle$	1	750.06(15)	0.061	2
	1	750.06(15)	0.038	2
	0	853.85(11)	0.06	2
	0	943.5(1.4)	2.25	2

Table A.1.: Experimental positions B^e of the Li-Cs *s*- and *p*-wave Feshbach resonances from previous work [Repp et al., 2013] and comparison to the current coupled channels calculation $\delta = B^e - B^t$.

LiCs molecular potential curves

B

From our observation of *s*-, *p*-, and *d*-wave Li-Cs FRs (see Ch. 2), we construct optimized LiCs molecular potentials of the electronic ground state. The parametrization of the molecular potentials is described for example in [Gerdes et al., 2008]. The potentials are represented in three parts: the repulsive short-range part $U_{\mathrm{SR}}(R)$, the intermediate range $U_{\mathrm{IR}}(R)$ and the asymptotic long range part $U_{\mathrm{LR}}(R)$, which are given by the following expressions:

$$U_{\mathrm{SR}}(R) = A + \frac{B}{R^q} \quad \text{for} \quad R < R_i, \tag{B.1}$$

$$U_{\mathrm{IR}}(R) = \sum_{k=0}^{n} a_k \xi(R)^k \quad \text{for} \quad R_i \leq R \leq R_o, \tag{B.2}$$

$$\text{with } \xi(R) = \frac{R - R_m}{R + bR_m}, \tag{B.3}$$

and

$$U_{\mathrm{LR}}(R) = -\frac{C_6}{R^6} - \frac{C_8}{R^8} - \frac{C_{10}}{R^{10}} - ... \pm E_{ex} \text{ for } R < R_o, \tag{B.4}$$

where the exchange energy is given by

$$E_{ex} = A_{ex} R^{\gamma} \exp\left(-\beta R\right). \tag{B.5}$$

It is negative for the singlet and positive for the triplet potential. The long range parameter C_i with $i > 10$ are used for smooth connection at R_o.

For the deep ground state we fitted an adiabatic Born-Oppenheimer correction [Tiemann et al., 2009] for the simultaneous description of both isotopes of Li. The correction potential $\mathrm{U}_{\mathrm{corr}}(\mathrm{R})$ is represented as

$$U_{\mathrm{corr}}(R) = \left(1 - \frac{M_{\mathrm{ref}}}{M}\right) \cdot U_{\mathrm{ad}}(R) \tag{B.6}$$

with

$$U_{\mathrm{ad}}(R) = \left(\frac{2R_m}{R + R_m}\right)^n \sum_i v_i \cdot \xi(R)^i \text{ , } i = 0, 1, 2, ... \tag{B.7}$$

with M_{ref} being the mass of the selected reference isotope ^{7}Li and n being the power of R in the leading term of the long range interactions, i.e. $n = 6$.

The parameters of the refined LiCs singlet and triplet molecular potential curves are listed in Table B.1 and B.2, respectively[1].

The molecular potentials are derived applying all known spectroscopic data for the states $X^1\Sigma^+$ and $a^3\Sigma^+$ in a least squares fit. Limitations in their usage for predicting molecular levels should be expected because Feshbach resonances were only observed for the isotope pair ^{6}Li-^{133}Cs, whereas laser spectroscopy [Staanum et al., 2007] was mainly performed on the other Li isotope, namely ^{7}Li, and only few data on the state $X^1\Sigma^+$ for ^{6}Li^{133}Cs exist. The extension of the Feshbach data to ^{7}Li-^{133}Cs and the conventional laser spectroscopy covering the isotopologue ^{6}Li^{133}Cs would be very important to improve the knowledge of the Born-Oppenheimer correction, which is significant because of the large mass change of the light Li atom.

The spin-spin interaction contains according to Eq. (2.19), second-order spin-orbit contributions. These are modeled by the following parameters in atomic units: $a_{\text{SO1}} = -1.99167$, $b_1 = 0.7$, and $a_{\text{SO2}} = -0.012380$, $b_2 = 0.28$.

---

[1] The LiCs molecular potential curves were obtained and provided by Prof. E. Tiemann from Leibniz Universität Hannover, Germany.

For $R < R_i = 2.652$Å	
A	-0.1013528 $\times 10^5$ cm^{-1}
B	0.416877623 $\times 10^6$ cm^{-1} Å^q
q	3.81097
For 2.652Å $= R_i \le R \le R_o = 11.5183$Å	
b	-0.1
R_m	3.66796875 Å
a_0	-5875.52991 cm^{-1}
a_1	-0.252618710975387017 $\times 10^{01}$ cm^{-1}
a_2	0.367457215900665178 $\times 10^{05}$ cm^{-1}
a_3	0.435933198105685460 $\times 10^{04}$ cm^{-1}
a_4	-0.402453029905940202 $\times 10^{05}$ cm^{-1}
a_5	-0.347796521563863062 $\times 10^{05}$ cm^{-1}
a_6	0.315821171411499881 $\times 10^{04}$ cm^{-1}
a_7	-0.266304026591134665 $\times 10^{06}$ cm^{-1}
a_8	-0.181048129129882972 $\times 10^{07}$ cm^{-1}
a_9	0.914704228273577802 $\times 10^{07}$ cm^{-1}
a_{10}	0.543792503606051728 $\times 10^{08}$ cm^{-1}
a_{11}	-0.259549932529230207 $\times 10^{09}$ cm^{-1}
a_{12}	-0.105117170881063318 $\times 10^{10}$ cm^{-1}
a_{13}	0.496159149355857754 $\times 10^{10}$ cm^{-1}
a_{14}	0.129151145791594467 $\times 10^{11}$ cm^{-1}
a_{15}	-0.659976526444605789 $\times 10^{11}$ cm^{-1}
a_{16}	-0.963897189939636536 $\times 10^{11}$ cm^{-1}
a_{17}	0.614868214102462158 $\times 10^{12}$ cm^{-1}
a_{18}	0.341835223965027527 $\times 10^{12}$ cm^{-1}
a_{19}	-0.393705919840090967 $\times 10^{13}$ cm^{-1}
a_{20}	0.675695993178769775 $\times 10^{12}$ cm^{-1}
a_{21}	0.165425882904185527 $\times 10^{14}$ cm^{-1}
a_{22}	-0.132394231585170703 $\times 10^{14}$ cm^{-1}
a_{23}	-0.409738756116212656 $\times 10^{14}$ cm^{-1}
a_{24}	0.607920685011780469 $\times 10^{14}$ cm^{-1}
a_{25}	0.412071559575104687 $\times 10^{14}$ cm^{-1}
a_{26}	-0.127770461445448859 $\times 10^{15}$ cm^{-1}
a_{27}	0.376742627231593516 $\times 10^{14}$ cm^{-1}
a_{28}	0.957403474032970469 $\times 10^{14}$ cm^{-1}
a_{29}	-0.940140735588818906 $\times 10^{14}$ cm^{-1}
a_{30}	0.265036457934536914 $\times 10^{14}$ cm^{-1}
For $R > R_o = 11.5183$Å	
C_6	0.1486670$\times 10^8$ cm^{-1} Å^6
C_8	0.4343228$\times 10^9$ cm^{-1} Å^8
C_{10}	0.1951222$\times 10^{11}$ cm^{-1} Å^{10}
C_{25}	-0.1090612$\times 10^{27}$ cm^{-1} Å^{25}
A_{ex}	0.11330361$\times 10^6$ cm^{-1} Å$^{-\gamma}$
γ	5.0568
β	2.2006 Å^{-1}
For all R	
v_0	-2.02390 cm^{-1}

Table B.1.: Parameters of the $X^1\Sigma^+$ state of LiCs given with respect to the Li(2s)+Cs(6s) asymptote.

For $R < R_i = 4.345$Å	
A	-0.36140433 $\times 10^3$ cm^{-1}
B	+ 0.847547458 $\times 10^{10}$ cm^{-1} Å^q
q	11.55385
For 4.345Å $= R_i \leq R \leq R_o =$ 11.5183Å	
b	-0.4
R_m	5.24804688 Å
a_0	-309.4623 cm^{-1}
a_1	-0.364219 cm^{-1}
a_2	0.134782215491288798 $\times 10^4$ cm^{-1}
a_3	0.537311993871410536 $\times 10^2$ cm^{-1}
a_4	-0.464917969357558093 $\times 10^3$ cm^{-1}
a_5	-0.175749884668625532 $\times 10^4$ cm^{-1}
a_6	-0.370441589928719986 $\times 10^5$ cm^{-1}
a_7	-0.278341242922687888 $\times 10^4$ cm^{-1}
a_8	0.457470834692090517 $\times 10^6$ cm^{-1}
a_9	0.177854005800842642 $\times 10^5$ cm^{-1}
a_{10}	-0.276200432485941378 $\times 10^7$ cm^{-1}
a_{11}	0.431748264218297321 $\times 10^6$ cm^{-1}
a_{12}	0.921774583938866295 $\times 10^7$ cm^{-1}
a_{13}	-0.348640828981605452 $\times 10^7$ cm^{-1}
a_{14}	-0.163264106046121176 $\times 10^8$ cm^{-1}
a_{15}	0.962454228859609924 $\times 10^7$ cm^{-1}
a_{16}	0.120056635752306953 $\times 10^8$ cm^{-1}
a_{17}	-0.931029427120562643 $\times 10^7$ cm^{-1}
For $R > R_o =$ 11.5183Å	
C_6	0.1486670$\times 10^8$ cm^{-1} Å^6
C_8	0.4343228$\times 10^9$ cm^{-1} Å^8
C_{10}	0.1951222$\times 10^{11}$ cm^{-1} Å^{10}
C_{25}	-0.421260895$\times 10^{25}$ cm^{-1} Å^{25}
A_{ex}	0.11330361$\times 10^6$ cm^{-1} Å$^{-\gamma}$
γ	5.0568
β	2.2006 Å^{-1}

Table B.2.: Parameters of the $a^3\Sigma^+$ state of LiCs given with respect to the Li(2s)+Cs(6s) asymptote.

g-wave Feshbach resonance in Cs

In the course of our measurements of Li-Cs d-wave Feshbach resonances, we found a g-wave Feshbach resonance of Cs atoms in their lowest hyperfine state $|3,3\rangle$. We perform atom-loss spectroscopy with a sample of 3×10^4 Cs atoms at a temperature of 300 nK and determine the trapping frequencies to be $\omega_{\mathrm{Cs}} = 2\pi \times (11, 147, 133)$ Hz, where the external magnetic field and gravity are parallel to the z-axis. The atom-loss signal is depicted in Fig. C.1. The experimental resonance position $B^e = 358.12(5)$ G is obtained by fitting a Gaussian profile to the data and agrees very well with theoretical predictions [Berninger et al., 2013b].

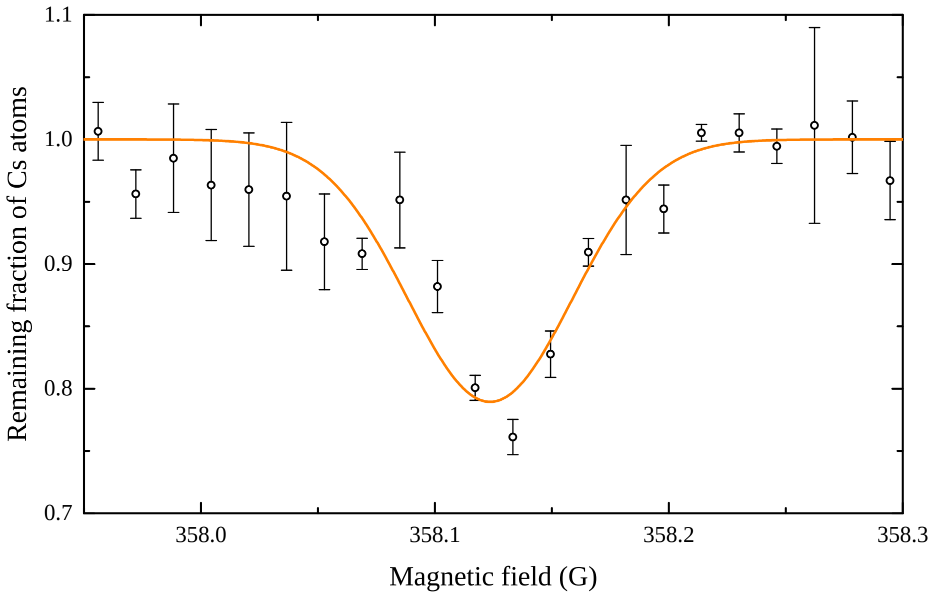

Figure C.1.: Atom-loss spectroscopy of Cs atoms in the absolute atomic ground state $|3,3\rangle$ at a magnetic field around 358 G. The remaining fraction of Cs atoms after a hold time of 50 ms is shown. Each data point is the average of at least four measurements and the error bars represent their standard error. The orange curve is a fit of a Gaussian function to the measurements.

Bibliography

Abo-Shaeer, J. R., Raman, C., Vogels, J. M., and Ketterle, W. (2001). Observation of Vortex Lattices in Bose-Einstein Condensates. *Science*, 292(5516):476–479.

Acharya, B., Ji, C., and Platter, L. (2016). Effective-field-theory analysis of Efimov physics in heteronuclear mixtures of ultracold atomic gases. *Physical Review A*, 94(3).

Aikawa, K., Frisch, A., Mark, M., Baier, S., Grimm, R., and Ferlaino, F. (2014). Reaching Fermi degeneracy via universal dipolar scattering. *Phys. Rev. Lett.*, 112:010404.

Aikawa, K., Frisch, A., Mark, M., Baier, S., Rietzler, A., Grimm, R., and Ferlaino, F. (2012). Bose-Einstein condensation of Erbium. *Phys. Rev. Lett.*, 108:210401.

Alexandrov, A. S. (2007). *Polarons in Advanced Materials*. Springer.

Alexandrov, A. S. and Devreese, J. T. (2009). *Advances in Polaron Physics*. Springer-Verlag GmbH.

Alt, E., Grassberger, P., and Sandhas, W. (1967). Reduction of the three-particle collision problem to multi-channel two-particle Lippmann-Schwinger equations. *Nuclear Physics B*, 2(2):167 – 180.

Amado, R. D. and Noble, J. V. (1972). Efimov's effect: A new pathology of three-particle systems. II. *Phys. Rev. D*, 5:1992–2002.

Anderson, M. H., Ensher, J. R., Matthews, M. R., Wieman, C. E., and Cornell, E. A. (1995). Observation of Bose-Einstein condensation in a dilute atomic vapor. *Science*, 269(5221):198–201.

Andrews, M. R., Townsend, C. G., Miesner, H.-J., Durfee, D. S., Kurn, D. M., and Ketterle, W. (1997). Observation of Interference Between Two Bose Condensates. *Science*, 275(5300):637–641.

Ardila, L. A. P. and Giorgini, S. (2015). Impurity in a Bose-Einstein condensate: Study of the attractive and repulsive branch using quantum Monte Carlo methods. *Phys. Rev. A*, 92:033612.

Arias, A. (2014). A reservoir optical dipole trap for creating a Bose-Einstein condensate of ^{133}Cs. Master's thesis, Ruprecht-Karls-Universität Heidelberg, Germany.

Arimondo, E. (1991). Laser manipulation of atoms and ions. In Arimondo, E., Strumia, F., and Phillips, W., editors, *Laser manipulation of atoms and ions*, Course CXVIII, Proceedings of the International School of Physics "Enrico Fermi". North-Holland, Amsterdam.

Arimondo, E., Inguscio, M., and Violino, P. (1977). Experimental determinations of the hyperfine structure in the alkali atoms. *Rev. Mod. Phys.*, 49:31–75.

Arora, B., Safronova, M. S., and Clark, C. W. (2011). Tune-out wavelengths of alkali-metal atoms and their applications. *Phys. Rev. A*, 84(043401).

Astrakharchik, G. E. and Pitaevskii, L. P. (2004). Motion of a heavy impurity through a Bose-Einstein condensate. *Phys. Rev. A*, 70:013608.

ATLAS Collaboration (2012). Observation of a new particle in the search for the Standard Model Higgs boson with the ATLAS detector at the LHC. *Physics Letters B*, 716(1):1 – 29.

Audi, G., Wapstra, A., and Thibault, C. (2003). The Ame2003 atomic mass evaluation. *Nuclear Physics A*, 729(1):337 – 676. The 2003 NUBASE and Atomic Mass Evaluations.

Aymar, M. and Dulieu, O. (2005). Calculation of accurate permanent dipole moments of the lowest $^{1,3}\Sigma^+$ states of heteronuclear alkali dimers using extended basis sets. *J. Chem. Phys.*, 122(20):204302.

Bailey, V. A. and Townsend, J. S. (1921). The motion of electrons in gases. *Philosophical Magazine*, 42:873–891.

Baranov, M. (2008). Theoretical progress in many-body physics with ultracold dipolar gases. *Phys. Rep.*, 464(3):71 – 111.

Baranov, M. A., Dalmonte, M., Pupillo, G., and Zoller, P. (2012). Condensed matter theory of dipolar quantum gases. *Chem. Rev.*, 112(9):5012–5061.

Barontini, G., Weber, C., Rabatti, F., Catani, J., Thalhammer, G., Inguscio, M., and Minardi, F. (2009). Observation of heteronuclear atomic Efimov resonances. *Phys. Rev. Lett.*, 103:043201.

Barontini, G., Weber, C., Rabatti, F., Catani, J., Thalhammer, G., Inguscio, M., and Minardi, F. (2010). Erratum: Observation of heteronuclear atomic Efimov resonances [Phys. Rev. Lett. 103, 043201 (2009)]. *Phys. Rev. Lett.*, 104:059901(E).

Bartenstein, M., Altmeyer, A., Riedl, S., Geursen, R., Jochim, S., Chin, C., Denschlag, J. H., Grimm, R., Simoni, A., Tiesinga, E., Williams, C. J., and Julienne, P. S. (2005). Precise determination of ^{6}Li cold collision parameters by radio-frequency spectroscopy on weakly bound molecules. *Phys. Rev. Lett.*, 94:103201.

Bartenstein, M., Altmeyer, A., Riedl, S., Jochim, S., Chin, C., Denschlag, J. H., and Grimm, R. (2004). Crossover from a Molecular Bose-Einstein Condensate to a Degenerate Fermi Gas. *Phys. Rev. Lett.*, 92:120401.

Baym, G. and Pethick, C. (1991). *Landau Fermi-Liquid Theory: Concepts and Applications*. Wiley-VCH, New York.

Bedaque, P. F., Braaten, E., and Hammer, H.-W. (2000). Three-body recombination in Bose gases with large scattering length. *Phys. Rev. Lett.*, 85:908–911.

Bedaque, P. F. and van Kolck, U. (2002). Effective field theory for few-nucleon systems. *Annu. Rev. Nucl. Part. Sci.*, 52(1):339–396.

Bell, S. C., Junker, M., Jasperse, M., Turner, L. D., Lin, Y.-J., Spielman, I. B., and Scholten, R. E. (2010). A slow atom source using a collimated effusive oven and a single-layer variable pitch coil Zeeman slower. *Rev. Sci. Instrum.*, 81(1):013105.

Benvenuti, C., Cazeneuve, J., Chiggiato, P., Cicoira, F., Escudeiro Santana, A., Johanek, V., Ruzinov, V., and Fraxedas, J. (1999). A novel route to extreme vacua: The non-evaporable getter thin film coatings. *Vacuum*, 53(1-2):219–225.

Bergmann, K., Theuer, H., and Shore, B. W. (1998). Coherent population transfer among quantum states of atoms and molecules. *Rev. Mod. Phys.*, 70:1003–1025.

Berninger, M., Zenesini, A., Huang, B., Harm, W., Nägerl, H.-C., Ferlaino, F., Grimm, R., Julienne, P. S., and Hutson, J. M. (2011). Universality of the three-body parameter for Efimov states in ultracold cesium. *Phys. Rev. Lett.*, 107:120401.

Berninger, M., Zenesini, A., Huang, B., Harm, W., Nägerl, H.-C., Ferlaino, F., Grimm, R., Julienne, P. S., and Hutson, J. M. (2013a). Feshbach resonances, weakly bound molecular states, and coupled-channel potentials for cesium at high magnetic fields. *Phys. Rev. A*, 87:032517.

Berninger, M., Zenesini, A., Huang, B., Harm, W., Nägerl, H.-C., Ferlaino, F., Grimm, R., Julienne, P. S., and Hutson, J. M. (2013b). Supplemental material: Feshbach resonances, weakly bound molecular states, and coupled-channel potentials for cesium at high magnetic fields.

Bethe, H. A. (1935). Theory of disintegration of nuclei by neutrons. *Phys. Rev.*, 47:747–759.

Blackman, R. B. and Tukey, J. W. (1959). Particular pairs of windows. In *The Measurement of Power Spectra, From the Point of View of Communications Engineering*, pages 95–101. Dover, New York.

Blinova, A. A., Boshier, M. G., and Timmermans, E. (2013). Two polaron flavors of the Bose-Einstein condensate impurity. *Phys. Rev. A*, 88:053610.

Bloch, I., Dalibard, J., and Nascimbene, S. (2012). Quantum simulations with ultracold quantum gases. *Nat Phys*, 8(4):267–276.

Bloch, I., Dalibard, J., and Zwerger, W. (2008). Many-body physics with ultracold gases. *Rev. Mod. Phys.*, 80:885–964.

Bloom, R. S., Hu, M.-G., Cumby, T. D., and Jin, D. S. (2013). Tests of universal three-body physics in an ultracold Bose-Fermi mixture. *Phys. Rev. Lett.*, 111:105301.

Blume, D. (2012). Few-body physics with ultracold atomic and molecular systems in traps. *Rep. Prog. Phys.*, 75(4):046401.

Blume, D. and Greene, C. H. (2000). Monte Carlo hyperspherical description of helium cluster excited states. *J. Chem. Phys.*, 112(18):8053–8067.

Blume, D., Greene, C. H., and Esry, B. D. (2000). Comparative study of He_3, Ne_3, and Ar_3 using hyperspherical coordinates. *J. Chem. Phys.*, 113(6):2145–2158.

Blume, D., Greene, C. H., and Esry, B. D. (2014). Erratum: Comparative study of He_3, Ne_3, and Ar_3 using hyperspherical coordinates. *J. Chem. Phys.*, 141(6).

Blume, D. and Yan, Y. (2014). Generalized Efimov scenario for heavy-light mixtures. *Phys. Rev. Lett.*, 113:213201.

Boesten, H. M. J. M., Tsai, C. C., Gardner, J. R., Heinzen, D. J., and Verhaar, B. J. (1997). Observation of a shape resonance in the collision of two cold ^{87}Rb atoms. *Phys. Rev. A*, 55:636–640.

Bogolubov, N. N. and Bogolubov, N. N. (2000). *Polaron Theory: Model Problems.* Gordon and Breach, Amsterdam.

Botelho, S. S. and Melo, C. A. R. S. d. (2005). Quantum Phase Transition in the BCS-to-BEC Evolution of p-wave Fermi Gases. *Journal of Low Temperature Physics*, 140(5):409–428.

Bourdel, T., Cubizolles, J., Khaykovich, L., Magalhães, K. M. F., Kokkelmans, S. J. J. M. F., Shlyapnikov, G. V., and Salomon, C. (2003). Measurement of the interaction energy near a Feshbach resonance in a ^{6}Li Fermi gas. *Phys. Rev. Lett.*, 91:020402.

Bourdel, T., Khaykovich, L., Cubizolles, J., Zhang, J., Chevy, F., Teichmann, M., Tarruell, L., Kokkelmans, S. J. J. M. F., and Salomon, C. (2004). Experimental Study of the BEC-BCS Crossover Region in Lithium 6. *Phys. Rev. Lett.*, 93:050401.

Braaten, E. and Hammer, H.-W. (2006). Universality in few-body systems with large scattering length. *Phys. Rep.*, 428(5â€“6):259–390.

Braaten, E. and Hammer, H.-W. (2007). Efimov physics in cold atoms. *Ann. Phys.*, 322(1):120–163.

Braaten, E., Hammer, H.-W., Kang, D., and Platter, L. (2008). Three-body recombination of identical bosons with a large positive scattering length at nonzero temperature. *Phys. Rev. A*, 78:043605.

Bredas, J. L. and Street, G. B. (1985). Polarons, bipolarons, and solitons in conducting polymers. *Accounts of Chemical Research*, 18(10):309–315.

Büchler, H. P., Demler, E., Lukin, M., Micheli, A., Prokof'ev, N., Pupillo, G., and Zoller, P. (2007). Strongly Correlated 2D Quantum Phases with Cold Polar Molecules: Controlling the Shape of the Interaction Potential. *Phys. Rev. Lett.*, 98:060404.

Burchianti, A., Valtolina, G., Seman, J. A., Pace, E., De Pas, M., Inguscio, M., Zaccanti, M., and Roati, G. (2014). Efficient all-optical production of large ^{6}Li quantum gases using D_1 gray-molasses cooling. *Phys. Rev. A*, 90:043408.

Casteels, W., Tempere, J., and Devreese, J. T. (2011). Response of the polaron system consisting of an impurity in a Bose-Einstein condensate to Bragg spectroscopy. *Phys. Rev. A*, 83:033631.

Castin, Y., Dalibard, J., and Cohen-Tannoudji, C. (1991). The limits of Sisyphus cooling. In Moi, L., Gozzini, S., Gabbanini, C., Arimondo, E., and Strumia, F., editors, *Light induced kinetic effects on atoms, ions and molecules*. ETS Editrice Pisa.

Cetina, M., Jag, M., Lous, R. S., Fritsche, I., Walraven, J. T. M., Grimm, R., Levinsen, J., Parish, M. M., Schmidt, R., Knap, M., and Demler, E. (2016). Ultrafast many-body interferometry of impurities coupled to a Fermi sea. *Science*, 354(6308):96–99.

Cheng, C.-H. and Yip, S.-K. (2005). Anisotropic Fermi Superfluid via p-Wave Feshbach Resonance. *Phys. Rev. Lett.*, 95:070404.

Chevy, F. (2006). Universal phase diagram of a strongly interacting Fermi gas with unbalanced spin populations. *Phys. Rev. A*, 74:063628.

Chin, C., Flambaum, V. V., and Kozlov, M. G. (2009). Ultracold molecules: new probes on the variation of fundamental constants. *New J. Phys.*, 11(5):055048.

Chin, C., Grimm, R., Julienne, P., and Tiesinga, E. (2010). Feshbach resonances in ultracold gases. *Rev. Mod. Phys.*, 82:1225–1286.

Chin, C. and Julienne, P. S. (2005). Radio-frequency transitions on weakly bound ultracold molecules. *Phys. Rev. A*, 71:012713.

Christensen, R. S., Levinsen, J., and Bruun, G. M. (2015). Quasiparticle Properties of a Mobile Impurity in a Bose-Einstein Condensate. *Physical Review Letters*, 115(16).

Chu, S. (1998). Nobel lecture: The manipulation of neutral particles. *Rev. Mod. Phys.*, 70:685–706.

CMS Collaboration (2012). Observation of a new boson at a mass of 125 GeV with the CMS experiment at the LHC. *Physics Letters B*, 716(1):30 – 61.

Cohen-Tannoudji, C. N. (1998). Nobel lecture: Manipulating atoms with photons. *Rev. Mod. Phys.*, 70:707–719.

Combescot, R., Recati, A., Lobo, C., and Chevy, F. (2007). Normal State of Highly Polarized Fermi Gases: Simple Many-Body Approaches. *Phys. Rev. Lett.*, 98:180402.

Conwell, E. M. (2005). Charge transport in DNA in solution: The role of polarons. *Proceedings of the National Academy of Sciences of the United States of America*, 102(25):8795–8799.

Coon, S. A. and Holstein, B. R. (2002). Anomalies in quantum mechanics: The $1/r^2$ potential. *Am. J. Phys*, 70(5):513–519.

Corman, L., Chomaz, L., Bienaimé, T., Desbuquois, R., Weitenberg, C., Nascimbène, S., Dalibard, J., and Beugnon, J. (2014). Quench-Induced Supercurrents in an Annular Bose Gas. *Phys. Rev. Lett.*, 113:135302.

Courteille, P., Freeland, R. S., Heinzen, D. J., van Abeelen, F. A., and Verhaar, B. J. (1998). Observation of a Feshbach resonance in cold atom scattering. *Phys. Rev. Lett.*, 81:69–72.

Cucchietti, F. M. and Timmermans, E. (2006). Strong-coupling polarons in dilute gas Bose-Einstein condensates. *Phys. Rev. Lett.*, 96:210401.

Cui, Y., Shen, C., Deng, M., Dong, S., Chen, C., Lü, R., Gao, B., Khoon Tey, M., and You, L. (2017). Observation of “broad” d-wave Feshbach resonances with a triplet structure. *arXiv:1709.08794*.

Dagotto, E. (1994). Correlated electrons in high-temperature superconductors. *Rev. Mod. Phys.*, 66:763–840.

Dalfovo, F., Giorgini, S., Pitaevskii, L. P., and Stringari, S. (1999). Theory of Bose-Einstein condensation in trapped gases. *Rev. Mod. Phys.*, 71:463–512.

Dalibard, J. (1999). Collisional dynamics of ultra-cold atomic gases. In Inguscio, M., Stringari, S., and Wieman, C. E., editors, *Bose-Einstein Condensation in Atomic Gases*, Course CXL, Proceedings of the International School of Physics "Enrico Fermi", page 321. IOS Press, Amsterdam.

Dalibard, J. and Cohen-Tannoudji, C. (1989). Laser cooling below the Doppler limit by polarization gradients: simple theoretical models. *J. Opt. Soc. Am. B*, 6(11):2023–2045.

Danzl, J. G., Haller, E., Gustavsson, M., Mark, M. J., Hart, R., Bouloufa, N., Dulieu, O., Ritsch, H., and Nägerl, H.-C. (2008). Quantum Gas of Deeply Bound Ground State Molecules. *Science*, 321(5892):1062–1066.

Davis, K. B., Mewes, M. O., Andrews, M. R., van Druten, N. J., Durfee, D. S., Kurn, D. M., and Ketterle, W. (1995). Bose-Einstein condensation in a gas of sodium atoms. *Phys. Rev. Lett.*, 75:3969–3973.

Debatin, M. (2013). Creation of Ultracold RbCs Ground-State Molecules. PhD thesis, University of Innsbruck.

Deiglmayr, J., Grochola, A., Repp, M., Dulieu, O., Wester, R., and Weidemüller, M. (2010). Permanent dipole moment of LiCs in the ground state. *Phys. Rev. A*, 82:032503.

Deiglmayr, J., Grochola, A., Repp, M., Mörtlbauer, K., Glück, C., Lange, J., Dulieu, O., Wester, R., and Weidemüller, M. (2008). Formation of Ultracold Polar Molecules in the Rovibrational Ground State. *Phys. Rev. Lett.*, 101:133004.

Deiglmayr, J., Pellegrini, P., Grochola, A., Repp, M., Côté, R., Dulieu, O., Wester, R., and Weidemüller, M. (2009a). Influence of a Feshbach resonance on the photoassociation of LiCs. *New J. Phys.*, 11(5):055034.

Deiglmayr, J., Repp, M., Dulieu, O., Wester, R., and Weidemüller, M. (2011a). Population redistribution in optically trapped polar molecules. *Eur. Phys. J. D*, 65:99–104.

Deiglmayr, J., Repp, M., Grochola, A., Dulieu, O., Wester, R., and Weidemüller, M. (2011b). Dipolar effects and collisions in an ultracold gas of LiCs molecules. volume 264, page 012014.

Deiglmayr, J., Repp, M., Grochola, A., Mörtlbauer, K., Glück, C., Dulieu, O., Lange, J., Wester, R., and Weidemüller, M. (2009b). Formation of ultracold dipolar molecules in the lowest vibrational levels by photoassociation. *Faraday Discuss.*, 142:335–349.

Deiglmayr, J., Repp, M., Wester, R., Dulieu, O., and Weidemüller, M. (2011c). Inelastic collisions of ultracold polar LiCs molecules with caesium atoms in an optical dipole trap. *Phys. Chem. Chem. Phys.*, 13:19101.

Delves, L. (1958). Tertiary and general-order collisions. *Nuclear Physics*, 9(3):391–399.

Delves, L. (1960). Tertiary and general-order collisions (ii). *Nuclear Physics*, 20(0):275–308.

DeMarco, B., Bohn, J. L., Burke, J. P., Holland, M., and Jin, D. S. (1999). Measurement of p-Wave Threshold Law Using Evaporatively Cooled Fermionic Atoms. *Phys. Rev. Lett.*, 82:4208–4211.

DeMarco, B. and Jin, D. S. (1999). Onset of Fermi Degeneracy in a Trapped Atomic Gas. *Science*, 285(5434):1703–1706.

DeMille, D. (2002). Quantum computation with trapped polar molecules. *Phys. Rev. Lett.*, 88:067901.

DeMille, D., Bay, F., Bickman, S., Kawall, D., Krause, D., Maxwell, S. E., and Hunter, L. R. (2000). Investigation of PbO as a system for measuring the electric dipole moment of the electron. *Phys. Rev. A*, 61:052507.

Derevianko, A., Babb, J. F., and Dalgarno, A. (2001). High-precision calculations of van der Waals coefficients for heteronuclear alkali-metal dimers. *Phys. Rev. A*, 63:052704.

DeSalvo, B., Patel, K., Johansen, J., and Chin, C. (2017). Observation of a Degenerate Fermi Gas Trapped by a Bose-Einstein Condensate. *arXiv:1706.01220.*

Devreese, J. T., editor (1972). *Polarons in Ionic Crystals and Polar Semiconductors.* North Holland, Amsterdam.

Devreese, J. T. (1996). Polarons. *Encyclopedia of Applied Physics*, 14:383.

Devreese, J. T. (2007). Fröhlich polarons from 0D to 3D: concepts and recent developments. *J. Phys.: Condens. Matter*, 19(25):255201.

Devreese, J. T. and Alexandrov, A. S. (2009). Fröhlich polaron and bipolaron: recent developments. *Rep. Prog. Phys.*, 72(6):066501.

Dieckmann, K., Stan, C. A., Gupta, S., Hadzibabic, Z., Schunck, C. H., and Ketterle, W. (2002). Decay of an ultracold fermionic lithium gas near a Feshbach resonance. *Phys. Rev. Lett.*, 89:203201.

D'Incao, J. P. and Esry, B. D. (2005). Scattering length scaling laws for ultracold three-body collisions. *Phys. Rev. Lett.*, 94:213201.

D'Incao, J. P. and Esry, B. D. (2006a). Enhancing the observability of the Efimov effect in ultracold atomic gas mixtures. *Phys. Rev. A*, 73:030703.

D'Incao, J. P. and Esry, B. D. (2006b). Mass dependence of ultracold three-body collision rates. *Phys. Rev. A*, 73:030702.

D'Incao, J. P. and Esry, B. D. (2009). Ultracold three-body collisions near overlapping Feshbach resonances. *Phys. Rev. Lett.*, 103:083202.

D'Incao, J. P. and Greene, C. (2014). Private communication.

Drewsen, M., Laurent, P., Nadir, A., Santarelli, G., Clairon, A., Castin, Y., Grison, D., and Salomon, C. (1994). Investigation of sub-Doppler cooling effects in a cesium magneto-optical trap. *Appl. Phys. B*, 59:283.

Duarte, P. M., Hart, R. A., Hitchcock, J. M., Corcovilos, T. A., Yang, T.-L., Reed, A., and Hulet, R. G. (2011). All-optical production of a lithium quantum gas using narrow-line laser cooling. *Phys. Rev. A*, 84:061406.

Dulieu, O. and Julienne, P. S. (1995). Coupled channel bound states calculations for alkali dimers using the Fourier grid method. *J. Chem. Phys.*, 103:60.

Dyke, P., Pollack, S. E., and Hulet, R. G. (2013). Finite-range corrections near a Feshbach resonance and their role in the Efimov effect. *Phys. Rev. A*, 88:023625.

Eberhard, R. (2016). Imaging of a degenerate Fermi gas of ultracold Lithium atoms. Bachelor's thesis, Ruprecht-Karls-Universität Heidelberg, Germany.

Efimov, V. (1970). Energy levels arising from resonant two-body forces in a three-body system. *Phys. Lett. B*, 33(8):563–564.

Efimov, V. (1971). Weakly bound states of three resonantly-interacting particles. *Sov. J. Nuc. Phys.*, 12:589.

Efimov, V. (1973). Energy levels of three resonantly interacting particles. *Nucl. Phys. A*, 210(1):157–188.

Efimov, V. (1979). Low-energy properties of three resonantly interacting particles. *Sov. J. Nuc. Phys.*, 29:546.

Efron, B. and Tibshirani, R. (1993). *An Introduction to the Bootstrap*. Chapman and Hall/CRC.

Eismann, U., Khaykovich, L., Laurent, S., Ferrier-Barbut, I., Rem, B. S., Grier, A. T., Delehaye, M., Chevy, F., Salomon, C., Ha, L.-C., and Chin, C. (2016). Universal Loss Dynamics in a Unitary Bose Gas. *Physical Review X*, 6(2).

Enss, T. and Zwerger, W. (2009). Superfluidity near phase separation in Bose-Fermi mixtures. *The European Physical Journal B*, 68(3):383–389.

Esry, B. D. and D'Incao, J. P. (2007). Efimov physics in ultracold three-body collisions. *J. Phys. Conf. Ser.*, 88(1):012040.

Esry, B. D., Greene, C. H., and Burke, J. P. (1999). Recombination of three atoms in the ultracold limit. *Phys. Rev. Lett.*, 83:1751–1754.

Esry, B. D., Lin, C. D., and Greene, C. H. (1996). Adiabatic hyperspherical study of the Helium trimer. *Phys. Rev. A*, 54:394–401.

Essin, A. M. and Griffiths, D. J. (2006). Quantum mechanics of the $1/x^2$ potential. *Am. J. Phys*, 74(2):109–117.

Esslinger, T., Sander, F., Weidemüller, M., Hemmerich, A., and Hänsch, T. W. (1996). Subrecoil laser cooling with adiabatic transfer. *Phys. Rev. Lett.*, 76:2432–2435.

Faddeev, L. D. (1961). Scattering theory for a three-particle system. *Sov. Phys. JETP*, 12(5):1014–1019.

Fano, U. (1961). Effects of configuration interaction on intensities and phase shifts. *Phys. Rev.*, 124:1866–1878.

Faraoni, G. (2014). Nonlinear light propagation through a strongly interacting Rydberg gas. Master's thesis, Universita di Pisa, Facoltà di Scienze Matematiche, Fisiche e Naturali.

Fedichev, P. O., Reynolds, M. W., and Shlyapnikov, G. V. (1996). Three-body recombination of ultracold atoms to a weakly bound s level. *Phys. Rev. Lett.*, 77:2921–2924.

Fedorov, D. V., Jensen, A. S., and Riisager, K. (1994). Efimov States in Halo Nuclei. *Phys. Rev. Lett.*, 73:2817–2820.

Feltgen, R., Kirst, H., Köhler, K. A., Pauly, H., and Torello, F. (1982). Unique determination of the He2 ground state potential from experiment by use of a reliable potential model. *The Journal of Chemical Physics*, 76(5):2360–2378.

Ferlaino, F. and Grimm, R. (2010). Forty years of Efimov physics: How a bizarre prediction turned into a hot topic. *Physics*, 3:9.

Ferlaino, F., Knoop, S., Berninger, M., Harm, W., D'Incao, J. P., Nägerl, H.-C., and Grimm, R. (2009). Evidence for universal four-body states tied to an Efimov trimer. *Phys. Rev. Lett.*, 102:140401.

Ferlaino, F., Knoop, S., Mark, M., Berninger, M., Schöbel, H., Nägerl, H.-C., and Grimm, R. (2008). Collisions between tunable halo dimers: Exploring an elementary four-body process with identical bosons. *Phys. Rev. Lett.*, 101:023201.

Ferlaino, F., Zenesini, A., Berninger, M., Huang, B., Nägerl, H.-C., and Grimm, R. (2011). Efimov resonances in ultracold quantum gases. *Few-Body Syst.*, 51:113–133.

Ferrier-Barbut, I., Delehaye, M., Laurent, S., Grier, A. T., Pierce, M., Rem, B. S., Chevy, F., and Salomon, C. (2014). A mixture of Bose and Fermi superfluids. *Science*, 345(6200):1035.

Feshbach, H. (1958). Unified theory of nuclear reactions. *Ann. Phys.*, 5(4):357–390.

Feshbach, H. (1962). A unified theory of nuclear reactions. II. *Ann. Phys.*, 19(2):287–313.

Feynman, R. P. (1955). Slow Electrons in a Polar Crystal. *Phys. Rev.*, 97:660–665.

Filzinger, M. (2015). Bragg spectroscopy of an ultracold gas of ^{6}Li atoms. Bachelor's thesis, Ruprecht-Karls-Universität Heidelberg, Germany.

Fisher, M. E. (1998). Renormalization group theory: Its basis and formulation in statistical physics. *Rev. Mod. Phys.*, 70:653–681.

Fröhlich, H. (1954). Electrons in lattice fields. *Adv. Phys.*, 3(11):325–361.

Fuchs, J., Ticknor, C., Dyke, P., Veeravalli, G., Kuhnle, E., Rowlands, W., Hannaford, P., and Vale, C. J. (2008). Binding energies of ^{6}Li p-wave Feshbach molecules. *Phys. Rev. A*, 77:053616.

Gaebler, J. P., Stewart, J. T., Bohn, J. L., and Jin, D. S. (2007). p-Wave Feshbach Molecules. *Phys. Rev. Lett.*, 98:200403.

Gaunt, A. L., Schmidutz, T. F., Gotlibovych, I., Smith, R. P., and Hadzibabic, Z. (2013). Bose-Einstein Condensation of Atoms in a Uniform Potential. *Phys. Rev. Lett.*, 110:200406.

Gehm, M. E. (2003). Properties of ^{6}Li. available online at `https://www.physics.ncsu.edu/jet/techdocs/pdf/PropertiesOfLi.pdf`. revision 1.1, 26 Sep. 2003.

Gerdes, A., Hobein, M., Knöckel, H., and Tiemann, E. (2008). Ground state potentials of the NaK molecule. *Eur. Phys. J. D*, 49(1):67–73.

Gerken, M. (2014). Modulationtransferspektroskopie in ^{6}Li zur Laserkühlung mit grauer Melasse. Bachelor's thesis, Ruprecht-Karls-Universität Heidelberg, Germany.

Gerken, M. (2016). Gray molasses cooling of lithium-6 towards a degenerate Fermi gas. Master's thesis, Ruprecht-Karls-Universität Heidelberg, Germany.

Giannakeas, P. and Greene, C. H. (2017). Ultracold heteronuclear three-body systems: How diabaticity limits the universality of recombination into shallow dimers. *arXiv:1706.10280*.

Giorgini, S., Pitaevskii, L. P., and Stringari, S. (2008). Theory of ultracold atomic Fermi gases. *Rev. Mod. Phys.*, 80:1215–1274.

Goldberg, D. A. and Smith, S. M. (1972). Criteria for the elimination of discrete ambiguities in nuclear optical potentials. *Phys. Rev. Lett.*, 29:500–503.

GÃ³ral, K., Köhler, T., Gardiner, S. A., Tiesinga, E., and Julienne, P. S. (2004). Adiabatic association of ultracold molecules via magnetic-field tunable interactions. *J. Phys. B: At., Mol. Opt. Phys.*, 37(17):3457.

Greene, C. H. (2010). Universal insights from few-body land. *Phys. Today*, 63(3):40–45.

Greene, C. H., Giannakeas, P., and Pérez-Ríos, J. (2017). Universal few-body physics and cluster formation. *Rev. Mod. Phys.*, 89:035006.

Grier, A. T., Ferrier-Barbut, I., Rem, B. S., Delehaye, M., Khaykovich, L., Chevy, F., and Salomon, C. (2013). Λ-enhanced sub-Doppler cooling of lithium atoms in D_1 gray molasses. *Phys. Rev. A*, 87:063411.

Grimm, R., Weidemüller, M., and Ovchinnikov, Y. B. (2000). Optical dipole traps for neutral atoms. *Advances In Atomic, Molecular, and Optical Physics*, 42:95 – 170.

Grochola, A., Pashov, A., Deiglmayr, J., Repp, M., Tiemann, E., Wester, R., and Weidemüller, M. (2009). Photoassociation spectroscopy of the $B^1\Pi$ state of LiCs. *J. Chem. Phys.*, 131(5):054304.

Gross, N., Shotan, Z., Kokkelmans, S., and Khaykovich, L. (2009). Observation of universality in ultracold ^{7}Li three-body recombination. *Phys. Rev. Lett.*, 103:163202.

Gross, N., Shotan, Z., Kokkelmans, S., and Khaykovich, L. (2010). Nuclear-spin-independent short-range three-body physics in ultracold atoms. *Phys. Rev. Lett.*, 105:103203.

Gross, N., Shotan, Z., Machtey, O., Kokkelmans, S., and Khaykovich, L. (2011). Study of Efimov physics in two nuclear-spin sublevels of ^{7}Li. *C. R. Phys.*, 12:4 – 12.

Grusdt, F. and Demler, E. (2016). New theoretical approaches to Bose polarons. In Inguscio, M., Ketterle, W., and Stringari, S., editors, *Quantum Matter at Ultralow Temperatures*, Course 191, Proceedings of the International School of Physics "Enrico Fermi". IOS Press, Amsterdam.

Grusdt, F., Schmidt, R., Shchadilova, Y. E., and Demler, E. (2017). Strong-coupling Bose polarons in a Bose-Einstein condensate. *Phys. Rev. A*, 96:013607.

Grynberg, G. and Courtois, J.-Y. (1994). Proposal for a magneto-optical lattice for trapping atoms in nearly-dark states. *EPL (Europhysics Letters)*, 27(1):41.

Gullans, M. J., Diehl, S., Rittenhouse, S. T., Ruzic, B. P., D'Incao, J. P., Julienne, P., Gorshkov, A. V., and Taylor, J. M. (2017). Efimov States of Strongly Interacting Photons. *arXiv:1709.01955.*

Gurarie, V., Radzihovsky, L., and Andreev, A. V. (2005). Quantum Phase Transitions across a p-Wave Feshbach Resonance. *Phys. Rev. Lett.*, 94:230403.

Hadzibabic, Z., Stan, C. A., Dieckmann, K., Gupta, S., Zwierlein, M. W., Görlitz, A., and Ketterle, W. (2002). Two-Species Mixture of Quantum Degenerate Bose and Fermi Gases. *Phys. Rev. Lett.*, 88:160401.

Häfner, S. (2013). A tunable optical dipole trap for ^{6}Li and ^{133}Cs. Master's thesis, Ruprecht-Karls-Universität Heidelberg, Germany.

Häfner, S., Ulmanis, J., Kuhnle, E. D., Wang, Y., Greene, C. H., and Weidemüller, M. (2017). Role of the intraspecies scattering length in the Efimov scenario with large mass difference. *Phys. Rev. A*, 95:062708.

Hall, D. S., Matthews, M. R., Wieman, C. E., and Cornell, E. A. (1998). Measurements of Relative Phase in Two-Component Bose-Einstein Condensates. *Phys. Rev. Lett.*, 81:1543–1546.

Hammer, H.-W., Nogga, A., and Schwenk, A. (2013). *Colloquium* : Three-body forces: From cold atoms to nuclei. *Rev. Mod. Phys.*, 85:197–217.

Hammer, H.-W. and Platter, L. (2011). Efimov physics from a renormalization group perspective. *Philosophical Transactions of the Royal Society A: Mathematical, Physical and Engineering Sciences*, 369(1946):2679–2700.

Heck, R. (2012). All-optical formation of an ultracold gas of fermionic lithium close to quantum degeneracy. Master's thesis, Ruprecht-Karls-Universität Heidelberg, Germany.

Helfrich, K. and Hammer, H.-W. (2010). The heteronuclear Efimov effect. *EPJ Web Conf.*, 3(02007).

Helfrich, K., Hammer, H.-W., and Petrov, D. S. (2010). Three-body problem in heteronuclear mixtures with resonant interspecies interaction. *Phys. Rev. A*, 81:042715.

Herbig, J., Kraemer, T., Mark, M., Weber, T., Chin, C., Nägerl, H.-C., and Grimm, R. (2003). Preparation of a pure molecular quantum gas. *Science*, 301(5639):1510–1513.

Hernandez, J. P. (1991). Electron self-trapping in liquids and dense gases. *Rev. Mod. Phys.*, 63:675–697.

Hiyama, E. and Kamimura, M. (2012a). Linear correlations between ^{4}He trimer and tetramer energies calculated with various realistic ^{4}He potentials. *Phys. Rev. A*, 85:062505.

Hiyama, E. and Kamimura, M. (2012b). Variational calculation of ^{4}He tetramer ground and excited states using a realistic pair potential. *Phys. Rev. A*, 85:022502.

Ho, T.-L. and Diener, R. B. (2005). Fermion superfluids of nonzero orbital angular momentum near resonance. *Phys. Rev. Lett.*, 94:090402.

Hofstadter, R. (1961). Nobel lecture: The electron-scattering method and its application to the structure of nuclei and nucleons.

Holstein, T. (1959a). Studies of polaron motion: Part I. The molecular-crystal model. *Annals of Physics*, 8(3):325 – 342.

Holstein, T. (1959b). Studies of polaron motion: Part II. The "small" polaron. *Annals of Physics*, 8(3):343 – 389.

Hu, M.-G., Bloom, R. S., Jin, D. S., and Goldwin, J. M. (2014). Avalanche-mechanism loss at an atom-molecule Efimov resonance. *Phys. Rev. A*, 90:013619.

Hu, M.-G., Van de Graaff, M. J., Kedar, D., Corson, J. P., Cornell, E. A., and Jin, D. S. (2016). Bose Polarons in the Strongly Interacting Regime. *Phys. Rev. Lett.*, 117:055301.

Huang, B., O'Hara, K. M., Grimm, R., Hutson, J. M., and Petrov, D. S. (2014a). Three-body parameter for Efimov states in ^{6}Li. *Phys. Rev. A*, 90:043636.

Huang, B., Sidorenkov, L. A., and Grimm, R. (2015a). Finite-temperature effects on a triatomic Efimov resonance in ultracold cesium. *Phys. Rev. A*, 91:063622.

Huang, B., Sidorenkov, L. A., Grimm, R., and Hutson, J. M. (2014b). Observation of the second triatomic resonance in Efimov's scenario. *Phys. Rev. Lett.*, 112:190401.

Huang, L., Wang, P., Ruzic, B. P., Fu, Z., Meng, Z., Peng, P., Bohn, J. L., and Zhang, J. (2015b). Radio-frequency spectrum of the Feshbach molecular state to deeply bound molecular states in ultracold ^{40}K Fermi gases. *New J. Phys.*, 17(3):033013.

Huckans, J. H., Williams, J. R., Hazlett, E. L., Stites, R. W., and O'Hara, K. M. (2009). Three-body recombination in a three-state Fermi gas with widely tunable interactions. *Phys. Rev. Lett.*, 102:165302.

Hueck, K., Luick, N., Sobirey, L., Siegl, J., Lompe, T., and Moritz, H. (2017). Two-Dimensional Homogeneous Fermi Gases. *arXiv :1704.06315*.

Hund, F. (1926). Zur Deutung einiger Erscheinungen in den Molekülspektren. *Zeitschrift für Physik*, 36:657.

Hund, F. (1927). Zur Deutung der Molekelspektren. II. *Zeitschrift für Physik*, 42(2):93–120.

Hundhausen, E. and Pauly, H. (1964). Untersuchungen des Wechselwirkungspotentials von van der Waals-Molekülen mit Hilfe der „Regenbogenstreuung". *Z. Naturforschg.*, 19a:810–812.

Inouye, S., Andrews, M. R., Stenger, J., Miesner, H.-J., Stamper-Kurn, D. M., and Ketterle, W. (1998). Observation of Feshbach resonances in a Bose-Einstein condensate. *Nature*, 392(6672):151–154.

Jag, M., Zaccanti, M., Cetina, M., Lous, R. S., Schreck, F., Grimm, R., Petrov, D. S., and Levinsen, J. (2014). Observation of a strong atom-dimer attraction in a mass-imbalanced Fermi-Fermi mixture. *Phys. Rev. Lett.*, 112:075302.

Joachain, C. J. (1984). *Quantum Collision Theory.* Elsevier Science Ltd.

Johansen, J., DeSalvo, B. J., Patel, K., and Chin, C. (2017). Testing universality of Efimov physics across broad and narrow Feshbach resonances. *Nat Phys*, 13:731–735.

Jones, J. E. (1924a). On the Determination of Molecular Fields. I. From the Variation of the Viscosity of a Gas with Temperature. *Proceedings of the Royal Society of London. Series A, Containing Papers of a Mathematical and Physical Character*, 106(738):441–462.

Jones, J. E. (1924b). On the Determination of Molecular Fields. II. From the Equation of State of a Gas. *Proceedings of the Royal Society of London. Series A, Containing Papers of a Mathematical and Physical Character*, 106(738):463–477.

Jones, K. M., Tiesinga, E., Lett, P. D., and Julienne, P. S. (2006). Ultracold photoassociation spectroscopy: Long-range molecules and atomic scattering. *Rev. Mod. Phys.*, 78:483–535.

Jørgensen, N. B., Wacker, L., Skalmstang, K. T., Parish, M. M., Levinsen, J., Christensen, R. S., Bruun, G. M., and Arlt, J. J. (2016). Observation of attractive and repulsive polarons in a Bose-Einstein condensate. *Phys. Rev. Lett.*, 117:055302.

Julienne, P. S. and Mies, F. H. (1989). Collisions of ultracold trapped atoms. *J. Opt. Soc. Am. B*, 6(11):2257–2269.

Kalas, R. M. and Blume, D. (2006). Interaction-induced localization of an impurity in a trapped Bose-Einstein condensate. *Phys. Rev. A*, 73:043608.

Kaplan, D. B. (2005). Five lectures on effective field theory. *Lectures delivered at the 17th National Nuclear Physics Summer School 2005, Berkeley, CA, June 6-17, 2005*, arXiv:nucl–th/0510023.

Kerman, A. J., Vuletić, V., Chin, C., and Chu, S. (2000). Beyond Optical Molasses: 3D Raman Sideband Cooling of Atomic Cesium to High Phase-Space Density. *Phys. Rev. Lett.*, 84:439–442.

Ketterle, W., Durfee, D. S., and Stamper-Kurn, D. M. (1999). Making, probing and understanding Bose-Einstein condensates. In Inguscio, M., Stringari, S., and Wieman, C., editors, *Bose-Einstein Condensation in Atomic Gases*, Course CXL, Proceedings of the International School of Physics "Enrico Fermi", pages 67–176. IOS Press, Amsterdam.

Ketterle, W. and van Druten, N. J. (1996). Evaporative cooling of trapped atoms. *Adv. At., Mol., Opt. Phys.*, 37:181.

Ketterle, W. and Zwierlein, M. W. (2008). Making, probing and understanding ultracold fermi gases. In Inguscio, M., Ketterle, W., and Salomon, C., editors, *Ultra-cold Fermi Gases*, Course CLXIV, Proceedings of the International School of Physics "Enrico Fermi", pages 247–422. IOS Press, Amsterdam.

Khoa, D. T., von Oertzen, W., Bohlen, H. G., and Ohkubo, S. (2007). Nuclear rainbow scattering and nucleus-nucleus potential. *Journal of Physics G: Nuclear and Particle Physics*, 34(3):R111.

Khramov, A. Y., Hansen, A. H., Jamison, A. O., Dowd, W. H., and Gupta, S. (2012). Dynamics of Feshbach molecules in an ultracold three-component mixture. *Phys. Rev. A*, 86:032705.

Klawunn, M. and Recati, A. (2011). Fermi polaron in two dimensions: Importance of the two-body bound state. *Physical Review A*, 84(3).

Klempt, C., Henninger, T., Topic, O., Scherer, M., Kattner, L., Tiemann, E., Ertmer, W., and Arlt, J. J. (2008). Radio-frequency association of heteronuclear Feshbach molecules. *Phys. Rev. A*, 78:061602.

Knap, M., Shashi, A., Nishida, Y., Imambekov, A., Abanin, D. A., and Demler, E. (2012). Time-dependent impurity in ultracold fermions: Orthogonality catastrophe and beyond. *Phys. Rev. X*, 2:041020.

Knoop, S., Ferlaino, F., Berninger, M., Mark, M., Nägerl, H.-C., and Grimm, R. (2009a). Observation of an Efimov resonance in an ultracold mixture of atoms and weakly bound dimers. *J. Phys. Conf. Ser.*, 194(1):012064.

Knoop, S., Ferlaino, F., Mark, M., Berninger, M., Schobel, H., Nägerl, H.-C., and Grimm, R. (2009b). Observation of an Efimov-like trimer resonance in ultracold atom-dimer scattering. *Nat. Phys.*, 5(3):227–230.

Köhler, T., Góral, K., and Julienne, P. S. (2006). Production of cold molecules via magnetically tunable Feshbach resonances. *Rev. Mod. Phys.*, 78:1311–1361.

Kohstall, C., Zaccanti, M., Jag, M., Trenkwalder, A., Massignan, P., Bruun, G. M., Schreck, F., and Grimm, R. (2012). Metastability and coherence of repulsive polarons in a strongly interacting Fermi mixture. *Nature*, 485(7400):615–618.

Koschorreck, M., Pertot, D., Vogt, E., Fröhlich, B., Feld, M., and Köhl, M. (2012). Attractive and repulsive Fermi polarons in two dimensions. *Nature*, 485(7400):619–622.

Kotochigova, S., Tiesinga, E., and Julienne, P. S. (2000). Relativistic ab initio treatment of the second-order spin-orbit splitting of the $a^3\Sigma_u^+$ potential of rubidium and cesium dimers. *Phys. Rev. A*, 63:012517.

Kraemer, T., Mark, M., Waldburger, P., Danzl, J. G., Chin, C., Engeser, B., Lange, A. D., Pilch, K., Jaakkola, A., Nägerl, H.-C., and Grimm, R. (2006). Evidence for

Efimov quantum states in an ultracold gas of caesium atoms. *Nature*, 440(7082):315–318.

Kramers, H. A. (1929). Zur Aufspaltung von Multiplett-S-Termen in zweiatomigen Molekülen. II. *Zeitschrift für Physik*, 53(5):429–438.

Kunitski, M., Zeller, S., Voigtsberger, J., Kalinin, A., Schmidt, L. P. H., Schöffler, M., Czasch, A., Schöllkopf, W., Grisenti, R. E., Jahnke, T., Blume, D., and Dörner, R. (2015). Observation of the Efimov state of the helium trimer. *Science*, 348(6234):551–555.

Lahaye, T., Menotti, C., Santos, L., Lewenstein, M., and Pfau, T. (2009). The physics of dipolar bosonic quantum gases. *Rep. Prog. Phys.*, 72(12):126401.

Landau, L. D. (1933). Über die Bewegung der Elektronen in Kristalgitter. *Phys. Z. Sowjetunion*, 3:644.

Landau, L. D. and Lifshitz, E. M. (1991). *Quantum Mechanics: non-relativistic theory.* Pergamon Press.

Landau, L. D. and Pekar, S. I. (1948). Effective mass of a polaron. *Zh. Eksp. Teor. Fiz*, 18(5):419 – 423.

Lang, F., Winkler, K., Strauss, C., Grimm, R., and Denschlag, J. H. (2008). Ultracold triplet molecules in the rovibrational ground state. *Phys. Rev. Lett.*, 101:133005.

Lange, A. D., Pilch, K., Prantner, A., Ferlaino, F., Engeser, B., Nägerl, H.-C., Grimm, R., and Chin, C. (2009). Determination of atomic scattering lengths from measurements of molecular binding energies near Feshbach resonances. *Phys. Rev. A*, 79:013622.

Laurent, S., Pierce, M., Delehaye, M., Yefsah, T., Chevy, F., and Salomon, C. (2017). Connecting Few-Body Inelastic Decay to Quantum Correlations in a Many-Body System: A Weakly Coupled Impurity in a Resonant Fermi Gas. *Physical Review Letters*, 118(10):103403.

LeBlanc, L. J. and Thywissen, J. H. (2007). Species-specific optical lattices. *Phys. Rev. A*, 75:053612.

Lee, M. D., Köhler, T., and Julienne, P. S. (2007). Excited Thomas-Efimov levels in ultracold gases. *Phys. Rev. A*, 76:012720.

Lee, T. D., Low, F. E., and Pines, D. (1953). The motion of slow electrons in a polar crystal. *Phys. Rev.*, 90:297–302.

Lefebvre-Brion, H. and Field, R. W. (1986). *Perturbations in the spectra of diatomic molecules.* Academic Press, Orlando.

Lett, P. D., Watts, R. N., Westbrook, C. I., Phillips, W. D., Gould, P. L., and Metcalf, H. J. (1988). Observation of Atoms Laser Cooled below the Doppler Limit. *Phys. Rev. Lett.*, 61:169–172.

Levinsen, J., Parish, M. M., and Bruun, G. M. (2015). Impurity in a Bose-Einstein Condensate and the Efimov Effect. *Phys. Rev. Lett.*, 115:125302.

Li, W. and Das Sarma, S. (2014). Variational study of polarons in Bose-Einstein condensates. *Phys. Rev. A*, 90:013618.

Liang, Q.-Y., Venkatramani, A. V., Cantu, S. H., Nicholson, T. L., Gullans, M. J., Gorshkov, A. V., Thompson, J. D., Chin, C., Lukin, M. D., and Vuletic, V. (2017). Observation of three-photon bound states in a quantum nonlinear medium. *arXiv:1709.01478*.

Lim, T. K. (1986). Efimov effect and spin-polarized hypernuclear-atom systems. *Phys. Rev. A*, 34:4424–4425.

Lim, T. K., Duffy, S. K., and Damer, W. C. (1977). Efimov state in the ^{4}He trimer. *Phys. Rev. Lett.*, 38:341–343.

Lin, C. (1995). Hyperspherical coordinate approach to atomic and other coulombic three-body systems. *Phys. Rep.*, 257(1):1 – 83.

Lompe, T., Ottenstein, T. B., Serwane, F., Viering, K., Wenz, A. N., Zürn, G., and Jochim, S. (2010a). Atom-dimer scattering in a three-component Fermi gas. *Phys. Rev. Lett.*, 105:103201.

Lompe, T., Ottenstein, T. B., Serwane, F., Wenz, A. N., Zürn, G., and Jochim, S. (2010b). Radio-frequency association of Efimov trimers. *Science*, 330(6006):940–944.

Lu, M., Burdick, N. Q., and Lev, B. L. (2012). Quantum degenerate dipolar Fermi gas. *Phys. Rev. Lett.*, 108:215301.

Lu, Z. T., Corwin, K. L., Renn, M. J., Anderson, M. H., Cornell, E. A., and Wieman, C. E. (1996). Low-velocity intense source of atoms from a magneto-optical trap. *Phys. Rev. Lett.*, 77:3331–3334.

Macek, J. (1968). Properties of autoionizing states of He. *J. Phys. B: At. Mol. Phys.*, 1(5):831.

Machtey, O., Kessler, D. A., and Khaykovich, L. (2012a). Universal dimer in a collisionally opaque medium: Experimental observables and Efimov resonances. *Phys. Rev. Lett.*, 108:130403.

Machtey, O., Shotan, Z., Gross, N., and Khaykovich, L. (2012b). Association of Efimov trimers from a three-atom continuum. *Phys. Rev. Lett.*, 108:210406.

Madison, K. W., Chevy, F., Wohlleben, W., and Dalibard, J. (2000). Vortex Formation in a Stirred Bose-Einstein Condensate. *Phys. Rev. Lett.*, 84:806–809.

Mahan, G. D. (2000). *Many-Particle Physics.* Springer.

Maier, R. A. W., Eisele, M., Tiemann, E., and Zimmermann, C. (2015). Efimov resonance and three-body parameter in a lithium-rubidium mixture. *Phys. Rev. Lett.*, 115:043201.

Maier, R. A. W., Marzok, C., Zimmermann, C., and Courteille, P. W. (2010). Radio-frequency spectroscopy of ^{6}Li p-wave molecules: Towards photoemission spectroscopy of a p-wave superfluid. *Phys. Rev. A*, 81:064701.

Mark, M., Ferlaino, F., Knoop, S., Danzl, J. G., Kraemer, T., Chin, C., Nägerl, H.-C., and Grimm, R. (2007). Spectroscopy of ultracold trapped cesium Feshbach molecules. *Phys. Rev. A*, 76:042514.

Marti, G. E., MacRae, A., Olf, R., Lourette, S., Fang, F., and Stamper-Kurn, D. M. (2014). Coherent Magnon Optics in a Ferromagnetic Spinor Bose-Einstein Condensate. *Phys. Rev. Lett.*, 113:155302.

Marzok, C., Deh, B., Zimmermann, C., Courteille, P. W., Tiemann, E., Vanne, Y. V., and Saenz, A. (2009). Feshbach resonances in an ultracold ^{7}Li and ^{87}Rb mixture. *Phys. Rev. A*, 79:012717.

Massignan, P. and Bruun, G. M. (2011). Repulsive polarons and itinerant ferromagnetism in strongly polarized Fermi gases. *Eur. Phys. J. D*, 65:83â€“89.

Massignan, P., Zaccanti, M., and Bruun, G. M. (2014). Polarons, dressed molecules and itinerant ferromagnetism in ultracold Fermi gases. *Rep. Prog. Phys.*, 77(034401).

Mathy, C. J. M., Parish, M. M., and Huse, D. A. (2011). Trimers, Molecules, and Polarons in Mass-Imbalanced Atomic Fermi Gases. *Phys. Rev. Lett.*, 106:166404.

Matthews, M. R., Anderson, B. P., Haljan, P. C., Hall, D. S., Wieman, C. E., and Cornell, E. A. (1999). Vortices in a Bose-Einstein Condensate. *Phys. Rev. Lett.*, 83:2498–2501.

McCarron, D. J., King, S. A., and Cornish, S. L. (2008). Modulation transfer spectroscopy in atomic rubidium. *Meas. Sci. Technol.*, 19(10):105601.

McKay, D. C., Jervis, D., Fine, D. J., Simpson-Porco, J. W., Edge, G. J. A., and Thywissen, J. H. (2011). Low-temperature high-density magneto-optical trapping of potassium using the open 4S→ 5P transition at 405 nm. *Phys. Rev. A*, 84:063420.

Mehta, N. P., Rittenhouse, S. T., D'Incao, J. P., and Greene, C. H. (2008). Efimov states embedded in the three-body continuum. *Phys. Rev. A*, 78:020701.

Mehta, N. P., Rittenhouse, S. T., D'Incao, J. P., von Stecher, J., and Greene, C. H. (2009). General theoretical description of n-body recombination. *Phys. Rev. Lett.*, 103:153201.

Mies, F. H. and Raoult, M. (2000). Analysis of threshold effects in ultracold atomic collisions. *Phys. Rev. A*, 62:012708.

Mies, F. H., Williams, C. J., Julienne, P. S., and Krauss, M. (1996). Estimating Bounds on Collisional Relaxation Rates of Spin-Polarized 87Rb Atoms at Ultracold Temperatures. *J. Res. Nat. Inst. Stand. Technol.*, 101:521.

Mikkelsen, M., Jensen, A. S., Fedorov, D. V., and Zinner, N. T. (2015). Three-body recombination of two-component cold atomic gases into deep dimers in an optical model. *J. Phys. B: At., Mol. Opt. Phys.*, 48(8):085301.

Moerdijk, A. J., Verhaar, B. J., and Axelsson, A. (1995). Resonances in ultracold collisions of ^{6}Li, ^{7}Li, and ^{23}Na. *Phys. Rev. A*, 51:4852–4861.

Moroz, S. and Nishida, Y. (2014). Super Efimov effect for mass-imbalanced systems. *Phys. Rev. A*, 90:063631.

Mukherjee, B., Yan, Z., Patel, P. B., Hadzibabic, Z., Yefsah, T., Struck, J., and Zwierlein, M. W. (2017). Homogeneous Atomic Fermi Gases. *Phys. Rev. Lett.*, 118:123401.

Murata, K., Saito, H., and Ueda, M. (2007). Broken-axisymmetry phase of a spin-1 ferromagnetic Bose-Einstein condensate. *Phys. Rev. A*, 75:013607.

Naidon, P. and Endo, S. (2017). Efimov physics: a review. *Reports on Progress in Physics*, 80(5):056001.

Naidon, P., Endo, S., and Ueda, M. (2014a). Microscopic origin and universality classes of the Efimov three-body parameter. *Phys. Rev. Lett.*, 112:105301.

Naidon, P., Endo, S., and Ueda, M. (2014b). Physical origin of the universal three-body parameter in atomic Efimov physics. *Phys. Rev. A*, 90:022106.

Naidon, P. and Ueda, M. (2011). The Efimov effect in lithium 6. *C. R. Phys.*, 12(1):13 – 26.

Nakaichi-Maeda, S. and Lim, T. K. (1983). Zero-energy scattering and bound states in the ^{4}He trimer and tetramer. *Phys. Rev. A*, 28:692–696.

Nakajima, S., Horikoshi, M., Mukaiyama, T., Naidon, P., and Ueda, M. (2010). Nonuniversal Efimov atom-dimer resonances in a three-component mixture of ^{6}Li. *Phys. Rev. Lett.*, 105:023201.

Nakajima, S., Horikoshi, M., Mukaiyama, T., Naidon, P., and Ueda, M. (2011). Measurement of an Efimov trimer binding energy in a three-component mixture of ^{6}Li. *Phys. Rev. Lett.*, 106:143201.

Nascimbène, S., Navon, N., Jiang, K. J., Tarruell, L., Teichmann, M., McKeever, J., Chevy, F., and Salomon, C. (2009). Collective Oscillations of an Imbalanced Fermi Gas: Axial Compression Modes and Polaron Effective Mass. *Phys. Rev. Lett.*, 103:170402.

Ni, K.-K., Ospelkaus, S., de Miranda, M. H. G., Pe'er, A., Neyenhuis, B., Zirbel, J. J., Kotochigova, S., Julienne, P. S., Jin, D. S., and Ye, J. (2008). A high phase-space-density gas of polar molecules. *Science*, 322(5899):231–235.

Nielsen, E., Fedorov, D., Jensen, A., and Garrido, E. (2001). The three-body problem with short-range interactions. *Phys. Rep.*, 347(5):373 – 459.

Nielsen, E., Fedorov, D. V., and Jensen, A. S. (1998). The structure of the atomic helium trimers: halos and Efimov states. *J. Phys. B: At., Mol. Opt. Phys.*, 31(18):4085.

Nielsen, E. and Macek, J. H. (1999). Low-Energy Recombination of Identical Bosons by Three-Body Collisions. *Phys. Rev. Lett.*, 83:1566–1569.

Nishida, Y. (2015). Polaronic Atom-Trimer Continuity in Three-Component Fermi Gases. *Phys. Rev. Lett.*, 114:115302.

Nussenzveig, H. M. (1977). The Theory of the Rainbow. *Scientific American*, 236(4):116.

Ohashi, Y. (2005). BCS-BEC Crossover in a Gas of Fermi Atoms with a *p*-Wave Feshbach Resonance. *Phys. Rev. Lett.*, 94:050403.

Ospelkaus, C. and Ospelkaus, S. (2008). Heteronuclear quantum gas mixtures. *J. Phys. B: At., Mol. Opt. Phys.*, 41(20):203001.

Ospelkaus, C., Ospelkaus, S., Humbert, L., Ernst, P., Sengstock, K., and Bongs, K. (2006a). Ultracold heteronuclear molecules in a 3D optical lattice. *Phys. Rev. Lett.*, 97:120402.

Ospelkaus, S., Ospelkaus, C., Wille, O., Succo, M., Ernst, P., Sengstock, K., and Bongs, K. (2006b). Localization of bosonic atoms by fermionic impurities in a three-dimensional optical lattice. *Phys. Rev. Lett.*, 96:180403.

Ottenstein, T. B., Lompe, T., Kohnen, M., Wenz, A. N., and Jochim, S. (2008). Collisional stability of a three-component degenerate Fermi gas. *Phys. Rev. Lett.*, 101:203202.

Papoff, F., Mauri, F., and Arimondo, E. (1992). Transient velocity-selective coherent population trapping in one dimension. *Journal of the Optical Society of America B*, 9:321–331.

Papp, S. B. and Wieman, C. E. (2006). Observation of heteronuclear Feshbach molecules from a ^{85}Rb $-^{87}$ Rb gas. *Phys. Rev. Lett.*, 97:180404.

Park, J. W., Wu, C.-H., Santiago, I., Tiecke, T. G., Will, S., Ahmadi, P., and Zwierlein, M. W. (2012). Quantum degenerate Bose-Fermi mixture of chemically different atomic species with widely tunable interactions. *Phys. Rev. A*, 85:051602.

Pekar, S. I. (1946). Autolocalization of the electron in an inertially polarizable dielectric medium. *Zh. Eksp. Teor. Fiz.*, 16:335.

Petrov, D. (2010). *Many-Body Physics with Ultracold Gases: Lecture Notes of the Les Houches Summer School: Volume 94, July 2010*, chapter The Few-atom problem, page Chapter 3. OUP Oxford.

Petrov, D. S. and Werner, F. (2015). Three-body recombination in heteronuclear mixtures at finite temperature. *Phys. Rev. A*, 92:022704.

Phillips, W. D. (1998). Nobel lecture: Laser cooling and trapping of neutral atoms. *Rev. Mod. Phys.*, 70:721–741.

Phillips, W. D. and Metcalf, H. (1982). Laser deceleration of an atomic beam. *Phys. Rev. Lett.*, 48:596–599.

Pilati, S., Bertaina, G., Giorgini, S., and Troyer, M. (2010). Itinerant Ferromagnetism of a Repulsive Atomic Fermi Gas: A Quantum Monte Carlo Study. *Phys. Rev. Lett.*, 105:030405.

Pires, R. (2014). Efimov Resonances in an Ultracold Mixture with Extreme Mass Imbalance. PhD thesis, Ruprecht-Karls-Universität Heidelberg, Germany.

Pires, R., Repp, M., Ulmanis, J., Kuhnle, E. D., Weidemüller, M., Tiecke, T. G., Greene, C. H., Ruzic, B. P., Bohn, J. L., and Tiemann, E. (2014a). Analyzing Feshbach resonances: A ^{6}Li-^{133}Cs case study. *Phys. Rev. A*, 90:012710.

Pires, R., Ulmanis, J., Häfner, S., Repp, M., Arias, A., Kuhnle, E. D., and Weidemüller, M. (2014b). Observation of Efimov resonances in a mixture with extreme mass imbalance. *Phys. Rev. Lett.*, 112:250404.

Platter, L. (2009). Low-energy universality in atomic and nuclear physics. *Few-Body Syst.*, 46(3):139–171.

Pollack, S. E., Dries, D., and Hulet, R. G. (2009). Universality in three- and four-body bound states of ultracold atoms. *Science*, 326(5960):1683–1685.

Porsev, S. G. and Derevianko, A. (2003). Accurate relativistic many-body calculations of van der Waals coefficients C_8 and C_{10} for alkali-metal dimers. *J. Chem. Phys.*, 119(2):844–850.

Porsev, S. G., Safronova, M. S., Derevianko, A., and Clark, C. W. (2014). Relativistic many-body calculations of van der Waals coefficients for Yb-Li and Yb-Rb dimers. *Phys. Rev. A*, 89:022703.

Price, D. L. (2015). *Neutron Scattering - Magnetic and Quantum Phenomena*. Elsevier Science & Technology.

Prokofev, N. and Svistunov, B. (2008). Fermi-polaron problem: Diagrammatic Monte Carlo method for divergent sign-alternating series. *Phys. Rev. B*, 77:020408.

Punk, M., Dumitrescu, P. T., and Zwerger, W. (2009). Polaron-to-molecule transition in a strongly imbalanced Fermi gas. *Phys. Rev. A*, 80:053605.

Pupillo, G., Micheli, A., Büchler, H., and Zoller, P. (2008). Cold molecules: Creation and applications. chapter Condensed Matter Physics with Cold Polar Molecules. Taylor & Francis.

Quéméner, G. and Julienne, P. S. (2012). Ultracold molecules under control! *Chem. Rev.*, 112(9):4949–5011.

Ramsauer, C. (1921). Über den Wirkungsquerschnitt der Gasmoleküle gegenüber langsamen Elektronen. *Annalen der Physik*, 64:513–540.

Rath, S. P. and Schmidt, R. (2013). Field-theoretical study of the Bose polaron. *Phys. Rev. A*, 88:053632.

Regal, C. A., Greiner, M., and Jin, D. S. (2004). Observation of resonance condensation of fermionic atom pairs. *Phys. Rev. Lett.*, 92:040403.

Regal, C. A., Ticknor, C., Bohn, J. L., and Jin, D. S. (2003). Creation of ultracold molecules from a Fermi gas of atoms. *Nature*, 424(6944):47–50.

Rem, B. S., Grier, A. T., Ferrier-Barbut, I., Eismann, U., Langen, T., Navon, N., Khaykovich, L., Werner, F., Petrov, D. S., Chevy, F., and Salomon, C. (2013). Lifetime of the Bose gas with resonant interactions. *Phys. Rev. Lett.*, 110:163202.

Renner, C. (2014). Design and characterization of a dual-wavelength high-resolution imaging system. Staatsexamensarbeit, Ruprecht-Karls-Universität Heidelberg, Germany.

Rentrop, T., Trautmann, A., Olivares, F. A., Jendrzejewski, F., Komnik, A., and Oberthaler, M. K. (2016). Observation of the Phononic Lamb Shift with a Synthetic Vacuum. *Phys. Rev. X*, 6:041041.

Repp, M. (2013). Interspecies Feshbach Resonances in an Ultracold, Optically Trapped Bose-Fermi Mixture of Cesium and Lithium. PhD thesis, Ruprecht-Karls-Universität Heidelberg, Germany.

Repp, M., Pires, R., Ulmanis, J., Heck, R., Kuhnle, E. D., Weidemüller, M., and Tiemann, E. (2013). Observation of interspecies ^{6}Li-^{133}Cs Feshbach resonances. *Phys. Rev. A*, 87:010701.

Repp, M., Pires, R., Ulmanis, J., Schmidt, S., Müller, R., Meyer, K., Heck, R., Kuhnle, E., and Weidemüller, M. (2014). A helical Zeeman slower for sequential loading of two elements with large mass difference into optical dipole traps. *Manuscript in preparation.*

Rio Fernandes, D., Sievers, F., Kretzschmar, N., Wu, S., Salomon, C., and Chevy, F. (2012). Sub-doppler laser cooling of fermionic ^{40}K atoms in three-dimensional gray optical molasses. *Europhys. Lett.*, 100:63001.

Rittenhouse, S. T., von Stecher, J., Dâ€™Incao, J. P., Mehta, N. P., and Greene, C. H. (2011). The hyperspherical four-fermion problem. *J. Phys. B: At., Mol. Opt. Phys.*, 44(17):172001.

Roy, R., Green, A., Bowler, R., and Gupta, S. (2017). Two-Element Mixture of Bose and Fermi Superfluids. *Phys. Rev. Lett.*, 118:055301.

Roy, S., Landini, M., Trenkwalder, A., Semeghini, G., Spagnolli, G., Simoni, A., Fattori, M., Inguscio, M., and Modugno, G. (2013). Test of the universality of the three-body Efimov parameter at narrow Feshbach resonances. *Phys. Rev. Lett.*, 111:053202.

Rutherford, E. F. (1911). The scattering of α and β particles by matter and the structure of the atom. *Philosophical Magazine*, 21:669–688.

Rysti, J., Tuoriniemi, J., and Salmela, A. (2012). Effective ^{3}He interactions in dilute ^{3}He-^{4}He mixtures. *Phys. Rev. B*, 85:134529.

Sacha, K. and Timmermans, E. (2006). Self-localized impurities embedded in a one-dimensional Bose-Einstein condensate and their quantum fluctuations. *Phys. Rev. A*, 73:063604.

Sakurai, J. J. and Napolitano, J. J. (2010). *Modern Quantum Mechanics*. Addison-Wesley.

Salomon, C., Shlyapnikov, G. V., and Cugliandolo, L. F., editors (2013). *Many-Body Physics with Ultracold Gases*, volume 94 of *Lecture Notes of the Les Houches Summer School*. Oxford University Press.

Scalapino, D. (1995). The case for $d_{x^2-y^2}$ pairing in the cuprate superconductors. *Physics Reports*, 250(6):329 – 365.

Scazza, F., Valtolina, G., Massignan, P., Recati, A., Amico, A., Burchianti, A., Fort, C., Inguscio, M., Zaccanti, M., and Roati, G. (2017). Repulsive Fermi Polarons in a Resonant Mixture of Ultracold ^{6}Li Atoms. *Phys. Rev. Lett.*, 118:083602.

Scelle, R., Rentrop, T., Trautmann, A., Schuster, T., and Oberthaler, M. K. (2013). Motional Coherence of Fermions Immersed in a Bose Gas. *Phys. Rev. Lett.*, 111:070401.

Schirotzek, A., Wu, C.-H., Sommer, A., and Zwierlein, M. W. (2009). Observation of Fermi polarons in a tunable Fermi liquid of ultracold atoms. *Phys. Rev. Lett.*, 102:230402.

Schmidt, R. and Enss, T. (2011). Excitation spectra and rf response near the polaron-to-molecule transition from the functional renormalization group. *Phys. Rev. A*, 83:063620.

Schmidt, R., Enss, T., Pietilä, V., and Demler, E. (2012a). Fermi polarons in two dimensions. *Phys. Rev. A*, 85:021602.

Schmidt, R., Rath, S., and Zwerger, W. (2012b). Efimov physics beyond universality. *Eur. Phys. J. B*, 85(11):1–6.

Schmidt, S. (2011). Aufbau und Charakterisierung eines frequenzstabilisierten Diodenlasersystems zur Kühlung und Speicherung von Cs-Atomen. Diplomarbeit, Ruprecht-Karls-Universität Heidelberg, Germany.

SchÃ¶nhals, A. (2013). Imaging of ultracold cesium atoms at high magnetic fields. Master's thesis, Ruprecht-Karls-Universität Heidelberg, Germany.

Schreck, F., Khaykovich, L., Corwin, K. L., Ferrari, G., Bourdel, T., Cubizolles, J., and Salomon, C. (2001). Quasipure Bose-Einstein Condensate Immersed in a Fermi Sea. *Phys. Rev. Lett.*, 87:080403.

Schünemann, U., Engler, H., Grimm, R., Weidemüller, M., and Zielonkowski, M. (1999). Simple scheme for tunable frequency offset locking of two lasers. *Rev. Sci. Instrum.*, 70(1):242–243.

Schünemann, U., Engler, H., Zielonkowski, M., Weidemüller, M., and Grimm, R. (1998). Magneto-optic trapping of lithium using semiconductor lasers. *Opt. Commun.*, 158:263 – 272.

Schuster, T., Scelle, R., Trautmann, A., Knoop, S., Oberthaler, M. K., Haverhals, M. M., Goosen, M. R., Kokkelmans, S. J. J. M. F., and Tiemann, E. (2012). Feshbach spectroscopy and scattering properties of ultracold Li + Na mixtures. *Phys. Rev. A*, 85:042721.

Schwabl, F. (2007). *Quantenmechanik.* Springer-Verlag.

Sievers, F., Kretzschmar, N., Fernandes, D. R., Suchet, D., Rabinovic, M., Wu, S., Parker, C. V., Khaykovich, L., Salomon, C., and Chevy, F. (2015). Simultaneous sub-Doppler laser cooling of fermionic ^{6}Li and ^{40}K on the D_1 line: Theory and experiment. *Phys. Rev. A*, 91:023426.

Skorniakov, G. V. and Ter-Martirosian, K. A. (1957). Three Body Problem for Short Range Forces. I. Scattering of Low Energy Neutrons by Deuterons. *Sov. Phys. JETP*, 4(5):648 – 661.

Sørensen, P. K., Fedorov, D. V., Jensen, A. S., and Zinner, N. T. (2012). Efimov physics and the three-body parameter within a two-channel framework. *Phys. Rev. A*, 86:052516.

Sørensen, P. K., Fedorov, D. V., Jensen, A. S., and Zinner, N. T. (2013). Finite-range effects in energies and recombination rates of three identical bosons. *J. Phys. B: At., Mol. Opt. Phys.*, 46(7):075301.

Spethmann, N., Kindermann, F., John, S., Weber, C., Meschede, D., and Widera, A. (2012). Dynamics of single neutral impurity atoms immersed in an ultracold gas. *Phys. Rev. Lett.*, 109:235301.

Staanum, P., Pashov, A., Knöckel, H., and Tiemann, E. (2007). $X^1\Sigma^+$ and $a^3\Sigma^+$ states of LiCs studied by Fourier-transform spectroscopy. *Phys. Rev. A*, 75:042513.

Stan, C. A. and Ketterle, W. (2005). Multiple species atom source for laser-cooling experiments. *Rev. Sci. Instrum.*, 76(6):063113.

Steck, D. A. (2008). Cesium D Line Data. available online at `http://steck.us/alkalidata`. revision 2.0.1, 2 May 2008.

Steck, D. A. (2010). Sodium D Line Data. available online at `http://steck.us/alkalidata/sodiumnumbers.pdf`. revision 2.1.4, 23 December 2010.

Steck, D. A. (2015). Rubidium 87 D Line Data. available online at `http://steck.us/alkalidata/rubidium87numbers.pdf`. revision 2.1.5, 13 January 2015.

Stellmer, S., Tey, M. K., Huang, B., Grimm, R., and Schreck, F. (2009). Bose-Einstein condensation of strontium. *Phys. Rev. Lett.*, 103:200401.

Stoof, H. T. C., Koelman, J. M. V. A., and Verhaar, B. J. (1988). Spin-exchange and dipole relaxation rates in atomic hydrogen: Rigorous and simplified calculations. *Phys. Rev. B*, 38:4688–4697.

Strauss, C., Takekoshi, T., Lang, F., Winkler, K., Grimm, R., Hecker Denschlag, J., and Tiemann, E. (2010). Hyperfine, rotational, and vibrational structure of the $a^3\Sigma_u^+$ state of $^{87}Rb_2$. *Phys. Rev. A*, 82:052514.

Stuhler, J., Griesmaier, A., Koch, T., Fattori, M., Pfau, T., Giovanazzi, S., Pedri, P., and Santos, L. (2005). Observation of dipole-dipole interaction in a degenerate quantum gas. *Phys. Rev. Lett.*, 95:150406.

Sun, M. and Cui, X. (2017). Enhancing the Efimov correlation in Bose polarons with large mass imbalance. *Phys. Rev. A*, 96:022707.

Sun, M., Zhai, H., and Cui, X. (2017). Visualizing the Efimov Correlation in Bose Polarons. *Phys. Rev. Lett.*, 119:013401.

Suno, H., Esry, B. D., and Greene, C. H. (2003). Recombination of three ultracold fermionic atoms. *Phys. Rev. Lett.*, 90:053202.

Tempere, J., Casteels, W., Oberthaler, M. K., Knoop, S., Timmermans, E., and Devreese, J. T. (2009). Feynman path-integral treatment of the BEC-impurity polaron. *Phys. Rev. B*, 80:184504.

Thalhammer, G., Barontini, G., Catani, J., Rabatti, F., Weber, C., Simoni, A., Minardi, F., and Inguscio, M. (2009). Collisional and molecular spectroscopy in an ultracold Bose-Bose mixture. *New J. Phys.*, 11(5):055044.

Thomas, L. H. (1935). The interaction between a neutron and a proton and the structure of H^3. *Phys. Rev.*, 47:903–909.

Thompson, S. T., Hodby, E., and Wieman, C. E. (2005). Ultracold molecule production via a resonant oscillating magnetic field. *Phys. Rev. Lett.*, 95:190404.

Ticknor, C., Regal, C. A., Jin, D. S., and Bohn, J. L. (2004). Multiplet structure of Feshbach resonances in nonzero partial waves. *Phys. Rev. A*, 69:042712.

Tiecke, T. G. (2011). Properties of Potassium. available online at `http://www.tobiastiecke.nl/archive/PotassiumProperties.pdf`. revision 1.02, May 2011.

Tiemann, E., Knöckel, H., Kowalczyk, P., Jastrzebski, W., Pashov, A., Salami, H., and Ross, A. J. (2009). Coupled system $a\ {}^3\Sigma^+$ and $X\ {}^1\Sigma^+$ of KLi: Feshbach resonances and corrections to the Born-Oppenheimer approximation. *Phys. Rev. A*, 79:042716.

Tiesinga, E., Williams, C. J., and Julienne, P. S. (1998). Photoassociative spectroscopy of highly excited vibrational levels of alkali-metal dimers: Green-function approach for eigenvalue solvers. *Phys. Rev. A*, 57:4257–4267.

Timmermans, E., Tommasini, P., Hussein, M., and Kerman, A. (1999). Feshbach resonances in atomic Bose-Einstein condensates. *Phys. Rep.*, 315:199 – 230.

Tischer, R. (1967). Zum EPR-Spektrum des molekularen Sauerstoffs. *Z. Naturforschg.*, 22a:1711 – 1724.

Treutlein, P., Chung, K. Y., and Chu, S. (2001). High-brightness atom source for atomic fountains. *Phys. Rev. A*, 63:051401.

Truscott, A. G., Strecker, K. E., McAlexander, W. I., Partridge, G. B., and Hulet, R. G. (2001). Observation of Fermi Pressure in a Gas of Trapped Atoms. *Science*, 291(5513):2570–2572.

Tung, S.-K., Jiménez-García, K., Johansen, J., Parker, C. V., and Chin, C. (2014). Geometric scaling of Efimov states in a ^{6}Li-^{133}Cs mixture. *Phys. Rev. Lett.*, 113:240402.

Tung, S.-K., Parker, C., Johansen, J., Chin, C., Wang, Y., and Julienne, P. S. (2013). Ultracold mixtures of atomic ^{6}Li and ^{133}Cs with tunable interactions. *Phys. Rev. A*, 87:010702.

Tuoriniemi, J., Martikainen, J., Pentti, E., Sebedash, A., Boldarev, S., and Pickett, G. (2002). Towards Superfluidity of ^{3}He Diluted by ^{4}He. *Journal of Low Temperature Physics*, 129(5):531–545.

Ulmanis, J. (2015). Universality and non-universality in the heteronuclear Efimov scenario with large mass imbalance. PhD thesis, Ruprecht-Karls-Universität Heidelberg, Germany.

Ulmanis, J., Haefner, S., Pires, R., Werner, F., Petrov, D. S., Kuhnle, E. D., and Weidemüller, M. (2016a). Universal three-body recombination and Efimov resonances in an ultracold Li-Cs mixture. *Phys. Rev. A*, 93:022707.

Ulmanis, J., Häfner, S., Kuhnle, E. D., and Weidemüller, M. (2016b). Heteronuclear Efimov resonances in ultracold quantum gases. *Natl. Sci. Rev.*, 3(2):174–188.

Ulmanis, J., Häfner, S., Pires, R., Kuhnle, E. D., Wang, Y., Greene, C. H., and Weidemüller, M. (2016). Heteronuclear Efimov scenario with positive intraspecies scattering length. *Phys. Rev. Lett.*, 117:153201.

Ulmanis, J., Häfner, S., Pires, R., Kuhnle, E. D., Weidemüller, M., and Tiemann, E. (2015). Universality of weakly bound dimers and Efimov trimers close to Li-Cs Feshbach resonances. *New J. Phys.*, 17(5):055009.

Van Vleck, J. H. (1929). On σ-type doubling and electron spin in the spectra of diatomic molecules. *Phys. Rev.*, 33:467–506.

Vuletić, V., Chin, C., Kerman, A. J., and Chu, S. (1998). Degenerate Raman sideband cooling of trapped cesium atoms at very high atomic densities. *Phys. Rev. Lett.*, 81:5768–5771.

Wacker, L. J., Jørgensen, N. B., Birkmose, D., Winter, N., Mikkelsen, M., Sherson, J., Zinner, N., and Arlt, J. J. (2016). Universal Three-Body Physics in Ultracold KRb Mixtures. *Phys. Rev. Lett.*, 117:163201.

Wang, J., D'Incao, J. P., Esry, B. D., and Greene, C. H. (2012a). Origin of the three-body parameter universality in Efimov physics. *Phys. Rev. Lett.*, 108:263001.

Wang, Y. (2010). Universal efimov physics in three- and four-body collisions. PhD thesis, Kansas State University.

Wang, Y., D'Incao, J. P., and Esry, B. D. (2011). Ultracold three-body collisions near narrow Feshbach resonances. *Phys. Rev. A*, 83:042710.

Wang, Y., D'Incao, J. P., and Esry, B. D. (2013). *Ultracold Few-Body Systems*, volume 62 of *Advances in Atomic, Molecular, and Optical Physics*. Academic Press.

Wang, Y. and Esry, B. D. (2011). Universal three-body physics at finite energy near Feshbach resonances. *New J. Phys.*, 13(3):035025.

Wang, Y., Julienne, P., and Greene, C. H. (2015). Few-body physics of ultracold atoms and molecules with long-range interactions. In Madison, K. W., Bongs, K., Carr, L. D., Rey, A. M., and Zhai, H., editors, *Annual Review of Cold Atoms and Molecules*, volume 3, chapter 2, pages 77–134. World Scientific Publishing.

Wang, Y. and Julienne, P. S. (2014). Universal van der Waals physics for three cold atoms near Feshbach resonances. *Nat. Phys.*, 10:768.

Wang, Y., Laing, W. B., von Stecher, J., and Esry, B. D. (2012b). Efimov physics in heteronuclear four-body systems. *Phys. Rev. Lett.*, 108:073201.

Wang, Y., Wang, J., D'Incao, J. P., and Greene, C. H. (2012c). Universal three-body parameter in heteronuclear atomic systems. *Phys. Rev. Lett.*, 109:243201.

Weber, C., Barontini, G., Catani, J., Thalhammer, G., Inguscio, M., and Minardi, F. (2008). Association of ultracold double-species bosonic molecules. *Phys. Rev. A*, 78:061601.

Weber, T., Herbig, J., Mark, M., Nägerl, H.-C., and Grimm, R. (2003). Three-body recombination at large scattering lengths in an ultracold atomic gas. *Phys. Rev. Lett.*, 91:123201.

Weidemüller, M., Esslinger, T., Ol'shanii, M. A., Hemmerich, A., and Hänsch, T. W. (1994). A novel scheme for efficient cooling below the photon recoil limit. *Europhys. Lett.*, 27(2):109.

Wenz, A. N., Lompe, T., Ottenstein, T. B., Serwane, F., Zürn, G., and Jochim, S. (2009). Universal trimer in a three-component Fermi gas. *Phys. Rev. A*, 80:040702.

Wenz, A. N., ZÃ¼rn, G., Murmann, S., Brouzos, I., Lompe, T., and Jochim, S. (2013). From Few to Many: Observing the Formation of a Fermi Sea One Atom at a Time. *Science*, 342(6157):457–460.

Wigner, E. P. (1948). On the behavior of cross sections near thresholds. *Phys. Rev.*, 73:1002–1009.

Wild, R. J., Makotyn, P., Pino, J. M., Cornell, E. A., and Jin, D. S. (2012). Measurements of Tan's contact in an atomic Bose-Einstein condensate. *Phys. Rev. Lett.*, 108:145305.

Williams, J. R., Hazlett, E. L., Huckans, J. H., Stites, R. W., Zhang, Y., and O'Hara, K. M. (2009). Evidence for an excited-state Efimov trimer in a three-component Fermi gas. *Phys. Rev. Lett.*, 103:130404.

Wilson, K. G. (1983). The renormalization group and critical phenomena. *Rev. Mod. Phys.*, 55:583–600.

Wu, C. F. J. (1986). Jackknife, bootstrap and other resampling methods in regression analysis. *Ann. Statist.*, 14(4):1261–1295.

Wu, C.-H., Park, J. W., Ahmadi, P., Will, S., and Zwierlein, M. W. (2012). Ultracold fermionic Feshbach molecules of ^{23}Na^{40}K. *Phys. Rev. Lett.*, 109:085301.

Yao, X.-C., Chen, H.-Z., Wu, Y.-P., Liu, X.-P., Wang, X.-Q., Jiang, X., Deng, Y., Chen, Y.-A., and Pan, J.-W. (2016). Observation of Coupled Vortex Lattices in a Mass-Imbalance Bose and Fermi Superfluid Mixture. *Phys. Rev. Lett.*, 117:145301.

Yi, W. and Cui, X. (2015). Polarons in ultracold Fermi superfluids. *Phys. Rev. A*, 92:013620.

Zaccanti, M., Deissler, B., D'Errico, C., Fattori, M., Jona-Lasinio, M., Müller, S., Roati, G., Inguscio, M., and Modugno, G. (2009). Observation of an Efimov spectrum in an atomic system. *Nat. Phys.*, 5(8):586–591.

Zenesini, A., Huang, B., Berninger, M., Besler, S., Nägerl, H.-C., Ferlaino, F., Grimm, R., Greene, C. H., and von Stecher, J. (2013). Resonant five-body recombination in an ultracold gas of bosonic atoms. *New J. Phys.*, 15(4):043040.

Zenesini, A., Huang, B., Berninger, M., Nägerl, H.-C., Ferlaino, F., and Grimm, R. (2014). Resonant atom-dimer collisions in cesium: Testing universality at positive scattering lengths. *Phys. Rev. A*, 90:022704.

Zhang, R., Zhang, W., Zhai, H., and Zhang, P. (2014). Calibration of the interaction energy between Bose and Fermi superfluids. *Phys. Rev. A*, 90:063614.

Zhang, S. and Ho, T.-L. (2011). Atom loss maximum in ultra-cold Fermi gases. *New J. Phys.*, 13(5):055003.

Zhen, Z. and Macek, J. (1988). Loosely bound states of three particles. *Phys. Rev. A*, 38:1193–1201.

Zinner, N. (2014). Few-body physics in a many-body world. *Few-Body Syst.*, 55(8-10):599–604.

Zirbel, J. J., Ni, K.-K., Ospelkaus, S., Nicholson, T. L., Olsen, M. L., Julienne, P. S., Wieman, C. E., Ye, J., and Jin, D. S. (2008). Heteronuclear molecules in an optical dipole trap. *Phys. Rev. A*, 78:013416.

Zöllner, S., Bruun, G. M., and Pethick, C. J. (2011). Polarons and molecules in a two-dimensional Fermi gas. *Phys. Rev. A*, 83:021603.

Zürn, G., Lompe, T., Wenz, A. N., Jochim, S., Julienne, P. S., and Hutson, J. M. (2013). Precise characterization of ^{6}Li Feshbach resonances using trap-sideband-resolved rf spectroscopy of weakly bound molecules. *Phys. Rev. Lett.*, 110:135301.

Danksagung

An dieser Stelle möchte ich mich bei Allen bedanken, die zum Gelingen dieser Arbeit beigetragen haben. Besonderer Dank geht an

Prof. Matthias Weidemüller für die Möglichkeit in Deiner Arbeitsgruppe meine Doktorarbeit am interessanten und spannenden Mixtures-Experiment durchzuführen. Für Dein immer offenes Ohr, die stetige Unterstützung, Dein Vertrauen, dass Du mir stets entgegengebracht hast, sowie die Freiheit meine eigenen Ideen zu verwirklichen. In unseren zahlreichen Diskussionen konnte ich sehr viel von Dir lernen.

Prof. Selim Jochim für das Lesen dieser Arbeit, viele interessante Diskussionen sowie etliche Ratschläge zu unseren Experimenten.

Juris Ulmanis, Eva Kuhnle, Rico Pires und Marc Repp, aka „Mixtures Oldies“, für die gute Vorarbeit und die Planung des Experiments, sowie die gemeinsamen erfolgreichen Jahre im Labor.

Manuel „schaff mal was“ Gerken, Binh Tran, Bing Zhu, Melina Filzinger und Markus Neiczer für die tolle Zusammenarbeit, die abwechslungsreiche Zeit im Labor und viele hilfreiche Verbesserungsvorschäge zu dieser Arbeit. Ich wünsche Euch viel Erfolg bei Euren zukünftigen Experimenten!

Alda („danke Alda“) Arias, Arthur Schönhals, Zhaodi Pan, Carmen Renner, Quentin Fontaine, Yicheng Zhang, Robin Eberhard und Benjamin Kraus für eure wertvolle Arbeit im Labor, Erweiterungen und Verbesserungen des Experiments und theoretische Berechnungen. Ohne Euch wäre so manch eine Messung nicht möglich gewesen.

Rydbergs, Haitraps und EQMs für die schöne Zeit innerhalb und außerhalb des Labors, für die Aushilfe mit Geräten und sonstigen Materialen, für viele Diskussionen und hilfreiche Vorschläge bei unseren Messungen, sowie die kleinen sportlichen Auszeiten.

Dr. Tilman Enss für die intensive Zusammenarbeit am gemeinsamen Polaronenprojekt und den vielen lehrreichen Diskussionen. Danke nicht zuletzt für die Übernahme der Prüfung.

Prof. Eberhard Tiemann für die Berechnungen zu den Li-Cs Feshbach Resonanzen, Interpretation der p-Wellen Aufspaltung, sowie die hilfreichen Erklärungen zur Molekülphysik.

Prof. Chris Greene, Dr. Yujun Wang, Dr. Dmitry Petrov, and Dr. Felix Werner. Thank you all for your calculations of the Li-Cs Efimov effect and answering our questions about two- and few-body physics.

Meera Parish, Jesper Levinsen, and Shimpei Endo for discussions about the connection between the Efimov effect and the Bose polaron in Li-Cs.

Den Ultracold und QUO-Gruppen für die gute Zusammenarbeit, für interessante Diskussionen und das Ausleihen von Labormaterial.

Den mechanischen und elektronischen Werkstätten des Institus für die Unterstützung bei Erweiterungen und Verbesserungen des Experiments. Stellvertetend möchte ich mich bei ihren Leitern *Ralf Ziegler*, *Dr. Venelin Angelov* und *Frank Schumacher* bedanken. Ein besonderer Dank geht an *Esteban Rubio* für die fortwährende Unterstützung mit der Experimentiersteuerung und *Klaus Layer* für seine Geduld bei der Herstellung von AOM-Treibern.

Dominic Litsch, dass Du Dich um unsere Sicherheit kümmerst und viele technische Aufgaben löst.

Der HGSFP und der IMPRS-QD für die Bereitstellung eines Stipendiums, Ermöglichung von Konferenzreisen und Sommerschulen, sowie exzellenten Seminaren, Symposien und Graduiertenkursen.

Mario dafür, dass Du mein Interesse für Physik geweckt und den Spaß am Experimentieren gezeigt hast. Du hast mich mit Deiner Begeisterung angesteckt und mir viel beigebracht.

Meinen Eltern, meiner Schwester sowie allen meinen Freunden für Eure Unterstützung während meines gesamten Studiums.

Ramona für Deine Geduld mit mir, den großen Rückhalt den Du mir bietest und dass Du mich immer wieder motivierst.